4-19-2017 12:00 AM

Linear and Nonlinear Dynamics of Spin Waves in Ferromagnetic Nanowires

Zahra Haghshenasfard, *The University of Western Ontario*

Supervisor: Prof. Michael G. Cottam, *The University of Western Ontario*

A thesis submitted in partial fulfillment of the requirements for the Doctor of Philosophy degree in Physics

Abstract

Motivated by recent experimental developments, we present a theoretical study of some linear and nonlinear properties of spin waves in ferromagnetic nanostructures under conditions of microwave pumping. A microscopic (or Hamiltonian-based) approach is followed including terms for both the short-range exchange and the long-range dipole-dipole interactions, as well as the effects of an external magnetic field, single-ion anisotropy, biquadratic exchange and the Ruderman-Kittel-Kasuya-Yosida interactions, as appropriate. In ultrathin films and nanowires with thickness or lateral dimensions less than about 100 nm, the discreteness of the quantized spin waves (or magnons) and their spatial distributions become modified, making it appropriate to employ a microscopic approach to the nonlinear dynamics based on a lattice model.

First an application is made to the magnetization dynamics in trilayer nanowires, consisting of Permalloy layers separated by a nonmagnetic Ru spacer layer. The experimental results for different stripe widths are successfully analyzed using our microscopic theory. Next we investigate the nonlinear spin-wave properties of ultrathin films and ferromagnetic nanowires with rectangular cross sections as well as nanowires and nanotubes with circular cross sections. Numerical results are deduced for the spin-wave frequencies as a function of wave vector, for either parallel or perpendicular external field orientations. Also numerical applications are presented for the dependence of the threshold microwave field amplitudes for instability on the static applied field (the analog of the butterfly curves). Effects due to the discreteness of the spin-wave branches lead to structural features in the butterfly curves that are significantly different, due to edge effects, in nanowires compared with those in the bulk and for ultrathin films. Further, we examine the in-

stability thresholds for nonlinear processes in ferromagnetic stripes and films under perpendicular pumping with an microwave field.

Finally the quantum statistical properties are investigated for microwave-driven magnon system in the presence of four-magnon interactions. In particular, collapse-and-revival-phenomena for the time evolution of the average magnon number, squeezing, and super-Poissonian statistics of magnons are studied. Bulk systems are analyzed initially, and then the results are generalized to consider cross correlation and other behavior in two-mode magnon systems.

Keywords: Dipole-exchange spin waves, Spin wave instability, Nonlinear properties, Parallel pumping, Perpendicular pumping, Ferromagnetic nanostructures, Nanowires and nanotubes, Trilayer composite nanowires, Ferromagnetic resonance, Coherent magnon states, Four-magnon interactions, Magnon occupation number, Magnon squeezing, Magnon statistics.

Dedication

To my parents and Behdad

Acknowledgements

I am greatly indebted and would like to express my gratitude to my supervisor Professor Michael G. Cottam who suggested this research topic and offered guidance for this investigation. Because of this vast knowledge of physics, his dedication as a supervisor, and his compassionate nature working with him was an absolute pleasure. The knowledge I have gained working with him will guide me throughout my career as a physicist.

My sincere thanks to the advisory committee members, Dr. David Rosner, and Dr. Giovanni Fanchini for giving their valuable time and suggestions during the advisory committee meetings.

It is a pleasure to thank Dr. Hoa Nguyen, Dr. P. Lupo, and Dr. A. Adeyeye for their assistance in research collaborations.

Next I would like to thank Arash Akbari-Sharbaf for helping me throughout my time at Western, and especially during difficult times.

I would also like to thank the Department of Physics and Astronomy at the University of Western Ontario for giving me the opportunity to study and carry out this work.

And last but not least, I would like to thank my family. To my parents, thank you for teaching me the importance of hard work, respect of others, and integrity. To my husband, Behdad Hosseini, for his love and support.

Table of Contents

List of Figures

List of Abbreviations

3D, 2D, 1D, 0D	three-dimensional, two-dimensional, one-dimensional, zero-dimensional
AFM	antiferromagnetic
AFMR	antiferromagnetic resonance
BCS	Bardeen-Cooper-Schrieffer
BEC	Bose – Einstein condensation
BLS	Brillouin light scattering
CPW	coplanar waveguide
DE	Damon – Eshbach (mode)
DM	Dzyaloshinskii-Moriya (interaction)
FM	ferromagnetic
FMR	ferromagnetic resonance
GMR	giant magnetoresistance
h.c.	Hermitian conjugate
IEC	interlayer exchange coupling
ILS	inelastic light scattering
INS	inelastic neutron scattering
LLG	Landau-Lifshitz-Gilbert (equation)
MC	magnonic crystal
NW	nanowire
RKKY	Ruderman-Kittel-Kasuya-Yosida (interaction)
RLS	Raman light scattering
RPA	random-phase approximation
s.c.	simple cubic
SEM	scanning electron microscope (or micrograph)
SF	spin-flop (phase)
SW	spin wave
SWR	spin-wave resonance
VSM	vibrating sample magnetometer
YIG	yttrium iron garnet

Chapter 1

Introduction

The most significant advances in magnetism occurred in the 18th century with the discovery of the link between electricity and magnetism by Gauss, Ampere and Faraday, among others. Soon afterwards, Maxwell formulated the relation between electricity and magnetism mathematically [1]. Later, microscopic aspects of magnetism and the connection to macroscopic descriptions of magnetism were developed [2]. Since then, due to the advances in material growth and fabrication techniques at submicron and nanometer sizes, much attention has been given to studies of the magnetization dynamics of nano-sized magnetic structures, such as magnetic dots, wires, films, rings, etc, either singly or in arrays [3, 4, 5]. Also, magnetic nanoelements in multilayers have attracted tremendous interest due to their technological applications. For example, in 1988 the phenomenon of giant magnetoresistance (GMR) [6, 7] in ordered magnetic nanostructures was discovered. Later the 2007 Nobel prize was awarded to Fert and Grünberg for the discovery of GMR, which is now the basis of devices such as read heads of hard disks, solid-state magnetic sensors, magnetic-recording devices, spin-logic devices, etc [8]. The low cost and high sensitively are advantages of these devices, as well as these being much smaller and faster.

Magnetic materials occur in different types. The most common classification scheme includes diamagnetism and paramagnetism as representing weak magnetic behavior, while ferromagnetism, antiferromagnetism, and ferrimagnetism constitute strong magnetic behavior [9]. The magnetic

materials of interest can be classified with reference to their magnetic susceptibility χ defined as $\chi = {}^{\partial M}/_{\partial H_0}$, where M is the net macroscopic magnetic moment per unit volume (magnetization) and H_0 is the applied field. If $M \neq 0$, which is the case for ferromagnets and ferrimagnets, there is a magnetic moment even in a zero external magnetic field, i.e., a spontaneous magnetization. A nonzero spontaneous moment results from the ordering of the electron spins in a regular manner due to interactions. However, there is another important class of materials called antiferromagnets for which $M = 0$ and yet they also have a magnetically-ordered structure. Illustrations for the various magnetically-ordered structures are represented schematically in Fig. 1.1, where the arrows show the direction and magnitude of the net spin angular momentum at any lattice site. In the case of ferromagnets the spins preferentially line up parallel to each other, while for ferrimagnets and antiferromagnets the adjacent spins (on different sublattices) preferentially align antiparallel with respect to one another (canceling the net magnetization in the latter case). In ferrimagnets the magnitudes of the antiparallel moments are unequal. The above effects occur below a critical temperature, which is called the Curie temperature T_c for ferromagnets and ferrimagnets and the Néel temperature T_N for antiferromagnets. At higher temperatures the spontaneous magnetization vanishes and the materials become paramagnetic (with χ small and positive).

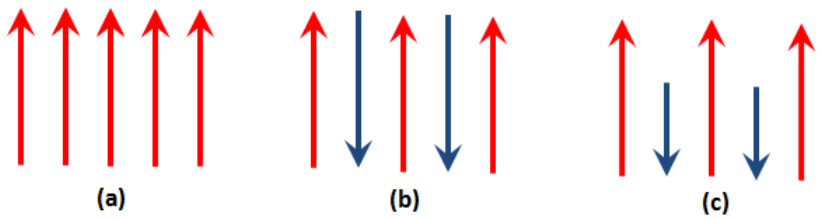

Figure 1.1: Simple schematic representation of spin vectors in one dimension for (a) a ferromagnet, (b) an antiferromagnet, and (c) a ferrimagnet.

1.1 Magnetic interactions

In ordered magnetic materials the strongest type of interaction, which is mainly responsible for the magnetic ordering is called the Heisenberg exchange interaction and was first explained by

Heisenberg in 1926. The nature of the interaction is electronic and is due to quantum-mechanical exchange arising as a consequence of the Pauli exclusion principle, which states that no two electrons in a system are allowed to occupy the same quantum state. Also the total wave function of the pair must be antisymmetric when the electrons are exchanged. This leads to a difference between the energies of the states for which the spins are either parallel or antiparallel. This is in addition to the classical Coulomb energy between the electrons. The Heisenberg Hamiltonian which describes this interaction between pairs of spins can usually be expressed in the form [10, 11, 12]

$$H_{\text{ex}} = -\frac{1}{2}\sum_{i,j} J_{i,j}\mathbf{S}_i \cdot \mathbf{S}_j, \tag{1.1}$$

where the summation is over all distinct pairs i and j and the factor of $1/2$ is to avoid double counting. The quantity $J_{i,j}$ is called the exchange interaction between spins $\mathbf{S}_i$ and $\mathbf{S}_j$ and is related to the overlap of the electronic wave functions centered at i and j. As a consequence, the exchange interaction is typically short-range. To a good approximation, $J_{i,j}$ is appreciable only between the nearest neighbors and will be denoted by J. The cases of $J > 0$ and $J < 0$ correspond to the parallel alignment (ferromagnets) and antiparallel alignment (antiferromagnets and ferrimagnets) of spins, respectively (see Fig. 1.1).

In a more general case, the Heisenberg interaction may take an anisotropic form [13, 14, 15] consistent with the symmetry of the material:

$$H_{\text{ex}} = -\frac{1}{2}\sum_{i,j} J_{i,j}\left(\varepsilon_x S_i^x S_j^x + \varepsilon_y S_i^y S_j^y + \varepsilon_z S_i^z S_j^z\right), \tag{1.2}$$

where ε_x, ε_y and ε_z are dimensionless parameters. The isotropic Heisenberg Hamiltonian, which corresponds to $\varepsilon_x = \varepsilon_y = \varepsilon_z = 1$, and the Ising Hamiltonian, which corresponds to $\varepsilon_x = \varepsilon_y = 0$, $\varepsilon_z = 1$, are cases of special interest.

Apart from the short-range direct exchange, there may be an indirect exchange which couples moments in some materials over relatively larger distances (e.g., several nm). In metals, when there is a weak or no direct overlap of the wave functions of neighboring electrons, this indirect exchange becomes important. This interaction in metals acts through the conduction electrons and

was introduced by Ruderman and Kittel [16]. Later Kasuya and Yosida [17, 18, 19, 14] explained this interaction in more details. Because of these developments, the indirect coupling of magnetic moments via conduction electrons is known as the Ruderman-Kittel-Kasuya-Yosida (RKKY) interaction. Rare-earth metals also show rather weak direct exchange, and therefore the RKKY interaction contributes to magnetic ordering in these materials. In some low-dimensional systems the RKKY coupling across a thin metallic layer between two other magnetic materials is of interest for device applications such as microwave resonators, magnetic filters, memory and spin-wave (SW) logic devices [20, 21, 3]

In addition to the RKKY interaction, there may be other exchange effects due to the biquadratic exchange. This interaction can be expressed as [22, 13, 12]

$$H_{\mathrm{BQ}} = \frac{1}{2}\sum_{i,j} J_{bq(i,j)} \left(\mathbf{S}_i \cdot \mathbf{S}_j\right)^2, \tag{1.3}$$

where the sign convention is such that a 90° relative orientation of the magnetizations would be favored due to this term alone when $J_{BQ} > 0$. Typically, this type of interaction might be small in bulk materials, but it can become important at surfaces and interfaces. The name biquadratic is in distinction to the simpler interactions in Eqs. (1.1) and (1.2), which are sometimes called bilinear.

A more general bilinear exchange interaction between two neighboring magnetic spins $\mathbf{S}_i$ and $\mathbf{S}_j$ was proposed by Dzyaloshinskii and Moriya. In 1960 Dzyaloshinskii [23] introduced a model to describe the helical magnetization in some material, namely chiral magnets (materials characterized by a lack of inversion symmetry). Later Moriya [24] explained that this mechanism is based on spin-orbit coupling. This antisymmetric exchange mechanism has the following form

$$H_{\mathrm{DM}} = \sum_{i,j} \mathbf{J}_{ij}^{DM} \cdot \left(\mathbf{S}_i \times \mathbf{S}_j\right), \tag{1.4}$$

where $\mathbf{J}_{ij}^{DM}$ is known a the Dzyaloshinskii-Moriya (DM) interaction.

The other main form of interaction in magnetic materials is due to magnetic dipole-dipole interactions described by Maxwell's equations [10]. Each spin has a magnetic moment and each magnetic dipole produces a magnetic field around itself. The classical dipolar interaction between

the moments gives rise to a contribution to the energy of

$$H_{\text{dip}} = \frac{1}{2}(g\mu_B)^2 \sum_{i,j} \sum_{\alpha,\beta} D_{i,j}^{\alpha\beta} S_i^{\alpha} S_j^{\beta}, \tag{1.5}$$

where g is the Landé factor, μ_B is the Bohr magneton, and α and β denote Cartesian components (x, y, z), while the dipolar interactions $D_{i,j}^{\alpha\beta}$ have the form

$$D_{i,j}^{\alpha\beta} = \frac{\left|\mathbf{r}_{i,j}\right|^2 \delta_{\alpha\beta} - 3r_{i,j}^{\alpha} r_{i,j}^{\beta}}{\left|\mathbf{r}_{i,j}\right|^5}. \tag{1.6}$$

Here $\mathbf{r}_{i,j} \equiv \mathbf{r}_i - \mathbf{r}_j$ is the vector connecting sites i and j. This interaction is long-range but it is typically much weaker than the exchange interaction between nearest-neighboring sites. This means that the exchange interaction predominantly is responsible for magnetic ordering as well as many static properties of magnetic systems. However, dipole-dipole interactions can add up to be significant in certain regimes for the dynamical properties at long enough wavelengths.

Another type of magnetic energy is known as magnetic anisotropy, which corresponds to the presence of a preferential magnetization direction along certain crystal axes in a material. In simple cases it has a uniaxial form and can be represented by [25]

$$H_{\text{an}} = -\sum_i K \left(S_i^z\right)^2, \tag{1.7}$$

where K is known as the anisotropy constant. When $K > 0$, the minimum energy corresponds to the magnetization parallel to the z axis (known as the easy axis) and when $K < 0$, the minimum energy is obtained when the magnetization lies in the xy plane (the easy plane). There may be various different origins for the magnetic anisotropy. One is crystalline (single-ion) anisotropy due to spin-orbit interaction effects and another is shape (magnetic dipole) anisotropy. If the magnetic anisotropy appears as a consequence of mechanical stress, it is called magnetostrictive anisotropy. Shape anisotropy arises due to the dipole fields between the bounding material surfaces, and hence this interaction become important in thin films and other nanostructures. In principle, it is contained within the Hamiltonian in Eq. (1.5).

Finally, in the presence of an applied magnetic field of magnitude H_0, there is an extra potential

energy term in the Hamiltonian called the Zeeman energy:

$$H_{\text{Zeeman}} = -g\mu_B \mathbf{H}_0 \cdot \sum_i \mathbf{S}_i. \tag{1.8}$$

The Zeeman energy tends to line up, or reorient, the magnetic moments in the direction of the applied field. It has to overcome the effects of magnetic anisotropy, or the competing effects of the other interactions already mentioned, to get the magnetic moments to be parallel to a hard direction for the magnetic material.

1.2 Concept of spin waves

Spin waves (SWs) are the lowest elementary excitations in magnetically ordered materials. Under suitable circumstances SWs can exhibit a variety of phenomena, such as dispersive or non-dispersive propagation, reciprocal or non-reciprocal wave propagation, damping characteristics, and a variety of SW instabilities [13, 26, 27, 28]. This richness has led to a number of actual applications in optical and microwave signal processing, frequency-selective limiters, high-frequency devices, and switches, etc, particularly on the nanometre scale.

Since Bloch's historic paper on the power-law temperature dependence of the spontaneous magnetization of ferromagnets [29] SWs have attracted much attention as low-lying excitations or spin fluctuations that occur in ordered magnetic materials. Since spins are described in terms of quantum-mechanical operators, the SWs are quantized, with the basic quantum being referred to as the magnon (although the terms spin waves and magnons are typically used interchangeably). Initially the experimental evidence for SWs came from the measurement of thermodynamic properties, like specific heat, while nowadays there are many sensitive and direct techniques for studying linear and nonlinear processes involving SW excitations. These techniques include, for example, the inelastic scattering of photons (light) or particles (e.g., neutrons) and magnetic resonance (see Section 1.6).

In his pioneering work Bloch [29] considered the spins semi-classically as deviating slightly

from their ground-state orientations, with this disturbance traveling with a wavelike behavior through the crystal. Nowadays, various approaches to SW theory can be followed. One method is the semi-classical description of SWs [30] in terms of spin precession. Another approach is quantum-mechanical involving either field-theoretical techniques or second quantization for the spins operators [31]. It is often helpful to picture magnons schematically as in Fig. 1.2 in terms of arrays of precessing spin vectors, where there is a small change of phase (related to the wave vector) from any one spin to a neighboring spin. In this semi-classical viewpoint the precession of a spin vector takes place due to the torque from an effective magnetic field that incorporates all the magnetic interactions with other spins as well as any applied magnetic field. In simple cases (such as at low temperatures compared with the Curie temperature T_c) the angle of precession is small, meaning that the component of the spin vector along the direction of net magnetization remains approximately constant.

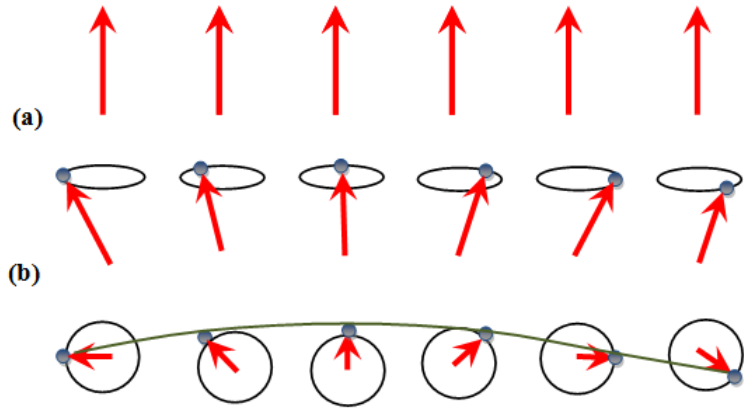

Figure 1.2: Schematic representation of spins in a ferromagnet: (a) the ground state, and (b) an excited state corresponding to a spin wave (SW) or magnon (in perspective and top view).

The properties of SWs depend on the types of interactions between spins as well as the types of ordered magnetic materials. These interactions arise mainly from (a) the short-range exchange interactions, which are quantum-mechanical in nature and are due to the overlap of wave functions on neighboring atoms, and (b) the long-range magnetic dipole-dipole interactions as in classical electromagnetism. Apart from the nature of the magnetic interactions, the boundaries (i.e., surfaces and interfaces) in a finite sample may change the SW behavior [13]. In an effectively infinite

material, excitations such as SWs are required to satisfy symmetry requirement based on Bloch's theorem, which states that a variable $\psi_{\mathbf{k}}(\mathbf{r})$ describing any excitation amplitude must have the special form [32]

$$\psi_{\mathbf{k}}(\mathbf{r}) = U_{\mathbf{k}}(\mathbf{r}) \exp(i\mathbf{k} \cdot \mathbf{r}), \tag{1.9}$$

where $U_{\mathbf{k}}(\mathbf{r})$ has the periodicity of the crystal lattice, and $\mathbf{k}$ represents the three-dimensional (3D) wave vector in the Brillouin zone of the reciprocal lattice of the crystal. For SWs $U_{\mathbf{k}}(\mathbf{r})$ is a component of the spin or magnetic moment, and the energy of the magnons is denoted by $\hbar\omega(\mathbf{k})$ with $\omega(\mathbf{k})$ representing the SW angular frequency.

A consequence in reciprocal space is that (when a Fourier transform of the interactions is made to a wave-vector representation [32]) the short-range exchange dominates at medium and large wave vectors in the Brillouin zone, but the long-range dipolar effects are important at small enough wave vectors. Typically in bulk ferromagnets the dipolar terms need to be included for wave vectors less than about 1/100 of the Brillouin zone boundary value, which is relevant for experimental techniques mentioned later, such as ferromagnetic resonance (FMR) and Brillouin light scattering (BLS) that probe the so-called magnetostatic and dipole-exchange regimes [25, 27].

It is appropriate here to comment on the definitions and conventions to be followed for the magnetic field variables. These are the magnetic flux density $\mathbf{B}$ and the magnetic intensity $\mathbf{H}$ along with the magnetization $\mathbf{M}$. In SI system they are related by $\mathbf{B} = \mu_0(\mathbf{H} + \mathbf{M})$, where the units are tesla (T) for $\mathbf{B}$ and A/m for $\mathbf{H}$ and $\mathbf{M}$; also $\mu_0 = 4\pi \times 10^{-7}$ H. m^{-1}. It is still common and convenient in the research literature to use the Gaussian-cgs system, where $\mathbf{B} = \mu_0(\mathbf{H} + 4\pi\mathbf{M})$. The units for $\mathbf{B}$ and $\mathbf{H}$ are gauss (G) and oersted (Oe), respectively and $\mu_0 = 1$ in (G/Oe). Clear accounts of the two systems are given by Arrott [33] and in electromagnetism textbooks (see [9]). We will employ the Gaussian system here, where the focus is on using the $\mathbf{H}$ field. For specific applications, we generally quote $\mu_0\mathbf{H}$ values in T, noting that 10^4 Oe is equivalent to $\mu_0\mathbf{H} = 1$ T. Also we will quote the saturation magnetization in terms of the so-called "saturation induction" (defined as $\mu_0\mathbf{M}$ or $4\pi\mu_0\mathbf{M}$ in the SI or Gaussian systems, respectively) in T units.

1.3 Spin waves in bulk materials

Here we summarize properties of the SWs in bulk (infinite-size) ferromagnets, where there are no surface (boundary) effects to consider. We assume that the bulk sample is placed in an applied field H_0 along the z direction. The Heisenberg Hamiltonian for the system is then given by

$$H = -\frac{1}{2}\sum_{i,j} J_{i,j}\mathbf{S}_i \cdot \mathbf{S}_j - g\mu_B H_0 \sum_i S_i^z, \tag{1.10}$$

which is the sum of the exchange and Zeeman energy terms. For simplicity we do not include other magnetic interactions such as dipole-dipole and single-ion anisotropy in the Hamiltonian at this stage. The Hamiltonian (1.10) can first be re-expressed in terms of the spin operators S_i^+, S_i^- and S_i^z at site i, with $S_i^\pm = S_i^x \pm S_i^y$ denoting the usual spin raising and lowering operators. The spin operators are neither bosons nor fermions operators, and they satisfy the commutation relations as follows [34]:

$$\left[S_i^+,\ S_j^-\right] = 2S_i^z\delta_{i,j}, \quad \left[S_i^z,\ S_j^\pm\right] = \pm S_i^\pm\delta_{i,j}, \qquad (\hbar = 1) \tag{1.11}$$

where we use the commutator notation that $[a, b] \equiv ab - ba$ for any operators. The Hamiltonian can be written as

$$H = -\frac{1}{2}\sum_{i,j} J_{i,j}\left[\frac{1}{2}\left(S_i^+S_j^- + S_i^-S_j^+\right) + S_i^zS_j^z\right] - g\mu_B H_0\sum_i S_i^z. \tag{1.12}$$

The relation between the wave vector $\mathbf{k}$ and frequency $\omega(\mathbf{k})$ of the SWs (i.e., the dispersion relation) can be calculated using macroscopic (continuum) or microscopic (Hamiltonian-based) approaches. We start with the microscopic method and then we continue with an outline of the macroscopic approach, demonstrating the consistency of the methods.

1.3.1 Microscopic approach

Here we adopt a quantum-mechanical approach based on the so-called Holstein-Primakoff representation [31]. The spin Hamiltonian can be transformed into an equivalent form in terms of boson

creation and annihilation operators $a_i^\dagger$ and a_i, respectively, using the expressions:

$$\begin{aligned} S_i^+ &= \sqrt{2S}\left(1 - \frac{a_i^\dagger a_i}{2S}\right)^{1/2} a_i, \\ S_i^- &= \sqrt{2S}\, a_i^\dagger \left(1 - \frac{a_i^\dagger a_i}{2S}\right)^{1/2}, \\ S_i^z &= S - a_i^\dagger a_i. \end{aligned} \tag{1.13}$$

Here the boson operators satisfy the standard quantum-mechanical commutation relations [34]

$$\left[a_i,\ a_j^\dagger\right] = \delta_{i,j}, \quad \left[a_i^\dagger,\ a_j^\dagger\right] = \left[a_i,\ a_j\right] = 0, \tag{1.14}$$

from which it can be proved that the spin commutation relations in Eq. (1.11) are recovered. At low temperatures ($T \ll T_c$), the spins are well aligned so that $S_i^z \simeq S$, which means $a_i^\dagger a_i \ll S$ and this allows us to expand the square roots in Eq. (1.13) to get

$$\left(1 - \frac{a_i^\dagger a_i}{2S}\right)^{1/2} = 1 - \frac{a_i^\dagger a_i}{4S} + \cdots. \tag{1.15}$$

This leads to

$$S_i^+ = \sqrt{2S}\left[a_i - \frac{a_i^\dagger a_i a_i}{4S} + \cdots\right], \tag{1.16}$$

and a similar result for S_i^-. Then the Hamiltonian (1.12) becomes approximately (on neglecting higher-order products of boson operators)

$$H = H^{(0)} - \frac{1}{2}S\sum_{i,j} J_{i,j}\left(a_i^\dagger a_j + a_j^\dagger a_i - a_i^\dagger a_i - a_j^\dagger a_j\right) + g\mu_B H_0 \sum_i a_i^\dagger a_i, \tag{1.17}$$

where $H^{(0)}$is just a constant, representing the energy of the ground state of the ferromagnet. Next we define the Fourier transformation of the boson operators and the exchange interaction from a position to a wave-vector representation by

$$
\begin{aligned}
a_i &= \frac{1}{\sqrt{N}}\sum_k a_k \exp\left(-i\mathbf{k}\cdot\mathbf{r}_i\right), \qquad a_i^\dagger = \frac{1}{\sqrt{N}}\sum_k a_k^\dagger \exp\left(i\mathbf{k}\cdot\mathbf{r}_i\right), \\
J_{i,j} &= \frac{1}{N}\sum_k J(\mathbf{k}) \exp\left[i\mathbf{k}\cdot\left(\mathbf{r}_i - \mathbf{r}_j\right)\right].
\end{aligned} \tag{1.18}
$$

Here N is the total number of magnetic sites and $\mathbf{k}$ is a 3D wave vector. Using (1.18) the Hamiltonian (1.17) takes the following simple form

$$
H = H^{(0)} + \sum_k \omega(\mathbf{k}) a_k^\dagger a_k, \tag{1.19}
$$

where the operators $a_k^\dagger$ and a_k create and annihilate a SW excitation of wave vector $\mathbf{k}$ and frequency $\omega(\mathbf{k})$, where

$$
\omega(\mathbf{k}) = g\mu_B H_0 + S\left[J(0) - J(\mathbf{k})\right]. \tag{1.20}
$$

This represents the SW dispersion relation, as can be seen from the operator equation [34]

$$
i\frac{da_k}{dt} = [a_k, H] = \omega(\mathbf{k}) a_k. \tag{1.21}
$$

On solving for the time dependence of this equation , we obtain $a_k \sim \exp\left(-i\omega(\mathbf{k})t\right)$, which represents an oscillator equation with angular frequency $\omega(\mathbf{k})$, giving us the SW dispersion relation.

If we consider the exchange to take the value J to the 6 nearest neighbors in a simple cubic lattice (with lattice constant a), it is easy to show that

$$
J(\mathbf{k}) = 2J\left[\cos\left(k_x a\right) + \cos\left(k_y a\right) + \cos\left(k_z a\right)\right]. \tag{1.22}
$$

Now if we take small $\mathbf{k}$ in the Brillouin zone, this expression approximates to $J(\mathbf{k}) \approx 6J - Jk^2a^2$ (with $k = |\mathbf{k}|$ and $k^2a^2 \ll 1$). Therefore at small k we obtain

$$
\omega(\mathbf{k}) = g\mu_B H_0 + Dk^2, \tag{1.23}
$$

where $D = SJa^2$ is often called the SW stiffness (or exchange stiffness). Therefore, in the exchange-dominated case, the SW frequency has a minimum value $g\mu_B H_0$ (the FMR frequency

described later) at $k \approx 0$, and it increases monotonically with $\mathbf{k}$.

The above results for a bulk material can be generalized to include the long-range magnetic dipole-dipole interaction as well as the exchange interaction. In this case, the Hamiltonian (1.19) becomes generalized to [35]

$$H = \sum_k U(\mathbf{k}) a_k^\dagger a_k + \frac{1}{2} V(\mathbf{k}) a_k a_{-k} + \frac{1}{2} V^*(\mathbf{k}) a_k^\dagger a_{-k}^\dagger, \tag{1.24}$$

where

$$\begin{aligned} U(\mathbf{k}) &= g\mu_B H_0 + S\left[J(0) - J(\mathbf{k})\right] + S\left[D^{z,z}(0) + \frac{1}{2} D^{z,z}(\mathbf{k})\right], \\ V(\mathbf{k}) &= \frac{1}{2} S\left[D^{x,x}(\mathbf{k}) - D^{y,y}(\mathbf{k}) - 2iD^{x,y}(\mathbf{k})\right]. \end{aligned} \tag{1.25}$$

Here the dipole sums are

$$D^{\alpha,\beta}(\mathbf{k}) = g^2 \mu_B^2 \sum_r \frac{3r^\alpha r^\beta - |\mathbf{r}|^2 \delta_{\alpha,\beta}}{|\mathbf{r}|^5} \exp\left(i\mathbf{k} \cdot \mathbf{r}\right), \tag{1.26}$$

and the results for the SW frequency can eventually be found as [35]

$$\omega(\mathbf{k}) = \left[U(\mathbf{k})^2 - |V(\mathbf{k})|^2\right]^{1/2}. \tag{1.27}$$

In a small k approximation in three dimensions, it can be shown that this takes the explicit form [13, 32]

$$\omega(\mathbf{k}) = \left[g\mu_B H_0 + Dk^2 - \omega_M \left(N_z - \sin^2(\theta_k)\right)\right]^{1/2} \left[g\mu_B H_0 + Dk^2 - \omega_M N_z\right]^{1/2}. \tag{1.28}$$

Here we denoted $\omega_M = 4\pi g \mu_B M_s$ with M_s denoting the saturation value of the magnetization, N_z is the demagnetizing factor in the z direction, and θ_k is the angle between $\mathbf{k}$ and the z axis. This is the dipole-exchange SW dispersion relation, and is sometimes called the Kittel formula.

The magnetostatic limit (where exchange effects are negligible), corresponds to $Dk^2 \ll \omega_M$ in Eq. (1.28). Then the dispersion relation simplifies further to take the form

$$\omega(\mathbf{k}) = \left[\omega_H \left(\omega_H + \omega_M \sin^2(\theta_k)\right)\right]^{1/2}, \tag{1.29}$$

where $\omega_H = g\mu_B (H_0 - N_z M_s)$.

1.3.2 Macroscopic approach

The relationship between the total magnetization **M** and the total angular momentum **J** is expressed as $\mathbf{M} = -g\mu_B \mathbf{J}$ and the net torque is equal to the rate of change of the angular momentum ($\tau = \partial \mathbf{J}/\partial t$). Therefore, the torque equation of motion for the total magnetization **M** in terms of the total effective magnetic field $\mathbf{H}_{\text{eff}}$ is given by

$$\frac{\partial \mathbf{M}}{\partial t} = -g\mu_B (\mathbf{M} \times \mathbf{H}_{\text{eff}}), \tag{1.30}$$

where **M** has a static part M_s (along z) and a fluctuating part **m** at angular frequency ω:

$$\mathbf{M}(\mathbf{r}, t) = M_s \hat{z} + \mathbf{m}(\mathbf{r}) e^{-i\omega t}. \tag{1.31}$$

Here $\hat{z}$ is a unit vector and the total effective field $\mathbf{H}_{\text{eff}}$ given by

$$\mathbf{H}_{\text{eff}}(\mathbf{r}, t) = H_0 \hat{z} + \mathbf{H}_{\text{ex}}(\mathbf{r}, t) + \mathbf{H}_{\text{dipole}}(\mathbf{r}, t) \tag{1.32}$$

comprising terms due to an applied field H_0 along the z axis, an exchange field $\mathbf{H}_{\text{ex}}$ and a dipole field $\mathbf{H}_{\text{dipole}}$. The latter two contributions can be deduced as described below. Fig. 1.3 shows the magnetization precession with and without damping (or energy dissipation). The role of damping is mentioned later in section 1.6.

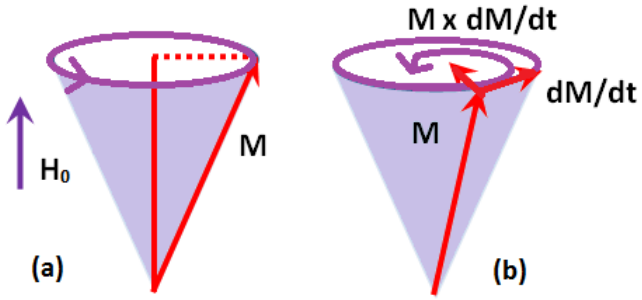

Figure 1.3: The magnetization precession for (a) undamped motion and (b) motion with damping.

In the macroscopic method, instead of boson operators, we employ the magnetization field

vector $\mathbf{M}(\mathbf{r})$. For a ferromagnet the exchange energy (1.1) becomes

$$E_{\text{ex}} = -\frac{1}{2g^2\mu_B^2}\int d^3r\, d^3r'\; J(\mathbf{r}-\mathbf{r}')\mathbf{M}(\mathbf{r})\cdot\mathbf{M}(\mathbf{r}'), \tag{1.33}$$

Because the exchange is a short-range interaction, we may use a Taylor series to expand $\mathbf{M}(\mathbf{r}')$ around the point $\mathbf{r}$:

$$\mathbf{M}(\mathbf{r}') = \mathbf{M}(\mathbf{r}) + (\mathbf{r}'-\mathbf{r})\cdot\nabla\mathbf{M}(\mathbf{r}) + \frac{1}{2}\left[(\mathbf{r}'-\mathbf{r})\cdot\nabla\right]^2\mathbf{M}(\mathbf{r}) + \cdots. \tag{1.34}$$

After some mathematical steps, the leading-order result for the energy becomes

$$E_{\text{ex}} = -\frac{1}{2}\int d^3r\left[F_0\mathbf{M}^2(\mathbf{r}) - F_2\mathbf{M}(\mathbf{r})\cdot\nabla^2\mathbf{M}(\mathbf{r})\right], \tag{1.35}$$

where the constants are

$$F_0 = \frac{1}{2g^2\mu_B^2}\int d^3r' J(\mathbf{r}'), \qquad F_2 = \frac{1}{6g^2\mu_B^2}\int d^3r' J(\mathbf{r}')\,|r'|^2\,. \tag{1.36}$$

Using the above equations the corresponding exchange field can be written as

$$H_{\text{ex}} = -\frac{\delta}{\delta\mathbf{M}(\mathbf{r})}E_{\text{ex}} = F_0\mathbf{M} + F_2\nabla^2\mathbf{M}. \tag{1.37}$$

Substituting (1.31) and (1.32) into the torque equation (1.30) leads to

$$-i\omega\mathbf{m}(\mathbf{r}) = g\mu_B\left[H_0 - F_2\nabla^2\right]\mathbf{m}(\mathbf{r})\times\hat{z}. \tag{1.38}$$

By assuming $\mathbf{m}(\mathbf{r}) \sim \exp(i\mathbf{k}\cdot\mathbf{r})$ for wave-like behavior, we obtain $\nabla^2\mathbf{m}(\mathbf{r}) = -k^2\mathbf{m}(\mathbf{r})$. Therefore Eq. (1.38) can be re-expressed as

$$-i\omega\mathbf{m}(\mathbf{r}) = g\mu_B\left[H_0 + F_2k^2\right]\mathbf{m}(\mathbf{r})\times\hat{z}. \tag{1.39}$$

The solution for the SW dispersion relation $\omega(\mathbf{k})$ can be found (noting $g\mu_BF_2 = M_sJa^2/g\mu_B$) as

$$\omega(\mathbf{k}) = g\mu_BH_0 + Dk^2, \tag{1.40}$$

which is the same as found before in Eq. (1.23), demonstrating the consistency of the methods.

Now we can take into account the long-range magnetic dipole-dipole interaction in the torque

equation (1.30) instead of the exchange interaction. The dipole-dipole contribution to the total field can be written as

$$\mathbf{H}_{\text{dipole}}(\mathbf{r}, t) = -N_z M_s \hat{z} + \mathbf{h}_{\text{dipole}}(\mathbf{r}) \exp(-i\omega t), \tag{1.41}$$

Substituting Eqs. (1.41) and (1.31) into (1.30) leads approximately to

$$-i\omega \mathbf{m}(\mathbf{r}) = g\mu_B \left[H_0 \mathbf{m}(\mathbf{r}) - M_s \mathbf{h}_{\text{dipole}}(\mathbf{r}) \right] \times \hat{z}. \tag{1.42}$$

This can be rearranged in component form as a susceptibility relationship:

$$\begin{pmatrix} m_x \\ m_y \\ m_z \end{pmatrix} = \frac{1}{4\pi} \begin{pmatrix} \chi_a & i\chi_b & 0 \\ -i\chi_b & \chi_a & 0 \\ 0 & 0 & 0 \end{pmatrix} \begin{pmatrix} h_{\text{dipole},x} \\ h_{\text{dipole},y} \\ h_{\text{dipole},z} \end{pmatrix}..$$

Here we have defined $\chi_a = \omega_M \omega_H / \left(\omega_H^2 - \omega^2 \right)$ and $\chi_b = \omega_M \omega / \left(\omega_H^2 - \omega^2 \right)$, with $\omega_m = 4\pi g \mu_B M_s$ and ω_H as before. Now we use Maxwell's equations in the magnetostatic limit ($c \to \infty$) :

$$\nabla \times \mathbf{h}_{\text{dipole}}(\mathbf{r}) = 0, \qquad \nabla \cdot \left[\mathbf{h}_{\text{dipole}}(\mathbf{r}) + 4\pi \mathbf{m}(\mathbf{r}) \right] = 0. \tag{1.43}$$

The first of the above equations is automatically satisfied if we introduce the magnetic scalar potential by $\mathbf{h}_{\text{dipole}}(\mathbf{r}) = \nabla \psi_{\mathbf{k}}(\mathbf{r})$ [9]. Substituting this potential into the second equation leads to

$$(1 + \chi_a) \left(\frac{\partial^2 \psi_{\mathbf{k}}}{\partial x^2} + \frac{\partial^2 \psi_{\mathbf{k}}}{\partial y^2} \right) + \chi_a \frac{\partial^2 \psi_{\mathbf{k}}}{\partial z^2}. \tag{1.44}$$

Then, using Eq. (1.9) and substituting for the susceptibility element χ_a, solving for ω gives

$$\omega(\mathbf{k}) = \left[\omega_H \left(\omega_H + \omega_M \sin^2(\theta_k) \right) \right]^{1/2}. \tag{1.45}$$

We can now combine the previous two calculations for the SW frequencies in the exchange case (1.40) and the dipole-dipole case (1.45) by including both $\mathbf{H}_{\text{ex}}(\mathbf{r}, t)$ and $\mathbf{H}_{\text{dipole}}(\mathbf{r}, t)$ in the torque equation (1.30). A simple way is to take the magnetostatic result for the SW frequency and make the replacement of ω_H with $\omega_H + Dk^2$ to include exchange. This leads to

$$\omega(\mathbf{k}) = \left[\left(\omega_H + Dk^2 \right) \left(\omega_H + Dk^2 + \omega_M \sin^2(\theta_k) \right) \right]^{1/2}. \tag{1.46}$$

This expression is consistent with the microscopic result in Eq. (1.29).

1.4 SWs in confined magnetic systems

As mentioned, the magnons for a simple bulk ferromagnet in 3D are characterized by a wave vector $\mathbf{k} = \left(k_x, k_y, k_z\right)$. By contrast, in magnetic nanostructures, where one (or more) of the spatial dimensions is of order tens or hundreds of nanometres, the magnons are spatially confined and are required to satisfy boundary conditions at the surfaces or interfaces. In a thin film, for example, the magnons are characterized by a 2D wave vector in the directions of translational symmetry parallel to the surfaces. In the direction perpendicular to the surfaces, the magnons may either take a standing-wave form with a quantized value for the third wave-vector component, or they may be localized with amplitude decaying away from one or both surfaces. Likewise in a nanowire there is a 1D wave vector along the length and standing-mode behavior or localization in the other two directions.

The SW behavior in low-dimensional ferromagnetic structures is therefore very different from that in bulk materials. It is because the translational symmetry is broken in the presence of surfaces and interfaces. As a consequence Bloch's theorem has to be modified, and boundary conditions have to be taken into account at the surfaces. Therefore, the SW modes become quantized, typically consisting of discrete branches [13].

As examples of low-dimensional structures, we now consider thin films with finite thickness L and parallel planar surfaces. The modified Bloch's theorem can be expressed as

$$\psi(\mathbf{r}_{\shortparallel}, z) = U_{\mathbf{k}\shortparallel}(\mathbf{r}_{\shortparallel}, z) \exp\left(i\mathbf{k}_{\shortparallel} \cdot \mathbf{r}_{\shortparallel}\right). \tag{1.47}$$

Here it is assumed that the film surfaces are in the xy plane and the z axis is perpendicular to the surfaces, so $\mathbf{r}_{\shortparallel} = (x, y)$ and $\mathbf{k}_{\shortparallel} = (k_x, k_y)$ are the 2D in-plane vectors. First, we consider the dipolar-dominated case. The general solution for the scalar potential $\psi_{\mathbf{k}}$ (see Eq. (1.44)) in the three spatial regions for z has the form

$$\psi_{\mathbf{k}} = \begin{cases} a_1 \exp(-k_{\shortparallel} z) \exp(i\mathbf{k}_{\shortparallel} \cdot \mathbf{r}_{\shortparallel}) & z > 0 \\ [a_2 \exp(ik_z z) + a_3 \exp(-ik_z z)] \exp(i\mathbf{k}_{\shortparallel} \cdot \mathbf{r}_{\shortparallel}) & 0 > z > -L \\ a_4 \exp(k_{\shortparallel} z) \exp(i\mathbf{k}_{\shortparallel} \cdot \mathbf{r}_{\shortparallel}), & z < -L \end{cases}$$

where a_i (with $i = 1, 2, 3, 4$) are constants and the quantity k_z, which can be real or imaginary, is given by

$$(1 + \chi_a)\left(k_z^2 + k_{\shortparallel}^2\right) - \chi_a k_z^2 = 0. \tag{1.48}$$

We then apply the usual electromagnetic boundary conditions [9] at $z = 0$ and $z = -L$. The solutions for the mode frequencies are particularly simple when $k_z = 0$. This case is referred to as the Voigt configuration. Eq. (1.48) can then be satisfied by setting $\chi_a = -1$ and the result is

$$\omega_B(k_z, \mathbf{k}_{\shortparallel}) = \left[g\mu_B H_0 \left(g\mu_B H_0 + \omega_M\right)\right]. \tag{1.49}$$

This represent the frequency of the bulk magnetostatic modes in the film. The second way to satisfy Eq. (1.48) is if $k_z = \pm i k_{\shortparallel}$ which leads to

$$\omega_{DE}(\mathbf{k}_{\shortparallel}) = g\mu_B \left[H_0(H_0 + 4\pi M_s) + (2\pi M_s)^2 \left(1 - \exp(-2k_{\shortparallel} L)\right)\right]^{1/2}. \tag{1.50}$$

This represents the dispersion relation for magnetostatic surface SWs in a magnetic film, which was originally derived by Damon and Eshbach [36, 37] (see also [38, 8, 13]).

Now we investigate the exchange-dominated SW modes for films. In the presence of a surface, the previous Eq. (1.37), which comes from a Taylor series expansion, is modified to

$$H_{\text{ex}} = F_0 \mathbf{M} + F_1 \frac{\partial}{\partial z} \mathbf{M} + F_2 \nabla^2 \mathbf{M}, \tag{1.51}$$

where F_1 is an additional constant. The extra term can be added to the torque equation of motion for a surface spin to deduce a boundary condition, which is found to be [13]

$$\frac{\partial \mathbf{m}(\mathbf{r})}{\partial z} - \eta \mathbf{m}(\mathbf{r}) = 0, \tag{1.52}$$

where η is called a pinning parameter. The above equation is often introduced as a phenomenolog-

ical assumption. We consider a thin film of thickness L as before (with the same pinning η at each surface, for simplicity). If we write $\mathbf{m}(\mathbf{r}) = \mathbf{m}_1(z)\exp(i\mathbf{k}_{\shortparallel}\cdot\mathbf{r}_{\shortparallel})$ and solve for the z-dependent part, two types of solution can occur. The first solution is where $\mathbf{m}_1$ is a linear combination of $\exp(ik_z z)$ and $\exp(-ik_z z)$ waves. These are "bulk standing" waves with dispersion relation

$$\omega_B(\mathbf{k}_{\shortparallel}) = g\mu_B H_0 + D\left(k_z^2 + k_{\shortparallel}^2\right), \tag{1.53}$$

provided k_z satisfies

$$\tan(k_z L) = \frac{2\eta k_z}{\left(\eta^2 - k_z^2\right)}. \tag{1.54}$$

This represents a wave-vector quantization of k_z. For example, if either $\eta = 0$ (zero pinning) or $|\eta| \gg 1$(large pinning), we obtain $\tan(k_z L) = 0$ which means:

$$k_z = \frac{n\pi}{L}, \tag{1.55}$$

where n is an integer number. This is the condition for fitting an integer number of half-wavelengths into the film thickness L.

A second solution for $\mathbf{m}_1$ is a linear combination of real exponential terms like $\exp(\kappa z)$ and $\exp(-\kappa z)$ representing decay from the two surfaces. These are localized surface waves with the dispersion relation

$$\omega_S(\mathbf{k}_{\shortparallel}) = g\mu_B H_0 + D\left(k_{\shortparallel}^2 - \kappa^2\right), \tag{1.56}$$

where κ is a decay constant related to the pinning parameter η and film thickness L by

$$\tan(\kappa L) = \frac{2\eta\kappa}{(\eta^2 + \kappa^2)}. \tag{1.57}$$

It can be proved that there are, at most, two surface SWs (two physical solutions of κ), roughly corresponding to one localized at each surface [13]. Fig. 1.4 shows examples for the variation of SW amplitudes across the film thickness.

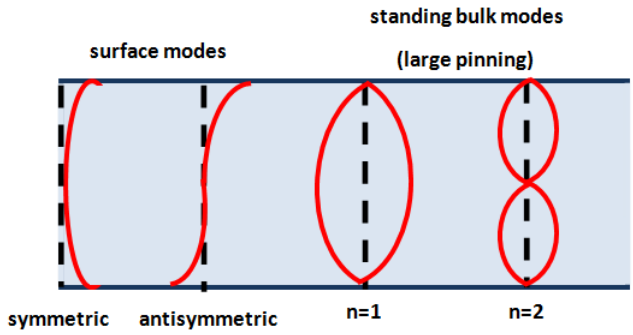

Figure 1.4: Examples for the variation of the SW amplitudes across the film thickness (see text).

Another type of low-dimensional structures corresponds to nanowires which have one direction of translational symmetry, so the excitations are characterized by a 1D wave vector. The modified Bloch's theorem is given by

$$\psi(x, y, z) = U_{k_z}(x, y, z) \exp(ik_z z), \tag{1.58}$$

where we assumed that the translational symmetry is in the z direction. The calculations for the SW dispersion relations will be discuss later in this thesis. In magnetic nanoparticles that are finite in all three dimensions, such as spheres, spherical shells and cuboids, there is no translational symmetry and Bloch's theorem does not apply. These material are usually labeled as being 0D, since there is no well-defined wave vector characterizing the SWs.

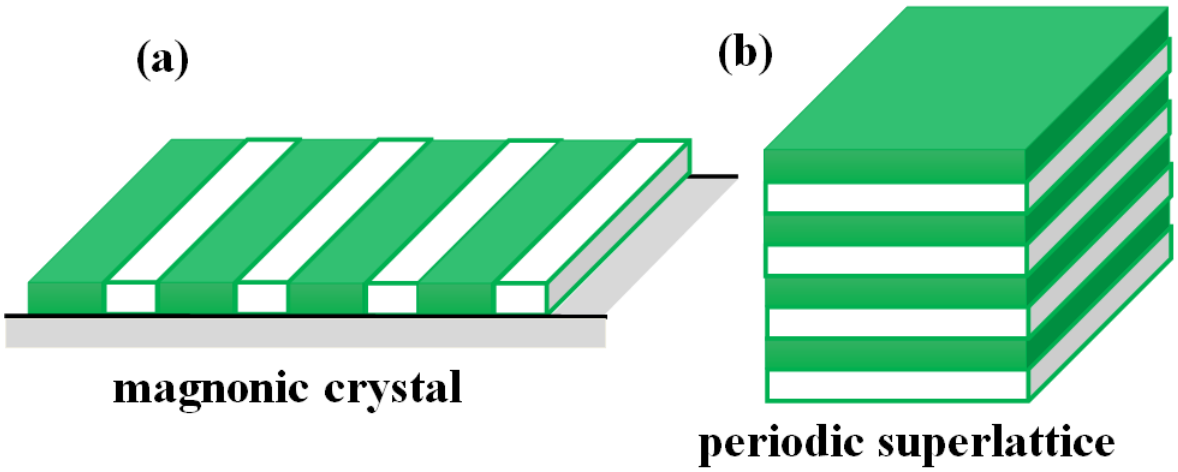

Figure 1.5: Simple geometry for: (a) a magnonic crystal (MC) and (b) a periodic superlattice.

Finally, nanostructures can be formed in periodic arrays, and some example are given in Fig. 1.5 [35]. A magnonic crystal (MC) is shown in Fig. 1.5(a) which consists of lateral arrays of nanowires arranged side-by-side with a non-magnetic intervening material. Another artificial multilayer nanostructures is a periodic superlattice represented in Fig. 1.5(b). This shows an alternating sequence of nanowires of different materials stacked vertically. These materials are currently attracting great attention due to their basic physics and potential technological applications.

1.5 Outline of nonlinear SW processes

Nonlinear processes occur because the SWs are not exact solutions, i.e., a linearization approximation is made in both the microscopic and macroscopic approaches. The nonlinear effects are important either at elevated temperatures (but below the Curie point T_c) or with microwave pumping at high-power levels. We focus on the latter case in this thesis, since particular SWs can be selectively excited in experiments. In either case, we may think of the nonlinearity as associated with the angle of precession becoming large.

Using the ferromagnetic resonance (FMR) method, described later in Section 1.6, the first nonlinear measurements were reported by Bloembergen and Damon [39] and Bloembergen and Wang [40]. The saturation of the main FMR peak and the appearance of a subsidiary absorption peak were observed at high power levels of "pumping". Their results, which were carried out with the pumping field transverse to the applied field, were explained by Suhl in his classical paper [41] as a parametric instability of a SW pair via the uniform precession ($\mathbf{k} = 0$) SW mode. Soon afterwards, Morgenthaler [42] and Schlömann *et al*. [43] independently proposed the parallel pumping experiment. In the parallel pumping configuration, the microwave field couples to the SW modes via a "wobble" of the magnetization in the z-direction, whereas in the perpendicular pumping process, the coupling occurs indirectly, as mentioned via the uniform mode with wave vector $\mathbf{k} \simeq 0$. In the resonance saturation case (also called a second-order Suhl process), two uniform magnons are annihilated and a SW pair with nonzero $\mathbf{k}$ and $-\mathbf{k}$ is created with frequency

$\omega \simeq \omega_p \simeq \omega_k$. Here ω_p denotes the pumping frequency. In the subsidiary resonance (first-order Suhl process) and parallel pumping process, a SW pair with $\mathbf{k}$ and $-\mathbf{k}$ is driven by one uniform mode magnon with frequency $\omega_0 = \omega_p/2$. The processes are depicted schematically in Fig. 1.6.

The three instability scattering processes (which will be discussed further in later chapters) conserve both energy and wave vector in a bulk material. The interest in nonlinear SW processes in ferromagnets has been revived by progress in the theory of nonlinear dynamics of dissipative systems [27], by related results obtained in the theory of magnetic solitons, and most recently by advances in the ability to produce nanostructured materials.

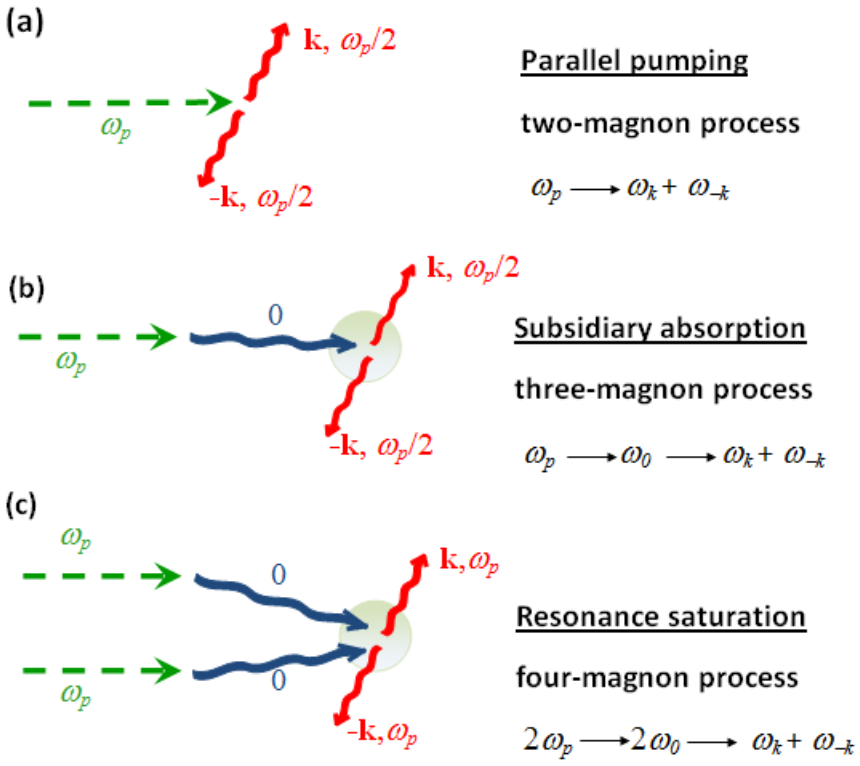

Figure 1.6: Schematic representation of the three parametric instability processes under pumping by a microwave field: (a) parallel pumping, (b) first-order Suhl process, and (c) second-order Suhl process. The last two processes occur in perpendicular pumping and involve intermediate uniform-precession (zero wave vector) magnons. The end result in all cases is a pair of magnons with wave vectors $\mathbf{k}$ and $-\mathbf{k}$.

1.6 Experimental techniques for SWs

Here we briefly describe some of the experimental techniques that can be used for direct studies of the SW properties. In general, the SWs are mostly investigated using inelastic light scattering (ILS), ferromagnetic resonance (FMR) and inelastic neutron scattering (INS) techniques (see, e.g., [44, 10, 45, 46, 47, 48, 49, 50, 15, 13]), among others. The first two techniques are particularly important for confined magnetic structures.

We start with ILS, which is important for measuring SWs at small nonzero wave vectors. Basically there are two techniques, namely Brillouin light scattering (BLS) and Raman light scattering (RLS). These are conceptually similar, but they involve different experimental methods to detect the frequency shifts. Both BLS and RLS involve a coupling between an electromagnetic wave (photon) and the excitation (typically a phonon or SW). The photon either loses energy (Stokes scattering), which leads to the release of a SW, or it gains energy (anti-Stokes scattering) by absorbing a SW (see Fig. 1.7). The shift in photon energy is called the Brillouin (or Raman) shift frequency, and it is equal to the energy of the created or absorbed SW. Therefore BLS and RLS may be used to measure the wave vectors, energies and frequencies of the SWs.

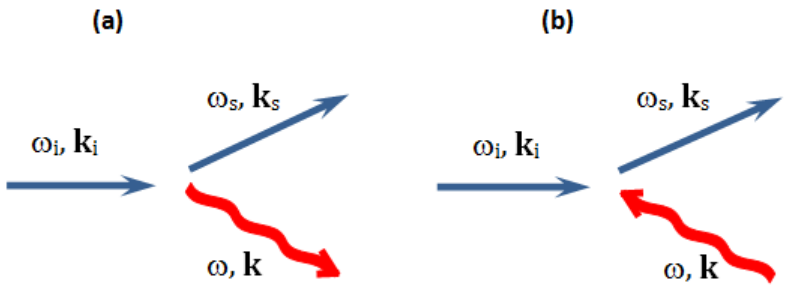

Figure 1.7: Depiction of (a) Stokes and (b) anti-Stokes processes in ILS. Here $\omega_{i(s)}$ and $\mathbf{k}_{i(s)}$ represent the frequency and wave vector of the incident (scattered) photons, while ω and $\mathbf{k}$ are the frequency and wave vector of the SW.

For measuring the Brillouin shift a spectrometer based on a Fabry-Perot interferometer is used which records shifts in the range of up to about 150 GHz. BLS is particularly important for acoustic phonons or for the lowest SWs in ferromagnets and ferrimagnets. In RLS, photons typically interact with vibrational transitions in the bonds between atoms in a molecule or optic phonons in

solids or the higher-frequency SWs in antiferromagnetic materials. The typical range of frequency shift in RLS is $\sim$ 150 GHz to $\sim$ 100 THz. The RLS technique typically uses grating spectrometers to measure the shifts.

Another powerful experimental technique used for probing SWs in ferromagnets at very small wave vectors is FMR. Typically a static magnetic field H_0 and a weak transverse oscillating pumping field h_p are applied to the magnetic sample. Earlier, in Subsection 1.3.2, we explained that there is a precessional motion of the magnetization $\mathbf{M}(\mathbf{r}, t)$ about the equilibrium z-direction. In a FMR experiment a resonance effect is achieved when the precessional frequency matches that of the pumping field. The theoretical analysis can be carried out by adding a damping (or dissipative) term to Eq. (1.30). This term usually has the form $\lambda(\mathbf{M} \times d\mathbf{M}/dt)/M_s$, giving the Landau-Lifshitz-Gilbert (LLG) equation [51], where λ is the damping parameter. Figure 1.8 shows a basic setup of a FMR experiments which involves placing a ferromagnet on the central conductor of a coplanar waveguide and applying the pumping field h_p. Typically the external magnetic field is spatially uniform throughout the sample, and only the uniform modes of the magnetization precession (i.e., the zero-wave vector SWs) are excited. The applied field H_0 (e.g., such that $\mu_0 H_0 \sim 0.01$ to 1 T) is sufficient to saturate all the magnetic domains in the magnetic sample and to set the equilibrium magnetization direction. The frequency of the pumping field can be in the MHz to GHz range. When the pumping frequency matches the SW frequency at zero wave vector (e.g., by sweeping the applied field), there is a resonance absorption of microwave energy which can be observed by a microwave diode. The linewidth of the resonance absorption is directly related to the damping, so FMR can be used to deduce damping effects. Further discussion of FMR will be given in Chapter 4 for applications to ferromagnetic nanowires.

We note that there are other types of magnetic resonance used for SWs. One of these is antiferromagnetic resonance (AFMR) which is a technique for probing the higher frequency $k \simeq 0$ SWs in antiferromagnetic materials. Another is called spin-wave resonance (SWR), which can be used to excite the standing bulk SWs set up across the thickness L of a thin film (see Section 1.4 and Fig. 1.4). Using SWR it is possible to study the dispersion relation of the SWs at discrete wave

vectors (see Eq. (1.54)) for magnetic films [35], as well as the surface SWs [25].

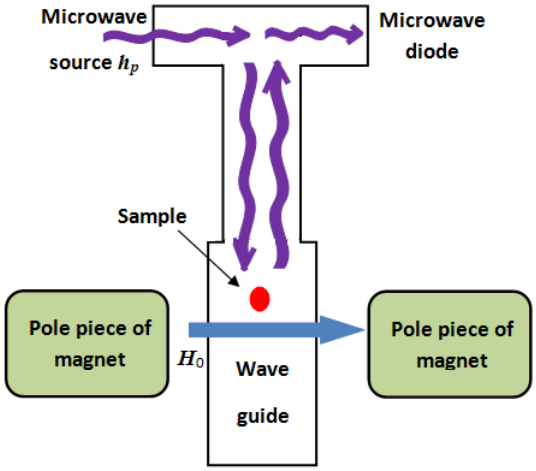

Figure 1.8: Schematic of a FMR experimental setup.

SWs are also detected through inelastic neutron scattering (INS), which is applicable to excitations with large wave vectors. This technique is well-established for studying excitations (such as phonons, plasmons and SWs) in bulk materials, and the scattered neutrons can be used to probe the SW dispersion relations across the full Brillouin zone, which is a tremendous advantage. However, this method is relatively insensitive to surface effects since neutrons have large penetration depths and their interaction with materials is very weak [35]. Also the instrumental resolution for INS is often lower that for BLS.

1.7 Thesis outline

The aim of this thesis is to investigate the nonlinear magnetization dynamics in ferromagnetic nanostructures (particularly nanowires) through the parametric instabilities under microwave pumping. In the thesis we employ a microscopic (or Hamiltonian-based) theory, which is appropriate for both linear and nonlinear dynamics of nanostructures. The Hamiltonian incorporates the short-range exchange and the long-range magnetic dipole-dipole interactions, as well as an external magnetic field applied in various directions. The magnetic anisotropy and biquadratic exchange

interactions are considered in some cases where they are important. We also investigate effects of the microwave pumping on the quantum statistics of the magnons, as outlined below.

Chapter 2 is based on a feature article published in a recent issue of Physics in Canada that was devoted to magnetism research [*M. G. Cottam and Z. Haghshenasfard, "Instability Processes for Magnons in Ferromagnetic Nanostructures", Physics in Canada* **72***, 63 (2016)*]. It covers some basic aspects of nonlinear SWs and previews some applications to nanowires (which are developed further in Chapter 5).

Chapter 3 is based on an invited presentation at the "Magnetism 2014" conference in Poznan, Poland [*Z. Haghshenasfard, H. Nguyen, and M. G. Cottam, "Spin-wave Instability Theory for Ferromagnetic Nanostructures", Acta Physica Polonica A* **127***, 192 (2015)*]. Nonlinear instability thresholds for quantized SWs in both ferromagnetic nanowires and ultra-thin films under the parallel pumping configuration are investigated and some preliminary nanowire results are compared with those for ultra-thin films.

Chapter 4 is based on collaborative research with experimentalists at the National University of Singapore [*P. Lupo, Z. Haghshenasfard, M. G. Cottam, and A. O. Adeyeye, "Ferromagnetic resonance study of interface coupling for spin waves in narrow NiFe/Ru/NiFe multilayer nanowires", Phys. Rev. B* **94***, 214431 (2016)*]. This work covers experimental and theoretical studies of magnetization behavior in trilayer composite nanowires, consisting of two Permalloy layers separated by a nonmagnetic Ru spacer layer. The theory involves generalizing earlier work for simple nanowires.

Chapter 5 is based on a recent publication [*Z. Haghshenasfard and M. G. Cottam, "Spin-Wave Instabilities of Ferromagnetic Nanowire Stripes Under Parallel Pumping", J. Phys. Condens. Matter* **28***, 18 (2016)*]. The SW instability thresholds of parametric processes in ferromagnetic nanowires under condition of pumping with a microwave field are considered. The external applied magnetic field is taken to be either parallel to the longitudinal axis or in a perpendicular direction.

Chapter 6 is based on a published paper [*Z. Haghshenasfard and M. G. Cottam, "Parallel Pumping of Spin Waves for Ferromagnetic Nanowires and Nanotubes With Circular Cross Sec-*

tions", IEEE Magnetics Letters **1***, 7 (2016)*]. This work describes the SW instability of a ferromagnetic nanowire with circular cross section as well as nanotubes under parallel pumping configuration. The numerical results are compared with those for nanowires with square cross sections.

Chapter 7 is based on a recent publication [*Z. Haghshenasfard, H. Nguyen, and M. G. Cottam, "Suhl instabilities for spin waves in ferromagnetic nanostripes and ultrathin films", J. Magn. Magn. Mat.* **426***, 380 (2017)*]. It covers the nonlinear SW theory in perpendicular pumping configuration which requires the inclusion of three-magnon (corresponding to the first-order Suhl process) and four-magnon (corresponding to the second-order Suhl process) nonlinear interactions into the Hamiltonian.

Chapter 8 is based on a recent publication [*Z. Haghshenasfard and M. G. Cottam,* "*Quantum statistics and squeezing for a microwave-driven interacting magnon system", J. Phys. Condens. Matter* **29***, 045803 (2017)*]. The statistical properties of a microwave-driven interacting magnon system are investigated. In particular, the non-classical quantum statistical properties of the system such as squeezing and collapse and revivals of the magnon occupation number are studied.

Chapter 9 is based on a recent publication [*Z. Haghshenasfard and M. G. Cottam, "Quantum statistics for a two-mode magnon system with microwave pumping: Application to coupled ferromagnetic nanowires", J. Phys. Condens. Matter* **29***, 195801 (2017)*]. Here we modify the calculations of Chapter 8 to apply to low-dimensional systems with microwave pumping. For a specific application we consider a ferromagnetic nanowire geometry formed by two lines of spins as a two-mode magnon system. Manipulation of the collapse-and-revival phenomena for the magnon number, as well as the control of the cross correlation between the two magnon modes, is demonstrated by tuning the parallel pumping field.

Finally Chapter 10 contains the overall conclusions of the thesis and some suggestions for future work.

Chapter 2

Instability processes for magnons in ferromagnetic nanostructures

The material in this chapter has been published as a "Physics in Canada" feature article on magnetism by me (with M. G. Cottam) listed as Ref. [52].

An understanding of the magnetization dynamics, both linear and nonlinear, in ordered magnetic materials such as ferromagnets is of fundamental interest and also has applications in the expanding fields of spintronics and magnonics. Here we supplement introductory material in Chapter 1 by describing some nonlinear processes in ultrathin films and nanowires, where the fundamental excitations of the systems, known as spin waves or magnons, are strongly influenced by their spatial confinement in the nanosystem and can be driven into a decay instability by application of a microwave-frequency electromagnetic wave above a high-power threshold level.

A description of the wave-like fluctuations as "spin waves" in unbounded ferromagnets (i.e., where boundary effects are negligible) is well known and given in most solid-state physics and magnetism textbooks [32, 27]. When the quantum-mechanical nature of the spin operators is taken into account, the excitations are called "magnons", by analogy with phonons as the quantized lattice vibrations in a solid. It is often helpful to picture magnons schematically as arrays of precessing spin vectors, where there is a small change of phase (related to the wave vector) from any

one spin to a neighboring spin. In this semi-classical viewpoint the precession of a spin vector takes place due to the torque from an effective magnetic field that incorporates all the magnetic interactions with other spins as well as any applied magnetic field. In simple cases (such as at low temperatures compared with the Curie temperature T_c) the angle of precession is small, meaning that the component of the spin vector along the direction of net magnetization remains approximately constant.

2.1 Interacting magnon gas

The dispersion relation of the magnons, which gives the angular frequency $\omega(\mathbf{k})$ of precession in terms of wave vector $\mathbf{k}$, depends on the nature of the interactions. These arise mainly from (a) the short-range exchange interactions, which are quantum-mechanical in nature and are due to the overlap of wave functions on neighboring atoms, and (b) the long-range magnetic dipole-dipole interactions as in classical electromagnetism. In a Hamiltonian formalism the contributions to the energy from these terms [32, 27, 25] are, respectively, proportional to $J(r_{12})\mathbf{S}_1 \cdot \mathbf{S}_2$ and $\mu_B^2 \left[\mathbf{S}_1 \cdot \mathbf{S}_2 - 3\left(\mathbf{S}_1 \cdot \hat{\mathbf{r}}_{12}\right)\left(\mathbf{S}_2 \cdot \hat{\mathbf{r}}_{12}\right)\right] / r_{12}^3$, where subscripts 1 and 2 label spin operators at two different atomic sites at a distance r_{12} apart and connected by unit vector $\hat{\mathbf{r}}_{12}$. The interaction strength J before the exchange term is important typically only between nearest neighbors, whereas the weaker dipolar terms (where μ_B denotes the Bohr magneton) have a more complicated directional dependence and falls off slowly like $1/r_{12}^3$.

A simple calculation of the magnon frequency, applicable for the one-dimensional (1D) system in Fig. 2.1 with the assumption that only exchange effects occur, is given, for example, in the book by Kittel [32]. This is based on using the torque equation of motion for each spin vector and seeking traveling-wave solutions for the fluctuating components. The final result is that ω increases as the 1D wave vector k increases, being proportional to $S\,J(ka)^2$ at small wave vector such that $ka \ll 1$, where a is the distance between spins and S is the spin quantum number. This result would be modified if effects due to dipolar terms and an applied magnetic field were included [27, 25] .

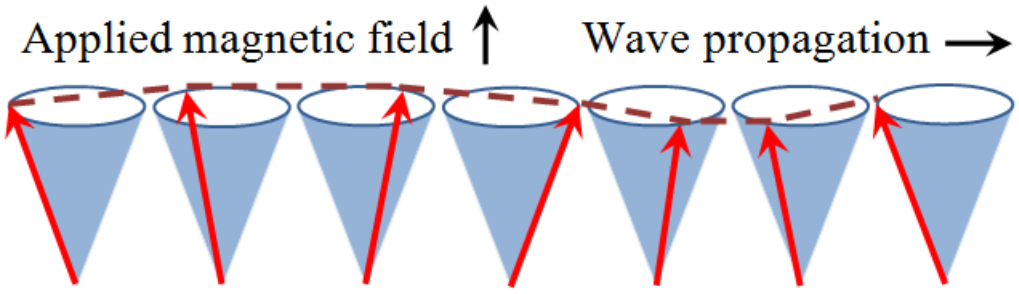

Figure 2.1: Schematic illustration of a spin wave (or magnon), taking for simplicity a long line of spin vectors (red arrows), undergoing precession about the direction of net magnetization, defined by the applied magnetic field. One complete wavelength of propagation is depicted, where the dashed line joining the heads of arrows is drawn as a guide to the eye to highlight the wave-like character.

A general consequence in reciprocal space, when a Fourier transform of the interactions is made to a wave-vector representation, is that the exchange terms dominate at medium and large wave vectors in the Brillouin zone, but the dipolar terms are important at small enough wave vectors. Typically in bulk ferromagnets the dipolar terms need to be included for wave vectors less than about 1/100 of the Brillouin zone boundary value, which is relevant for experimental techniques such as ferromagnetic resonance (FMR) and Brillouin light scattering (BLS) that probe the so-called magnetostatic and dipole-exchange regimes [25, 27].

The magnons, when treated in the simplest linear-wave approximation can be shown to behave as bosons, and the number of magnons with energy $\hbar\omega(\mathbf{k})$ excited at any temperature at equilibrium is described by the Bose-Einstein distribution function. In reality the magnon states are not exact eigenfunctions of the spin Hamiltonian, and consequently the magnons constitute a weakly interacting boson gas. On a semiclassical picture of spin waves, the origin of the interactions is associated with taking account of the finite angle of spin precession. Quantum mechanically the spin operators, which are analogous to the orbital angular momentum operators, do not satisfy the boson commutation relationships, and a mathematical transformations between spin operators and boson operators has to be applied [25, 27].

The Hamiltonian for the interacting magnon gas of a ferromagnet, in the notation of second quantization, can usefully be expressed as

$$H = \sum_{\mathbf{k},l} \omega_l(\mathbf{k}) b^\dagger_{\mathbf{k},l} b_{\mathbf{k},l} + H^{(3)} + H^{(4)} + \cdots \tag{2.1}$$

in leading order (provided the temperature is well below T_c), apart from a constant term. Here $b^\dagger_{\mathbf{k},l}$ and $b_{\mathbf{k},l}$ are the creation and annihilation operators, respectively, for a magnon of wave vector $\mathbf{k}$ and branch l. For a bulk (effectively unbounded) material with one branch, we have only $l = 1$, but this will not generally be so for nanostructures. The first term on the right of Eq. (2.1) has a form similar to that for the treatment of a simple-harmonic oscillator in quantum mechanics. The next two terms, $H^{(3)}$ and $H^{(4)}$, describe the leading-order three-magnon and four-magnon interaction processes, respectively. The first of these involves operator products like $b^\dagger_{\mathbf{k}',l'} b^\dagger_{\mathbf{k}-\mathbf{k}',l''} b_{\mathbf{k},l}$ and its Hermitian conjugate, which represent magnon splitting (i.e., a magnon is annihilated and two magnons are created) or the corresponding confluence. The last term in Eq. (2.1) involves products of four boson operators, e.g., two creation and two annihilation operators as for a pair of magnons scattering off one another to produce two other magnons with different wave vectors. It can be shown that the three-magnon processes are due to magnetic dipole-dipole interactions, whereas four-magnon scattering has contributions coming from both the exchange and dipolar interactions [25, 27].

2.2 Magnons in nanostructures

As mentioned, the magnons for a simple bulk ferromagnet in three dimensions (3D) are characterized by a 3D wave vector $\mathbf{k}$ and the branch label l is single-valued. By contrast, in magnetic nanostructures, where one (or more) of the spatial dimensions is of order tens or hundreds of nanometres, the magnons are spatially confined and are required to satisfy boundary conditions at the surfaces or interfaces (see Section 1.4). In a thin film, for example, the magnons are characterized by a 2D wave vector in the directions of translational symmetry parallel to the surfaces. In the direction perpendicular to the surfaces, the magnons may either take a standing-wave form with a quantized value for the third wave-vector component, or they may be localized with amplitude

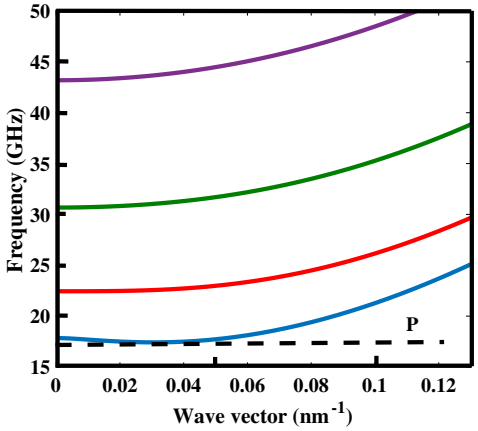

Figure 2.2: Dispersion relations, showing frequency versus 1D longitudinal wave vector, calculated for the lowest quantized magnons in a Permalloy nanowire (see text). The horizontal line labeled *P* is drawn at one half of the pumping frequency considered later.

decaying away from one or both surfaces. Likewise in a nanowire there is a 1D wave vector along the length and standing-mode behavior or localization in the other two directions.

An example is given in Fig. 2.2 showing the calculated dispersion relations for the lowest magnon branches in a Permalloy ($Ni_{80}Fe_{20}$) nanowire stripe with rectangular cross section 50 nm by 10 nm and in a longitudinal applied magnetic field of 0.202 T. The frequencies, which were obtained using a microscopic dipole-exchange theory [53] described later in which magnon interactions are ignored, are plotted versus the 1D wave vector in the small $|\mathbf{k}|$ regime accessible by FMR and BLS measurements. The initial dip for some branches, which is more pronounced for the lowest branch and has been confirmed experimentally, is due to the dipolar interactions competing with the exchange that eventually dominates at larger $|\mathbf{k}|$.

2.3 Magnon instabilities under microwave pumping

Typically FMR experiments are carried out at relatively low power levels: an oscillating magnetic field at microwave frequency is applied to a ferromagnet in a direction transverse to the magnetization direction. The microwave field can couple linearly to the oscillating magnetic moment of a magnon such that there is a resonant absorption of energy when a match is achieved (e.g., by

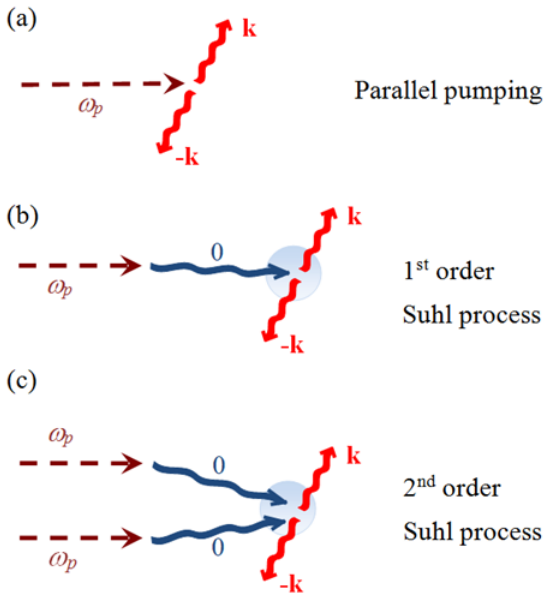

Figure 2.3: Schematic representation of the three parametric instability processes under pumping by a microwave field: (a) parallel pumping, (b) first-order Suhl process, and (c) second-order Suhl process. The last two processes occur in perpendicular pumping and involve intermediate uniform-precession (zero wave vector) magnons.

scanning the static applied field) between the microwave frequency and the precessional frequency of the magnon [32]. In fact, measurement of the FMR linewidth can yield information about the magnon damping (or reciprocal lifetime). This is long established for macroscopically large samples, but for ferromagnetic nanostructures such as nanowires the experimental [54] and theoretical [55] studies are quite recent.

For bulk samples it was noticed that, when the signal power was increased in FMR experiments, there was a premature saturation of the main resonance absorption and the appearance of a subsidiary resonance at higher frequency [40]. Subsequently these nonlinear effects with perpendicular microwave pumping were explained by Suhl [41] in terms of parametric instabilities involving the three- and four-magnon processes, respectively. They are now known as the first-order and second-order Suhl processes, respectively. An analogous instability under parallel microwave pumping was later identified by Schlömann and others [43]. The three types of processes are depicted schematically in Fig. 2.3; also there are several reviews (mainly for macroscopic samples) giving details [25, 27, 28, 56].

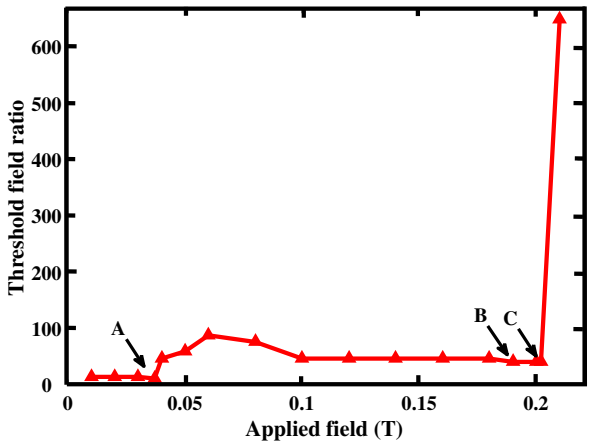

Figure 2.4: Threshold field ratio (see text) plotted as a function of applied magnetic field for the same Permalloy nanowire as in Fig. 2.2, calculated for parallel pumping with frequency $\omega_p/2\pi = 35$ GHz. The points A, B, and C are at field values related to features on the previous dispersion curves, as explained. The triangles indicate calculated points and the red line is a guide to the eye.

The outcome in all three processes is the production of a pair of magnons with wave vectors $\mathbf{k}$ and $-\mathbf{k}$ of equal magnitude, which implies that they have the same frequency. Parallel pumping (Fig. 2.3a) relies on the fact that the dipolar interactions cause the spin precession to be elliptical. Hence the parallel (or longitudinal) spin components, which are coupled to the pumping field, fluctuate resulting in the excitation of a magnon pair. The first- and second-order Suhl processes (Figs. 2.3b and 2.3c) involve the excitation initially of one (or two) uniform-precession magnons, meaning modes with $\mathbf{k} = 0$, followed by the production of the magnon pair via the $H^{(3)}$ and $H^{(4)}$ interaction terms mentioned earlier. From considerations of energy conservation it follows that the angular frequency of each magnon produced in the parallel pumping and first-order Suhl processes is $\omega_p/2$, whereas in the second-order Suhl process it is ω_p.

In a nanowire, however, the absence of wave-vector conservation in the directions perpendicular to its length gives two important features that are distinct from the macroscopic case: the interaction processes involve a "mixing" between different magnon branches, and there are strong density-of-states effects for the magnons due to the spatial confinement. When the threshold strengths of the pumping field for the onset of an instability in any magnon branch are calculated (using techniques described later that are analogous to those for ultra-thin films [57, 58]), we ob-

tain results as in Fig. 2.4 for the same Permalloy nanowire considered in Fig. 2.2. This shows the dimensionless threshold field ratio (conventionally defined as the threshold field amplitude divided by the FMR half-linewidth in magnetic field units) plotted against the applied field for parallel pumping with $\omega_p/2\pi = 35$ GHz. Referring back to the dispersion curves, the horizontal line P in Fig. 2.2 is drawn at half of the pumping frequency, which corresponds to production of the parametric magnons. With an applied value of 0.202 T, for which Fig. 2.2 is drawn, the line P coincides with the minimum in the lowest magnon branch. When the applied field is scanned up (or down) in value, the line P moves down (or up) relative to the dispersion curves. Thus for fields above 0.202 T the line does not intersect with any magnon branch, and so the instability threshold rapidly increases. This explains the critical point labeled C in Fig. 2.4. For lower applied field values there may in general be one or more intersection points, and so the decay is allowed. For nanostructures (as in this example) certain features on the discrete spectrum become emphasized, by contrast with the smooth behavior in macroscopic samples [25, 27]. Thus we may associate points labeled B and A in Fig. 2.4 as corresponding to when line P coincides with the $\mathbf{k} = 0$ magnons of the lowest and next-lowest branches, respectively. Other structural features can be attributed to density-of-states effects for the quantized magnons.

2.4 Conclusion

It is of great interest currently to extend the work on magnon instabilities to other types of magnetic nanostructures and to their arrays (as in magnonic crystals). Also, recent experiments have reported the observation of a Bose-Einstein condensation (BEC) in a macroscopic magnon gas at room temperature [59, 60] when driven far from equilibrium by application of an intense microwave pumping field. A macroscopic theoretical interpretation [61] was subsequently developed by utilizing the form of the three- and four-magnon interaction terms. Investigation of the possible occurrence of a magnon BEC in a magnetic nanostructure with spatially-confined magnons is an intriguing topic.

Chapter 3

Spin-wave instability theory for ferromagnetic nanostructures

The material in this chapter has been published as an article by me (with H. Nguyen, and M. G. Cottam) listed as Ref. [57].

The magnetization dynamics of ordered magnetic nanostructures (such as films, wires, rings, and their arrays) have generated much attention in recent years, and in particular, there has been renewed interest in spin-wave (SW) parametric processes in such structures (see, e.g., [62, 63, 64]). Following the pioneering work on SW instabilities in ferromagnetic systems under microwave pumping by Suhl [41], Schlömann [43], and others, there have been extensive experimental and theoretical efforts in this field (for reviews see, e.g., [26, 56, 25, 22, 28, 27]). Until recently, most of these studies applied to either unbounded samples or to spheres and films with dimensions of typically several mm or μm for which macroscopic descriptions are generally applicable. In finite samples boundary effects need to be taken into account, resulting in spatial quantization of the SW modes. In turn, there is a modification of the SW instability thresholds and additional selection rules under microwave pumping (see [65, 66, 26, 67]).

The focus here is a theoretical study of SW instability processes in structures where at least one of the sample dimensions is of the order 100 nm or less. The quantization of the SWs is much more

pronounced and surface effects become more dominant. Moreover, it becomes appropriate to use a microscopic (or Hamiltonian-based) method with a discrete lattice of effective spins interacting through exchange and dipole-dipole terms, rather than a macroscopic approach. Very recently such an approach was utilized to consider the special case of parallel pumping in ultra-thin magnetic films [58]. We are now motivated to extend the calculations to magnetic nanowires (which include stripes and ribbons) to compare these low-dimensional systems and also to consider the case of perpendicular pumping. The theoretical techniques are generalizations, in order to include the microwave pumping fields, of earlier work on films [68, 69] , wires [53, 70, 55] and magnonic crystals [71].

The calculations for the SW instability thresholds are outlined in Section 3.1, where we highlight effects of the different dimensionality (in terms of wave vectors and translational symmetry) for the film and wire cases. Then numerical examples are given in Section 3.2 for different materials to illustrate the two geometries and the crucial role of the dipole-dipole to exchange ratio for the interactions. Finally the conclusions are given in Section 3.3. Further details of the theoretical methods follow in later chapters of this thesis.

3.1 Theoretical method

The two ferromagnetic nanostructures considered here are ultrathin films and nanowires (or stripes) with a rectangular cross section. They have, respectively, two and one directions of translational symmetry and are depicted in Fig. 3.1. The ultrathin film with (010) surfaces is modeled as having N atomic layers of spins arranged, for simplicity, on a simple cubic (s.c.) lattice structure with lattice constant a , while the nanowire (stripe) is modeled as having a rectangular cross section of $n_x \times n_y = N$ atomic spins (in the xy plane). Typically, for both structures the preferred direction of spin ordering corresponds to the static magnetization along the z direction, unless changed by the applied static and microwave fields.

The total spin Hamiltonian for each structure can be written in a common form as

$$H = -\frac{1}{2}\sum_{in,jm} J_{in,jm}\mathbf{S}_{in}\cdot\mathbf{S}_{jm} + \frac{1}{2}g^2\mu_B^2\sum_{in,jm}\sum_{\alpha,\beta} D^{\alpha,\beta}_{in,jm}S^{\alpha}_{in}S^{\beta}_{jm} - g\mu_B\mathbf{H}_0\cdot\mathbf{S}_{in} + H_p, \tag{3.1}$$

where the indices i and j refer to the spin sites within any atomic layer (in the film case) or to those sites along the z-directed lines of spins (in the nanowire case), while n and m (= 1, 2, $\cdots$, N) label the layers of the film in the y direction or the spin sites in any cross section of the nanowire. The first term represents the short-range exchange interactions $J_{in,jm}$ acting between the spins $\mathbf{S}_{in}$ and $\mathbf{S}_{jm}$ at a distance apart specified by $\mathbf{r}_{in,jm}$. The second term describes the long-range dipole-dipole interactions between spins with the components of the coupling tensor given by

$$D^{\alpha\beta}_{in,jm} = \frac{\left|\mathbf{r}_{in,jm}\right|^2\delta_{\alpha\beta} - 3r^{\alpha}_{in,jm}r^{\beta}_{in,jm}}{\left|\mathbf{r}_{in,jm}\right|^5}, \tag{3.2}$$

where $\alpha, \beta = x, y, z$ and with g and μ_B denoting the Landé g-factor and Bohr magneton, respectively. The next term is the Zeeman energy due to a static applied magnetic field $\mathbf{H}_0$, which usually we take to be along the z direction. Finally, H_p is the interaction Hamiltonian corresponding to the microwave pumping magnetic field $\mathbf{h_0}$ written as:

$$H_p = -g\mu_B\exp(-i\omega_p t)\sum_i \mathbf{h_0}\cdot\mathbf{S}_{in}. \tag{3.3}$$

Here we have taken a time dependence corresponding to a Fourier component with angular frequency ω_p.

In order to study SWs and their instability properties at low temperatures $T \ll T_c$, we extend the procedures in recent work [58, 68, 69, 55, 53, 70]. First the Holstein-Primakoff representation [31] is used to transform the Hamiltonian in the absence of pumping from components of the spin operators $\mathbf{S}_{in}$ to boson creation and annihilation operators $a^{\dagger}_{in}$ and a_{in} (see Section 1.3). If the static applied field is along the defined z direction for either the film or the wire, then z is also the preferred direction of static magnetization, so this transformation is straightforward. In the case of the wire, however, we will also include calculations for the case of a transverse applied field, along x in Fig. 3.1(b), where the individual spins are canted away from the z axis and the static magnetization is spatially nonuniform. Then the procedure involves determining the equilibrium

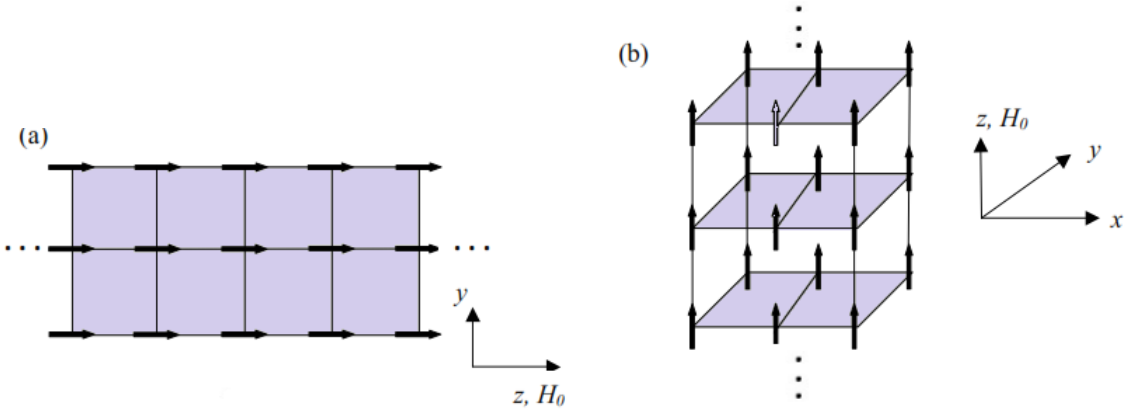

Figure 3.1: Assumed nanostructure geometries and choices of coordinate axes: (a) an ultrathin film with translational symmetry in the xz plane and finite thickness in the y direction (illustrated for $N = 3$ layers); (b) a rectangular nanowire with translational symmetry along the z direction and finite in the xy plane (illustrated for $N = 3 \times 2 = 6$ lines of spins).

orientations of the spins for any value of the transverse field and applying the Holstein-Primakoff transformation relative to these local axes for each spin (see [21]). In both of the above cases we expand the Hamiltonian of the system as $H = H^{(2)} + H^{(3)} + H^{(4)} + \cdots$, apart from a constant, with $H^{(m)}$ denoting the term with a product of m boson operators.

A canonical (generalized Bogoliubov) transformation can next be introduced, following [69, 55], to diagonalize $H^{(2)}$ giving

$$H^{(2)} = \sum_{q,l} \omega_l(\mathbf{q}) \alpha^{\dagger}_{q,l} \alpha_{q,l}, \tag{3.4}$$

where $\omega_l(\mathbf{q})$ is the frequency of the non-interacting SW branch l ($l = 1, 2, \ldots, N$) at wave vector denoted by $\mathbf{q}$. Here $\mathbf{q}$ is a two-dimensional (2D) wave vector in the case of a film, with $\mathbf{q} = (q_x, q_z)$ and a 1D wave vector for a nanowire, with $\mathbf{q} = (q_z)$. In the case of *parallel pumping*, where the microwave field $\mathbf{h_0}$ in Eq. (3.3) is parallel to the magnetization direction, the higher-order expansion terms, which describe three-magnon and four-magnon processes respectively, are unimportant. This is not the case, however, for *perpendicular pumping*.

For simplicity, we start with parallel pumping. The additional Hamiltonian term that describes the SW instability in this case is

$$H_p^{(2)} = h_0 \sum_{q,l,l'} \left[\exp(-i\omega_p t) P_{l,l'}(\mathbf{q}) \alpha^\dagger_{q,l} \alpha^\dagger_{-q,l'} + \text{h.c.} \right] \tag{3.5}$$

The amplitude factor $P_{l,l'}(\mathbf{q})$ is quoted in [58] for the film case, and for the present calculations we have derived analogous expressions for the wire geometry that apply when the static external field of magnitude H_0 is along either the z axis (longitudinal field) or the x axis (transverse field).

The next step is to derive the rate equations for the boson operators $\alpha^\dagger_{q,l}$ and $\alpha_{q,l}$ by forming their commutator with the effective Hamiltonian $H_{\text{eff}} = H^{(2)} + H_p^{(2)}$ for parallel pumping. This eventually gives rise to a set of N coupled equations for the boson operators $\alpha_{q,l}$, and another N equations for their conjugates, in the form

$$\frac{d}{dt}\alpha_{q,l} = -\left\{ i\omega_l(\mathbf{q}) + \eta_l(\mathbf{q}) \right\} \alpha_{q,l} - i h_0 \exp(-i\omega_p t) \sum_{l'} P_{l,l'}(\mathbf{q}) \alpha^\dagger_{-q,l'}. \tag{3.6}$$

Here we have introduced the role of energy dissipation phenomenologically via the damping constant $\eta_l(\mathbf{q})$ for the SW branch l, following the approach commonly used in macroscopic theories (see, e.g., [22, 28, 27, 65, 66]) as well as in [58] for a microscopic approach.

A numerical procedure to solve for the instability thresholds arising from the above type of coupled equations is outlined in [66, 72, 58]. In general, when the driving field h_0 is larger than a threshold value h_c, the rate at which energy is pumped into the SW system exceeds that lost to the system through relaxation mechanisms. The SW population increases exponentially above this threshold until it reaches a saturation depending on the nonlinear interactions. The set of coupled rate equations can be recast into a matrix form as an eigenvalue problem, and the onset of instability is associated with a change of sign of one of the eigenvalues. Typically, the calculations are carried out numerically as described later, but in a few special cases there are analytic expressions. For example, in the special case of a single-layer film ($N = 1$), where there is only one SW branch ($l = 1$), we find analytically that

$$h_c = \frac{\sqrt{(\eta_1(\mathbf{q}))^2 + (\triangle\omega_1(\mathbf{q}))^2}}{|P_{11}(\mathbf{q})|}, \tag{3.7}$$

where $\triangle\omega_l(\mathbf{q}) = \omega_l(\mathbf{q}) - \omega_p/2$. For a nanowire in the simplest non-trivial case, which corresponds to $N = 2$, we find that $h_c = \min(h_{c1}, h_{c2})$ for the two SW branches, where

$$h_{c,i} = \frac{\sqrt{\eta_1(\mathbf{q})\eta_2(\mathbf{q}) + (\triangle\omega_i(\mathbf{q}))^2}}{|P_{ii}(\mathbf{q})|}, \qquad (i = 1, 2). \tag{3.8}$$

In order to study SW instability thresholds under condition of perpendicular pumping an analogous approach can be followed. For simplicity, we shall restrict the discussion to the film case, where perpendicular pumping means that the microwave field $\mathbf{h_0}$ can be considered in terms of components along the in-plane x direction or the out-of-plane y direction. We conclude later that the corresponding threshold fields, denoted as h_{cx} and h_{cy}, are quite different. The effective Hamiltonian that leads to the instabilities of the system for the first-order Suhl process [41, 43] is $H_{\text{eff}} = H^{(2)} + H^{(3)} + H_p^{(\perp)}$, where the three-magnon term now plays an important role, along with the perpendicular microwave pumping term found explicitly from Eq. (3.3) and using the Holstein-Primakoff transformation. The relevant part that drives the SW instability consists of terms of the form $\alpha^\dagger_{q,l}\alpha^\dagger_{-q,l'}\alpha_{0,l''}$ for the operators, where the uniform (or zero wave-vector) mode can be replaced by a resonance term, as in [28, 27]. The second-order Suhl process, which depends on the four-magnon term $H^{(4)}$, will not be considered here.

Then, following the approach as described earlier, the set of N coupled rate equations can be formed. We eventually find results that are formally similar to Eq. (3.6), but with $P_{l,l'}(\mathbf{q})$ replaced by different expressions. Numerical examples will be given in Section 3.2; details of the calculations will be presented elsewhere (see Chapters 5, 6, and 7).

3.2 Numerical applications

In this section the previous theory will be applied to study the SW instabilities for some ultrathin films and nanowires. Examples for microwave pumping in either the parallel or perpendicular configuration will be given for the dispersion relations of the quantized SW modes and their instability

thresholds in different structures and magnetic materials. Typically we consider films with values of N up to about 50, and wires with different cross-sectional aspect ratios $n_x/n_y > 1$ and $N = n_x n_y$ up to about 15. The SWs in films, which are characterized by a 2D wave vector, depend on the magnitude $q = |\mathbf{q}|$ and in-plane propagation angle $\phi = \tan^{-1}(q_x/q_z)$. Hence they occur in bands that may become overlapping at large N. On the other hand, the SWs in wires depend only on a 1D wave vector so the spectrum consists of distinct lines (branches) that sometimes may hybridize.

Numerical calculations will be presented using bulk parameters appropriate to four magnetic materials, which are representative of widely differing dipolar-to-exchange interaction ratios. We can use the relationships that $H_{ex} = 6SJ/g\mu_B$ for the exchange field and $M_s = g\mu_B S/a^3$ for the saturation magnetization. Specifically, the materials are YIG (as a strong-exchange case), EuO and EuS (as intermediate cases), and $GdCl_3$ (as a strongly-dipolar case). For YIG we deduce $\mu_0 H_{ex} = 200$ T, $4\pi\mu_0 M_s = 0.176$ T, $S = 5/2$, and $g\mu_B = 28.0$ GHz/T [58]. Likewise, for EuO we take $\mu_0 H_{ex} = 38$ T, $4\pi\mu_0 M_s = 2.4$ T, $S = 7/2$, and $g\mu_B = 28.0$ GHz/T; for EuS we take $\mu_0 H_{ex} = 9.4$ T, $4\pi\mu_0 M_s = 1.5$ T, $S = 7/2$, and $g\mu_B = 28.0$ GHz/T; and finally for $GdCl_3$ we assume $\mu_0 H_{ex} = 0.54$ T, $4\pi\mu_0 M_s = 0.82$ T, $S = 7/2$, and $g\mu_B = 28.0$ GHz/T. Another parameter required for the calculations is the damping $\eta_l(\mathbf{q})$, which in principle may depend on $\mathbf{q}$ and on the branch label l. Here we will follow the simplification commonly adopted in the cited macroscopic calculations of adopting a constant value. YIG has a very small damping, for which we may assume a typical experimental value of 0.001 GHz (or $\Delta H \sim 0.3$ Oe for the equivalent resonance half-linewidth given by $\eta/g\mu_B$). For damping of the other materials we consider several values between 0.01 and 0.1 GHz. More discussion of parameter values is given in [58], and references therein.

We start with the applications to films. In Fig. 3.2 the lowest SW frequencies are plotted as a function of qa for several values of the propagation angle ϕ for (a) a EuO film with $N = 12$ and (b) a YIG film with $N = 50$. For any nonzero qa there is a range of frequencies, leading to SW bands (with $\phi = 0$ and $\pi/2$ defining the lower and upper boundaries, respectively). The widths of these bands become zero in the limit of $qa \to 0$, leading to a series of discrete frequencies, of which the

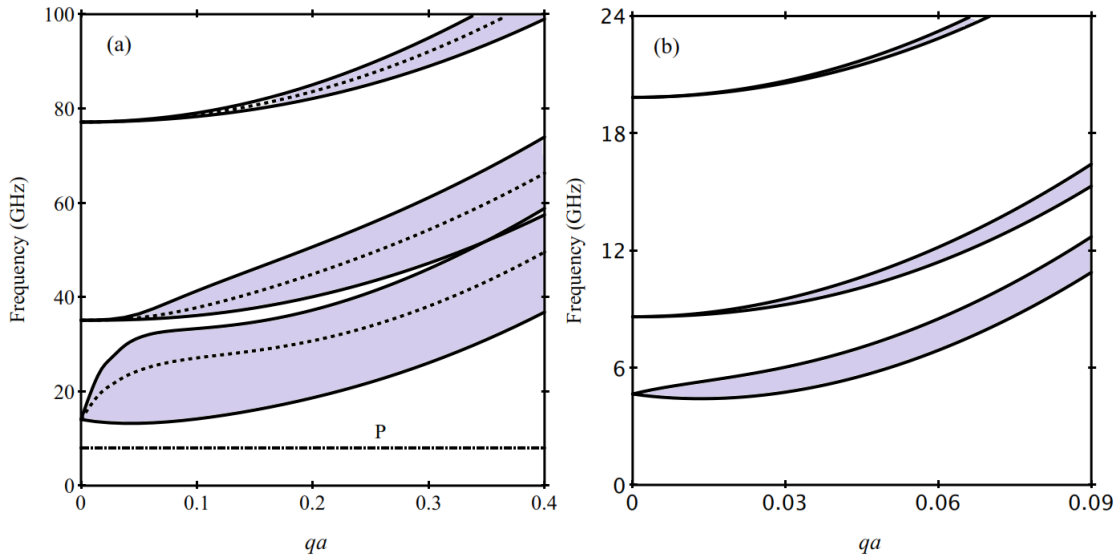

Figure 3.2: SW frequencies for the lowest three bands (shaded areas) in ultrathin films plotted versus dimensionless in-plane wave vector qa for (a) EuO with $N = 12$ and (b) YIG with $N = 50$, with $\mu_0 H_0 = 0.1$ T in both cases. The bottom and top of each band corresponds to propagation angle $\phi = 0$ and $\pi/2$, respectively. Also in case (a) the line for $\phi = \pi/4$ is included (dashed line) and the horizontal line (labeled P) indicates one half of the pumping frequency to be considered.

lowest lies very close to the angular frequency $g\mu_B \sqrt{H_0(H_0 + 4\pi M_s)}$ of the Damon-Eshbach (DE) mode at $q = 0$ in magnetostatic theory [36], as may be deduced from Eq. (1.50). This expression yields 14.0 and 4.65 GHz using the quoted M_s and H_0 for Fig.3.2(a) and 3.2(b), respectively, which are seen to be close to the numerical calculations. The separation of the bands increases with $H_{\rm ex}$ and decreases with N. This means relatively narrow, separated bands for YIG and wider bands for EuO that are beginning to overlap for $N = 12$ in Fig. 2(a). The top of the DE mode in magnetostatic theory corresponds to angular frequency $g\mu_B(H_0 + 2\pi M_s)$. This yields 36.4 GHz for EuO in Fig. 3.2(a), which is roughly where the first band levels off at small $qa \sim 0.1$ before increasing further due to exchange effects at larger wave vectors. The corresponding value is 5.3 GHz for the YIG film in Fig. 3.2(b). Another notable feature is the initial dip of the lower ($\phi = 0$) boundary of the first band, which is expected by analogy with properties of the magnetostatic backward volume modes [36]. Eventually at larger qa this boundary bends upwards due to effects of exchange interactions, which are stronger in YIG.

In Figs. 3.3 and 3.4 we present calculations for the threshold field h_c (relative to ΔH) plotted

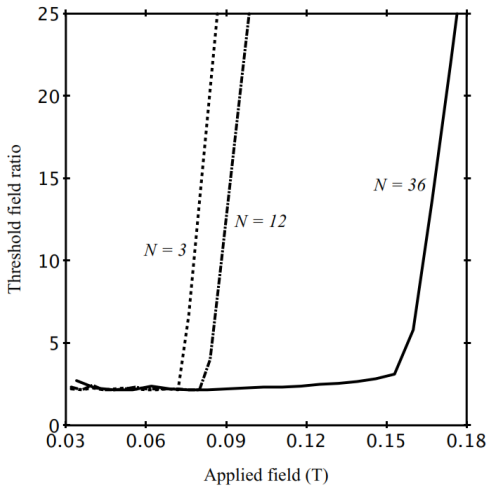

Figure 3.3: SW instability thresholds h_c expressed as a ratio of the half-linewidth ΔH and plotted versus applied field for EuO films with $N = 3$, 12 and 36. Parallel pumping at frequency $\omega_p/2\pi = 16$ GHz is considered with $\eta = 0.1$ GHz.

versus applied field H_0 for EuO films when the pumping-field frequency $\omega_p/2\pi = 16$ GHz. These results are the analogs of the so-called "butterfly curves" in macroscopic samples. The parallel pumping case is considered in Fig. 3.3 where we compare our results for three values of $N = 3$, 12 and 36. The three curves have a similar form with a mainly flat region below a cusp field, whereas above this field (occurring at about 0.07, 0.08, and 0.16 T, respectively, for the three values of N) the threshold h_c increases sharply. This behavior can be understood on the basis that the decay instability is generally dominated by the formation of two degenerate SWs with $\omega_l(\mathbf{q}) = \omega_p/2$ (see, e.g., references cited earlier and Eq. (3.7) for a special case). The horizontal line P drawn at 8 GHz in the dispersion curves of Fig. 3.2(a) when $\mu_0 H_0 = 0.1$ T lies below the bottom of the first SW band, so the decay threshold is high, whereas at smaller H_0 this line would intersect one or more of the SW bands and the decay would be more likely. The results shown in Fig. 3.4 apply for the first-order Suhl effect in the case of perpendicular pumping. The two curves, which have a similar overall form to those in Fig. 3.3, show the instability threshold curves for the cases where the pumping field is along x (parallel to the film surfaces) or along y (perpendicular to the film surfaces). We find that the h_c values are larger in the latter case, and this is related to the ellipticity of the spin precession.

Next we consider examples for nanowires. In Fig. 3.5 the frequencies of the lowest SW

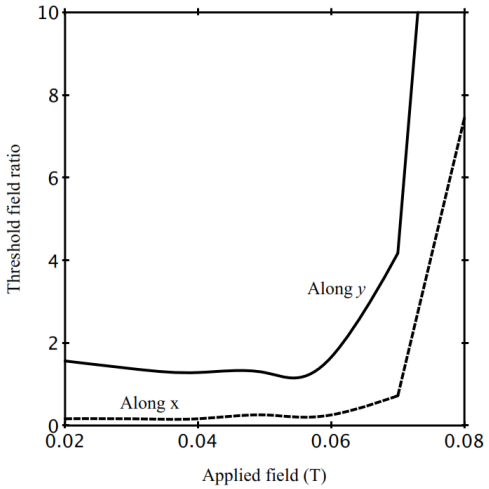

Figure 3.4: SW instability thresholds h_c expressed as a ratio of the half-linewidth ΔH and plotted versus applied field for a EuO film with $N = 10$ and $\eta = 0.01$ GHz. Perpendicular pumping at $\omega_p/2\pi = 16$ GHz is considered for the microwave field along x (dashed line) and along y (solid line).

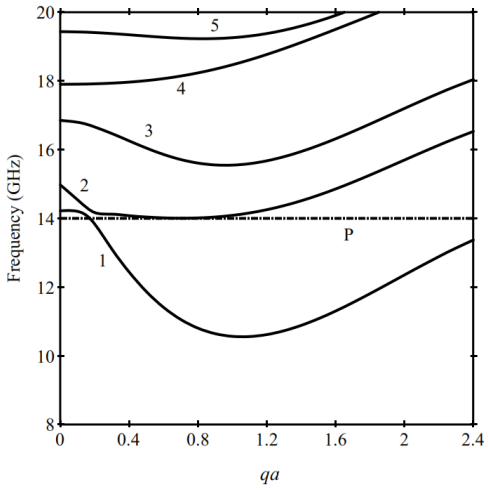

Figure 3.5: SW frequencies plotted versus dimensionless longitudinal wave vector qa for the lowest five branches of a 4×3 nanowire ($N = 12$) taking parameters as for $GdCl_3$ and a longitudinal applied field 0.117 T and $\eta = 0.1$ GHz. The horizontal line (labeled P) indicates one half of the pumping frequency to be considered.

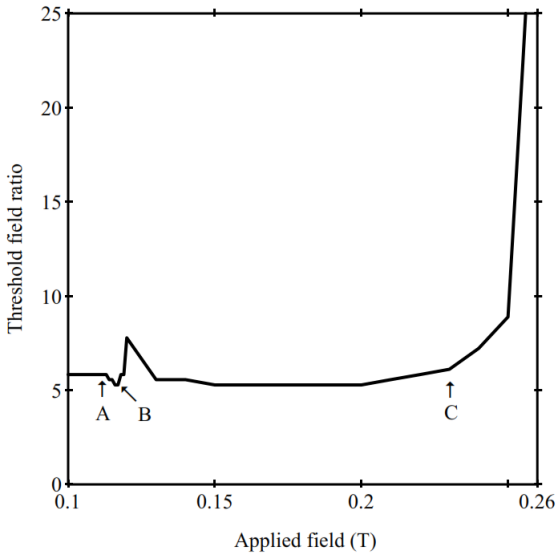

Figure 3.6: SW instability threshold h_c expressed as a ratio of the half-linewidth ΔH and plotted versus applied field for a 4×3 ($N = 12$) $GdCl_3$ nanowire. Parallel pumping at $\omega_p/2\pi = 28$ GHz is considered with $\eta = 0.1$ GHz.

branches of a $N = 12$ wire in a longitudinal applied field are plotted as a function of qa using parameters for $GdCl_3$, which is a strongly-dipolar material as mentioned. Since we now have a 1D wave vector (by contrast with the film case), the spectrum consists of a series of curves for the different branches instead of bands. Some branches show a minimum at a nonzero wave vector, which is a result of the interplay between the dipolar and exchange interactions (with features analogous to the magnetostatic backward volume modes characteristic of the wave vector being parallel to the net magnetization). In addition, we see some effects of hybridization (with mode repulsion) between branches labeled 1 and 2 for small qa. The butterfly curve for the same nanowire with parallel pumping is given in Fig. 3.6, which has several features labeled as A (at $\mu_0 H_0 = 0.11$ T), B (at 0.117 T) and C (at 0.23 T). They can all be associated with applied field values at which the line P in Fig. 3.5, drawn at one-half of the pumping frequency, coincides with a specific feature of the SW dispersion. Point A corresponds to the field when the one-half frequency is coincident with the $qa \approx 0$ part of branch 1, point B corresponds to the field value in Fig. 3.5 where the line is just touching the minimum in branch 2, and point C is analogous to the main cusp point in previous examples (i.e., the field value where the line is just touching the minimum in branch 1).

In Figs. 3.7 and 3.8 we examine the behavior in a nanowire when the static field is applied transversely (in the x direction), causing the spins to cant in that direction. We employ parameters for a 12×1 EuS wire (or ribbon-like structure). Results for the lowest SW frequencies plotted versus the transverse field at a fixed $qa \approx 0$ are given in Fig. 3.7(a), where the main dip at $\mu_0 H_0 \approx 0.20$ T provides us with the critical field value above which the net spin orientation or sample magnetization is along x. Below the critical field the competition between the applied field and the dipolar field leads to SW curves that decrease gradually with increasing H_0. Above the critical field the spins are reoriented perpendicular to the wire axes and the frequencies increase with increasing H_0. Next, in Fig. 3.7(b) we show the lowest SW frequencies plotted versus qa at a fixed H_0 above the critical value. In this case with the longitudinal wave vector perpendicular to the net magnetization direction, the SW frequencies all increase monotonically with increasing qa, unlike the behavior in a longitudinal field (see Fig 3.5). The lowest two branches are well separated at small qa, but become approximately degenerate at larger qa when exchange effects start to play a dominant role. The corresponding butterfly curve for the transversely-magnetized EuS wire in the case of parallel pumping is given in Fig. 3.8. We note two features labeled X and Y at $\mu_0 H_0 = 0.21$ T and 0.251 T respectively, which correspond to the one-half pumping frequency line coinciding with the minimum frequency for SW branch 2 (as in Fig. 3.7(b)) and then for SW branch 1.

3.3 Conclusions

We have presented a microscopic dipole-exchange theory for the SW instability thresholds of ferromagnetic nanostructures, specifically for films magnetized in-plane, longitudinally magnetized wires (or stripes), and transversely magnetized wires. Both the parallel and perpendicular (first-order Suhl) configurations for the pumping field were considered and the results were interpreted in terms of the SW modes, which are quantized differently in the two structures due to their differing symmetries. The results depend sensitively on the dipolar-to-exchange ratio, and this was

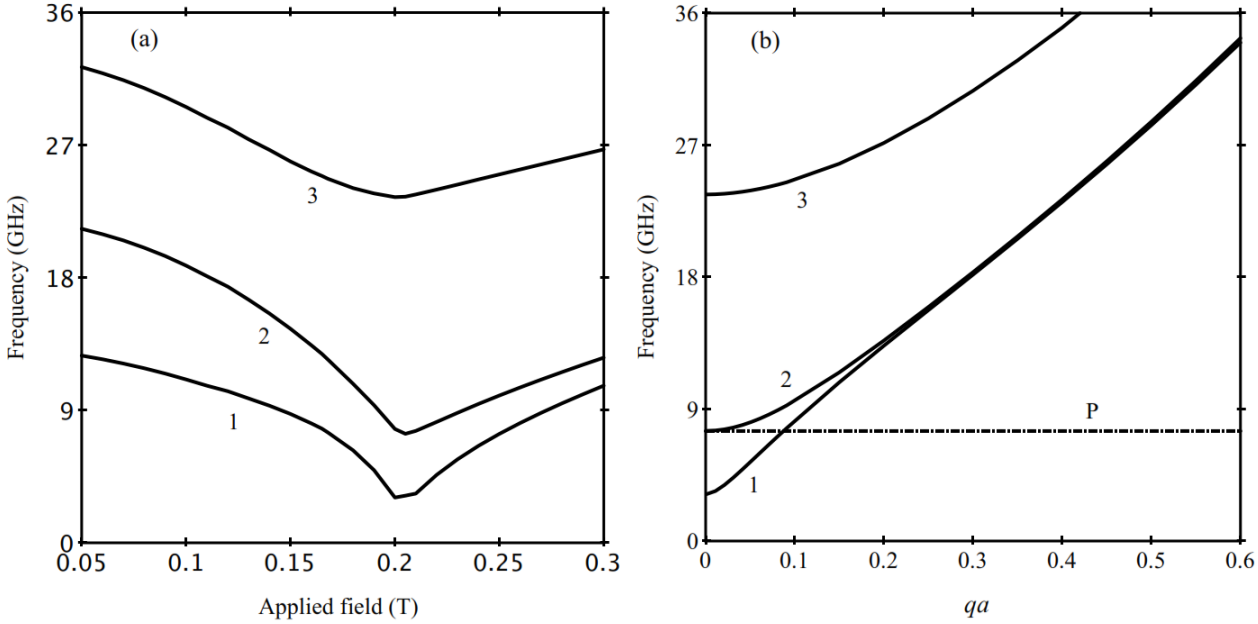

Figure 3.7: SW frequencies for the lowest three branches of a 12×1 EuS nanowire ($N = 12$) in a transverse applied field with $\eta = 0.03$ GHz: (a) plotted versus H_0 applied field below and above the transition at 0.20 T for a fixed $qa \approx 0$; (b) plotted versus qa for a fixed field 0.21 T which is above the transition. The horizontal line (labeled P) in (b) indicates one half of the pumping frequency to be considered.

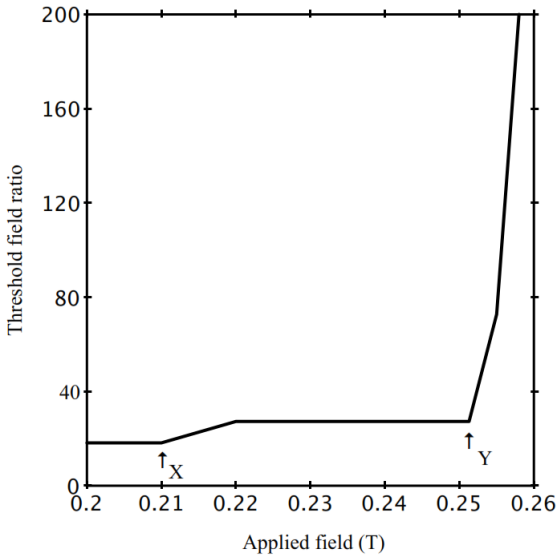

Figure 3.8: SW instability threshold h_c expressed as a ratio of the half-linewidth ΔH and plotted versus the transverse applied field (above the transition field in Fig. 3.7) for a 12×1 ($N = 12$) EuS nanowire with $\eta = 0.03$ GHz. Parallel pumping at $\omega_p/2\pi = 215$ GHz is considered.

illustrated taking parameters for different magnetic materials. In future work it would be of interest to explore more fully the role of damping and also to include effects of surface anisotropy. A complication in the case of the damping is that the spin relaxation often takes place through different mechanisms (e.g., magnon-magnon interactions, scattering from impurities or surface inhomogeneities, etc). For example, recent experiments [54] on Permalloy nanowires (stripes) showed contributions to the damping due to three-magnon processes and edge roughness.

Chapter 4

Interface coupling for spin waves in NiFe/Ru/NiFe multilayer nanowires

The material in this chapter has been published as an article by me (with P. Lupo, M. G. Cottam, and A. O. Adeyeye) listed as Ref. [73].

Recently, magnonic crystals (MCs) have attracted a lot of interest promoted by the need for miniaturization and low-power devices as well as the possibility for long-range propagation of information as provided by the spin-wave (SW) signals [74, 75]. In general, SW-based MCs (which are the lateral periodic arrays mentioned in Section 1.4) can be easily fabricated in the nanometric scale with the current advanced lithography techniques and they hold great promise for down-scaling microwave devices operated in the GHz frequency regime [20, 3]. The dispersion relations of the SWs have been found to be crucially dependent on the short-range magnetic interactions (i.e., exchange coupling, interlayer coupling) as well as the long-range (i.e., dipolar and magnetostatic coupling) [76, 77, 78]. The interplay of these interactions is substantially modified when the geometry and length scales of the MCs are gradually downscaled, resulting in the formation of multi-band features in the SW spectrum [79, 80].

Nanowire (NW) arrays provide an ideal MC model for studying the impact of geometric confinement on the magnetization dynamics at the sub-micrometer and nanometer scales [81, 82]. In

particular, ferromagnetic NWs are characterized by the absence of a static demagnetizing field when the external magnetic field is applied along the length of the stripes. This provides a typical quasi-2D FMR spectrum [71]. Nevertheless, when the width of the stripes is reduced below a certain limit the aspect ratio becomes high enough to considerably affect the magnetization reversal mechanisms and thus the corresponding ferromagnetic dynamics in the NW [83].

Interlayer-coupled NWs represent another interesting prospect for tuning the propagation of SWs in MCs composed of long stripes [84]. The role of interlayer exchange coupling (IEC), such as the RKKY interaction (see Section 1.1), between the ferromagnetic layers of a multi-component NW, with layers separated by a nonmagnetic spacer, affects significantly the type of magnetic ordering. In turn, it may lead to the development of different regimes of ferromagnetic SW dynamics [77]. The influence of width on the dynamical behavior of simpler NW arrays (i.e., in the absence of IEC) has already been widely studied [78, 85]. Also in previous work on NW arrays with IEC mechanisms present [82], the effects on the SW dynamics of the additional contributions coming from both the bilinear RKKY and the biquadratic exchange coupling (see Section 1.1) were investigated. Attention was restricted, however, to NWs where the widths (270 nm or more) were such that the in-plane shape anisotropy (representing the difference between the energy for magnetization along the preferred longitudinal axis versus the transverse direction) was small. By contrast, the motivation for the present study is narrower NWs where the stripe aspect ratio is such that the shape anisotropy energy becomes important and the IEC (particularly the biquadratic exchange) is found to be modified due the lateral edges of the stripes. The overall consequences are that the biquadratic and RKKY couplings compete, both with each other and the enhanced shape anisotropy effects, resulting in a more complex magnetic ground state (depending on the applied magnetic field) as well as novel features in the SW spectrum as studied by FMR.

In this chapter, we present a systematic study of the influence of the Ru spacer layer thickness (t) in the range of 0.7 to 2.0 nm on the interlayer coupling between the Permalloy ($Ni_{80}Fe_{20}$) layers. Specifically, we investigate $Ni_{80}Fe_{20}$ / Ru /$Ni_{80}Fe_{20}$ trilayer NWs with different widths (W) in a range from 90 to 190 nm. Both the static and dynamic properties of the interlayer-coupled

NWs were investigated as a function of t and W using a vibrating sample magnetometer (VSM) and broadband FMR microscopy, respectively.

On the theoretical side, we study both the static and dynamical aspects of the interlayer-coupled NWs, by employing a microscopic (or Hamiltonian-based) approach, supplemented by macroscopic numerical simulations for the hysteresis loops. For this purpose, we have generalized previous microscopic dipole-exchange theory used for interlayer-coupled complete films [86] and individual ferromagnetic NWs [87] to the exchange- and dipolar-coupled bilayer NWs being considered here. As in [86], we include the effects of biquadratic and RKKY exchange coupling across the spacer layer, as well as dipolar coupling, and the role of single-ion anisotropy in addition to the shape anisotropy of the NWs. The role of the interlayer exchange coupling on the static and dynamic magnetization behavior of wider trilayer NWs [82] was previously considered using micromagnetic simulations and FMR experiment [86, 82]. By contrast, we find that in present multilayer NWs with smaller widths, both shape anisotropy and single-ion anisotropy as well as the lateral and depth quantization of the SWs become more important, as mentioned above, leading to a significantly modified behavior. These systems are of interest because the strong shape anisotropy, competing with the other interactions, leads to overall antiferromagnetic (AFM), spin-flop (SF), and ferromagnetic (FM) ordering (depending on the external field).

The structure of this chapter is as follows. In Section 4.1 we outline the sample fabrication and the experimental techniques used by our collaborators at the National University of Singapore for measuring the hysteresis loops and the FMR. Details of our theoretical techniques are given in Section 4.2. Then in Section 4.3 the results for the static and dynamical properties are presented, and comparisons with the theory follow in Section 4.4. The conclusions are given in Section 4.5.

4.1 Experiment

Periodic arrays of NWs with widths of W = 190, 140, 110 and 90 nm, and pitch p = 280 nm, were fabricated on a Si substrate over a large area (4×4 mm) using using deep-ultraviolet lithography and

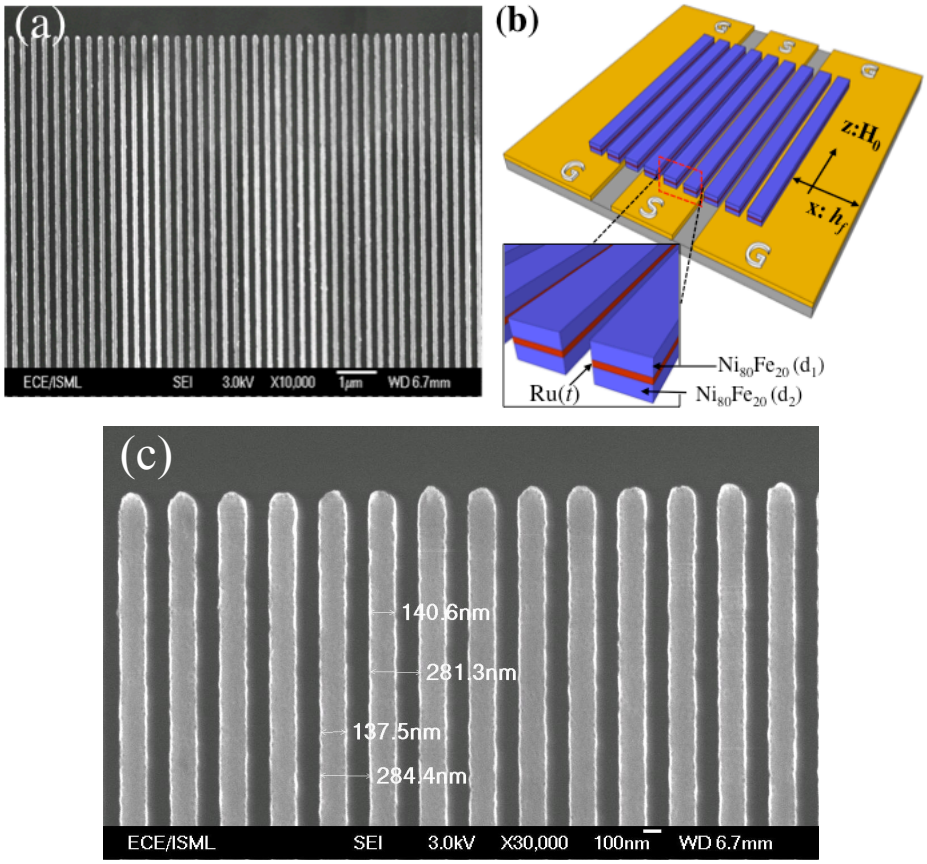

Figure 4.1: (a) SEM of an array of $Ni_{80}Fe_{20}$ (20 nm) / Ru (0.7 nm) / $Ni_{80}Fe_{20}$ (10 nm) structures, each with width $W = 110$ nm; (b) Geometry of the trilayer NWs, where $d_1 = 10$ nm and $d_2 = 20$ nm, on top of the CPW; (c) High-magnification ($\times 30,000$) SEM to illustrate the degree of spatial inhomogeneity in an array where nominally $W = 140$ nm and the periodic length is nominally 280 nm.

a lift-off method. Trilayer stacked systems with composition $Ni_{80}Fe_{20}(d_2)$ / Ru (t) / $Ni_{80}Fe_{20}(d_1)$ were deposited in a physical vapor deposition chamber with a base pressure lower than 2×10^{-8} Torr. The $Ni_{80}Fe_{20}$ layers with $d_1 = 10$ nm and $d_2 = 20$ nm were deposited by electron-beam evaporation at a rate of 0.2 nm/s, while the Ru spacer with thicknesses $t = 0.7$ and 2 nm was deposited by DC magnetron sputtering at a rate of 0.003 nm/s and a constant Ar working pressure of 3 mTorr. For the NW arrays with $W = 90$ and 140 nm the Ru thickness is $t = 1$, 1.5, and 2 nm, while for $W = 190$ and 110 nm the Ru thickness is $t = 0.7$, 1.5, and 2 nm. The stacking structures were fabricated in subsequent deposition steps without breaking the vacuum. A scanning electron microscope (SEM) image for a NW array with $W = 110$ nm is shown in Fig. 4.1(a).

The static magnetic switching was characterized using a vibrating sample magnetometer (VSM)

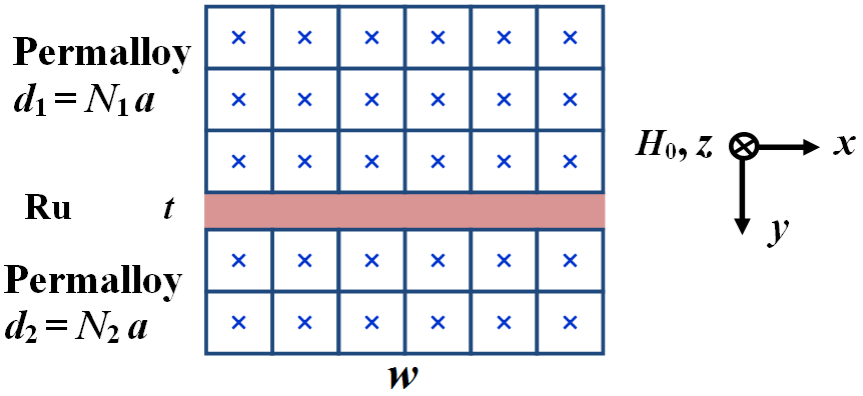

Figure 4.2: Schematic cross section of a $Ni_{80}Fe_{20}$ (d_1) / Ru (t) /$Ni_{80}Fe_{20}$ (d_2) trilayer NW of width W with translational symmetry along the z axis and finite dimensions in the xy plane. The finite cells (cuboids with sides of length a and an effective spin at the center) are shown.

with the external magnetic field (H_0) applied along the NWs longitudinal axis (z axis). The ferromagnetic dynamic response was measured at room temperature using a vector network analyzer by sweeping the frequency from 50 MHz to 20 GHz. For these FMR measurements a coplanar waveguide (CPW) was fabricated using standard optical lithography and followed by the deposition of Al_2O_3 (50 nm) / Ti (5 nm) / Au (150 nm) and lift-off. The vector network analyzer is connected to the CPW by a G-S-G-type microwave probe, the signal line is 40 μm wide and the gap with the ground line is 25.5 μm. The samples were loaded on top of the CPW with the metallic surface in contact with it. The frequency sweeping was repeated with different magnetic fields in the range from negative saturation (H_0 = -1400 Oe) to positive saturation (H_0 = 1400 Oe). The microwave magnetic field h_f produced by the signal line of CPWs was applied orthogonally to the external static field H_0, i.e. along the x axis, as shown in Fig. 4.1(b). As emphasized later, the quality of the lithography at the very small length scales is an important design factor, and to illustrate this we include a high-magnification (30,000 times) SEM in Fig. 4.1(c).

4.2 Theory

The microscopic (or Hamiltonian-based) theory is used here to analyze the dependence of the inhomogeneous static magnetization and the lowest few SW frequencies on the applied magnetic field

H_0. The static results obtained from the microscopic approach can alternatively be studied using a micromagnetic simulation, as will be explained later. The theory is analogous to that in previous work where the focus was on individual ferromagnetic NWs [87]. Here we generalize to multilayer NWs with the spacer geometry described earlier. The modified theoretical method employs a Hamiltonian that includes additional competing effects such as RKKY and biquadratic exchange coupling across the spacer as well as the anisotropy. Both these interactions were introduced in Section 1.1.

The nanowire is modeled as having a rectangular cross section that consists of $N = (N_1 + N_2)\, W/a$ atomic spins (in the xy plane) extending along the z direction (see Fig. 4.2). We analyze here a general case in which one nanowire has N_1 layers of spins and the other has N_2 layers. The total spin Hamiltonian for the trilayer system can be expressed as

$$\begin{aligned} H &= -\frac{1}{2}\sum_{in,jm} J_{in,jm}\mathbf{S}_{in}\cdot\mathbf{S}_{jm} + \frac{1}{2}(g\mu_B)^2\sum_{in,jm}\sum_{\alpha,\beta} D^{\alpha\beta}_{in,jm} S^{\alpha}_{in} S^{\beta}_{jm} \\ &\quad -g\mu_B H_0\sum_{in} S^{z}_{in} + H_{An} + H_{BQ}, \end{aligned} \tag{4.1}$$

where i and j label the spin sites along the z-directed lines formed by the spins, while indices n and m $(= 1, 2, \cdots, N)$ refer to all the spin sites in any cross section of the nanowire. The first term in Eq. (4.1) describes the short-range Heisenberg (bilinear) exchange interaction between the effective spins $\mathbf{S}_{in}$ and $\mathbf{S}_{jm}$ at a distance apart specified by $\mathbf{r}_{in,jm}$. The exchange $J_{in,jm}$ between sites $\mathbf{r}_{in}$ and $\mathbf{r}_{jm}$ is taken to be J for all nearest neighbors in either of the $Ni_{80}Fe_{20}$ layers, and zero otherwise. We also indicate the additional interlayer RKKY interaction through an exchange contribution $-J_R$ for coupling closest sites across the interface. With this notation an antiferromagnetic coupling is favored when $J_R > 0$. The second term represents the long range dipole-dipole interactions within and between the $Ni_{80}Fe_{20}$ layers. The dipolar interactions $D^{\alpha\beta}_{in,jm}$ are given by Eq. (3.2). The third term in Eq. (4.1) represents the Zeeman energy due to the z-directed external magnetic field H_0. The next term gives the energy due to single-ion anisotropy (if any)

$$H_{An} = -\sum_{in} K_{in} \left(S^z_{in}\right)^2, \tag{4.2}$$

where the coefficient K_{in} may depend in general on the position of the spins (i, n). For example, it may take a different value at the lateral edges due to roughness. Finally, the last term describes the interface biquadratic exchange

$$H_{BQ} = \frac{1}{2} \sum_{in,jm} J_{BQ\,(in,jm)} \left(\mathbf{S}_{in} \cdot \mathbf{S}_{jm}\right)^2. \tag{4.3}$$

For simplicity, we take the biquadratic exchange (with value denoted by J_{BQ}) to couple only a site i in the interface layer of one nanowire to the corresponding site i in the interface layer of the other nanowire. The sign convention is such that a 90° relative orientation of the layer magnetizations across the interface would be favored due to this term alone when $J_{BQ} > 0$. We next consider the net effect of the above Hamiltonian terms in determining the equilibrium orientation of the spins. Then the SW dynamics for the system will be developed.

4.2.1 Equilibrium spin configuration

Due to the competition between the RKKY coupling and magnetic interactions, such as the other bilinear and biquadratic exchange interactions, dipole-dipole interactions (including shape anisotropy of the NWs) as well as any single-ion anisotropy, the spins will generally be canted relative to the symmetry axes. Consequently the magnetization become spatially nonuniform, particularly near the interface and the lateral edges. For sufficiently large values of the applied field the magnetization vectors in the trilayer NWs prefer a parallel relative alignment along the field direction, otherwise an overall AFM or SF phase may occur in appropriate cases.

First the theory involves determining the equilibrium spin orientation according to mean-field methods at low temperatures ($T \ll T_c$). Within the microscopic theory, we follow a similar approach to that described for complete films [58], except that now the spin orientations no longer depend only on the layer number in the xz plane. Instead we replace $\mathbf{S}_{in}$ by $(\bar{S}^x_n, \bar{S}^y_n, \bar{S}^z_n)$ in any cross section, where $\bar{S}^x_n = S \sin\theta_n \cos\alpha_n$, $\bar{S}^y_n = S \sin\theta_n \sin\alpha_n$ and $\bar{S}^z_n = S \cos\theta_n$ are the components

in mean-field theory, and we have introduced two sets of angles $\{\theta_n\}$ and $\{\alpha_n\}$ in spherical polar coordinates, independent of label i. Then the total free energy $\bar{E}$ can be obtained using Eqs. (4.1) - (4.3), as a function of the angles $\{\theta_n, \alpha_n\}$, all of which will be small for large applied field H_0 (in the FM phase). Next the components of the effective field for a spin in any cross section n of the NW can be found using $g\mu_B H_{\rm eff}^{\alpha,n} = -\delta\bar{E}/\delta\bar{S}_n^{\alpha}$ with $\alpha = x, y, z$.

A starting configuration of angles $\{\theta_n, \alpha_n\}$ is now chosen to approximate the ground state. In fact, we employ several starting configurations in order to avoid difficulties with local minima and to find the true $T = 0$ ground state. Then each spin can be rotated to be along the direction of its local effective field, giving a new set of angles that satisfy

$$\tan\alpha_n = \frac{H_{\rm eff}^{y,n}}{H_{\rm eff}^{x,n}}, \qquad |\tan\theta_n| = \frac{\left[\left(H_{\rm eff}^{x,n}\right)^2 + \left(H_{\rm eff}^{y,n}\right)^2\right]^{1/2}}{\left|H_{\rm eff}^{z,n}\right|}. \tag{4.4}$$

This process can be repeated iteratively until convergence to a self-consistent static-equilibrium configuration is achieved, giving the required set of angles.

For a supplementary analysis of the static magnetic phase behavior (in particular, for interpreting the hysteresis loops) we performed static simulations using the LLG Micromagnetic Simulator software [88] and standard bulk magnetic parameters for $Ni_{80}Fe_{20}$. The details of this method were described in our previous work on the wide trilayer NWs [82] where the shape-anisotropy effects were much smaller. In the present case we were able to use smaller discretized cells of size 5 nm $\times$ 5 nm $\times$ 5 nm, as well as the previous size 10 nm $\times$ 10 nm $\times$ 10 nm, which is expected to give improved accuracy. The only exception was in the case of NWs with the largest width $W = 190$ nm, where use of a 5 nm cell was impractical.

4.2.2 SW frequencies

We proceed to consider the magnetization dynamics for the SWs and therefore the frequencies of the FMR modes as the function of the applied field H_0. To carry out this calculation, by analogy with the general method used in previous work for individual stripes [87, 70], we apply a

transformation of axes from the global coordinates (x, y, z) assigned to each spin to a set of local coordinates (X, Y, Z) chosen such that the new Z axis is along the equilibrium direction of that spin. Next, the spin Hamiltonian is transformed into an equivalent form in boson operators using the Holstein-Primakoff transformation defined relative to the "*local*" axes. The transformed Hamiltonian can be expanded as $H = H^{(0)} + H^{(1)} + H^{(2)} + \cdots$, where $H^{(m)}$ denotes the term with a product of m boson operators. Now $H^{(0)}$ is a constant and so has no role in the dynamical behavior, while $H^{(1)}$ vanishes by symmetry. Thus the linear SW spectrum is then obtained from $H^{(2)}$, and the higher-order terms will not be considered here. The general form of the quadratic Hamiltonian $H^{(2)}$ can be written as

$$H^{(2)} = \sum_{n,m,k} \left[A^{(2)}_{n,m}(k) a^{\dagger}_{k,n} a_{k,m} + B^{(2)}_{n,m}(k) a_{k,n} a_{-k,m} + C^{(2)}_{n,m}(k) a^{\dagger}_{k,n} a^{\dagger}_{-k,m} \right], \tag{4.5}$$

where k is the wave number along the wire axis, and $a^{\dagger}_{k,n}$ and $a_{k,n}$ are creation and annihilation operators respectively. The expressions for the coefficients $A^{(2)}_{n,m}(k)$ and $B^{(2)}_{n,m}(k)$, which depend on the canting angels $\{\theta_n, \alpha_n\}$, become complicated and are not quoted here.

The final step is to derive the spectrum of the SW frequencies. This can be done by diagonalizing the second-order Hamiltonian $H^{(2)}$ using a canonical (generalized Bogoliubov) transformation as described in [87, 70]. This eventually gives rise to a dynamical block matrix formed by

$$\begin{pmatrix} \mathbf{A}(k) & 2\mathbf{B}(k) \\ -2\mathbf{B}^{*}(-k) & -\tilde{\mathbf{A}}(-k) \end{pmatrix}, \tag{4.6}$$

where $\mathbf{A}$ and $\mathbf{B}$ denote the matrices of dimension $N_1 + N_2$ formed by the coefficients appearing in Eq. (4.5), and the tilde denotes a transpose. The positive eigenvalues of the above large matrix correspond to the total of $N = N_1 + N_2$ physical SW frequencies, and there is a degenerate (in magnitude) set formed by the negative eigenvalues. In order to compare the theory results with the FMR data, the expression for $A^{(2)}_{n,m}(k)$ and $B^{(2)}_{n,m}(k)$ at zero wave vector is used to deduce the lowest frequency modes from the matrix resulting from Eq. (4.6). The "diagonalized" form of $H^{(2)}$ can be expressed as (apart from a constant)

$$H^{(2)} = \sum_{k} \sum_{l=1}^{N} \omega_{k,l} \alpha_{k,l}^{\dagger} \alpha_{k,l}, \tag{4.7}$$

where $\omega_{k,l}$ are the discrete SW modes at wave vector k with integer l (= 1, 2, ... , N) being a branch number, while $\alpha_{k,l}^{\dagger}$ and $\alpha_{k,l}$ are the new (diagonalized) boson operators for creation and annihilation of the modes.

4.3 Results and discussion

4.3.1 Static magnetic properties

In Fig. 4.3 we show the hysteresis loops of the $Ni_{80}Fe_{20}$ / Ru (t) / $Ni_{80}Fe_{20}$ NWs for widths of (a)-(c) 90 nm and (d)-(e) 140 nm at different values of t. We focus our discussion initially on the smallest of these t values (i.e., 1 nm) where the biquadratic coupling (J_{BQ}) plays a significant role in the magnetic reversal process. Then later we will describe the main changes introduced by a thicker Ru layer. Although the Ru thickness of 1 nm can lead to an antiparallel coupling via the RKKY interaction, as shown in previous work [82], it is worthwhile to note that in a simple two-sublattice antiferromagnetic we would have a state with zero net magnetization. This is not the case here since we are studying asymmetric structures with $d_2 \neq d_1$. The $M - H_0$ loops for the two samples with t = 1 nm show broadly similar features to one another, suggesting a similar magnetic switching process at overall $M \neq 0$ (see Figs. 4.3(a) and (d)).

Both the $M - H_0$ loops start with a saturated state at high positive field with a ferromagnetic (parallel) alignment of the magnetizations between the top and bottom $Ni_{80}Fe_{20}$ layers. The net magnetization decreases gradually as the value of external field is reduced due to the magnetization reversal process, which is driven by the interplay of shape anisotropy, induced by the nanofabrication, and the interlayer exchange coupling (IEC) induced through the thin Ru spacer layer. As the field decreases, a multi-domain ground state develops along the NW in both the $Ni_{80}Fe_{20}$ layers. This configuration is characterized by an opposite alignment between the magnetic domains of the top and bottom layers [82]. The formation of this ground state is favored by the RKKY compo-

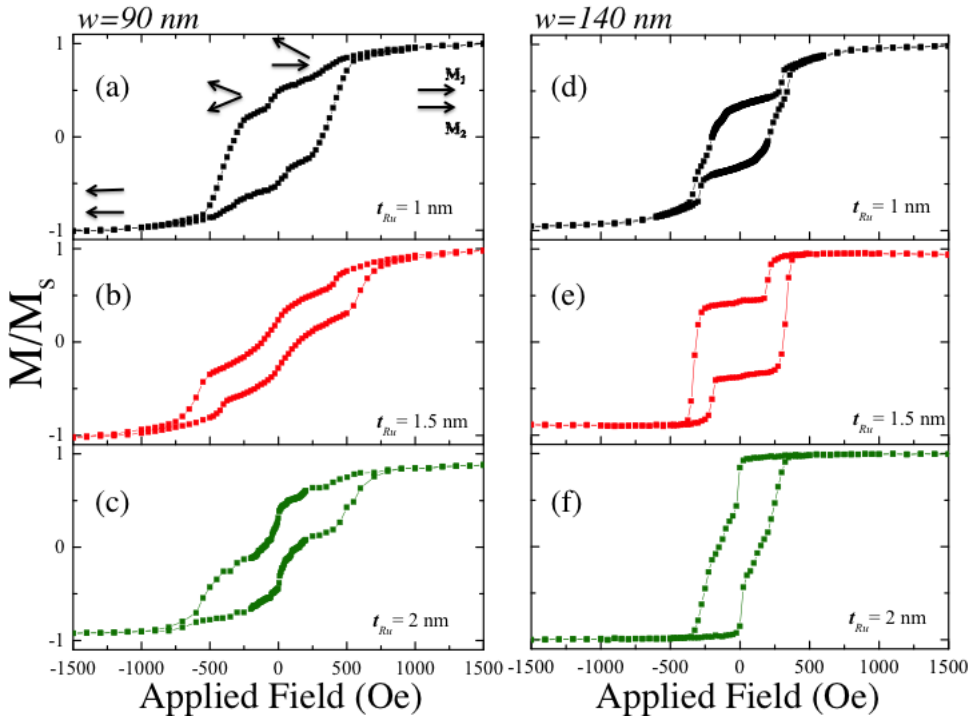

Figure 4.3: $M - H_0$ loops for $Ni_{80}Fe_{20}$ (20 nm) / Ru (t) / $Ni_{80}Fe_{20}$ (10 nm) NW arrays with W = 90 nm and (a) t = 1 nm, (b) 1.5 nm, (c) 2 nm in the first column; and W = 140 nm and (d) t = 1 nm, (e) 1.5 nm, (f) 2 nm in the second column. The sketches of magnetization states are shown for W = 90 nm as insets in panel (a).

nent (J_R) of the IEC. Nevertheless, the simultaneous presence of additional comparable biquadratic (J_{BQ}) coupling introduces an inhibiting field in the reversal process, since the magnetization inside the domains is forced to rotate (mainly in the xz plane) and against the strong demagnetization field. As already mentioned (see also [86, 82]) the RKKY coupling favors antiparallel alignment of the magnetization while biquadratic coupling prefers a 90° alignment of the two layers. As a result, the magnetization rotation in the NW proceeds gradually with a reversal first starting in the top layer (d_1 = 10 nm), which corresponds to the magnetic switching present at 400 Oe for the 90nm-width (Fig. 4.3(a)) and 300 Oe for the 140 nm-width (Fig. 4.3(d)). The early switching in the top (thinner) layer is confirmed by the drop of the net magnetization to roughly one third of the saturation magnetization value. This is, in part, due to the presence of a RKKY coupling that forces the antiparallel alignment between the magnetization in the two $Ni_{80}Fe_{20}$ layers. A similar reversal process takes place more gradually in the thicker layer, which corresponds to the smoother slope in the two loops between 250 Oe $\geq H_0 \geq$ -250 Oe. Decreasing the field favors an increase in

the canting angle (ϕ) between the average magnetization vectors of the two $Ni_{80}Fe_{20}$ layers. This angle ϕ depends on the ratio between the RKKY and biquadratic parts of the IEC (i.e., by J_R and J_{BQ}), but it also involves in a complicated fashion the shape anisotropy and the applied field. The rotation is sharper for the wider NW sample (W = 140 nm) compared to the narrow one (W = 90 nm), which suggests that the RKKY coupling is higher than the biquadratic coupling, and thus the canting angle is smaller. Instead, for the 90 nm-width NWs, the biquadratic coupling is expected to be relatively larger, and thus the in-plane rotation takes place more gradually. When the applied field is further decreased, an opposite SF phase is obtained, with the magnetization vectors being antiparallel to one another and roughly transverse to H_0. Then at larger negative field the opposite ferromagnetic ground state is reached.

The J_R and J_{BQ} components of the IEC both decrease in magnitude as t is increased. In particular, for t = 1.5 nm in both the 90 and 140 nm-width NWs, the magnetization crosses the first switching point at H_0 = 250 Oe (Figs. 4.3(b)-(e)), slightly lower than in the previous case, which is related to the switching in the thinner $Ni_{80}Fe_{20}$ layer (d_1 = 10 nm). This is followed by a SF phase for W = 90 nm, where the demagnetization field is strong enough to oppose the in-plane rotation, while for W = 140 nm a steady antiparallel alignment between the magnetization of the $Ni_{80}Fe_{20}$ layers is reached. When the applied field is further decreased, a reversal of the SF phase is obtained for W = 90 nm, which is followed by the opposite saturated ground state. For W = 140 nm, the antiparallel alignment switches directly to the saturated ferromagnetic ground state.

When t is increased to 2 nm (Figs. 4.3(c) and (f)), the RKKY coupling is drastically decreased, while the biquadratic coupling is too weak to have any noticeable effect. Therefore, the switching occurs close to zero field and it is followed by a smooth slope of the hysteresis loop down to about -250 Oe, which is due to the magnetization rotation in the thicker layer (d_2 = 20 nm). Then, the opposite saturated ferromagnetic state is reached.

The effect of a relatively stronger J_{BQ} has been studied using samples with W = 110 and 190 nm, where the thinner Ru spacer (i.e., 0.7 nm) seems to enhance the biquadratic coupling of the IEC, and, at the same time, a wider NW (when W = 190 nm) reduces the contribution from the

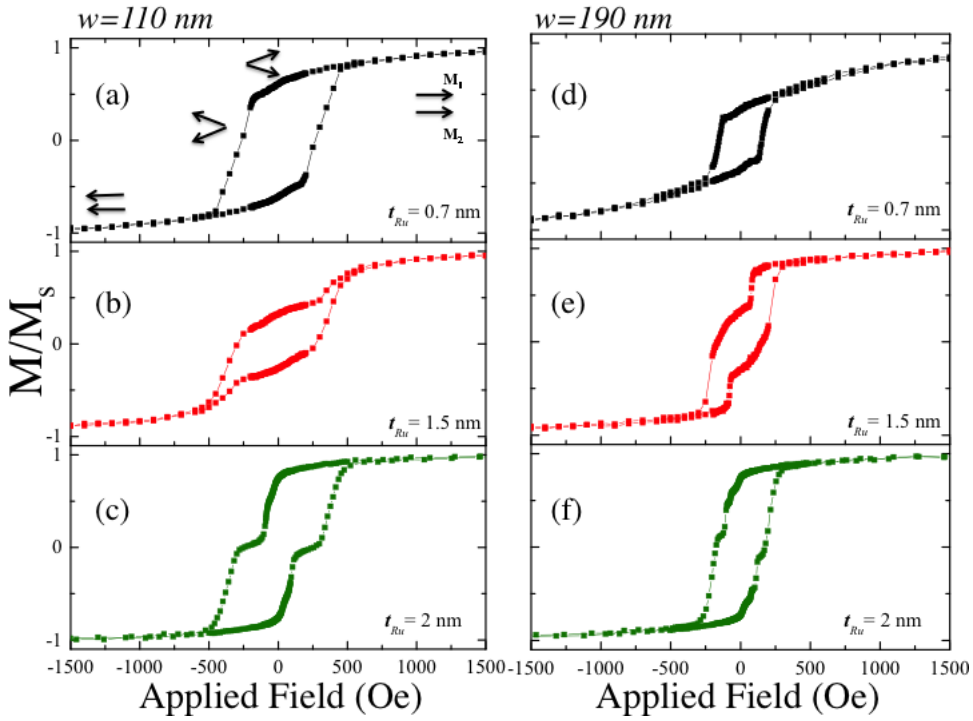

Figure 4.4: $M - H_0$ loops for $Ni_{80}Fe_{20}$ (20 nm) / Ru (t) /$Ni_{80}Fe_{20}$ (10 nm) NWs array with W = 110 nm and (a) t = 0.7 nm, (b) 1.5 nm, (c) 2 nm in the first column; and W = 190 nm and (d) t = 0.7 nm, (e) 1.5 nm, (f) 2 nm in the second column. The sketches of magnetization states are shown for W = 110 nm as insets in panel (a).

shape anisotropy. The hystereis loops for the $Ni_{80}Fe_{20}$/Ru (0.7 nm)/$Ni_{80}Fe_{20}$ NWs are included in Fig. 4.4 for widths of (a) 110 nm and (d) 190 nm respectively. In these samples the thinner Ru thickness induces a stronger interlayer exchange coupling between $Ni_{80}Fe_{20}$ layers compared to the previous case discussed. Nevertheless, the presence of a significant biquadratic coupling, stronger than the RKKY coupling, favors a preferential 90° alignment of magnetization. Consequently, the formation of an antiparallel alignment between the magnetization vectors of the two layers is opposed. The magnetic switching is similar in the two samples.

At high positive fields the magnetizations in the two $Ni_{80}Fe_{20}$ layers are ferromagnetically aligned. Decreasing the field from the saturation, the net magnetization decreases gradually with the formation of a multidomain magnetic ground state. Due to the dominant biquadratic coupling, the magnetization reversal process evolves as a gradual rotation of the magnetization in the plane, and thus the angle difference between the magnetization of the two $Ni_{80}Fe_{20}$ layers increases as

the field decreases. This rotation takes place simultaneously in both top and bottom layer without showing any significant switching field. When the field is further decreased below zero, the magnetization alignment goes through the change of the reciprocal orientation of the vectors in the spin-flop phase. This switching proceeds gradually down to the applied field value of -200 and -120 Oe for W = 110 and 190 nm respectively. At this point, when the applied field crosses over the switching point a complete reversal of the magnetization is obtained. This happens at a higher absolute field value for the narrower NWs array than for the wider one due to the presence of a stronger demagnetization anisotropy in the former case. Finally, the two layers are magnetized along the same direction and the negative saturation point is reached.

The J_{BQ} value drops off sharply when t = 1.5 nm, and thus the RKKY J_R coupling, together with the shape anisotropy, play the leading role in the magnetization reversal process. For t = 1.5 nm (Fig. 4.4(b) and (e)), when the applied field is decreased from the positive saturation state the magnetization starts switching at 250 and 50 Oe for the 110 and 190 nm-width NWs, respectively. A smooth rotation of the magnetization takes place in the narrower NW array (i.e., W = 110 nm) characterized by a SF phase and then the opposite saturation ground state. In the NW array with W = 190 nm, the magnetization follows a similar switching process, but the weaker demagnetization field strength allows for a faster reversal, and then the opposite ferromagnetic alignment is reached at lower applied field. When t is increased to 2 nm (Fig. 4.4(c) and (f)), the bilinear coupling is further decreased, and the biquadratic coupling is ineffective. Therefore, after the switching at zero field, the magnetization passes through a narrow stage of antiparallel alignment, and then it reaches the saturated ferromagnetic state.

4.3.2 Dynamic magnetic properties

We now turn to the dynamic response of the $Ni_{80}Fe_{20}$ / Ru (t) / $Ni_{80}Fe_{20}$ NW arrays when the biquadratic coupling plays an important role. We focus attention on the systems with t = 1 nm (where W = 90 and 140 nm), and then on t = 0.7 nm (where W= 90 and 140 nm). Both cases show a strong IEC exchange coupling, but in the first case the RKKY and biquadratic strength are

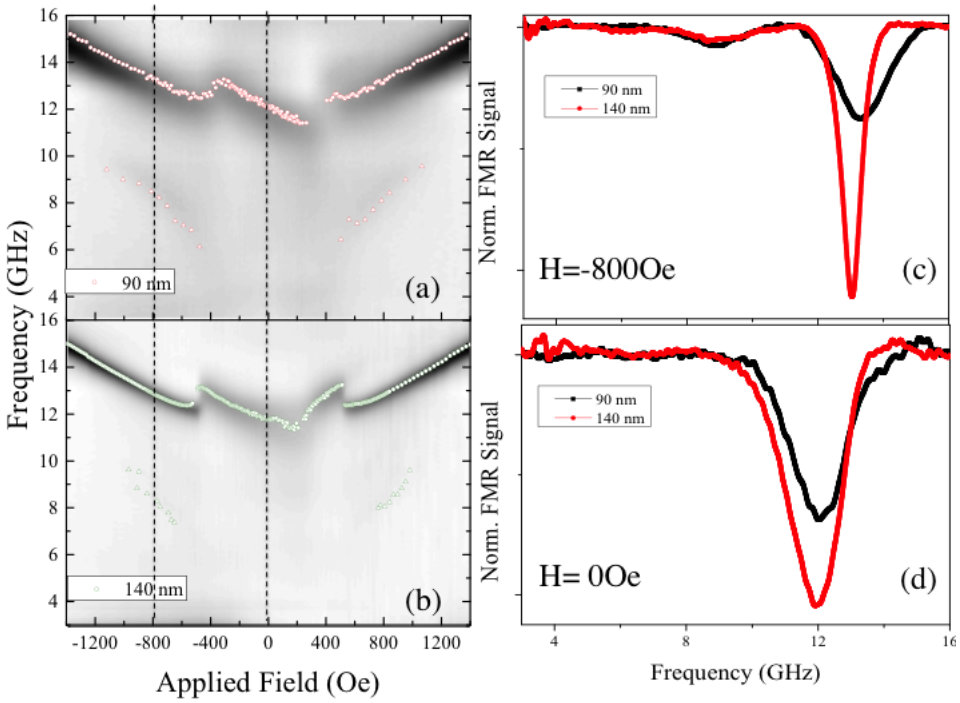

Figure 4.5: 2D FMR absorption spectra for $Ni_{80}Fe_{20}$ (20 nm) / Ru (1 nm) / $Ni_{80}Fe_{20}$ (10 nm) NW arrays with (a) W = 90 nm and (b) W = 140 nm. The points corresponded to relative maximum of the amplitude extracted from the measurements. (c) and (d) FMR frequency line scan for different applied fields.

comparable or slightly different, whereas in the second case the biquadratic term dominates.

In Figs. 4.5(a)-(b) we show the FMR absorption curves taken at various fields for the $Ni_{80}Fe_{20}$ / Ru (1 nm) / $Ni_{80}Fe_{20}$ NWs with a width of (a) 90 nm and (b) 140 nm. Starting from negative saturation, the absorption frequency monotonically decreases until two resonance modes can be identified in the FMR spectrum of each sample. This is also highlighted in Fig. 4.5(c), which shows two absorption peaks in the frequency line scan taken at H_0 = -800 Oe. The lower-frequency mode can be identified as an ”optical” mode in the sense that it involves out-of-phase aspects of the spin precession in the two $Ni_{80}Fe_{20}$ NWs. This can be due to the formation of a SF phase that introduces a z-component of the static magnetization, which is out-of-phase compared to the in-plane components. The conventional FMR measurement is more sensitive to the in-phase spin precession (an "acoustic" mode), whereas the absorption due to out-of-phase magnetization is only generated by the components of the in-phase spins and thus is weaker. The coexistence of both acoustic and optical modes is evident for 1200 Oe $\geq |H_0| \geq$ 400 Oe, while at lower $|H_0|$ values the

amplitude is below the detectable limit. Figure 4.5(d) shows a frequency scan line at the remanence value, where only the acoustic mode is present. At H_0 = -400 Oe both spectra show shifts in the acoustic mode resonance towards higher frequency (Figs. 4.5(a)-(b)). Afterwards, the absorption frequency gradually decreases until H_0 = 200 Oe when another shift at higher frequency occurs in the acoustic mode. In particular for W = 90 nm, a gap in the mode is present between 200 and 400 Oe, when the new higher-frequency mode starts. For W = 140 nm, the frequency shift occurs twice: first at 200 Oe with a transfer to an additional acoustic branch at higher frequency and then, at about 300 Oe, from the former branch to a lower frequency branch. This can be explained by the presence of nearly degenerate acoustic modes.

In Figs. 4.6(a)-(b) we show the FMR absorption curves for the $Ni_{80}Fe_{20}$ / Ru (0.7 nm) / $Ni_{80}Fe_{20}$ NWs with a width of (a) 110 nm and (b) 190 nm. These systems are characterized by a dominant biquadratic component of the IEC. Therefore, the presence of out-of-phase resonance modes is strongly favored, and a more complicated spectrum arises. This is expected in a system where there is symmetry breaking, arising here from the different thicknesses of the $Ni_{80}Fe_{20}$ layers. Typically, a lowering in the symmetry increases the number of the observed FMR absorption peaks [89]. From the negative saturation field, the resonance frequency of the main mode decreases monotonically. Similarly to the case with t = 1 nm, multiple modes are found as soon as the magnetization starts to reverse its alignment. For W = 110 nm two symmetrical modes at lower and higher frequency than the main acoustic mode are observed from H_0 = -1000 Oe. Both of them can be identified as optical modes. As discussed previously, in this NW array the biquadratic coupling dominates over a weak RKKY coupling, which forces the magnetization to rotate in the plane against the shape anisotropy and thus the out-of-phase precession dynamics is enhanced. Instead for W = 190 nm only the optical modes belonging to the lower-frequency family are detected. Figure 4.6(c) shows a line scan at H_0 = -200 Oe of the FMR spectra where the presence of multiple peaks is clearly observable in both 110 and 190 nm-width NW arrays. The coexistence of both acoustic and optical modes is clearly present also in the remanence state for W = 190 nm, as shown in Fig. 4.6(d), while only the higher optical mode is present for W = 110 nm. When

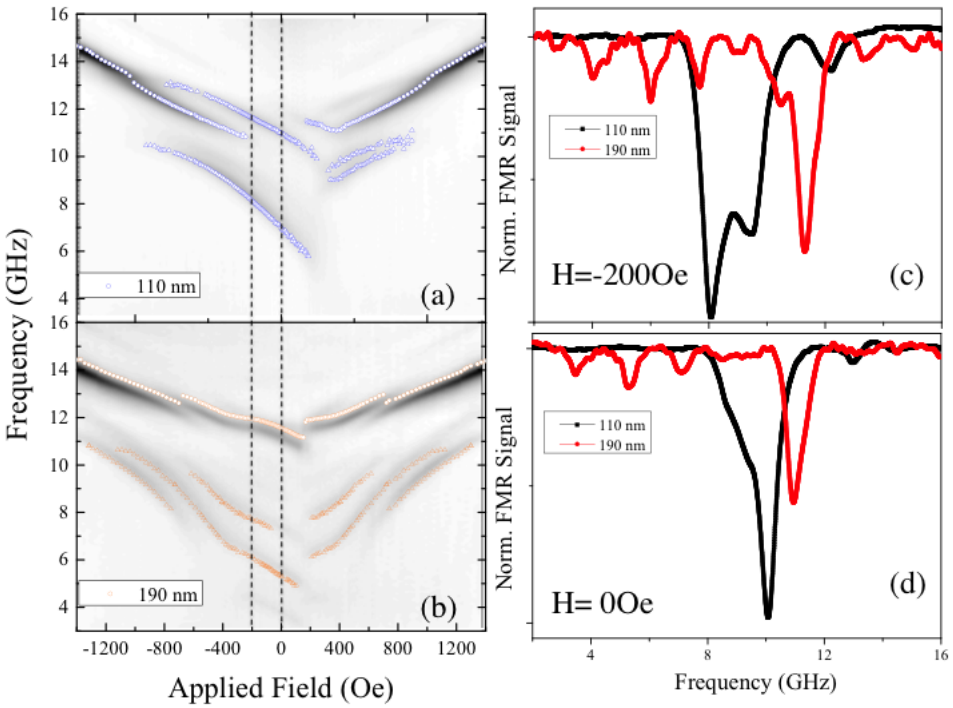

Figure 4.6: 2D FMR absorption spectra for $Ni_{80}Fe_{20}$ (20 nm) / Ru (0.7 nm) / $Ni_{80}Fe_{20}$ (10 nm) NW arrays with (a) W = 110 nm and (b) W = 190 nm. The points correspond to the relative maximum of the amplitude extracted from the measurements. (c) and (d) FMR frequency line scan for different applied fields.

increasing the field towards positive saturation, a shift upwards in the frequency for the acoustic mode takes place in both the spectra, similarly to the previous case. A similar family of optical modes is observed also for positive fields in the 190 nm-width NW array, symmetrically to the negative fields half. By contrast, for W = 110 nm, the optical mode at higher frequency becomes weaker and new optical mode at frequencies lower than the acoustic are observed. On a further increase of the applied field, the new branches merge (before disappearing due to low intensity) and only the acoustic mode is present up to positive saturation.

4.4 Comparison of experimental and theoretical results

Now we apply the theory described in Section 4.2 to compare with the experimental FMR data. Specifically, we calculate the discrete SW frequencies $\omega_{k,l}$ for the lowest few modes in the experimental range, and we put $k \approx 0$. The relevant magnetic parameters for $Ni_{80}Fe_{20}$ have been

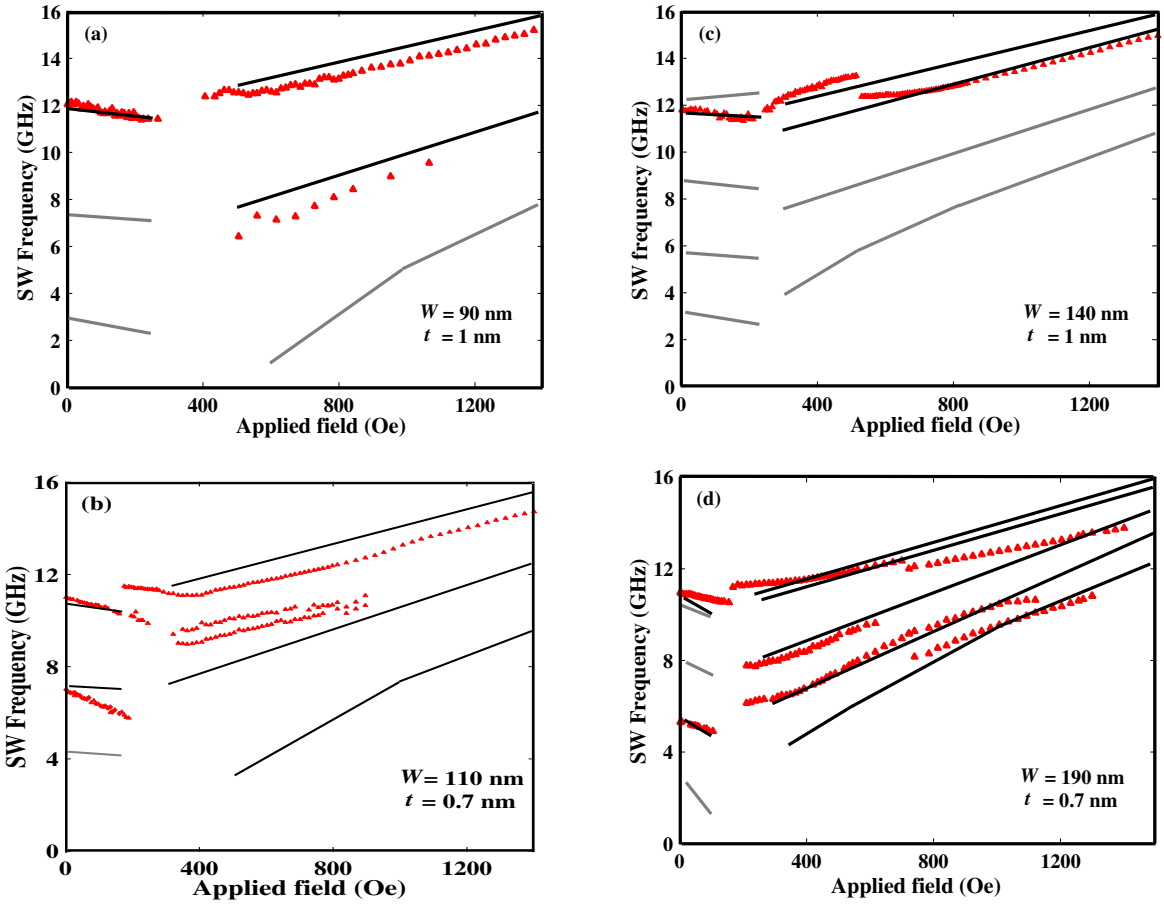

Figure 4.7: Experimental (red triangles) and calculated (solid lines) 2D FMR spectra of the $Ni_{80}Fe_{20}$ / Ru(t) / $N_{80}Fe_{20}$ trilayer NWs for (a) $W = 90$ nm ($t = 1$ nm); (b) $W = 110$ nm ($t = 0.7$ nm); (c) $W = 140$ nm ($t = 1$ nm); and (d) $W = 190$ nm ($t = 0.7$ nm).

discussed in our recent work on multilayer films [86]. The exchange stiffness D, the saturation magnetization M_s, and $g\mu_B$ are related to the effective parameters in the spin Hamiltonian, as shown in [58]. For Permalloy we take approximately $D = 24\,\mathrm{T\,nm^2}$, $M_s = 7.2 \times 10^5$ A/m (corresponding to saturation induction 0.905 T), and $g\mu_B = 29.5\,\mathrm{GHz/T}$, consistent with the literature (see, e.g., [90, 1]). Also we choose the effective lattice parameter as $a = 5$ nm, which is smaller than the exchange length $a_{ex} = \sqrt{D/4\pi M_s} \cong 5.2$ nm as required. Values for the dimensionless ratio J_R/J_{BQ} and the single-ion anisotropy (if any) were obtained by fitting the H_0 dependence of the SWs at zero wave vector to the FMR data.

In doing this we used numerical estimates for J_R/J_{BQ} obtained from the micromagnetic simulation [88] of the static properties as an initial guideline. In most cases, these estimates were

remarkably close to the final values. First, the fitting values for the RKKY coupling, relative to the bulk exchange J, were J_R/J were-0.062, -0.035, -0.064 and -0.01 for widths $W = 90$ nm ($t = 1$ nm), $W = 110$ nm ($t = 0.7$ nm), $W = 140$ nm ($t = 1$ nm), and $W = 190$ nm ($t = 0.7$ nm), respectively. The single-ion anisotropy field $S K_{in}/g\mu_B$ was found to be important only for the smallest width $W = 90$ nm (equivalent to an effective anisotropy field of ~ -150 Oe acting at each effective spin). Then the values found for the ratio J_R/J_{BQ} were 2, 6, 0.75 and 7 for the cases in the same order as mentioned above.

Here only the lowest modes corresponding to the range of measured frequencies of the FMR results are shown. In Figs. 4.7(a)-(d) experimental and calculated 2D FMR spectra of the $Ni_{80}Fe_{20}$ / Ru(t) / $Ni_{80}Fe_{20}$ trilayer system are presented for NWs with different widths as a function of the Ru spacer layer thickness t. In Fig. 4.7(a) the results are shown for the case with width $W = 90$ nm ($t = 1$ nm). Two FMR modes are clear. The additional peaks apart from the main resonance arise due to spatial confinement of the quantized SWs, and are predicted by theory. Our microscopic theory gives an excellent fit to the main FMR mode and fairy good fit for the additional weak mode. The lowest SW branch shows the expected soft-mode behavior. Calculations of the lowest SW frequencies (at zero wave vector) versus field H_0 for the case with larger $W = 110$ nm ($t = 0.7$ nm) are shown in Fig. 4.7(b), where there is a fair agreement between the theory and the experiment. From the experiments it is difficult to be sure if there are actually two modes close together with frequencies $\sim$ 8 GHz (when $H_0 \sim 800$ Oe), since these optical SW are of very weak intensity and are broadened, or if there is just one mode, as theory would suggest. Figure 4.7(c) shows a similar plot for the case with $W = 140$ nm ($t = 1$ nm). We see an excellent fit to FMR modes. The transition field from AFM phase to a SF phase occurs at $H_c \sim 230$ Oe, while the AFM phase occurs at smaller field value $H_0 < H_c$. The SF phase is favored in the range $H_c < H_0 \lesssim 500$ Oe, and $H_0 \gtrsim 500$ Oe corresponds to a FM phase. The results in this figure are strongly indicative of a transfer of intensity occurring at about $H_0 \sim 500$ Oe, i.e., in going from the SF region to the FM region. Finally results for the largest case with $W = 190$ nm ($t = 0.7$ nm) are presented in Fig. 4.7(d). Again theory gives a very good fit to the lowest three branches.

From the comparison of theory with experiment we see that, contrasting with the trilayer systems of complete films [86], the biquadratic exchange plays a more important role for trilayer NWs. The single-ion anisotropy field is small compared with the shape anisotropy and seems to be important only for the smaller case of $W = 90$ nm (where it is equivalent to small anisotropy field of ~ -150 Oe). It was sufficiently small to be ignored for other cases. Also the RKKY exchange interaction depends on the thickness of the Ru spacer layer as well as the width of the NWs. We remark that a significant challenge in comparing the theory and experiment is that it is difficult in the modeling to replicate the exact inhomogeneity in the NWs due to lithography at these small length scales. A typical indication of the inhomogeneity effects is provided by Fig. 4.1(c).

4.5 Conclusions

In conclusion, we have fabricated arrays of ferromagnetic NWs of Permalloy with different Ru spacer layer thicknesses. For this system, we studied experimentally and theoretically how the static and dynamic properties of the NW stripes can be tuned by varying both the the Ru spacer thickness and the width of the NWs.

Based on previous work on trilayer complete films and wide stripes of the same materials, we know that the interlayer exchange coupling (IEC) through the Ru spacer layer occurs via the bilinear RKKY and biquadratic exchange, which compete with one another as well as with the other interactions present. The narrower NWs studied here are of particular interest, because the shape anisotropy and the lateral quantization effects of the SWs become more pronounced, modifying the features of the observed (using FMR) switching behavior between the different magnetic phases and the appearance of additional (optical) SW modes. This is successfully borne out by the theoretical analysis which we have presented. It is also interesting that the role of the biquadratic exchange component of the IEC seems to be much more important, possibly because of the influence of the lateral edges which are relatively closer together in this study. This may serve to motivate future theoretical work on the mechanism for biquadratic exchange in the vicinity of lateral edges.

We showed that changing the Ru thickness leads to control of the IEC interactions and therefore to the possibility of the different magnetic ordering states (AFM, SF, FM) being realized. From the combination of experiment, microscopic theory and micromagnetic simulations we also demonstrated that there is a strong connection between interlayer coupling and the features of the FMR modes. The experimental results are well accounted for by the presented theory and simulation. Finally, with the use of our FMR technique, we demonstrated the effects of the different coupling mechanisms on both acoustic and optical SW modes.

In future work, it may be of interest to employ other experimental techniques to probe the spatially quantized SWs. The use of Brillouin light scattering (BLS) would be specially relevant, since the excited SWs would have small, nonzero wave vector k and the microscopic theory in this chapter would still be applicable. Also, on the theoretical side, employing Green's function techniques to generalize the microscopic theory would be useful, since they would enable the SW mode intensities to be deduced.

Chapter 5

Spin-wave instabilities of ferromagnetic nanowire stripes under parallel pumping

The material in this chapter has been published as an article by me (with M. G. Cottam) listed as Ref. [87].

As mentioned earlier, the nonlinear properties of spin waves (SWs) have been topics of intense interest, including parametric instabilities of the modes under microwave pumping (see, e.g., [91, 92, 62, 63]) in nanostructures (and arrays) composed of thin films, wires, rings, etc. To a large extent this has been a result of progress in the fabrication of high quality nanostructured magnetic materials and arrays with smaller sizes and sharp interfaces, and there is also the continuing need for a proper understanding of the nonlinear magnetization dynamics at surfaces and interfaces on this length scale. The historical background to work on SW parametric processes has been given in Chapters 1, 2, and 3. Some of the experimental and theoretical efforts devoted to this field are reviewed in [27, 25, 28, 56, 22, 26, 45, 53, 93].

Most of these references cited have either considered unbounded samples (without the need to account explicitly for surfaces) or have considered finite samples, mainly spheres and films, with macroscopic dimensions. In such cases the theoretical interpretations can be conveniently calculated by using a macroscopic method. In the finite samples a SW theory that takes the boundary

conditions at the surfaces into account must be used, leading in general to a spatial quantization of the SW modes because of localized surface (or edge) modes or standing-type waves. As a consequence some important differences arise, such as fine structure for the microwave absorption spectra, modification of the SW spectra, and additional selection rules when there is microwave pumping [65, 72]. Reviews of the theoretical studies in finite films and spherical samples, emphasizing SW quantization effects have been given, for example, in [25, 26, 65].

Additionally, there have been considerable experimental and theoretical studies of the magnetization dynamics of ferromagnetic nanowires, particularly those with a rectangular cross section, which are the focus in this chapter. Many of these relate to the linear SW properties (see, e.g. [94, 95]), often with applications to techniques such as FMR and BLS. Also periodic arrays of these nanowires have attracted much attention in the context of magnonic crystals [3, 96]. A notable investigation of nonlinear SW properties, specifically of the damping using FMR, was made by Boone *et al*. [54].

As emphasized in previous chapters, for nanostructures with sufficiently small dimensions, such as ultrathin ferromagnetic films or stripes with just a few atomic layers in thickness, the discrete nature of the quantized SWs become more pronounced. Thus we employ a microscopic (or Hamiltonian) theory here, which involves using a discrete lattice of spins within a Hamiltonian formalism that includes terms for the long-range dipole-dipole and the short-range exchange interactions, instead of the electromagnetic field variables. In a recent work [58] the effects of a microwave pumping field applied along the in-plane magnetization direction in ultrathin ferromagnetic films were studied using the microscopic theory. Specifically it was shown that the quantized SW bands and their spatial properties lead to modifications in the shape of the typical "butterfly curve" (describing the threshold microwave field for instability plotted versus applied field).

The aim of the present chapter is to generalize the previous parallel-pumping calculations for complete ultrathin films to apply to magnetic nanowires (which include stripes or ribbons of finite width and thickness as particular cases of interest) as well as to consider the inhomogeneously-magnetized wires when there is a transverse applied field. This is important because of the role

of the lateral edges and the shape anisotropy in nanowires. Our focus is a theoretical study of SW instability processes in long (effectively-infinite) ferromagnetic nanowires with a uniform rectangular cross section under parallel pumping when the applied field is either parallel or perpendicular to the wire axis. The quantized SW branches are characterized by a 1D wave number k along the length axis of translational symmetry. Also there are edge modes associated with the lateral edges in the wire geometry. Consequently the SW properties are found to be quite different from the film case, and we show that the results for the SW instability thresholds display different features. The behavior is found to depend sensitively on the ratio of magnetic dipole-dipole to exchange interactions, and we present numerical examples for two magnetic materials which are representative of different regimes, namely, for Permalloy (strong exchange) and EuS (intermediate exchange). Results in this chapter extend some of the calculations in Chapter 3 and provide details of the theory.

This chapter is organized as follows. First the theoretical model for the nanowire stripes (with rectangular cross section) is described in Section 5.1 in terms of lines of interacting spins, and the application is made to the SW modes and parallel pumping with a microwave field. The applied field can be taken either parallel or perpendicular to the wire axis. Here we transform the total dipole-exchange Hamiltonian (with pumping terms included) from spin operators to boson creation and annihilation operators. Then the coupled operator equations for the SW parametric processes are derived and solved following an analogous approach to that used in [58] for thin films. In Sections 5.2 and 5.3 the numerical results are illustrated for longitudinal and transverse applied fields, respectively, where in the latter case the sample may be inhomogeneously magnetized. Nanowires with different cross sections and aspect ratios are chosen, together with different magnetic materials (using Permalloy and EuS). Finally we summarize our results and discuss extensions in Section 5.4.

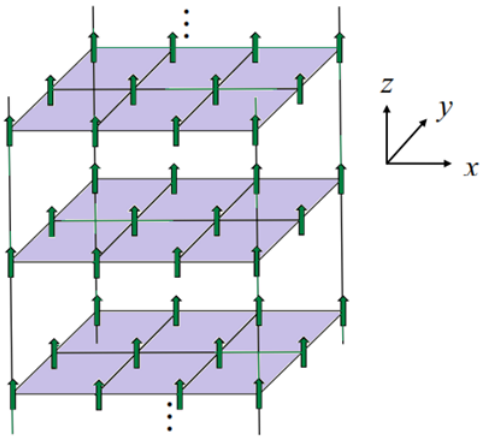

Figure 5.1: Assumed geometry for a rectangular nanowire with translational symmetry along the z direction and finite in the xy plane. It is illustrated here for $N = 4 \times 3 = 12$ lines of spins, and applied magnetic field along the z direction.

5.1 Theoretical formalism for parallel pumping

The nanowire geometry is depicted in Fig. 5.1, where we assume the system to be effectively infinite in the z direction and to have finite dimensions in the xy plane. The rectangular cross section consists of N spins, which are arranged on a simple cubic lattice (lattice parameter a). There are n_x spins in the x direction and n_y in the y direction, where generally we assume $n_x \geq n_y$. The system can be considered as N $(= n_x n_y)$ lines of spins extending along the z axis, which is the direction of translational symmetry.

The total spin Hamiltonian for the nanowire can be expressed as

$$H = \frac{1}{2}\sum_{in,jm}\sum_{\alpha,\beta}\chi^{\alpha\beta}_{in,jm}S^{\alpha}_{in}S^{\beta}_{jm} - g\mu_B\left[\mathbf{H}_0 + \mathbf{h}(t)\right]\cdot\sum_{in}\mathbf{S}_{in}, \tag{5.1}$$

where the indices i and j refer to the spatial coordinates of the spin sites in the z direction, while n and m $(= 1, 2, ..., N)$ label the positions of the spins in any particular cross section of the nanowire, and α and β denote Cartesian components. The first term in the Hamiltonian, involving the tensorial interaction $\chi^{\alpha,\beta}_{in,jm}$, describes both the short-range exchange and long-range dipole-dipole coupling between components of the spins $\mathbf{S}_{in}$ and $\mathbf{S}_{jm}$, where

$$\chi^{\alpha\beta}_{in,jm} = -J_{in,jm}\delta_{\alpha\beta} + (g\mu_B)^2 D^{\alpha\beta}_{in,jm} \tag{5.2}$$

with $D^{\alpha\beta}_{in,jm}$ given by Eq. (3.2). Here the exchange interaction $J_{in,jm}$ between spin operators at sites (i,n) and (j,m) is taken to be J for the nearest neighbors only and zero otherwise. By contrast, the dipole-dipole terms couple all sites in the sample, where we denote $\mathbf{r}_{in,jm} = \mathbf{r}_{in} - \mathbf{r}_{jm}$.

The final term in Eq. (5.1) represents the Zeeman energy for coupling between the spin system and the total field, which consists of the static component of magnitude H_0, assumed to be applied either longitudinally (along the z direction for the wire axis) or transversely (perpendicular to the wire axis and in the x direction) and the microwave field. In the latter case, if H_0 is sufficiently large, the spins will be reoriented approximately along the x axis. The microwave pumping field $\mathbf{h}(t)$ may be along any direction, but since we are focusing on parallel-pumping instabilities we will typically take $\mathbf{h}(t)$ to be along the z axis when the applied field is longitudinal and along the x axis when the applied field is transverse and large enough.

5.1.1 Longitudinal applied field

When the applied magnetic field is along the wire axis, the equilibrium orientation of the spins is also in the same z direction (see Fig. 5.1). To examine the SW properties, following the general approach in our earlier work on parallel pumping in ultrathin films [58], we transform to boson operators using the Holstein-Primakoff representation [31] in the form (see Subsection 1.3.1):

$$S^{x}_{in} + iS^{y}_{in} = \sqrt{2S}\left(1 + a^{\dagger}_{in}a_{in}/2S\right)^{1/2} a_{in}, \qquad S^{z}_{in} = S - a^{\dagger}_{in}a_{in}. \tag{5.3}$$

where S is the spin quantum number, and $a^{\dagger}_{in}$ and a_{in} are the boson creation and annihilation operators, respectively. Next, the transformed Hamiltonian of the system is expanded as $H = H^{(0)} + H^{(1)} + H^{(2)} + H^{(3)} + ...$, with $H^{(m)}$ denoting the term with a product of m boson operators. We are taking the case of relatively low temperatures $T \ll T_c$. The zeroth-order term $H^{(0)}$ is just a constant and plays no role in dynamical properties, while the first-order term $H^{(1)}$ vanishes by symmetry for these ferromagnetic nanowires with longitudinal fields. The second-order term $H^{(2)}$ describes the non-interacting SWs and, after making a 1D Fourier transformation along the wire axis, it can be expressed as

$$H^{(2)} = \sum_{n,m,k} \left[A^{(2)}_{n,m}(k) a^{\dagger}_{k,n} a_{k,m} + B^{(2)}_{n,m}(k) a^{\dagger}_{k,n} a^{\dagger}_{-k,m} + B^{(2)*}_{n,m}(k) a_{k,n} a_{-k,m} \right] + H^{(2)}_{p}. \quad (5.4)$$

Here k is the wave number along the z direction of symmetry, and the coefficients in the first term are

$$A^{(2)}_{n,m}(k) = \left\{ g\mu_B H_0 + S \sum_{p=1}^{N} [J_{n,p}(0) - g^2 \mu_B^2 D^{z,z}_{n,p}(0)] \right\} \delta_{m,n} - S J_{n,m}(k) - \frac{1}{2} S g^2 \mu_B^2 D^{z,z}_{n,m}(k), \quad (5.5)$$

$$B^{(2)}_{n,m}(k) = \frac{1}{4} S g^2 \mu_B^2 \left(D^{x,x}_{n,m}(k) - D^{y,y}_{n,m}(k) + 2i D^{x,y}_{n,m}(k) \right). \quad (5.6)$$

Finally $H^{(2)}_p$ is the additional Hamiltonian term arising from the parallel microwave pumping field and is given by

$$H^{(2)}_p = \sum_{n,k} g\mu_B h_0 \exp(-i\omega_p t) a^{\dagger}_{kn} a_{kn}, \quad (5.7)$$

where we have taken a time dependence corresponding the single Fourier component with angular frequency ω_p for pumping. We note that the higher-order terms $H^{(3)}$ and $H^{(4)}$, which describe the three-magnon and four-magnon interaction processes respectively between the SWs, are not required for a description of the parallel pumping instabilities.

The linear SW spectrum is required as a preliminary to carry out the SW instability calculation. For this, we need to diagonalize the second-order Hamiltonian $H^{(2)}$ in Eq. (5.4) in the absence of the pumping term, using a generalized Bogoliubov transformation as described in our previous work [53, 70]. To summarize, we introduce a new set of boson operators $\{\alpha^{\dagger}_{-k,n}, \alpha_{k,n}\}$ defined by

$$\alpha_{k,n} = \sum_{l=1}^{N} \left(S_{n,l}(k) \alpha_{k,l} + S^{*}_{n+N,l}(k) \alpha^{\dagger}_{-k,l} \right),$$

$$\alpha^{\dagger}_{-k,n} = \sum_{l=1}^{N} \left(S^{*}_{n+N,l+N}(k) \alpha^{\dagger}_{-k,l} + S_{n+N,l}(k) \alpha_{k,l} \right). \quad (5.8)$$

Here $S_{n,m}(k)$ is an element of a $2N \times 2N$ matrix $\mathbf{S}_k$. We can rewrite the above Bogoliubov transformation more compactly in a matrix form, whereupon it can be shown [53, 70] that the l^{th} column

of the matrix $\mathbf{S}_k$, denoted by $\mathbf{S}_l(k)$, can be found by solving the eigenvalue equation:

$$\begin{pmatrix} \mathbf{A}(k) & 2\mathbf{B}(k) \\ -2\mathbf{B}^*(-k) & -\tilde{\mathbf{A}}(-k) \end{pmatrix} \mathbf{S}_l(k) = \pm\omega_l(k)\mathbf{S}_l(k), \tag{5.9}$$

where the + sign is taken for $1 \leq l \leq N$ and the – sign for $N+1 \leq l \leq 2N$. The full quadratic Hamiltonian can then be written in the form (apart from a constant term)

$$H^{(2)} = \sum_{k,l=1}^{N} \omega_l(k)\alpha^\dagger_{k,l}\alpha_{k,l} + H_p^{(2)}. \tag{5.10}$$

The diagonalized first term describes a system of N non-interacting SWs with frequency $\omega_l(k)$ at 1D wave vector k for the branch l (with $l = 1, 2, \ldots, N$). The required part of the pumping term $H_p^{(2)}$ that describes the SW instability in this case becomes

$$H_p^{(2)} = h_0 \sum_{l,l',k} \left[\exp(-i\omega_p t) P_{l,l'}(k) \alpha^\dagger_{k,l} \alpha^\dagger_{-k,l'} + \text{h.c.} \right] \tag{5.11}$$

This part is not necessarily diagonal in terms of the new boson operators, and the amplitude factor $P_{l,l'}(k)$ is given by

$$P_{l,l'}(k) = g\mu_B \sum_{n=1}^{N} S^*_{n,l}(k) S^*_{n+N,l'}(-k). \tag{5.12}$$

Following the general procedure used to investigate parallel pumping in the previous macroscopic methods (see, e.g., [27, 66, 72]) or the microscopic method for ultrathin films [58], we now derive the rate equations for the boson operators $\alpha^\dagger_{k,l}$ and $\alpha_{k,l}$ by forming their commutator with $H^{(2)}$. The role of energy dissipation is conventionally introduced into the rate equations phenomenologically via the damping constant (denoted as $\eta_l(k)$ for the SW branch l) by making the replacement $\omega_l(k) \to \omega_l(k) - i\eta_l(k)$ for the SW frequency. This leads to a set of N coupled equation for the boson operators $\alpha_{k,l}$ and another N equations for their conjugates, in the form

$$\frac{d}{dt}\alpha_{k,l} = -\left(i\omega_l(k) + \eta_l(k)\right)\alpha_{k,l} - ih_0 \exp(-i\omega_p t) \sum_{l'} P_{l,l'}(k) \alpha^\dagger_{-k,l'}. \tag{5.13}$$

To solve these equations we note that the SWs are excited parametrically in pairs (see Fig. 1.6(a)),

each at frequency $\omega_p/2$ and with wave numbers k and $-k$. Therefore, by assuming $\alpha_{-k,l} = \exp(iq_k)\alpha_{k,l}$ (with q_k as a real phase), the rapidly time-varying operators $\alpha_{k,l}$ can be rewritten as

$$b_{k,l} \sim \langle \alpha_{k,l} \rangle \exp[i(\omega_p/2)t] \exp(iq_k/2). \tag{5.14}$$

Eventually Eq. (5.13) becomes

$$\frac{d}{dt} b_{k,l} = -\left(i\triangle\omega_l(k) + \eta_l(k)\right) b_{k,l} - ih_0 \sum_{l'} P_{l,l'}(k) b^*_{k,l'}, \tag{5.15}$$

where we denote $\triangle\omega_l(k) = \omega_l(k) - (\omega_p/2)$ for the shifted frequencies. We can now examine the nature of the solutions of Eq. (5.15) and its conjugate by considering a characteristic time dependence for $b_{k,l}$ and $b^*_{k,l}$ like $\exp(\beta t)$, where β may be complex.

It is convenient to reformulate the problem by denoting $b_{k,l} = b'_{k,l} + ib''_{k,l}$ and $P_{l,l'}(k) = P'_{l,l'}(k) + iP''_{l,l'}(k)$ for the real and imaginary parts, in order to define the column matrices

$$\mathbf{b}_k = \begin{pmatrix} b'_{k,1} \\ \vdots \\ b'_{k,N} \\ b''_{k,1} \\ \vdots \\ b''_{k,N} \end{pmatrix}, \quad \mathbf{P}_{l,l'}(k) = \begin{pmatrix} P'_{1,l'}(k) \\ \vdots \\ P'_{N,l'}(k) \\ P''_{1,l'}(k) \\ \vdots \\ P''_{N,l'}(k) \end{pmatrix}. \tag{5.16}$$

Then the coupled equations in (5.15) can formally be written as

$$\begin{pmatrix} \mathbf{D}^{(2)}(k) & \mathbf{E}^{(2)}(k) \\ \mathbf{F}^{(2)}(k) & \mathbf{G}^{(2)}(k) \end{pmatrix} \mathbf{b}_k = \beta(k)\mathbf{b}_k, \tag{5.17}$$

where $\mathbf{D}^{(2)}(k), \mathbf{E}^{(2)}(k), \mathbf{F}^{(2)}(k), \mathbf{G}^{(2)}(k)$ are each $N \times N$ matrices defined by the matrix elements

$$\begin{aligned} D^{(2)}_{l,l'}(k) &= -\eta_{l'}(k)\delta_{ll'} + h_0 P''_{l,l'}(k), \quad E^{(2)}_{l,l'}(k) = \triangle\omega_{l'}(k)\delta_{ll'} - h_0 P'_{l,l'}(k), \\ F^{(2)}_{l,l'}(k) &= -\triangle\omega_{l'}(k)\delta_{ll'} - h_0 P'_{l,l'}(k), \quad G^{(2)}_{l,l'}(k) = -\eta_{l'}(k)\delta_{ll'} - h_0 P''_{l,l'}(k). \end{aligned} \tag{5.18}$$

An analytical solution of Eq. (5.17) is straightforward only in the simplest non-trivial case of $N = 2$. In this situation with just two coupled lines of spins forming the nanowire we have two SW

branches, so there are four eigenvalues $\beta_n(k)$, with $n = 1, 2, 3, 4$. We find that $P_{l,l'}(k)$ is real in this case, and

$$\beta_{1,2}(k) = -\tfrac{1}{2}\left(\eta_1(k) + \eta_2(k)\right) \pm \tfrac{1}{2}\sqrt{[\eta_1(k) - \eta_2(k)]^2 - 4[\triangle\omega_1(k)]^2 + 4[h_0 P_{1,1}(k)]^2}\ . \tag{5.19}$$

The expressions for the other eigenvalues $\beta_{3,4}(k)$ involve replacing $\triangle\omega_1$ and $P_{1,1}$ in Eq. (5.19) by $\triangle\omega_2$ and $P_{2,2}$, respectively. The SW amplitude grows exponentially in time, signaling the onset of a SW instability, whenever any $\beta_n(k) > 0$. We deduce from the above results that the instability threshold in this $N = 2$ case occurs when the pumping field amplitude h_0 exceeds the value $h^c = \min(h_1^c, h_2^c)$ for the two SW branches, where

$$h_i^c = \frac{\sqrt{\eta_1(k)\eta_2(k) + \left(\triangle\omega_i(k)\right)^2}}{\left|P_{i,i}(k)\right|}, \qquad (i = 1, 2). \tag{5.20}$$

In the general case with $N \geq 3$, the $2N \times 2N$ eigenvalue problem represented by Eq. (5.17) can be solved numerically to obtain the set of eigenvalues $\beta_n(k)$ with $n = 1, 2, \ldots, 2N$. For a given wave vector k the SW instability threshold is found by determining the value of the pumping field amplitude h_0 for any one of the eigenvalues to have a positive real part. We note that the damping parameter η in Eq. (5.20) in principle depends on k and branch l. For the numerical examples presented later we use the simplification, as in [58], of adopting a constant value for the small k region (independent of branch label l).

5.1.2 Transverse applied field

In this subsection we turn attention to the instability threshold for ferromagnetic nanowires when the magnetic field is applied in the x direction perpendicular to the length axis of the wire. Due to competition between the Zeeman and other interactions, there is a low-field phase in which the spins are canted relative to the symmetry axis. As a consequence the magnetization becomes spatially nonuniform in this case, since the canting angles vary. For large enough value of H_0, as

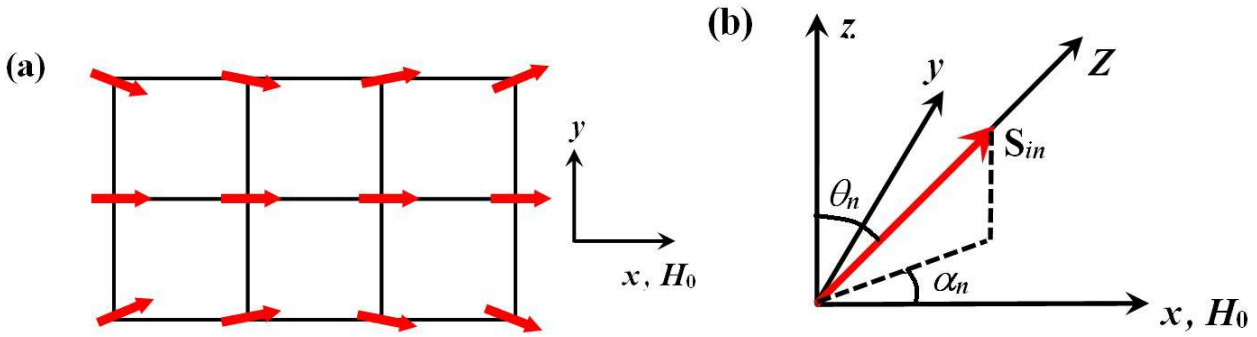

Figure 5.2: Case of a nanowire in a transverse applied magnetic field. (a) Cross section of a $N = 4 \times 3 = 12$ nanowire showing the canted spins when H_0 is large and along the x axis. (b) The individual spins $\mathbf{S}_{in}$ are canted relative to the global x, y, z axes.

we discuss below, the spins will reorient to having a net magnetization in the transverse direction (along x), but the individual spins will still be canted as depicted in Fig. 5.2(a).

The first step in studying the SWs is to determine the equilibrium orientations of the spins according to mean-field theory. We assume that the equilibrium orientation of the spin at site (i, n) is characterized by two angles α_n and θ_n, which will be independent of i, in polar coordinates (see Fig. 5.2(b)). Hence we may write $\mathbf{S}_{in} = S(\sin\theta_n\cos\alpha_n, \sin\alpha_n\sin\theta_n, \cos\theta_n)$, similarly to Subsection 4.2.1, and using Eq. (5.1) the total energy functional E becomes

$$\begin{aligned} E/L \;=\; & -\tfrac{1}{2}S^2\sum_{n,m}J_{n,m}(0)\,(\sin\theta_n\cos\alpha_n\sin\theta_m\cos\alpha_m + \sin\alpha_n\sin\theta_n\sin\alpha_m\sin\theta_m + \cos\theta_n\cos\theta_m) \\ & -g\mu_B H_0 S\sum_n \sin\theta_n\cos\alpha_n + \tfrac{1}{2}g^2\mu_B^2 S^2\sum_{n,m}(D^{x,x}_{n,m}(0)\sin\theta_n\cos\alpha_n\sin\theta_m\cos\alpha_m \\ & + D^{x,y}_{n,m}(0)\sin\theta_n\cos\alpha_n\sin\alpha_m\sin\theta_m + D^{y,x}_{n,m}(0)\sin\alpha_n\sin\theta_n\sin\theta_m\cos\alpha_m \\ & + D^{y,y}_{n,m}(0)\sin\alpha_n\sin\theta_n\sin\alpha_m\sin\theta_m + D^{z,z}_{n,m}(0)\cos\theta_n\cos\theta_m), \end{aligned} \tag{5.21}$$

where L is the (macroscopically large) number of cross-sectional layers along the length of the wire. To find the angles $\{\alpha_n, \theta_n\}$ we minimize the energy E of the system at low temperature by requiring that $\delta E/\delta\alpha_n = 0$ and $\delta E/\delta\theta_n = 0$ for each value of n. This leads to the $2N$ coupled equations quoted in Appendix A, which later can be solved numerically by an iterative approach. It is also shown there, however, that if the polar angles $\{\theta_n\}$ are approximated by assuming that $\theta_n \equiv \theta$ (the same value for all n) in Eqs. (A.1) and (A.2) and the α_n are assumed to be small, we arrive at the simple result that

$$\theta = \begin{cases} \sin^{-1}(H/H_c) & \text{if } H < H_c, \\ \pi/2 & \text{otherwise,} \end{cases} \tag{5.22}$$

where the critical reorientation field H_c is defined by

$$H_c = \frac{S\, g\mu_B}{N} \sum_{n,m} \left(D^{x,x}_{n,m}(0) - D^{z,z}_{n,m}(0) \right). \tag{5.23}$$

Although this result is approximate, because it ignores effects at the lateral edges where θ_n may vary and α_n may be large, we will show that it gives a useful estimate of the reorientation field for the net magnetization to become transverse.

With the equilibrium spin configurations having been determined, we may rewrite the spin Hamiltonian in terms of local Cartesian axes (X, Y, Z) for each spin, where the Z axis is along the equilibrium direction for that spin (see Fig. 5.2(b)), rather than the global axes (x, y, z). Then the boson operators are introduced as before, but are defined relative to the local axes. The results for the SWs and their instabilities in the ferromagnetic nanowires follow as in the previous subsection. Thus the linear SW spectrum is again obtained formally by diagonalizing Eq. (5.4) in the absence of pumping. The expressions for the Hamiltonian terms $A^{(2)}_{n,m}(k)$ and $B^{(2)}_{n,m}(k)$ become more complicated, because they now depend on the equilibrium angles, and are quoted in Appendix B. The SW instabilities under parallel pumping can also be investigated by following the same procedure as described in Subsection 5.1.1, but for simplicity we will restrict attention to the high-field case ($H > H_c$) where the net magnetization (and the parallel pumping field) are along the x direction.

5.2 Numerical results for the longitudinal case

In this section numerical calculations are presented for nanowires with different lateral dimensions as well as for magnetic materials with different relative strengths of the magnetic dipole-dipole and exchange interactions. Specifically, we consider nanowires composed of Permalloy (as a material with strong exchange) and EuS (having weaker exchange). Both materials have been extensively studied experimentally (e.g., by BLS) and their relevant parameters are fairly well known [90, 5].

As in the corresponding calculations for films [58], the material parameters in our approach are the exchange stiffness D, the bulk exchange field H_{ex}, the saturation magnetization M_s, the spin quantum number S, and $g\mu_B$ (related to the gyromagnetic ratio). The expressions $D = SJa^2/g\mu_B$, $H_{ex} = 6SJ/g\mu_B$, and $M_s = g\mu_B S/a^3$ provide the correspondence between the above parameters and the Hamiltonian terms in Eq. (5.1). For Permalloy we have approximately $D = 24\,\mathrm{T\,nm^2}$, $4\pi\mu_0 M_s = 0.072$ T, and $g\mu_B = 29.5\,\mathrm{GHz/T}$. For EuS we take $D = 0.56\,\mathrm{T\,nm^2}$ as deduced from $\mu_0 H_{ex} = 9.4$ T, $4\pi\mu_0 M_s = 0.12$ T, $S = 7/2$, and $g\mu_B = 28.0\,\mathrm{GHz/T}$. Another parameter is the damping η, which in principle may depend on k and branch l. Here we use a simplification as in most previous calculations of adopting a constant value. Permalloy is known to have a small damping, typically ~ 0.01 GHz, which corresponds to $\Delta H \sim 3.4$ Oe for the equivalent FMR half-linewidth $\eta/g\mu_B$ (see, e.g. [97]). For EuS we take the value $\eta = 0.1\,\mathrm{GHz}$.

Numerical results for the simpler case of a longitudinal applied field are given below to illustrate the analytical theory in Section 5.1, while the transverse-field case will be discussed in the following section. In both cases it is necessary to have a good characterization of the linear SW dispersion relations for the lowest few branches (small values of l). Typically the nanowire samples with rectangular cross section are fabricated by starting from a very thin film of the material which is then etched laterally to produce the wire stripes (see, e.g., [45]) with a width much larger than the thickness. Thus, for a $n_x \times n_y$ wire in the notation of Section 5.1, we define the aspect ratio by $p = n_x/n_y$, which will usually be large compared to unity.

In Fig. 5.3(a) we show the dispersion relations for the lowest SW frequencies plotted as a function of wave-vector k for a 9×4 (or $N = 36$ lines of spins) nanowire of EuS, taking a value $a \simeq 0.60$ nm for the equivalent simple-cubic lattice parameter (deduced by equating a^3 to the volume per spin in the material). The SW frequencies show an initial decrease and a minimum for the lowest curves at small nonzero wave-vector k. This is a consequence of interplay between the dipole-dipole and exchange interactions. At slightly larger k the exchange effects begin to dominate over the dipolar contributions to the SW frequency, and consequently the SW frequencies increase with k. These results are calculated using Eqs. (5.4)-(5.10), together with a numerical evaluation

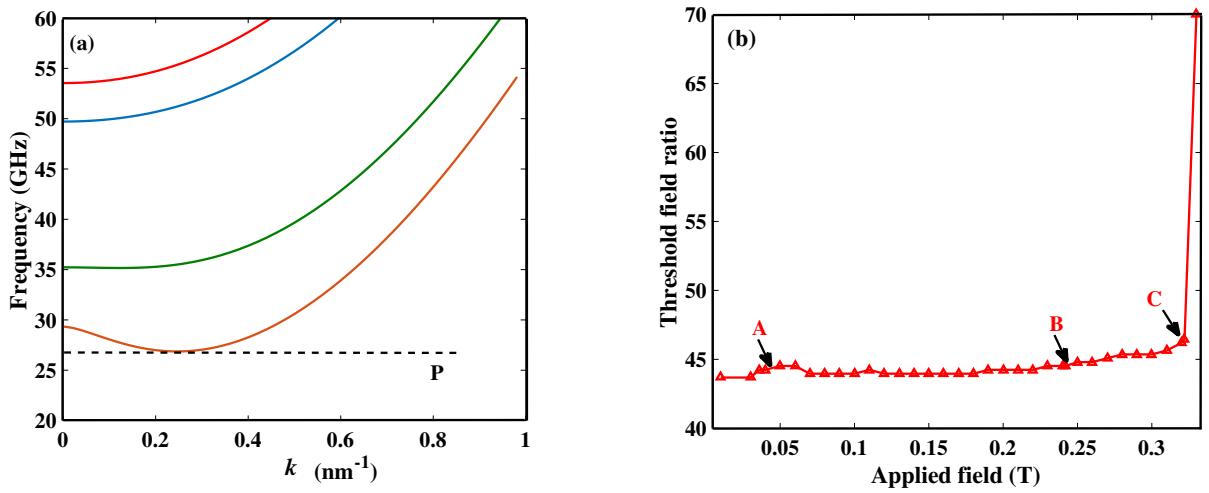

Figure 5.3: (a) Calculated SW frequencies plotted versus longitudinal wave vector k for the lowest four branches of a 9×4 EuS nanowire ($N = 36$), at longitudinal field $\mu_0 H_0 = 0.322$ T. The horizontal line P is drawn at one half of the pumping frequency to be considered later. (b) SW instability threshold expressed as a ratio of the half-linewidth ΔH and plotted versus applied field H_0. We take the pumping frequency $\omega_p/2\pi = 54$ GHz, and damping parameter $\eta = 0.1$ GHz. The triangle symbols indicate the calculated points and the connecting lines are a guide to the eye.

of the dipole-dipole sums.

The threshold field h^c (expressed here as a ratio to the resonance half width ΔH) plotted versus the applied field H_0 is shown in Fig. 5.3(b) for the same EuS nanowire as above for parallel pumping at frequency 54 GHz. This plot is the analog of the so-called "butterfly curve" for macroscopic materials, but here it has a modified shape since it shows several additional structural features at particular values of the applied field. The points labeled as A (at 0.036 T), B (at 0.242 T), and C (at 0.322 T) can be associated with the field values at which a horizontal line drawn at one half of the pumping frequency, namely at 27 GHz (such as point P in Fig. 5.3(a)), coincides with a specific feature on the SW dispersion curves. Thus points A and B correspond to the field values when the one-half pumping frequency is coincident with the zero wave-vector $k = 0$ frequencies of SW branches 2 and 1, respectively, and point C corresponds to the field value at which the horizontal line is tangential to the minimum in branch 1.

Some analogous results for the behavior in a ribbon-like EuS structure are shown in Figs. 5.4(a) and (b), taking now a larger value for the aspect ratio p. Specifically we consider a 36×1 EuS nanowire with the same pumping frequency as before. The SW dispersion results are displayed

in Fig. 5.4(a) for several lowest branches versus k at a fixed applied field $\mu_0 H_0 = 0.289$ T. The general features are similar to those for the previous structure except that some of the dispersion curves are closer together in frequency. The behavior found for the instability threshold curve is given in Fig. 5.4(b), where we have noted some features labeled as A (when $\mu_0 H_0 = 0.289$ T), B (at 0.364 T), C (at 0.415 T), and D (at 0.422 T). These correspond respectively to the condition for one half of pumping frequency to coincide with the $k = 0$ frequency (or frequency minimum) of the third SW branch, the frequency minimum for the second branch, the $k = 0$ frequency of the lowest branch, and the frequency minimum of the lowest branch. Other structural features can be attributed to density-of-state effects for the quantized magnons.

As a general indication of how much a wide stripe differs in behavior from a complete film of the same thickness as regards the SW frequencies, we may compare estimates for the uniform mode (lowest mode at $k \approx 0$). According to the simplest macroscopic theory for an infinitely-long, uniformly magnetized ferromagnet stripe (see [98, 99]), the uniform-mode angular frequency is given by

$$\omega_{UM} = \left[\omega_0 \left(\omega_0 + \omega_m\right) + N_x \omega_m^2\right]^{1/2}, \tag{5.24}$$

where we define $\omega_0 = g\mu_B H_0$ and $\omega_m = 4\pi\, g\mu_B M_s$ as frequencies related to the longitudinal applied field and saturation magnetization, respectively, and the demagnetization factor in the x direction is related to the aspect ratio by

$$N_x = \frac{1}{2\pi}\left[4 \arctan\left(\frac{1}{p}\right) + 2p \ln(p) + \frac{1 - p^2}{p} \ln\left(1 + p^2\right)\right], \tag{5.25}$$

where p is the ratio of the thickness to the width of the wire. For $p \gtrsim 3$ we have approximately $N_x = \left(\ln(p) + \frac{3}{2}\right)/p\pi$. In the case of the 36×1 EuS nanowire considered with $\mu_0 H_0 = 0.289$ T, the above expressions yield $\omega_{UM}/2\pi = 22.0$ GHz (using $N_x = 0.045$), which is very close to the value 22.3 GHz found for the lowest discrete SW branch at zero wave vector in Fig. 5.4(a). The results are not exactly the same because the dipole-exchange SW theory takes account of the perturbation of the effective dipole fields at the lateral edges. By contrast, if we put $N_x = 0$

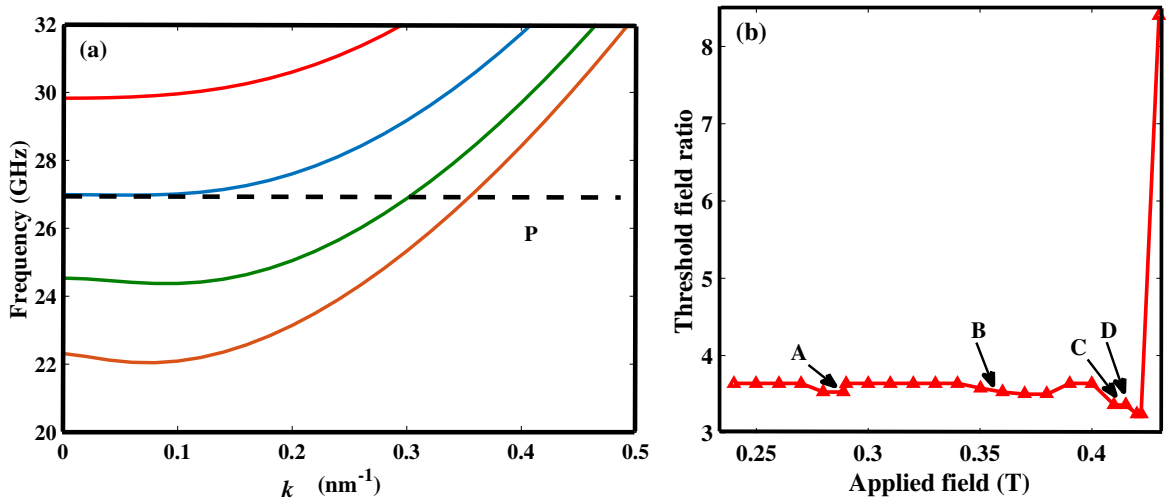

Figure 5.4: (a) SW frequencies plotted versus longitudinal wave vector k for the lowest four branches of a 36×1 EuS nanowire ($N = 36$) at longitudinal field $\mu_0 H_0 = 0.289$ T. The horizontal line P indicates one-half of the pumping frequency. (b) SW instability threshold expressed as a ratio of the half-linewidth ΔH and plotted versus applied field. Parallel pumping at $\omega_p/2\pi = 54$ GHz is considered with damping $\eta = 0.1$ GHz.

in Eq. (5.24) to correspond to a complete film, we would get $\omega_{UM}/2\pi = 20.1$ GHz which is significantly different from the stripe result, even when p is as large as 36 here. Also we note that more sophisticated versions of the macroscopic theory (e.g., as in [54]) include variations of the (dipolar) demagnetizing field across the stripe width, so the comparison becomes modified.

Next we present some analogous calculations for Permalloy nanowires where the exchange is relatively much larger. As a consequence, the frequencies increase more sharply with k (after the initial dip) than in the EuS case, and so the relevant range of wave vectors for parallel pumping applications is smaller. In Figs. 5.5(a) and (b) we show the lowest discrete frequencies plotted versus k and the corresponding instability threshold curve, respectively, for a Permalloy nanowire with a 12×2 structure ($N = 24$). We are now employing an effective lattice parameter $a = 5$ nm for Permalloy, chosen so that the cell size in the calculations is less than the exchange length, as mentioned earlier. Hence the cross section of the modeled nanowire is 60 nm by 10 nm, with aspect ratio $p = 6$. In Fig. 5.5(b) the points A, B, and C, which correspond to applied field values $\mu_0 H_0 = 0.026$, 0.158 and 0.173 T respectively, occur when one-half of pumping frequency coincides with either the $k = 0$ frequency or frequency minimum for the first two SW branches in

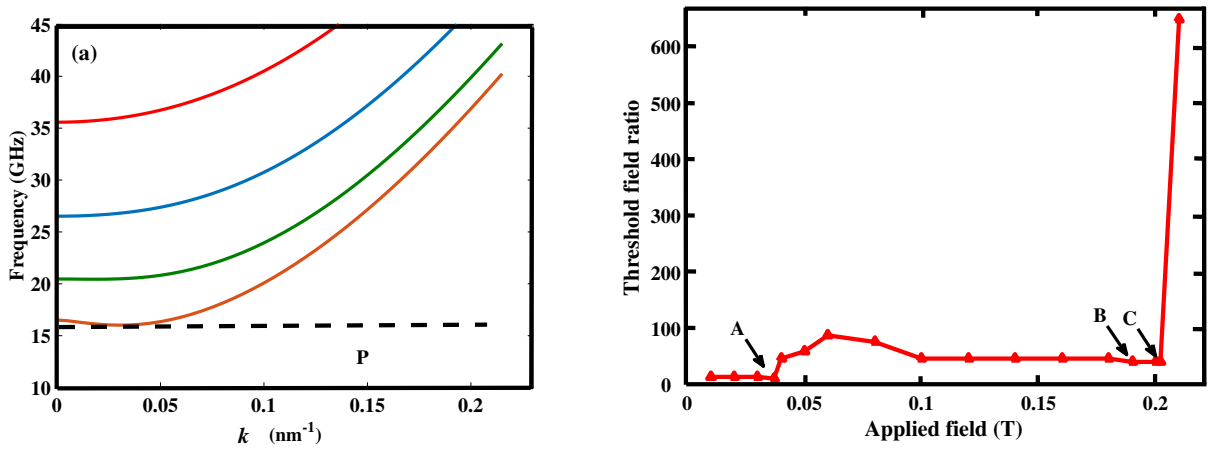

Figure 5.5: (a) SW frequencies plotted versus longitudinal wave vector k for the lowest four branches of a Permalloy nanowire with cross section 60 nm × 10 nm at longitudinal field $\mu_0 H_0 = 0.173$ T. The horizontal line P indicates one-half of the pumping frequency. (b) SW instability threshold expressed as a ratio of the half-linewidth ΔH and plotted versus applied field. Parallel pumping at $\omega_p/2\pi = 32$ GHz is considered with damping $\eta = 0.01$ GHz.

the dispersion plot.

Once again there is a close correspondence between the $k = 0$ frequency of the lowest branch, which is around 16.5 GHz when $\mu_0 H_0 = 0.173$ T as in Fig. 5.5(a), and the macroscopic uniform-mode frequency $\omega_{UM}/2\pi = 16.9$ GHz obtained from Eqs. (5.24) and (5.25). It differs significantly from the film result ($\omega_{UM}/2\pi = 12.7$ GHz), showing the importance of finite width and edge effects for the nanowire.

5.3 Numerical results for the transverse case

We first present some numerical results for the SW frequencies by considering both their k dependence and their dependence on the transverse applied field H_0. We consider a $N = 24 \times 1$ Permalloy nanowire taking $a = 5$ nm as before, which corresponds to a cross section 120 nm × 5 nm and aspect ratio $p = 24$. In Fig. 5.6 we show the first few SW branches at zero wave vector ($k = 0$) plotted versus applied field. The lowest curves display a pronounced change at ~ 0.105 T, which represents the critical field at which the magnetization reorients to the transverse direction in a nanowire (see, e.g., the analogous behavior observed experimentally for cylindrical Ni

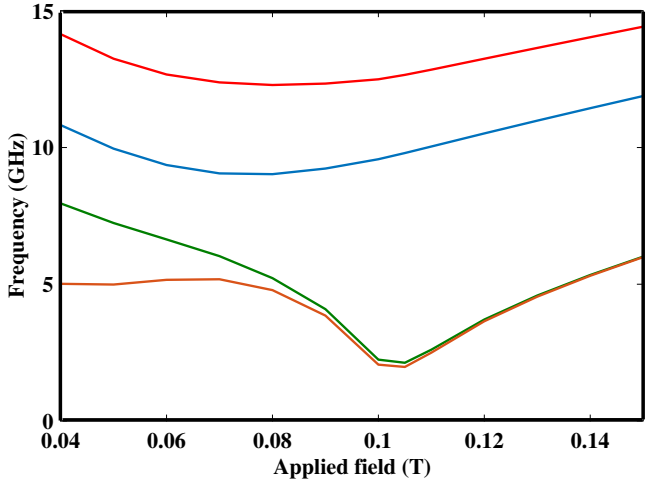

Figure 5.6: Calculated SW frequencies at zero wave-vector plotted versus transverse applied field for a $N = 24 \times 1$ Permalloy nanowire (cross section 120 nm $\times$ 5 nm), taking $\eta = 0.01$ GHz.

nanowires [100]). The behavior of the SWs is found to be quite distinct for the applied field being less or greater than this field value. The frequency of the lowest branch at the minimum is small but nonzero as a consequence of magnetization being spatially nonuniform. At large enough field value, the spins are aligned perpendicular to the length of the wire axis (along the x axis), and the SW frequencies increase monotonically due to the Zeeman term in the energy. At field values below H_c the spin orientations are canted away from the symmetry axis (with $\theta_n \neq \pi/2$). The transition at H_c is not sharp (since, e.g., the spins at the transverse edges may reorient at a slightly different field value from those in the middle of the cross section), but we note in the present case that the approximate result in Eq. (5.23) yields a $\mu_0 H_0$ value ~ 0.1 T, which is close to that deduced from Fig. 5.6.

Next we present results for the SW instabilities in the same Permalloy stripe taking $H_0 > H_c$. In Fig. 5.7(a) the lowest SW frequencies are plotted versus wave vector k at a fixed applied field $\mu_0 H_0 = 0.337$ T. The SW frequencies increase with k and the lowest curve actually consists of two lines close together (as can also be seen by referring also to Fig. 5.6). The calculated threshold field for instability (expressed relative to the resonance half-line width ΔH, as before) is presented in Fig. 5.7(b) as a function of the static applied field. We note three features, which are labeled as A (at 0.152 T), B (at 0.213 T), and C (at 0.337 T). These can be associated with the field values at

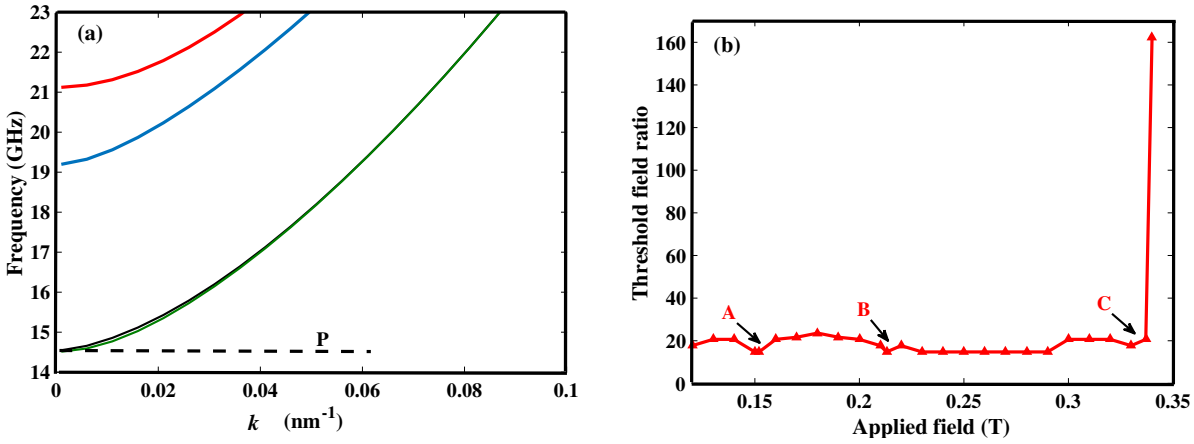

Figure 5.7: (a) SW frequencies plotted versus wave vector k for the lowest four branches of a Permalloy nanowire with cross section 120 nm × 5 nm at transverse field 0.337 T ($> \mu_0 H_c$). The horizontal line P indicates one-half of the chosen pumping frequency. (b) SW instability threshold expressed as a ratio of the half-linewidth ΔH and plotted versus applied field. Parallel pumping (along the x axis) at $\omega_p/2\pi = 29$ GHz is considered with $\eta = 0.01$ GHz. Features marked A, B, and C are discussed in the text.

which the horizontal line P in Fig. 5.7(a), drawn at one-half pumping frequency, is coincident with the $k = 0$ points on the lowest dispersion curves.

A similar example, but for a $N = 10 \times 2$ Permalloy nanowire (cross section 50 nm × 10 nm and aspect ratio $p = 5$) is considered next. In Fig. 5.8(a) we show the dispersion relation curve at a fixed applied field $\mu_0 H_0 = 0.26$ T ($> \mu_0 H_c$). The SW frequencies increase with increasing k as in Fig. 5.7(a), but the splitting between the lowest two modes (at very small k) is now more evident, because of the increased thickness and reduced aspect ratio. The corresponding butterfly curve for the Permalloy nanowire is presented in Fig. 5.8(b). This plot shows two features labeled A (at 0.225 T) and B (at 0.26 T) which correspond to the one-half of pumping frequency coinciding with the $k = 0$ frequency for the narrowly-split SW branches 1 and 2 in Fig. 5.8(a).

In addition to the results for Permalloy, we present numerical calculations for a EuS nanowire where the exchange is relatively much weaker. We take the case of a $N = 18 \times 2$ EuS nanowire (aspect ratio $p = 9$) under parallel pumping and with $\mu_0 H_0 > \mu_0 H_c \sim 0.27$ T. The critical field can be estimated either from $k = 0$ plots of the SW frequencies versus H_0 or from Eq. (5.23), which give similar values in this case. In Fig. 5.9(a) the lowest SW frequencies are plotted versus wave-vector at a fixed applied field 0.305 T; all the SW frequencies increases with k as expected in

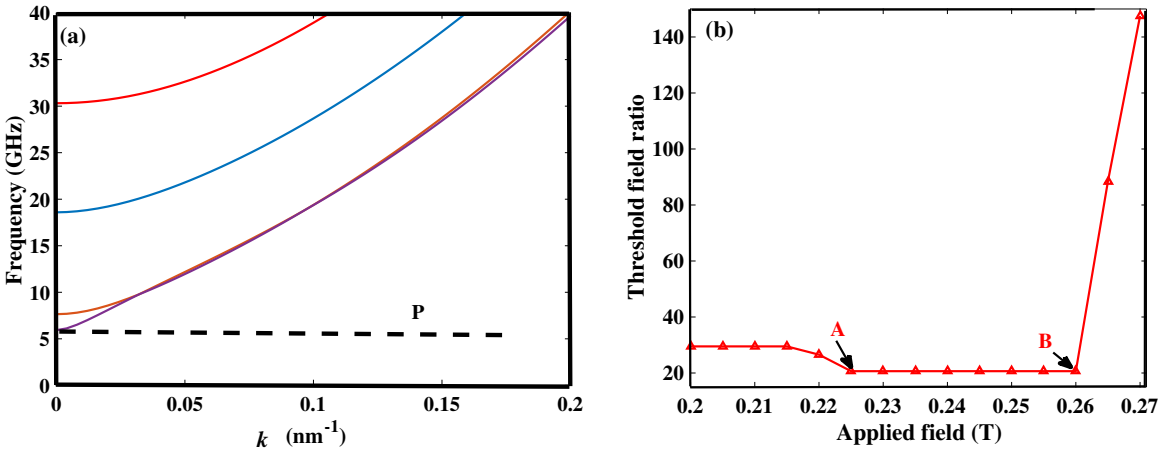

Figure 5.8: (a) SW frequencies plotted versus wave vector k for the lowest four branches of a $N = 10 \times 2$ Permalloy nanowire (cross section 50 nm $\times$ 10 nm) at transverse field $\mu_0 H_0 = 0.26$ T. The horizontal line P indicates one-half of the pumping frequency. (b) SW instability threshold expressed as a ratio of the half-linewidth ΔH and plotted versus applied field for parallel pumping at $\omega_p/2\pi = 12$ GHz with $\eta = 0.01$ GHz.

this transverse field orientation. In Fig. 5.9(b) we present the calculated SW instability threshold versus applied field for the EuS nanowire. There are two main features labeled A (at 0.305 T) and B (at 0.602 T), which correspond to the one-half pumping frequency line coinciding with the $k = 0$ frequencies for SW branches 1 and 2, respectively, in Fig. 5.9(a).

Similar results are obtained for other sizes of EuS nanostripes. In this context we note that for thicker EuS samples the use of Eq. (5.23) to estimate the critical reorientation field H_c becomes less precise than for Permalloy, because the exchange effects are less dominant. For example, for a $N = 16 \times 4$ EuS stripe, Eq. (5.23) yields $\mu_0 H_c \sim 0.35$ T, whereas a better estimate from the dependence of the $k = 0$ SW frequencies on transverse applied field gives $\mu_0 H_c \sim 0.41$ T due to consideration of the edge modes.

5.4 Conclusions

In conclusion, we have presented a microscopic dipole-exchange theory for the SW instability thresholds of ferromagnetic nanowire stripes or ribbons under pumping with a microwave field where the applied field is taken to be either parallel or transverse to the longitudinal axis. Our

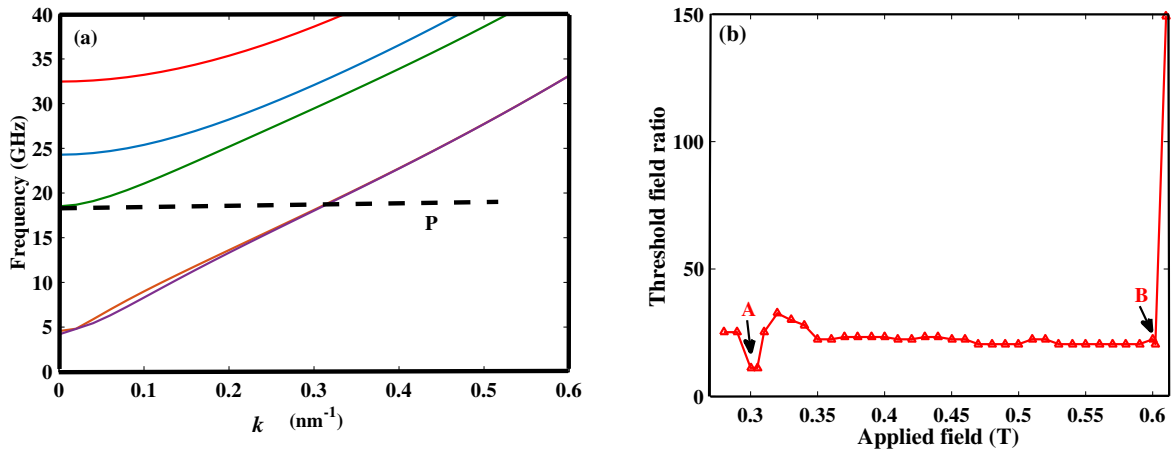

Figure 5.9: (a) SW frequencies plotted versus longitudinal wave vector k for the lowest five branches of a 18×2 EuS nanowire ($N = 36$) at transverse $\mu_0 H_0 = 0.305$ T. The horizontal line P indicates one-half of the pumping frequency. (b) SW instability threshold expressed as a ratio of the half-linewidth ΔH and plotted versus applied field. Parallel pumping at $\omega_p/2\pi = 37$ GHz is considered with $\eta = 0.03$ GHz.

microscopic theory allows us to probe the instability thresholds of these nanowires for cases where the spatial quantization effects of the discrete SWs are important and where the continuum approximations used in the macroscopic approach may be inappropriate. The focus has been on geometries where the pumping field is parallel to the net magnetization of the sample.

In the case of a longitudinal applied field, the magnetization is uniform and lies along the symmetry (or z) axis. The SW instability calculations were carried out for any general magnitude of H_0. When the applied field is perpendicular to the wire axis, there is a canting of the spin directions and the reorientation of the static magnetization leads to two phases and two distinct regimes corresponding to H_0 being less than or greater than a critical field H_c. We found the SW frequencies for all transverse field values but, for simplicity, we investigated the SW instabilities only when $H_0 > H_c$, since the equilibrium spin orientations are again in a fixed direction (along the x axis) in this case.

For both field orientations, the results were interpreted in terms of the spectrum of SW modes, which consist of branches at discrete frequencies. The shape and separation of these SW branches (and hence the predicted instabilities) depend sensitively on the dipolar-to-exchange ratio. This behavior was illustrated for different magnetic materials, where we presented numerical calculations

for stripes of Permalloy and EuS, taking different values of width and thickness. It is found that the "butterfly curves" for the instability threshold versus applied field are significantly modified compared to either macroscopic samples [22] or ultrathin films [58]. Compared to the film case, the SW properties are quite different for a stripe since they are characterized by a 1D (instead of 2D) wave vector, and the lateral edges of stripes give rise to lateral quantization and edge modes. The butterfly curves presented here show structural features related to the discrete SW branches of the stripes as discussed.

It would be of interest to explore more fully and rigorously the role of damping in the present theory (where we introduced damping phenomenologically into the rate equations, by analogy with previous work), and also to include possible effects of surface anisotropy. The magnon-magnon contribution to the damping for nanowire stripes can, in fact, be calculated within the same microscopic formalism as employed here (see [55]), but there may also be damping contributions from other mechanisms (such as magnon-phonon interactions, impurities, surface roughness, etc.). Finally we remark that our calculations could be extended to cases where a pumping field is perpendicular to the sample magnetization, as in the first- and second-order Suhl effects (see Chapter 7). Also our formulation can be modified to apply to nanowire structures, such as arrays of long ferromagnetic nanocylinders or nanotubes (see Chapter 6).

Chapter 6

Parallel pumping of spin waves for circular ferromagnetic nanowires and nanotubes

The material in this chapter has been published as a letter article by me (with M. G. Cottam) listed as Ref. [101].

Using the microscopic (or Hamiltonian-based) technique [70, 53], we have recently studied the effects of a microwave pumping field in NWs or stripes with rectangular cross sections [87]. This was the topic of Chapter 5. In particular, it was shown that the instability thresholds versus applied magnetic field (butterfly curves) are extensively modified compared with those for films and bulk samples due to the spatial confinement and edge modes in the NW stripes.

The aim of the present chapter is a theoretical study of SW instability processes in cylindrical NWs and nanotubes, both having circular cross sections, following the methods of Chapter 5. Specifically, the butterfly curves are calculated with emphasis on the size and geometries of NWs. Using parameters for Permalloy, numerical applications are made to wires and tubes with different radii. Comparisons are also made with NWs having square cross sections.

This short chapter is organized as follows. In Section 6.1, the theoretical model for NWs and nanotubes with circular cross sections is described and the calculations for the SW instability thresholds are given. Numerical examples for samples with different sizes are presented in Section

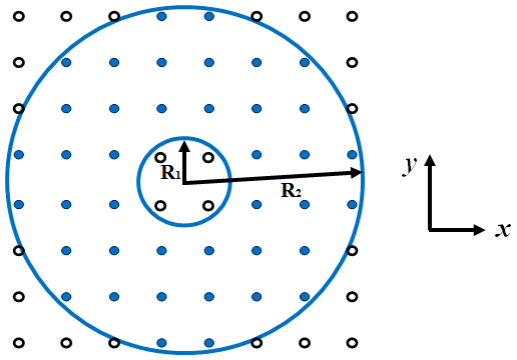

Figure 6.1: Schematic cross section of a nanotube with inner and outer radii R_1 and R_2 respectively in the xy plane and translational symmetry along the z direction. The wire case corresponds to $R = 0$. Only the spins within the physical area of the tube are considered.

6.2, followed by the conclusion in Section 6.3.

6.1 Theoretical formalism

We mainly consider NWs and nanotubes with circular cross sections in this chapter. The geometry is depicted in Fig. 6.1, where we assume the tube to be effectively infinite in the z direction and to have inner and outer radii R_1 and R_2, respectively, in the xy plane. The circular wire case corresponds simply to putting $R_1 = 0$. There is a finite number N of spins in the cross section and the system has translational symmetry in the z direction. The system is modeled in terms of a simple cubic lattice of effective spins with lattice constant a less than or comparable with the exchange length ($a_{\text{ex}} \sim 5$ or 6 nm) of Permalloy (or $Ni_{80}Fe_{20}$).

The dipole-exchange spin Hamiltonian with a microwave pumping term included is given by Eq. (5.1). The SW instability calculations at low-temperatures ($T \ll T_c$) proceed broadly by the method used in our recent work [58, 87], (see also Section 5.1) . Briefly, the spin Hamiltonian in the absence of pumping is transformed into an equivalent form with boson operators using the Holstein-Primakoff representation [31]. Next, the transformed Hamiltonian is expanded in these operators as $H = H^{(0)} + H^{(1)} + H^{(2)} + H^{(3)} + \cdots$, where $H^{(m)}$ denotes the term with a product of m boson operators. Now $H^{(0)}$ is just a constant and $H^{(1)}$ vanishes by symmetry. Then $H^{(2)}$ provides the linear SW spectrum and the higher-order terms will not be consider here for parallel pumping.

The next step is introducing a canonical (generalized Bogoliubov) transformation to diagonalize $H^{(2)}$, which is given by

$$H^{(2)} = \sum_{k,l} \omega_l(k) \alpha^{\dagger}_{k,l} \alpha_{k,l}. \tag{6.1}$$

Again $\omega_l(k)$ represents the noninteracting SW frequency for any branch l (with $l = 1, 2, \ldots, N$) at wave vector k, while $\alpha^{\dagger}_{k,l}$ and $\alpha_{k,l}$ are the corresponding creation and annihilation operators. The relevant part of the pumping field that describes the SW instability is given by (5.7). Next, the $2N$ coupled rate equations for the boson operators and can be formed by using their commutator with the effective Hamiltonian and with the damping being introduced phenomenologically as in earlier work [87]. Following the previous chapter, the SW instability can then be studied as a $2N \times 2N$ matrix eigenvalue problem to deduce the overall threshold value h_c of the pumping amplitude for the onset of an instability in any of the coupled SW branches at any k. Typically, these calculations are carried out numerically, although there is an analytical solution for a special case corresponding to the simplest non-trivial case of $N = 2$ for a rectangular cross-section wire [87].

6.2 Numerical applications

In this section the above theory will be applied to study the SW instabilities for some cylindrical NWs and nanotubes, together with brief comparisons being made with nanosquares of a comparable cross-section area.

Numerical calculations are presented using as parameters the exchange stiffness D, the saturation magnetization M_s, and $g\mu_B$, as before. These are simply related to the effective parameters in the spin Hamiltonian (5.1), as shown by Nguyen *et al.* [58]. Specifically, results are shown for a relatively strong-exchange material such as Permalloy ($Ni_{80}Fe_{20}$), where the parameters are well known and here we take the same values quoted in Section 5.2. The damping parameter η is chosen to have the value 0.01 GHz. Also we choose the lattice parameter $a = 5$ nm, which is smaller than the exchange correlation length $a_{\text{ex}} \sim 5.2$ nm, as required.

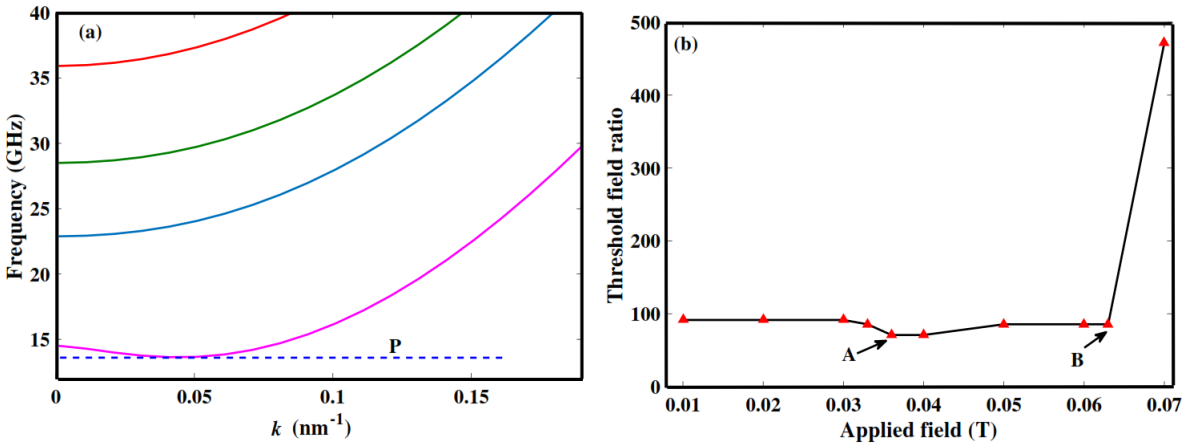

Figure 6.2: (a) Calculated SW frequencies plotted versus longitudinal wave vector k for the lowest four branches of a cylindrical Permalloy NW (R_2 = 13 nm) at longitudinal field $\mu_0 H_0$ = 0.036 T. The horizontal line P is drawn at one-half of the pumping frequency to be considered later. (b) SW instability threshold expressed as a ratio of the half-linewidth $\triangle H = \eta/g\mu_B$ and plotted versus applied field H_0. We take the pumping frequency $\omega_p/2\pi$ = 29 GHz.

We start with the geometry of a cylindrical NW. The SW frequencies versus longitudinal wave vector k are plotted in Fig. 6.2(a) for the lowest four branches of a cylindrical NW with R_2 = 13 nm. The first branch shows the expected initial dip and a minimum at nonzero wave vector, which is the result of the interplay between the competing dipole-dipole and exchange interactions. The instability threshold curve for the same NW is then presented in Fig. 6.2(b), and it has two main features labeled as A (at 0.036 T) and B (at 0.063 T) corresponding to the one-half pumping frequency coinciding, respectively, with either the zero wave vector frequency or the frequency minimum for the first SW branch.

Some analogous results for a cylindrical NW with a larger value for the radius (R_2 = 16.5 nm) are shown in Figs. 6.3(a) and (b). The results for the lowest SW branches are given first in Fig. 6.3(a). Then Fig. 6.3(b) shows the corresponding instability threshold curve which has several features labeled as A (at 0.061 T), B (at 0.203 T), C (at 0.389 T), and D (at 0.405 T). These are associated with applied field values at which the horizontal line P in Fig. 6.3(a), drawn at one-half of the pumping frequency, coincides with either the k = 0 frequency or the frequency minimum for the first three SW branches. In this case the SW branches are slightly closer together and the minimum in the lowest SW branch is more pronounced.

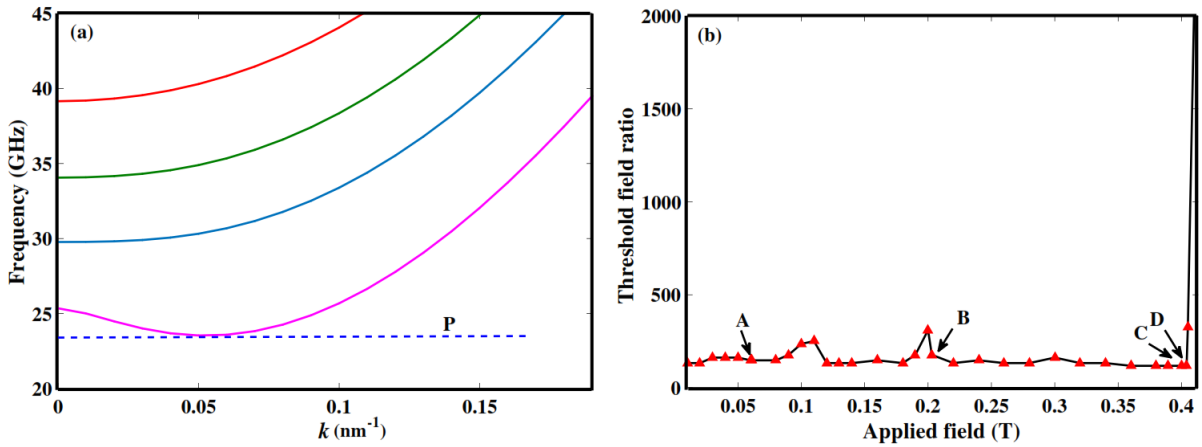

Figure 6.3: (a) Calculated SW frequencies plotted versus longitudinal wave vector k for the lowest four branches of a cylindrical Permalloy NW (R_2 = 16.5 nm) at longitudinal field $\mu_0 H_0$ = 0.405 T. The horizontal line P is drawn at one-half of the pumping frequency to be considered later. (b) SW instability threshold expressed as a ratio of the half-linewidth $\triangle H = \eta/g\mu_B$ and plotted versus applied field. We take the pumping frequency $\omega_p/2\pi$ = 47 GHz.

In Figs. 6.4(a) and (b) we examine the SW behavior in a Permalloy nanotube taking R_1 = 13 nm and R_2 = 16.5 nm. First, in Fig. 6.4(a) we show the dispersion relation results for the lowest four branches plotted as a function of wave vector k at a fixed applied field H_0 of 0.238 T. The corresponding instability threshold curve is given in Fig. 6.4(b), where we have noted some features labeled as A (at 0.037 T), B (at 0.225 T), and C (at 0.228 T). These again correspond to the one-half pumping frequency coinciding with the k = 0 frequency or frequency minimum of the first two SW branches, but the strength of some features are modified due to different SW density of states in a tube.

Finally, for comparison to illustrate the shape dependence, we show numerical applications to NWs with a square cross section. NWs with rectangular cross sections (typically with width large compared to thickness) were already investigated in our recent work [87] (see Chapter 5). To see the effects of the curvature in cylindrical NWs, we present calculations here for a similar-sized nanosquare in Figs. 6.5(a) and (b). In Fig. 6.5(a) the lowest SW frequencies are plotted versus k at a fixed applied field of 0.307 T for a Permalloy nanosquare with sides of length L = 35 nm. In Fig. 6.5(b) we present the calculated SW instability threshold as a function of applied field for the nanosquare. Four main features labeled as A (at 0.039 T), B (at 0.13 T), C (at 0.224 T) and D

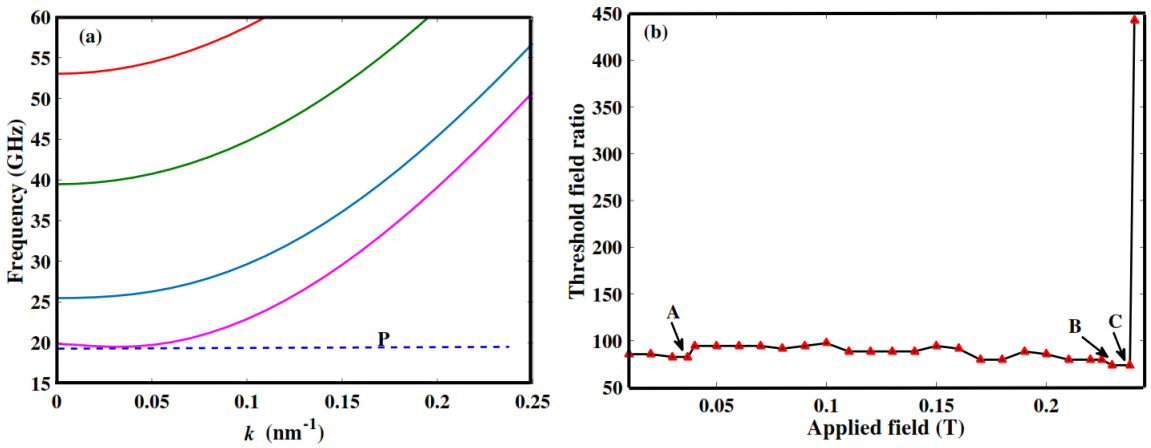

Figure 6.4: (a) Calculated SW frequencies plotted versus longitudinal wave vector k for the lowest four branches of a Permalloy nanotube with circular cross section (R_1 = 13 nm and R_2 = 16.5 nm) at longitudinal field of 0.238 T. The horizontal line P is drawn at one-half of the pumping frequency to be considered later. (b) SW instability threshold expressed as a ratio of the half-linewidth $\triangle H = \eta/g\mu_B$ and plotted versus applied field. We take the pumping frequency $\omega_p/2\pi$ = 39 GHz.

(at 0.307 T) are noted which correspond to the one-half pumping frequency line coinciding with either the $k = 0$ frequency or the frequency minimum for the three first SW branches. As can be seen, both the dispersion relation and the butterfly curves are significantly different in their detailed structure from those for cylindrical NWs.

6.3 Conclusions

In this chapter we have applied our previously developed microscopic dipole-dipole exchange theory to study the SW instabilities with the parallel pumping field for ferromagnetic NWs and nanotubes with circular cross sections. In particular, the numerical results presented for the dispersion relation and instability threshold curves were deduced for longitudinally magnetized Permalloy cylindrical NWs, nanotubes and nanosquares.

By contrast with our previous results for NW stripes, we now see that the minimum of the first branch in the dispersion relation curves for compact samples such as cylindrical NWs, nanotubes and nanosquares, is more pronounced than in the stripe case. Also the separation between the SW branches is modified. Thus studying these compact samples is of interest, e.g., in work relating to

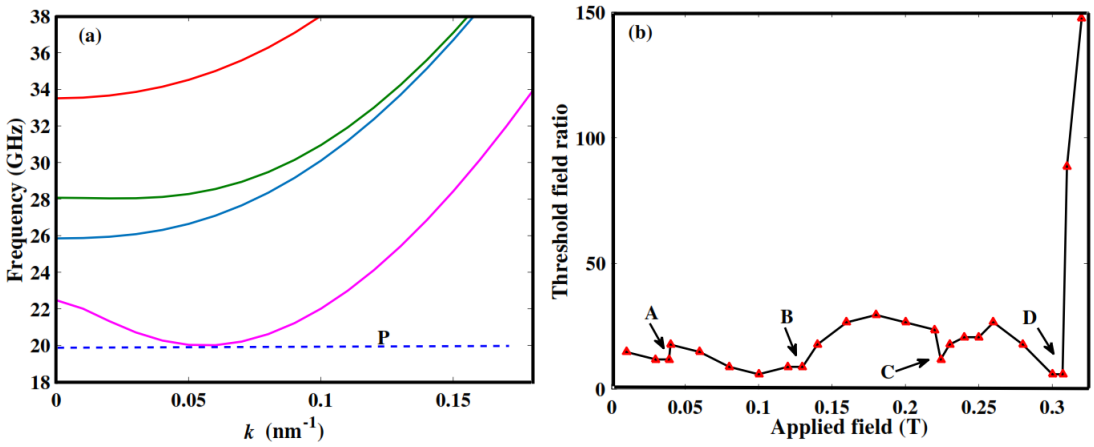

Figure 6.5: (a) Calculated SW frequencies plotted versus longitudinal wave vector k for the lowest four branches of a Permalloy nanosquare (L = 35 nm) at longitudinal field of 0.307 T. The horizontal line P is drawn at one half of the pumping frequency to be considered later. (b) SW instability threshold expressed as a ratio of the half-linewidth $\triangle H = \eta/g\mu_B$ and plotted versus applied field. We take the pumping frequency $\omega_p/2\pi$ = 40 GHz.

magnon Bose-Einstein condensation [59, 102] where the minimum in the dispersion curve plays an important role.

Our microscopic theory can be applied to more complicated and exotic structures than those discussed here, such as magnonic-crystal periodic arrays of ferromagnetic cylindrical NWs or nanotubes. Additionally, it would be of interest to explore more fully the role of damping and also to include effects of surface anisotropy.

Chapter 7

Suhl instabilities for spin waves in ferromagnetic nanostripes and ultrathin films

The material in this chapter has been published by me (with H. Nguyen and M. G. Cottam) as an article listed as Ref. [103].

Recent advances in materials growth and fabrication techniques have generated much attention for studies of the magnetization dynamics of nanoscale magnetic structures, such as dots, films, wires, and their arrays (see [5, 3, 4] for reviews). In particular, the nonlinear effects giving instabilities of the SWs under microwave pumping [62, 91, 63, 92] have been investigated intensively in both experimental and theoretical studies. The historical background to SW instabilities was discussed in previous chapters (particularly Chapters 1 and 2), and the main emphasis in Chapter 3, 5, and 6 was on the parallel pumping configuration. We now turn our attention to the perpendicular-pumping case, which was originally investigated for bulk materials both experimentally by Bloembergen and Wang [40] and theoretically by Suhl [41].

The previously-mentioned phenomena of subsidiary absorption and resonance saturation, which can be explained theoretically in terms of first-order and second-order Suhl processes, are currently

of great interest especially in the context of the nonlinear interaction in large angle switching of the magnetization using time-dependent fields [104, 105, 106] and in precessional switching [107, 108]. Until recently most of these studies were carried out using a macroscopic description, which eventually breaks down in sufficiently thin films and likewise in nanowires. An alternative is to employ a microscopic (or Hamiltonian-based) theory where a finite lattice of effective spins interact via the exchange and dipole-dipole interactions in the Hamiltonian (see, e.g., previous calculations for *linear* SWs in ultrathin films and stripes [68, 53, 69]). Likewise, it can be advantageous for the nonlinear processes in the perpendicular-pumping context to employ a microscopic approach for the parametrically-excited (and other) SWs in the smallest sample sizes under consideration.

In this chapter, therefore, we go an important stage further in the develpment of the nonlinear theory. Specifically we extend the previous microscopic theory of SW instabilities to the perpendicular-pumping case as in high-power FMR. By contrast with the treatment for parallel pumping, this requires the inclusion of three-magnon and four-magnon nonlinear processes into the formalism. Thus our work concerns the first- and second-order Suhl instabilities, where we consider nanowire stripes as well as the limiting case of ultrathin films when at least one of the sample dimensions is of the order 100 nm or less. The quantized SW branches are characterized by a 1D wave number along the symmetry axis for nanowires and a 2D in-plane wave vector for ultrathin films. Consequently, nanowires and films present quite different SW properties from each other, and it is shown that their SW instability thresholds are very different. Numerical results are presented for magnetic materials with different ratio of exchange and dipolar interactions and for wires and films with different aspect ratios and sizes.

This chapter is organized as follows. In Section 7.1 we describe the theoretical model for the rectangular-shaped nanowire stripes and the ultrathin films. This involves an extension of our previously mentioned work on parallel pumping to the perpendicular-pumping case where the three- and four-magnon interactions play an important role. Specifically, a first-order Suhl instability of the SWs at one half of the pumping frequency can be driven by three-magnon processes, whereas

in the second-order Suhl instability two uniform magnons are annihilated and a SW pair with frequencies close to the pumping frequency are created by means of the four-magnon scattering processes (see Chapters 1 and 2). Some special cases of the general formalism for particular sample geometries are analyzed in Section 7.2. Then numerical calculations for the first-order Suhl processes are presented in Section 7.3 for different materials and sample sizes to illustrate the contrasting behavior for two geometries and the role of the dipole-dipole interaction strength relative to the exchange interaction (using Permalloy, EuS and YIG). The numerical results for second-order Suhl processes are provided briefly in Section 7.4. Finally we summarize these results and discuss some extensions in Section 7.5.

7.1 Theoretical formalism for perpendicular pumping

We consider both nanowire stripes and ultrathin films in this work, where the geometries are depicted in Fig. 7.1. A ferromagnetic stripe will be modeled as having a constant rectangular cross section with finite dimensions in the xy plane, while the system is effectively infinite in the z direction. A simple-cubic lattice of effective spins (with lattice constant a) fills the volume of the wire, so there is a finite number N ($= n_x n_y$) spins in each cross section of width $w = n_x a$ and thickness $d = n_y a$ (see Fig. 7.1(a)), where n_x and n_y are integers and without loss of generality we assume $n_x \geq n_y$. The system has translational symmetry in the z direction only, so the SW modes will be characterized by a 1D wave vector $\mathbf{q} = (q_z)$. An ultrathin ferromagnetic film with (010) surfaces is modeled as having N ($= n_y$) atomic layers of spins, again arranged on a simple cubic lattice structure (see Fig. 7.1(b)). The static field H_0 is applied in-plane, and the system has two directions of translational symmetry. Hence the SWs are characterized in this case by a 2D wave vector $\mathbf{q} = (q_x, q_z)$, so they can propagate at an angle ϕ to the field direction. Formally the film geometry represents the $w \to \infty$ limit of the stripe, so we may study both narrow and wide stripes in our calculations.

For both structures the direction of net magnetization is along the z direction. Hence there are

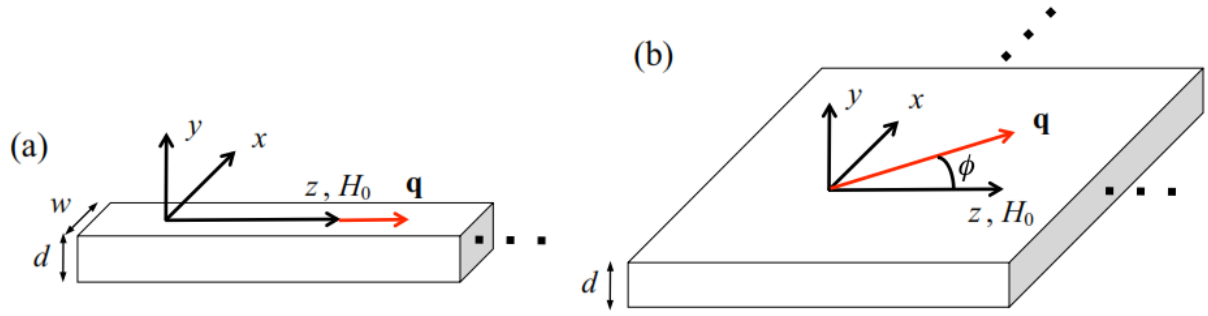

Figure 7.1: Assumed geometry and choice of coordinate axes for the nanostructures: a) a long nanowire with rectangular cross section (width w and thickness d) and applied field H_0 along the length axis; (b) an ultrathin film with thickness d and in-plane applied field H_0.

two cases for the perpendicular microwave pumping field, which may either have component $h_x(t)$ along the x axis or $h_y(t)$ along the y axis. These are non-equivalent in their effect for a nanowire stripe (provided $n_x \neq n_y$) and for a film. In terms of the microscopic model, the dipole-exchange spin Hamiltonian with a microwave pumping term included can be expressed as

$$\begin{aligned} H &= -\frac{1}{2}\sum_{in,jm} J_{in,jm}\mathbf{S}_{in}\cdot\mathbf{S}_{jm} \\ &\quad +\frac{1}{2}(g\mu_B)^2\sum_{in,jm}\sum_{\alpha,\beta} D^{\alpha\beta}_{in,jm} S^{\alpha}_{in} S^{\beta}_{jm} - g\mu_B H_0\sum_{in} S^{z}_{in} - g\mu_B \mathbf{h}(t)\cdot\sum_{in}\mathbf{S}_{in}\,. \end{aligned} \tag{7.1}$$

The notation in the nanowire case (following [53, 87]) is that i and j label the spin sites along the z-directed lines formed by the spins, while indices n and m ($= 1, 2, \cdots, N$) enumerate all the spin sites in any cross section of the nanowire (with $N = n_x n_y$). For the film case (following [69, 58]) n and m ($= 1, 2, \cdots, N$) refer to the atomic layers in the xz plane, while labels i and j refer to the sites within any atomic layer. The first two terms in Eq. (7.1) describe the short-range exchange and long-range dipole-dipole interactions between the effective spins $\mathbf{S}_{in}$ and $\mathbf{S}_{jm}$, respectively. The exchange $J_{in,jm}$ between sites $\mathbf{r}_{in}$ and $\mathbf{r}_{jm}$ is taken to be J for all nearest neighbors and zero otherwise, while the dipolar interactions $D^{\alpha\beta}_{in,jm}$ is given by Eq. (3.2). The next term in Eq. (7.1) represents the Zeeman energy due to the z-directed external magnetic field H_0, and the last term gives the effect of the perpendicular microwave pumping field $h(t)$, which can act either along the x or y axis.

The SW instability calculation for ultrathin ferromagnetic films proceeds by extending the method used in previous work [58, 87] for the parallel pumping case in these structures. Briefly, the Holstein-Primakoff representation [31] is first employed to transform from the spin operators to boson creation and annihilation operators $a_{in}^{\dagger}$and a_{in}. Then the Hamiltonian of the system at low temperatures $T \ll T_c$ is expanded in terms of the boson operators as $H = H^{(0)} + H^{(1)} + H^{(2)} + \cdots$, with $H^{(m)}$ denoting the term with a product of m boson operators. The zeroth-order term $H^{(0)}$ is just a constant, while $H^{(1)}$ vanishes by symmetry for these ferromagnetic stripes and films with the chosen direction of H_0. The non-interacting SWs are described by the second-order term $H^{(2)}$, which takes the following form in the absence of the pumping field:

$$H^{(2)} = \sum_{n,m,\mathbf{q}} \left[A_{n,m}^{(2)}(\mathbf{q}) a_{\mathbf{q},n}^{\dagger} a_{\mathbf{q},m} + B_{n,m}^{(2)}(\mathbf{q}) a_{\mathbf{q},n} a_{-\mathbf{q},m} + C_{n,m}^{(2)}(\mathbf{q}) a_{\mathbf{q},n}^{\dagger} a_{-\mathbf{q},m}^{\dagger} \right]. \tag{7.2}$$

Here we have made wave-vector Fourier transforms with respect to the directions of translational symmetry, i.e., the z direction for a nanowire and the x and z directions for a film. Thus $\mathbf{q}$ is a 1D wave vector for a nanowire with $\mathbf{q} = (q_z)$ and a 2D in-plane wave vector in the case of a film with $\mathbf{q} = (q_x, q_z)$. The coefficients $A_{n,m}^{(2)}(\mathbf{q})$, $B_{n,m}^{(2)}(\mathbf{q})$, and $C_{n,m}^{(2)}(\mathbf{q})$ in Eq. (7.2) depend on the Hamiltonian parameters. Their explicit expressions can be found in Ref. [69] and are not quoted here.

The above second-order Hamiltonian $H^{(2)}$ can be diagonalized by following the method described in previous work for linearized SWs in ultrathin films and nanowires (see, e.g., [70, 68]). A generalized Bogoliubov transformation is made from the set of operators $\left\{a_{\mathbf{q},n}, a_{\mathbf{q},n}^{\dagger}\right\}$ to a new set of boson operators $\left\{\alpha_{\mathbf{q},n}, \alpha_{\mathbf{q},n}^{\dagger}\right\}$ using

$$a_{\mathbf{q},n} = \sum_{l=1}^{N} \{ S_{n,l}(\mathbf{q}) \alpha_{\mathbf{q},l} + S_{n+N,l}^{\star}(\mathbf{q}) \alpha_{-\mathbf{q},l}^{\dagger} \}, \tag{7.3}$$

along with the Hermitian conjugate expression for $a_{\mathbf{q},n}^{\dagger}$. Here $S_{n,l}(\mathbf{q})$ is an element of the $2N \times 2N$ transformation matrix $\mathbf{S}(\mathbf{q})$ obtained as defined in Ref. [70] (see also Subsection 5.1.1). Then, apart from a constant, the second-order Hamiltonian $H^{(2)}$, in the absence of pumping, can be rewritten in the diagonalized form as

$$H^{(2)} = \sum_{\mathbf{q},l} \omega_l(\mathbf{q}) \alpha^\dagger_{\mathbf{q},l} \alpha_{\mathbf{q},l}, \tag{7.4}$$

where $\omega_l(\mathbf{q})$ is the frequency of the non-interacting SW branch l ($l = 1, 2, \cdots, N$) at wave vector $\mathbf{q}$. As discussed elsewhere, the form of the SW dispersion is quite different in wires and films, consisting of discrete lines in the former case and bands (with a dependence on the propagation direction) in the latter case.

It is well known from the seminal work by Suhl [41] that there is a first-order parametric process of SW instabilities that occurs through a uniform mode and the three-magnon Hamiltonian term $H^{(3)}$ and a second-order parametric process that occurs through two uniform modes and the four-magnon term $H^{(4)}$. Therefore we need to explore the explicit form of these Hamiltonian terms for the assumed nanowire and film geometries.

Following recent work on SW damping in nanowires [55], we may express the three-magnon term $H^{(3)}$ initially as

$$H^{(3)} = \sum_{n,m} \sum_{\mathbf{q},\mathbf{k}} \left[A^{(3)}_{n,m}(\mathbf{k}) a^\dagger_{\mathbf{k},n} a^\dagger_{\mathbf{q},m} a_{\mathbf{k}+\mathbf{q},m} + A^{(3)\star}_{n,m}(\mathbf{k}) a^\dagger_{\mathbf{q},n} a_{\mathbf{q}-\mathbf{k},n} a_{\mathbf{k},m} \right], \tag{7.5}$$

where

$$A^{(3)}_{n,m}(\mathbf{k}) = -\frac{1}{4} S \sqrt{\frac{S}{2}} (g\mu_B)^2 \left\{ \sum_l \left[D^{xz}_{n,l}(0) + i D^{yz}_{n,l}(0) \right] \delta_{n\,m} + 4 \left[D^{xz}_{n,m}(\mathbf{k}) + i D^{yz}_{n,m}(\mathbf{k}) \right] \right\}. \tag{7.6}$$

The four-magnon term $H^{(4)}$ is

$$\begin{aligned} H^{(4)} = \sum_{n,m} \sum_{\mathbf{q},\mathbf{k},\mathbf{k}'} \Big\{ & A^{(4)}_{n,m}(\mathbf{k}) \left[a^\dagger_{\mathbf{k},n} a^\dagger_{\mathbf{k}',m} a_{\mathbf{q},m} a_{\mathbf{k}+\mathbf{k}'-\mathbf{q},m} + a^\dagger_{\mathbf{q},n} a^\dagger_{\mathbf{k}',n} a_{\mathbf{k},m} a_{-\mathbf{k}+\mathbf{k}'+\mathbf{q},n} \right] \\ + & B^{(4)}_{n,m}(\mathbf{k}) a^\dagger_{\mathbf{k}',n} a^\dagger_{\mathbf{q},m} a_{-\mathbf{k}+\mathbf{k}',n} a_{\mathbf{k}+\mathbf{q},m} + C^{(4)}_{n,m}(\mathbf{k}) a^\dagger_{-\mathbf{k},m} a^\dagger_{\mathbf{k}',n} a^\dagger_{\mathbf{q},n} a_{-\mathbf{k}+\mathbf{k}'+\mathbf{q},n} \\ + & C^{(4)\star}_{n,m}(\mathbf{k}) a^\dagger_{\mathbf{k}',n} a_{\mathbf{q},n} a_{-\mathbf{k}+\mathbf{k}'-\mathbf{q},n} a_{\mathbf{k},m} \Big\}, \end{aligned} \tag{7.7}$$

where

$$A^{(4)}_{n,m}(\mathbf{k}) = \frac{1}{4} \left[J_{n,m}(\mathbf{k}) + 0.5 (g\mu_B)^2 D^{zz}_{n,m}(\mathbf{k}) \right], \tag{7.8}$$

$$B^{(4)}_{n,m}(\mathbf{k}) = -\frac{1}{2}\left[J_{n,m}(\mathbf{k}) - (g\mu_B)^2 D^{zz}_{n,m}(\mathbf{k})\right], \tag{7.9}$$

$$C^{(4)}_{n,m}(\mathbf{k}) = \frac{1}{8}(g\mu_B)^2\left[D^{yy}_{n,m}(\mathbf{k}) - D^{xx}_{n,m}(\mathbf{k}) - 2iD^{xy}_{n,m}(\mathbf{k})\right]. \tag{7.10}$$

In the above equations the quantities $J_{n,m}(\mathbf{q})$ and $D^{\alpha\beta}_{n,m}(\mathbf{q})$ denote the wave-vector Fourier transforms of the exchange and dipolar interactions, respectively, with respect to $\mathbf{q}$ for a nanowire or film.

The next step involves rewriting $H^{(3)}$ and $H^{(4)}$, as well as the pumping part of the Hamiltonian, in terms of the new boson operators. We find

$$\begin{aligned} H^{(3)} = \sum_{l_1,l_2,l_3}\sum_{\mathbf{k},\mathbf{q}}\Big\{ & V_1(\mathbf{k},\mathbf{q}|l_1,l_2,l_3)\,\alpha^\dagger_{\mathbf{k},l_1}\alpha^\dagger_{\mathbf{q},l_2}\alpha_{\mathbf{k}+\mathbf{q},l_3} + V_2(\mathbf{k},\mathbf{q}|l_1,l_2,l_3)\,\alpha^\dagger_{\mathbf{k},l_1}\alpha_{-\mathbf{q},l_2}\alpha_{\mathbf{k}+\mathbf{q},l_3} \\ & + V_3(\mathbf{k},\mathbf{q}|l_1,l_2,l_3)\,\alpha^\dagger_{\mathbf{k},l_1}\alpha^\dagger_{\mathbf{q},l_2}\alpha^\dagger_{-\mathbf{k}-\mathbf{q},l_3} + V_4(\mathbf{k},\mathbf{q}|l_1,l_2,l_3)\,\alpha_{-\mathbf{k},l_1}\,\alpha_{-\mathbf{q},l_2}\alpha_{\mathbf{k}+\mathbf{q},l_3}\Big\}, \end{aligned} \tag{7.11}$$

$$\begin{aligned} H^{(4)} = \sum_{l_1,l_2,l_3,l_4}\sum_{\mathbf{k},\mathbf{k}',\mathbf{q}}\Big\{ & \Lambda_1\left(\mathbf{k},\mathbf{k}',\mathbf{q}|l_1,l_2,l_3,l_4\right)\alpha^\dagger_{\mathbf{k},l_1}\alpha^\dagger_{\mathbf{k}',l_2}\alpha_{\mathbf{q},l_3}\alpha_{\mathbf{k}+\mathbf{k}'-\mathbf{q},l_4} \\ & + \Lambda_2\left(\mathbf{k},\mathbf{k}',\mathbf{q}|l_1,l_2,l_3,l_4\right)\alpha^\dagger_{\mathbf{k},l_1}\alpha_{-\mathbf{k}',l_2}\alpha_{\mathbf{q},l_3}\alpha_{\mathbf{k}+\mathbf{k}'-\mathbf{q},l_4} \\ & + \Lambda_3\left(\mathbf{k},\mathbf{k}',\mathbf{q}|l_1,l_2,l_3,l_4\right)\alpha^\dagger_{\mathbf{k},l_1}\alpha^\dagger_{\mathbf{k}',l_2}\alpha^\dagger_{-\mathbf{q},l_3}\alpha_{\mathbf{k}+\mathbf{k}'-\mathbf{q},l_4} \\ & + \Lambda_4\left(\mathbf{k},\mathbf{k}',\mathbf{q}|l_1,l_2,l_3,l_4\right)\alpha^\dagger_{\mathbf{k},l_1}\alpha^\dagger_{\mathbf{k}',l_2}\alpha^\dagger_{-\mathbf{q},l_3}\alpha^\dagger_{-\mathbf{k}-\mathbf{k}'+\mathbf{q},l_4} \\ & + \Lambda_5\left(\mathbf{k},\mathbf{k}',\mathbf{q}|l_1,l_2,l_3,l_4\right)\alpha_{-\mathbf{k},l_1}\alpha_{-\mathbf{k}',l_2}\alpha_{\mathbf{q},l_3}\alpha_{\mathbf{k}+\mathbf{k}'-\mathbf{q},l_4}. \end{aligned} \tag{7.12}$$

The expressions for the amplitude factors $V_i(\mathbf{k},\mathbf{q}|l_1,l_2,l_3)$ and $\Lambda_i\left(\mathbf{k},\mathbf{k}',\mathbf{q}|l_1,l_2,l_3,l_4\right)$ are quite lengthy, mainly because of the dependence on SW band indices, and the important results are quoted in Appendix C. Additionally, the contribution to the Hamiltonian of the transverse pumping takes one of two forms, denoted as $H^\perp_{p,x}$ if the pumping field is in the x direction or $H^\perp_{p,y}$ if the field is in the y direction. To leading order the Hamiltonian contributions are

$$H^{\perp}_{p,x} = -g\mu_B h_x e^{-i\omega_p t}\sqrt{\frac{S}{2}}\sum_{\mathbf{q},n,l}\alpha^{\dagger}_{0,l}\left[S^{\star}_{n,l}(0)+S^{\star}_{n+N,l}(0)\right]+\text{h.c.}, \tag{7.13}$$

$$H^{\perp}_{p,y} = -ig\mu_B h_y e^{-i\omega_p t}\sqrt{\frac{S}{2}}\sum_{\mathbf{q},n,l}\alpha^{\dagger}_{0,l}\left[S^{\star}_{n,l}(0)-S^{\star}_{n+N,l}(0)\right]+\text{h.c.}, \tag{7.14}$$

where we have assumed pumping at a single angular frequency ω_p.

7.1.1 First-order Suhl instability

In the first-order Suhl process, a pair of degenerate SWs (with wave vectors $\mathbf{q}$ and $-\mathbf{q}$) can be driven into instability via the three-magnon interaction [27, 41]. Thus, to leading order the effective Hamiltonian for the first-order Suhl instability is $H^{(1)}_{\text{eff}} = H^{(2)} + H^{(3)} + H^{\perp}_{p}$, where $H^{\perp}_{p}$ stands for either $H^{\perp}_{p,x}$ or $H^{\perp}_{p,y}$ according to direction of pumping. This effective Hamiltonian for pumping in the x direction is

$$\begin{aligned} H^{(1)}_{\text{eff},x} &= \sum_{\mathbf{q}\neq 0,l}\omega_l(\mathbf{q})\alpha^{\dagger}_{\mathbf{q},l}\alpha_{\mathbf{q},l}+\sum_{l_1,l_2,l_3}\sum_{\mathbf{q}}\left\{V_1(\mathbf{q}|l_1,l_2,l_3)\,\alpha^{\dagger}_{\mathbf{q},l_1}\alpha^{\dagger}_{-\mathbf{q},l_2}\alpha_{0,l_3}+\text{h.c.}\right\} \\ &\quad -g\mu_B h_x e^{-i\omega_p t}\sqrt{\frac{S}{2}}\sum_{n,l}\left\{\alpha^{\dagger}_{0,l}\left[S^{\star}_{n,l}(0)+S^{\star}_{n+N,l}(0)\right]+\text{h.c.}\right\}, \end{aligned} \tag{7.15}$$

and there is an analogous expression for pumping in the y direction.

By analogy with earlier work [58], the next step is to derive the rate equations for boson operators $\alpha_{\mathbf{q},l}$ and $\alpha^{\dagger}_{\mathbf{q},l}$ by forming their commutators with $H^{(1)}_{\text{eff},x}$ or $H^{(1)}_{\text{eff},y}$. We also introduce the role of energy dissipation into the rate equation via the damping constant $\eta_l(\mathbf{q})$ for the SW branch l by making the replacement $\omega_l(\mathbf{q}) \longrightarrow \omega_l(\mathbf{q}) - i\eta_l(\mathbf{q})$ for the SW frequency. The set of N coupled equation for the boson operators $\alpha_{\mathbf{q},l}$ takes the following forms for the two pumping directions:

$$\frac{d\alpha_{\mathbf{q},l}}{dt} = -\left(i\omega_l(\mathbf{q})+\eta_l(\mathbf{q})\right)\alpha_{\mathbf{q},l} - ie^{-i\omega_p t}h_x\sum_{l'}P_{l,l'}(\mathbf{q})\alpha^{\dagger}_{-\mathbf{q},l'}, \qquad (x \text{ pumping}), \tag{7.16}$$

$$\frac{d\alpha_{\mathbf{q},l}}{dt} = -\left(i\omega_l(\mathbf{q}) + \eta_l(\mathbf{q})\right)\alpha_{\mathbf{q},l} + e^{-i\omega_p t}h_y\sum_{l'}Q_{l,l'}(\mathbf{q})\alpha^{\dagger}_{-\mathbf{q},l'}, \qquad (y \text{ pumping}). \tag{7.17}$$

Here we have introduced the notation that

$$P_{l,l'}(\mathbf{q}) = -g\mu_B\sqrt{\frac{S}{2}}\sum_{l''}V_1(\mathbf{q}|l,l',l'')\left\{\frac{\sum_n\left[S^{\star}_{n,l''}(0) + S^{\star}_{n+N,l''}(0)\right]}{\omega_p - \omega_{l''}(0) + i\eta_{l''}(0)}\right\}, \tag{7.18}$$

$$Q_{l,l'}(\mathbf{q}) = g\mu_B\sqrt{\frac{S}{2}}\sum_{l''}V_1(\mathbf{q}|l,l',l'')\left\{\frac{\sum_n\left[S^{\star}_{n,l''}(0) - S^{\star}_{n+N,l''}(0)\right]}{\omega_p - \omega_{l''}(0) + i\eta_{l''}(0)}\right\}, \tag{7.19}$$

with the explicit expression for V_1 given in Appendix C.

To solve these equations we follow the standard procedure (see, e.g., [25, 27, 66, 109]) of rewriting the rapidly time-varying operators $\alpha_{\mathbf{q},l}$, utilizing the fact that a pair of SWs will be parametrically excited, each at at frequency $\omega_p/2$. Therefore by assuming $\alpha_{-\mathbf{q},l} = \exp(i\psi_{\mathbf{q}})\alpha_{\mathbf{q},l}$ (with $\psi_{\mathbf{q}}$ as a real phase), the rapidly time-varying operators $\alpha_{\mathbf{q},l}$ can be rewritten using

$$b_{\mathbf{q},l} \sim \left\langle\alpha_{\mathbf{q},l}\right\rangle\exp\left(i(\omega_p/2)t\right)\exp(i\psi_{\mathbf{q}}/2). \tag{7.20}$$

Eventually Eq. (7.20) becomes

$$\frac{db_{\mathbf{q},l}}{dt} = -\left(i\Delta\omega_l(\mathbf{q}) + \eta_l(\mathbf{q})\right)b_{\mathbf{q},l} - ih_x\sum_{l'}P_{l,l'}(\mathbf{q})b^{\star}_{\mathbf{q},l'}, \tag{7.21}$$

when the pumping field is along the x direction and there is a similar result with $h_xP_{l,l'}(\mathbf{q})$ replaced by $ih_yQ_{l,l'}(\mathbf{q})$ when the pumping field is along the y axis. We have defined $\triangle\omega_l(\mathbf{q}) = \omega_l(\mathbf{q}) - (\omega_p/2)$. The solutions of Eq. (7.21) and its complex conjugate can be examined by considering a characteristic time dependence for $b_{\mathbf{q},l}$ or $b^{*}_{\mathbf{q},l}$ of the form $\exp(\beta\mathrm{t})$, where β may be complex. At this stage it is helpful the recast the problem in a matrix form. Since $b_{\mathbf{q},l}$, $P_{ll'}(\mathbf{q})$ and $Q_{ll'}(\mathbf{q})$ are complex in general, having the forms $b_{\mathbf{q},l} = b^{'}_{\mathbf{q},l} + ib^{''}_{\mathbf{q},l}$ and $P_{l,l'}(\mathbf{q}) = P^{'}_{l,l'}(\mathbf{q}) + iP^{''}_{l,l'}(\mathbf{q})$ and $Q_{l,l'}(\mathbf{q}) = Q^{'}_{l,l'}(\mathbf{q}) + iQ^{''}_{l,l'}(\mathbf{q})$, we introduce the $1\times 2N$ column matrices defined by

$$\mathbf{b_q} = \begin{pmatrix} b'_{\mathbf{q},1} \\ \vdots \\ b'_{\mathbf{q},N} \\ b''_{\mathbf{q},1} \\ \vdots \\ b''_{\mathbf{q},N} \end{pmatrix}, \qquad \mathbf{P}(\mathbf{q}) = \begin{pmatrix} P'_{1,l'}(\mathbf{q}) \\ \vdots \\ P'_{N,l'}(\mathbf{q}) \\ P''_{1,l'}(\mathbf{q}) \\ \vdots \\ P''_{N,l'}(\mathbf{q}) \end{pmatrix}, \qquad \mathbf{Q}(\mathbf{q}) = \begin{pmatrix} Q'_{1,l'}(\mathbf{q}) \\ \vdots \\ Q'_{N,l'}(\mathbf{q}) \\ Q''_{1,l'}(\mathbf{q}) \\ \vdots \\ Q''_{N,l'}(\mathbf{q}) \end{pmatrix}. \tag{7.22}$$

Then, we can rewrite the above coupled rate equations as

$$\begin{pmatrix} \mathbf{D}^{(2)}(\mathbf{q}) & \mathbf{E}^{(2)}(\mathbf{q}) \\ \mathbf{F}^{(2)}(\mathbf{q}) & \mathbf{G}^{(2)}(\mathbf{q}) \end{pmatrix} \mathbf{b_q} = \beta(\mathbf{q})\, \mathbf{b_q}, \tag{7.23}$$

where $\mathbf{D}^{(2)}(\mathbf{q})$, $\mathbf{E}^{(2)}(\mathbf{q})$, $\mathbf{F}^{(2)}(\mathbf{q})$ and $\mathbf{G}^{(2)}(\mathbf{q})$ are $N \times N$ matrices with matrix elements defined by

$$\begin{aligned} D^{(2)}_{l,l'}(\mathbf{q}) &= -\eta_{l'}(\mathbf{q})\delta_{l,l'} + h_x P''_{l,l'}(\mathbf{q}), \qquad E^{(2)}_{l,l'}(\mathbf{q}) = \Delta\omega_{l'}(\mathbf{q})\delta_{l,l'} - h_x P'_{l,l'}(\mathbf{q}), \\ F^{(2)}_{l,l'}(\mathbf{q}) &= -\Delta\omega_{l'}(\mathbf{q})\delta_{l,l'} - h_x P'_{l,l'}(\mathbf{q}), \qquad G^{(2)}_{l,l'}(\mathbf{q}) = -\eta_{l'}(\mathbf{q})\delta_{l,l'} - h_x P''_{l,l'}(\mathbf{q}), \end{aligned} \tag{7.24}$$

for pumping along the x axis. For the pumping field along the y axis, the corresponding results are

$$\begin{aligned} D^{(2)}_{l,l'}(\mathbf{q}) &= -\eta_{l'}(\mathbf{q})\delta_{l,l'} + h_y Q'_{l,l'}(\mathbf{q}), \qquad E^{(2)}_{l,l'}(\mathbf{q}) = \Delta\omega_{l'}(\mathbf{q})\delta_{l,l'} + h_y Q''_{l,l'}(\mathbf{q}), \\ F^{(2)}_{l,l'}(\mathbf{q}) &= -\Delta\omega_{l'}(\mathbf{q})\delta_{l,l'} + h_y Q''_{l,l'}(\mathbf{q}), \qquad G^{(2)}_{l,l'}(\mathbf{q}) = -\eta_{l'}(\mathbf{q})\delta_{l,l'} - h_y Q'_{l,l'}(\mathbf{q}). \end{aligned} \tag{7.25}$$

The solution of the eigenvalue problem represented by Eq. (7.23) is carried out numerically as described later, but in a few special cases there are analytic expressions. However, in the general case of nanowires with $N \geq 3$, and films with $N \geq 2$, the $2N \times 2N$ eigenvalue problem represented by Eq. (7.23) has to be solved numerically to obtain the set of eigenvalues $\beta_n(k)$ with $n = 1, 2, \ldots, 2N$. For a given wave vector $\mathbf{q}$ the SW instability threshold is found by determining the value of the pumping field amplitude h_0 for any one of the eigenvalues to have a positive real part. We note that the damping parameter η in Eq. (7.34) in principle depends on $\mathbf{q}$ and branch l. For the numerical examples presented later we use the simplification, as in [58], of adopting a constant value for the small $\mathbf{q}$ region (independent of branch label l).

7.1.2 Second-order Suhl instability

Similarly, the second-order Suhl process proceeds via the four-magnon interaction, and the effective Hamiltonian in this case has the form $H^{(2)}_{\rm eff} = H^{(2)} + H^{(4)} + H^{\perp}_{p}$ in leading order. By considering only the dominant scattering term Λ_1 in $H^{(4)}$, the effective Hamiltonian for investigating the second-order Suhl process under perpendicular pumping field along the x axis takes the form

$$\begin{aligned} H^{(2)}_{{\rm eff},x} &= \sum_{\mathbf{q},l} \omega_l(\mathbf{q}) \alpha^{\dagger}_{\mathbf{q},l} \alpha_{\mathbf{q},l} + \sum_{l_1,l_2,l_3,l_4} \sum_{\mathbf{q}} \Lambda_1\left(\mathbf{q}|l_1,l_2,l_3,l_4\right) \alpha^{\dagger}_{\mathbf{q},l_1} \alpha^{\dagger}_{-\mathbf{q},l_2} \alpha_{0,l_3} \alpha_{0,l_4} \\ & \quad -g\mu_B h_x e^{-i\omega_p t} \sqrt{\frac{S}{2}} \sum_{n,l} \Big\{ \alpha^{\dagger}_{0,l} \left[S^{\star}_{n,l}(0) + S^{\star}_{n+N,l}(0) \right] + \text{h.c.} \Big\}, \end{aligned} \tag{7.26}$$

while there is a similar expression when the pumping field is along the y axis. Here Λ_1 is a coefficient introduced in Eq. (7.12) and having the explicit form given in Eq. (C.3).

Essentially the same steps as in Subsection 7.1.1 may now be followed, so we shall quote just the final results. An eigenvalue equation for $\beta(\mathbf{q})$ having the same form as in Eq. (7.23) is again obtained, but the elements of the submatrices are redefined as

$$\begin{aligned} D^{(2)}_{l,l'}(\mathbf{q}) &= -\eta_{l'}(\mathbf{q})\delta_{l,l'} + h_x^2 R^{''}_{l,l'}(\mathbf{q}), \qquad E^{(2)}_{l,l'}(\mathbf{q}) = \Delta\omega_{l'}(\mathbf{q})\delta_{l,l'} - h_x^2 R^{'}_{l,l'}(\mathbf{q}), \\ F^{(2)}_{l,l'}(\mathbf{q}) &= -\Delta\omega_{l'}(\mathbf{q})\delta_{l,l'} - h_x^2 R^{'}_{l,l'}(\mathbf{q}), \qquad G^{(2)}_{l,l'}(\mathbf{q}) = -\eta_{l'}(\mathbf{q})\delta_{l,l'} - h_x^2 R^{''}_{l,l'}(\mathbf{q}), \end{aligned} \tag{7.27}$$

for the pumping along the x axis. For pumping field along the y axis the results are

$$\begin{aligned} D^{(2)}_{l,l'}(\mathbf{q}) &= -\eta_{l'}(\mathbf{q})\delta_{l,l'} + h_y^2 T^{'}_{l,l'}(\mathbf{q}), \qquad E^{(2)}_{l,l'}(\mathbf{q}) = \Delta\omega_{l'}(\mathbf{q})\delta_{l,l'} + h_y^2 T^{''}_{l,l'}(\mathbf{q}), \\ F^{(2)}_{l,l'}(\mathbf{q}) &= -\Delta\omega_{l'}(\mathbf{q})\delta_{l,l'} + h_y^2 T^{''}_{l,l'}(\mathbf{q}), \qquad G^{(2)}_{l,l'}(\mathbf{q}) = -\eta_{l'}(\mathbf{q})\delta_{l,l'} - h_y^2 T^{'}_{l,l'}(\mathbf{q}). \end{aligned} \tag{7.28}$$

In this case we denote $\Delta\omega_l(\mathbf{q}) = \Big(\omega_l(\mathbf{q}) - \omega_p\Big)$, noting that the frequency shift is now by an amount ω_p and the above equations involve the real and imaginary parts of $R_{l_1,l_2}(\mathbf{q})$ and $T_{l_1,l_2}(\mathbf{q})$ where

$$R_{l_1,l_2}(\mathbf{q}) = (g\mu_B)^2 \frac{S}{2} \sum_{l_3,l_4} \Lambda_1(\mathbf{q}|l_1,l_2,l_3,l_4) \left\{ \frac{\sum\limits_{n} \left[S^{\star}_{n,l_3}(0) + \tau S^{\star}_{n+N,l_3}(0) \right]}{\omega_p - \omega_{l_3}(0) + i\eta_{l_3}(0)} \right\}$$

$$\times \left\{ \frac{\sum_n \left[S^{\star}_{n,l_4}(0) + \tau S^{\star}_{n+N,l_4}(0) \right]}{\omega_p - \omega_{l_4}(0) + i\eta_{l_4}(0)} \right\}, \tag{7.29}$$

with $\tau = 1$, while $T_{l_1,l_2}(\mathbf{q})$ is obtained by taking $\tau = -1$. The solution of the eigenvalue equation can again be carried out numerically, but it is now more complicated in practical terms because of the multiple summations over SW branch labels.

7.2 Special cases

Before proceeding to numerical examples in the following sections we consider some special cases where the previous general formalism simplifies to provide analytic expressions for the instability thresholds, depending on N.

We start with the first-order Suhl effect, taking $N = 1$ which means a single line of spins in the nanowire case and a monolayer of spins in the film case. The $N = 1$ nanowire represents a trivial case, since the three-magnon interactions vanish by symmetry for a longitudinal applied field, and so there is no first-order Suhl instability. For the $N = 1$ film, however, it is easily shown that the two eigenvalues correspond to

$$\beta(\mathbf{q}) = -\eta_1(\mathbf{q}) \pm \left[\left| h_x P_{1,1}(\mathbf{q}) \right|^2 - \{\Delta\omega_1(\mathbf{q})\}^2 \right]^{1/2}, \tag{7.30}$$

when the pumping field is along the x direction, i.e., in the plane of the film. As mentioned, the SW instability occurs when $\mathrm{Re}[\beta(\mathbf{q})] > 0$ for one of these eigenvalues (specifically the one with the upper sign), leading to a threshold pumping-field amplitudes h_x^c given by

$$h_x^c = \frac{\left[\eta_1^2(\mathbf{q}) + (\Delta\omega_1(\mathbf{q}))^2 \right]^{1/2}}{\left| P_{1,1}(\mathbf{q}) \right|}. \tag{7.31}$$

There is an analogous expression for h_y^c, but with $P_{1,1}(\mathbf{q})$ replaced by $Q_{1,1}(\mathbf{q})$, that applies when the pumping field is along the y direction, perpendicular to the plane of the film. Thus we conclude that $h_x^c \neq h_y^c$ and the explicit calculations lead to

$$\frac{h_y^c}{h_x^c} = \left|\frac{P_{1,1}(\mathbf{q})}{Q_{1,1}(\mathbf{q})}\right| = \frac{s_0 + t_0}{s_0 - t_0} > 1\,. \tag{7.32}$$

Here s_0 and t_0 are factors arising in the Bogoliubov transformation to diagonalize the uniform mode (zero wave vector) magnons when $N = 1$; explicitly at general wave vector $\mathbf{q}$ we may write $s_\mathbf{q} = \cosh\theta_\mathbf{q}$ and $t_\mathbf{q} = \sinh\theta_\mathbf{q}$ where

$$\tanh(2\theta_\mathbf{q}) = \frac{-1/2 g^2\mu_B^2[D^{xx}(\mathbf{q}) - D^{yy}(\mathbf{q})]}{g\mu_B H_0 + 2SJ[2 - \cos(q_x a) - \cos(q_z a)] - 1/2 g^2\mu_B^2[2D^{zz}(0) + D^{zz}(\mathbf{q})]}\,. \tag{7.33}$$

We note also that the factor $V_1(\mathbf{q}|1,1,1)$, which enters into the expressions for $P_{1,1}(\mathbf{q})$ and $Q_{1,1}(\mathbf{q})$ through Eqs. (7.18) and (7.19), simplifies in this case to $A^{(3)}(\mathbf{q})(s_\mathbf{q} + t_\mathbf{q})(s_0 s_\mathbf{q} + t_0 t_\mathbf{q})$ and so replaces Eq. (C.1).

The simplest non-trivial case for the first-order Suhl instability in a nanowire stripe occurs when $N = 2$, corresponding to two coupled lines of spins. In this case $P_{i,j}(\mathbf{q})$ is approximately pure imaginary (for small SW damping), and assuming further that $\eta_1(\mathbf{q}) = \eta_2(\mathbf{q}) \equiv \eta(\mathbf{q})$ for the two SW branches we find

$$h_x^c = \sqrt{\frac{\left(\Delta\omega_1^2 + \eta^2\right)\left(\Delta\omega_2^2 + \eta^2\right)}{\eta^2\left(P''^2_{1,1} + P''^2_{2,2}\right) + \left(P''_{1,1}\Delta\omega_2 + P''_{2,2}\Delta\omega_1\right)^2}}\,,$$

$$h_y^c = \sqrt{\frac{\left(\Delta\omega_1^2 + \eta^2\right)\left(\Delta\omega_2^2 + \eta^2\right)}{\eta^2\left(Q''^2_{1,1} + Q''^2_{2,2}\right) + \left(Q''_{1,1}\Delta\omega_2 + Q''_{2,2}\Delta\omega_1\right)^2}}\,. \tag{7.34}$$

We will see from later numerical examples that the ratio of the above threshold fields is typically very close to unity (because of the small splitting in frequency between the two SW branches), unlike the h_y^c/h_x^c ratio in the case of a monolayer film.

For the second-order Suhl instability there is significant simplification of the general expressions only when $N = 1$, corresponding to a single line of spins or a monotonic film in our two geometries. The expressions for the threshold fields for the two directions of perpendicular pump-

ing are formally similar to those in the first-order Suhl case, and we find

$$h_x^c = \frac{\left[\eta_1^2(\mathbf{q}) + (\Delta\omega_1(\mathbf{q}))^2\right]^{1/4}}{\left|R_{1,1}(\mathbf{q})\right|^{1/2}}\,, \tag{7.35}$$

$$h_y^c = \frac{\left[\eta_1^2(\mathbf{q}) + (\Delta\omega_1(\mathbf{q}))^2\right]^{1/4}}{\left|T_{1,1}(\mathbf{q})\right|^{1/2}}\,. \tag{7.36}$$

The relevant expressions for $R_{1,1}(\mathbf{q})$ and $T_{1,1}(\mathbf{q})$ can be deduced using Eq. (7.29), and leads to

$$h_x^c = h_y^c = \frac{\left[\eta_1^2(\mathbf{q}) + (\Delta\omega_1(\mathbf{q}))^2\right]^{1/4}\left[\eta_1^2(0) + (\omega_p - \omega_1(0))^2\right]^{1/2}}{g\mu_B\,|S\,\Lambda_1(\mathbf{q}, -\mathbf{q}, 0|1, 1, 1, 1)/2|^{1/2}} \tag{7.37}$$

in the case of the $N = 1$ wire, for which Λ_1 reduces to $[A^{(4)}(\mathbf{q}) + A^{(4)}(0) + B^{(4)}(\mathbf{q})]$. The threshold-field results for a $N = 1$ film are slightly more complicated: expressions having the same form as in Eq. (7.37) still apply, but with $|\Lambda_1|^{1/2}$ being replaced by $(s_0 + t_0)|\Lambda_1|^{1/2}$ for h_x^c and by $(s_0 - t_0)|\Lambda_1|^{1/2}$ for h_y^c and with Λ_1 being evaluated using Eq. (C.3).

7.3 Numerical results for the first-order Suhl instability

In this section we will apply the above theory to study the first-order Suhl instability for some nanowires and ultrathin films. In particular, numerical calculations are presented for Permalloy and YIG, as examples of materials with strong exchange, and for EuS, as a material having weaker exchange and hence an added role for dipole-dipole interactions. The relevant magnetic parameters for these materials have already been discussed in Chapter 4 (for Permalloy) and in our work on parallel pumping [58, 87] (see also Chapter 3 and 5). We also require the damping η, which in principle may depend on $\mathbf{q}$ and branch l. Again we use a simplification, as in most previous calculations, of adopting a constant value. Permalloy is known to have a small damping, typically $\sim$ 0.01 GHz, which corresponds to $\Delta H \sim 3.4$ Oe for the equivalent resonance half-linewidth $\eta/g\mu_B$. On the other hand, YIG is known to have an even smaller damping, namely $\sim$ 0.001 GHz or $\Delta H \sim 0.3$ Oe. For EuS we assume the value $\eta = 0.1$ GHz.

Taking the perpendicular microwave pumping to be either along the x axis or along the y axis, we give examples for the dispersion relations and instability thresholds of SWs in different nanostructures and materials. Typically, we consider nanowires with different cross-sectional aspect ratio $p = n_x/n_y \geqslant 1$ and total number of spins $N = n_x n_y$ and complete films with N being the number of atomic layers. As mentioned, the SWs in a nanowire depend on 1D wave vector $\mathbf{q} = (q_z)$ and hence the dispersion relations consist of distinct branches, while the SWs in a film are characterized by an in-plane 2D wave vector $\mathbf{q} = (q_x, q_z)$. In the latter case the SW modes depend on an amplitude $q = |\mathbf{q}|$ and an in-plane propagation angle $\phi = \arctan(q_x/q_z)$ as in Fig. 7.1, and the spectrum consists of bands that may overlap at sufficiently large N. We start with the applications to nanowires and then films for the intermediate exchange case (with EuS) before proceeding to the strong exchange materials (with Permalloy and YIG).

7.3.1 Intermediate exchange case

Starting with EuS, where the exchange and dipole-dipole effects are comparable for the long-wavelength SW dynamics, we consider a nanowire with $n_x = n_y = 2$ ($N = 4$). In Fig. 7.2(a) the frequencies of the SW branches of the EuS nanowire are shown, plotted as a function of 1D wave vector q. There are four SW modes, but two of them (corresponding to the line labeled 2) are essentially degenerate in this case since $n_x = n_y$. The monotonic increase of all curves with increasing q signifies that the dynamics is dominated by exchange in such a small structure. These results were obtained using Eqs. (7.2)-(7.4), along with a numerical evaluation of the dipole-dipole sums. The dependence of the SW frequencies on the longitudinal applied field is rather straightforward (see, e.g., Fig. 7.2(b) for the lowest SW branch). Next the corresponding SW instability threshold, calculated as a function of applied field is shown in Fig. 7.2 (c) where a perpendicular pumping frequency $\omega_p/2\pi = 47$ GHz is considered. We note that in this example of a nanowire with a square cross section, we have $h_x^c = h_y^c$ by symmetry. The figure for the threshold field has the form of a typical "butterfly curve", showing just one main feature, the cusp at 0.034 T, which can be identified with the field value at which a horizontal line (labeled P) drawn at one-half

of the pumping frequency coincides with the lowest SW frequency (at $q \approx 0$ on the first branch) in Fig. 7.2(a). When the applied field exceeds this characteristic value, the horizontal line lies below the SW branches and the instability threshold rapidly rises.

If we were to increase n_x in the above example (keeping n_y fixed) to form a wider stripe, we would find two main effects: (i) the number of SW branches increases and they begin to cluster to form bands, and (ii) some of the branches develop a pronounced dip at small q due to the long-range dipolar effects in the larger sample (see, e.g., discussion in [53]). The limit where n_x has become very large corresponds to a film geometry, which we discuss next. Some results for the SW dispersion relations of EuS films, with frequency plotted versus qa with $q = |\mathbf{q}|$, are given in Fig. 7.3 for two different thicknesses. First, in Fig. 7.3(a) for $N = 5$, the lowest two SW bands are shown by the shaded regions. Bands occur because the propagation angle ϕ, denoting the polar angle between wave vector $\mathbf{q}$ and z axis (see Fig. 7.1), may vary. The lower boundary of each band corresponds to $\phi = 0$ and the upper boundary to $\phi = \pm\pi/2$, giving a behavior that is in contrast to the case of a nanowire where the 1D wave vector results in discrete SW curves. When N is increased sufficiently, as in Fig. 7.3(b) for EuS with $N = 15$, the bands have moved close enough together to start overlapping. We note that for $qa \approx 0$, where exchange effects are negligible for the dynamics, the SW frequency of the lowest branch is close (within 1% typically) to the value $g\mu_B \{H_0 (H_0 + 4\pi M_s)\}^{1/2}$, representing the Damon-Eshbach (DE) mode frequency [36] for a continuous film at zero wave vector.

Next we discuss the first-order Suhl calculations for the threshold field h^c under perpendicular pumping for these same EuS films, taking the pumping field frequency $\omega_p/2\pi = 18$ GHz. For the thinner film with $N = 5$ (not shown) it is found that the curves for h_x^c and h_y^c are similar to the behavior in Fig. 7.2(b) in having a relatively flat form below a cusp (at $\mu_0 H_0 = 0.06$ T in the present case) above which there is a sharp increase. The main difference here is that h_x^c and h_y^c are significantly different in magnitude, as might be expected by extension of the discussion in Section 7.2 for the special case of a $N = 1$ film. For example, when $N = 5$ our numerical calculations indicate that the h_y^c/h_x^c ratio is approximately 7.1 if $\mu_0 H_0 = 0.03$ T. This compares with $h_y^c/h_x^c \simeq 9.3$

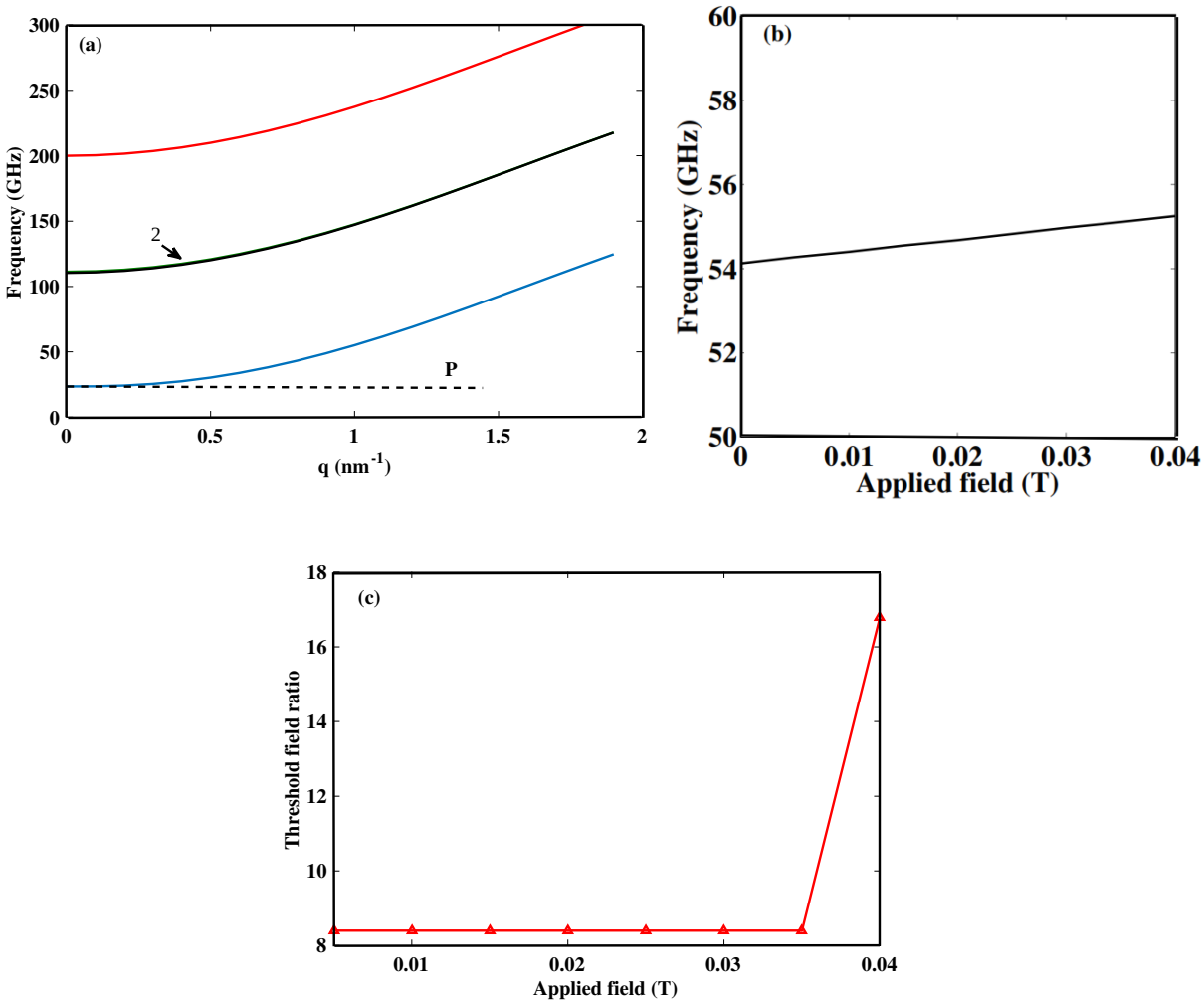

Figure 7.2: First-order Suhl effect for a 2×2 EuS nanowire ($N = 4$): (a) SW frequencies of the four lowest modes plotted versus longitudinal wave vector q when the longitudinal applied field is 0.034 T. The horizontal line P indicates one-half of the pumping frequency. (b) SW frequencies of the lowest branch plotted versus applied field at fixed wave vector $q = 1$ nm^{-1}. (c) Threshold field ratio $h^c/\Delta H$ as a function of the applied magnetic field. Perpendicular pumping along either the x or y direction at frequency $\omega_p/2\pi =$ 47 GHz is considered with damping $\eta = 0.1$ GHz. The triangle symbols indicate the calculated points and the connecting lines are a guide to the eye. See text for further discussion.

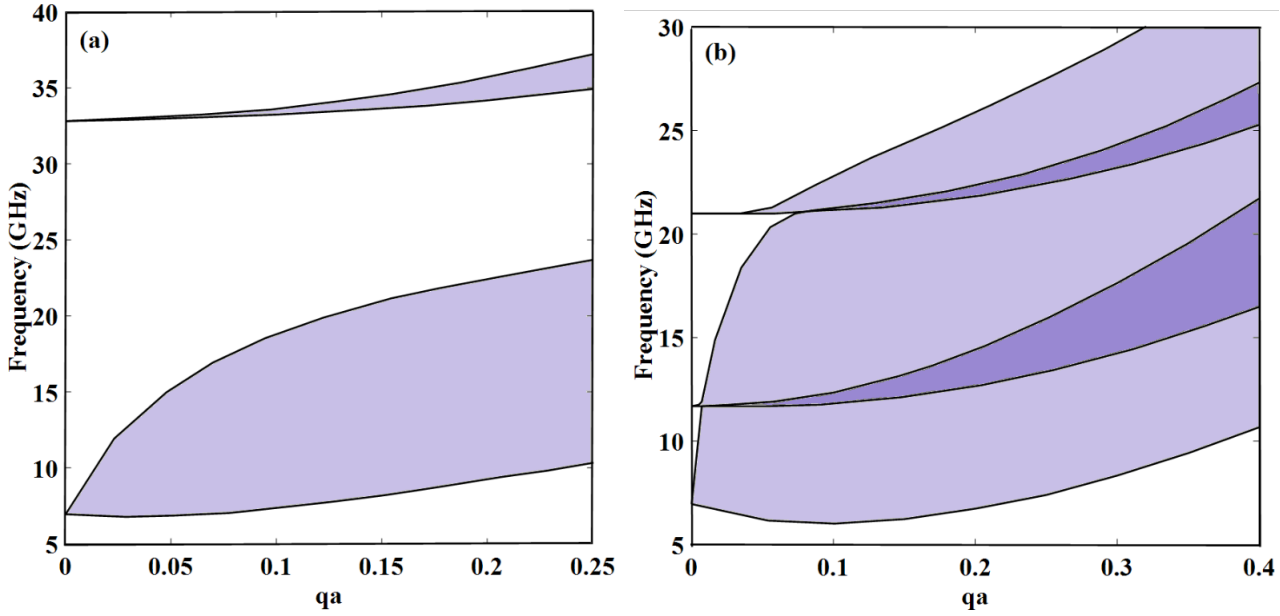

Figure 7.3: SW dispersion relations, showing frequency versus qa for EuS films with (a) $N = 5$ and (b) $N = 15$ atomic layers. The applied magnetic field is 0.04 T in both cases. The shading indicates the region corresponding to the SW bands, with the darker shading in (b) corresponding to regions of overlap.

as predicted for a monolayer $N = 1$ film according to Eq. (7.32). The general trend found, as N is increased from a small value, is that h_y^c/h_x^c reduces slightly in value. Thus, when $N = 15$ we find $h_y^c/h_x^c \simeq 5.5$ for $\mu_0 H_0 = 0.03$ T. The plots for the threshold field ratios versus H_0 for the $N = 15$ EuS film are presented in Fig. 7.4. They exhibit the characteristic cusp at a field value of 0.06 T, but below this value the curves begin to show other features (i.e., a weak peak at around 0.05 T), rather than being essentially flat. This modified behavior can be attributed to density-of-states effects related to the fact that there is now a degree of overlap between the SW bands, as seen in Fig. 7.3(b). Another difference is that the initial dip in the SW dispersion curve for the lowest branch at small wave vector, which was mentioned earlier, has now become more pronounced. We note the property that $h_y^c/h_x^c > 1$ will persist even for macroscopically thick films (see [66, 72]), since the SW precession in the xy plane is still elliptical.

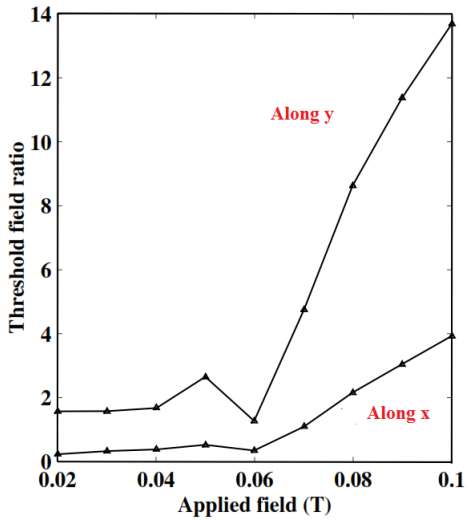

Figure 7.4: First-order Suhl threshold field ratio, $h^c/\Delta H$, as a function of the applied magnetic field for the same EuS film with $N = 15$ as in Fig. 7.3(b). Perpendicular pumping at frequency $\omega_p/2\pi = 18$ GHz is considered with damping $\eta = 0.04$ GHz. The two curves refer to the two different orientations of the pumping field along the x axis and along the y axis. The triangle symbols indicate the calculated points and the connecting lines are a guide to the eye.

7.3.2 Strong-exchange case

We now present calculations for Permalloy and YIG nanostructures, which represent materials with strong exchange effects relative to the dipole-dipole effects for the SW dynamics. In both cases we may model the structures using an effective lattice constant a, defining cubic cells with an effective spin. A necessary validity criterion is that a must be chosen to be smaller than, or comparable with the exchange correlation length of the material (e.g., see previous linear SW calculations [53]). We start by considering a Permalloy nanowire with $n_x = 5$ and $n_y = 1$ (so $N = 5$), taking an effective lattice parameter $a = 5$ nm. Thus the rectangular cross section of the modeled nanowire is 25 nm by 5 nm, with aspect ratio $p = 5$. In Fig. 7.5(a) the lowest few SW frequencies of this structure are plotted versus 1D wave vector q for a fixed applied field of 0.042 T. In this case the initial dip is inperceptibly small, so all the SW frequencies increases with q since the exchange effects dominate over the dipolar contributions to the SW frequency.

Next, in Fig. 7.5(b) we show the calculated threshold fields h_x^c and h_y^c (as before, expressed as a ratio to the resonance half width ΔH) plotted versus applied field. This is done for the same

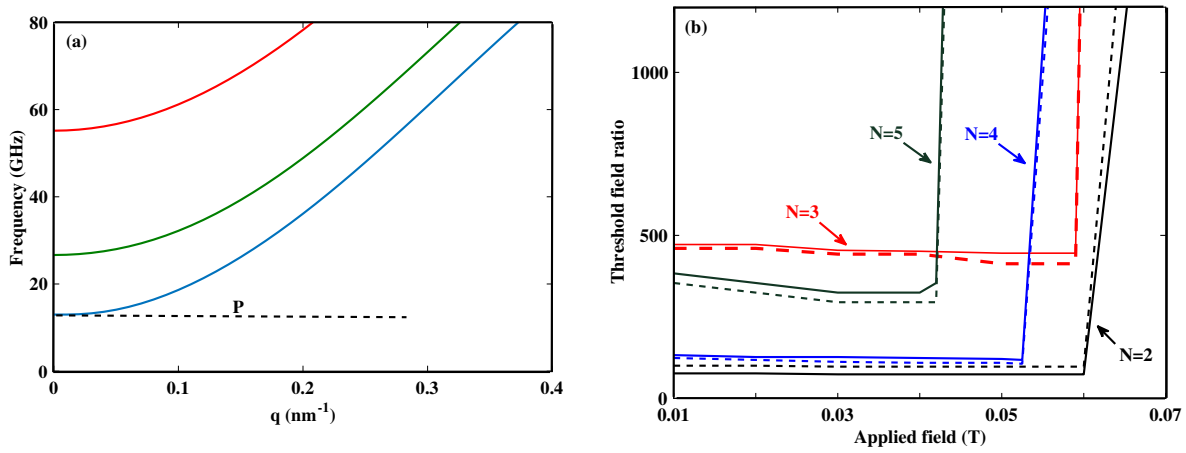

Figure 7.5: Calculations for Permalloy nanowire stripes with $N = n_x \times n_y$. (a) SW frequencies plotted versus longitudinal wave vector q for the lowest few branches of a Permalloy $N = 5 \times 1$ nanowire, corresponding to cross section 25 nm $\times$ 5 nm for longitudinal field 0.042 T. The horizontal line P indicates one-half of the pumping frequency. (b) First-order Suhl threshold field ratios, in term of $h^c/\Delta H$, as a function of the applied magnetic field for nanowires with $N = 2$, 3, 4, and 5 lines of spins. Pumping frequencies $\omega_p/2\pi = 32$, 30, 28 and 26 GHz, respectively, are considered with damping $\eta = 0.01$ GHz for pumping along the x axis (dashed lines) and y axis (solid lines).

Permalloy nanostripe as above with cross section 25 nm $\times$5 nm , as well as for several other nanostripes with different aspect ratios corresponding to sizes 10 nm $\times$5 nm ($N = 2$), 15 nm $\times$5 nm ($N = 3$), and 20 nm $\times$5 nm ($N = 4$). The results with perpendicular pumping field along the x-axis (dashed lines) and along the y-axis (solid lines) are shown. In the plots we note that the ratios h_y^c/h_x^c for the two perpendicular directions are all close to unity for these narrow stripes. This is in accordance with the discussion in Section 7.2 for nanowire stripes with $N = 2$, but the behavior contrasts with the situation for wide magnetic stripes (where $N \gg 1$), which approximate to thin films, due to the cumulative effects of the long-range dipolar interactions. From the figure we may note a symmetry-related property at small N that the magnitudes of the threshold field ratios for odd and even N are significantly different (by a factor of ~ 3 for the cases considered). Each of the curves in Fig. 7.5(b) has the one main cusp feature that corresponds to the one-half pumping frequency line coinciding with the $q = 0$ frequency of the first SW branch. For example, for the nanoribbon with cross sections 25 nm $\times$5 nm the cusp is at $\mu_0 H_0 = 0.042$ T, which correspond to the field value for the one-half pumping frequency to be coincident with the $q = 0$ frequency of the

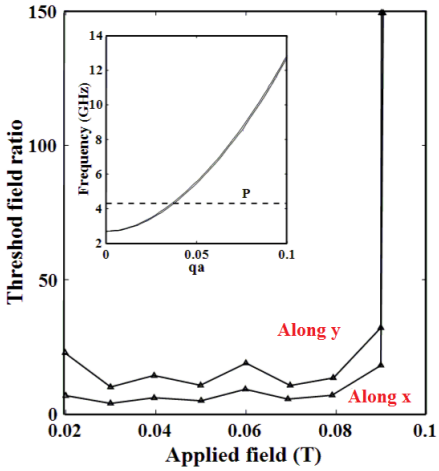

Figure 7.6: The inset shows the narrow band of SW frequencies plotted versus qa for a YIG films with $N = 1$ and applied magnetic field 0.04 T. The horizontal dashed line is at one half of the pumping frequency considered. The main panel shows the first-order Suhl thresholds as a function of the applied magnetic field. Perpendicular pumping at $\omega_p/2\pi = 9$ GHz is considered with damping $\eta = 0.001$ GHz. The two curves refer to two different orientations of the pumping field along the x or y axis. The triangle symbols indicate the calculated points and the connecting lines are a guide to the eye.

lowest SW branch in Fig. 7.5(a).

Next we consider films, showing in the inset to Fig. 7.6 the SW dispersion relation for a one-layer ($N = 1$) YIG film taking the applied field as 0.04 T. There is just one SW band, which is very narrow (because of the dominant exchange) compared to those discussed for EuS films. It is seen that the DE mode frequency at zero wave vector, $g\mu_B \{H_0 (H_0 + 4\pi M_s)\}^{1/2} = 2.6$ GHz, still predicts very well the $q = 0$ value in the figure. In the main panel of Fig. 7.6 we present calculations for the first-order Suhl thresholds plotted versus applied magnetic field for this YIG film when the pumping field frequency $\omega_p/2\pi = 9$ GHz. Again results are shown for the cases when the microwave pumping field is along the x- and y-directions. The variations for applied field values less than about 0.09 T are mainly attributable to SW density-of-state effects. The threshold field ratio strongly depends on the direction of the microwave pumping field with $h_y^c/h_x^c > 1$ in accordance with the prediction from Eq. (7.32). When we consider thicker YIG films, there are multiple SW bands. For large enough N these eventually overlap as in the EuS case, giving a qualitatively similar behavior. However, the overlap does not occur in YIG until $N \sim 100$ due to the relatively strong exchange in this material.

7.4 Numerical results for the second-order Suhl instability

In this section we briefly describe some results for the second-order Suhl instability in the two geometries under consideration, again taking the pumping field to be along either the x- or y-axis. For simplicity, however, and because the numerical calculations are so intensive, we focus just on a single line of spins in a nanowire and one atomic layer in a film (i.e., we have $N = 1$ in both cases). As in the previous section we start with applications for the weaker-exchange case (EuS) and then proceed to strong-exchange materials (Permalloy and YIG).

First, for a EuS $N = 1$ nanowire we show in Fig. 7.7(a) the second-order Suhl calculations for the threshold field h^c versus applied field for the nanowire, taking a pumping frequency $\omega_p/2\pi = 52$ GHz. The curve has a moderately flat region below the cusp field at 0.068 T, whereas above this field the decay instability (which is now dominated by the formation of a SW pair with $\omega_l(q) \approx \omega_p$) has a sharply increasing threshold, as in the first-order Suhl case. By symmetry, the results are independent of the orientation of the perpendicular pumping field. Next, Fig. 7.7(b) shows the dependence of the calculated threshold field on the applied magnetic field for a $N = 1$ EuS film under perpendicular pumping. Since the SW dispersion spectrum now consists of a band, rather than a discrete line as for the $N = 1$ nanowire, and the frequency at small q is lower, we consider a smaller value for the pumping frequency $\omega_p/2\pi = 9.0$ GHz. In this plot we have also shown the ratio h_y^c/h_x^c which decreases with increasing applied field value in accordance with results in Section 7.2.

Next we present second-order Suhl calculations for Permalloy and YIG structures. In Fig. 7.8 we illustrate results for the threshold field h^c as a function of applied field for Permalloy (red line) and YIG (blue line) nanowires with one line of spins $N = 1$. By symmetry, the curves are independent of the two directions of perpendicular pumping. For Permalloy we have taken the pumping-field frequency $\omega_p/2\pi = 12$ GHz and damping $\eta = 0.001$ GHz, while the corresponding values for YIG are $\omega_p/2\pi = 34$ GHz and $\eta = 0.01$ GHz. The curve for Permalloy shows one feature at 0.057 T which corresponds to the pumping frequency coinciding with the $q = 0$ frequency for the first SW branches in the corresponding dispersion plot. For YIG nanowire the curve has a

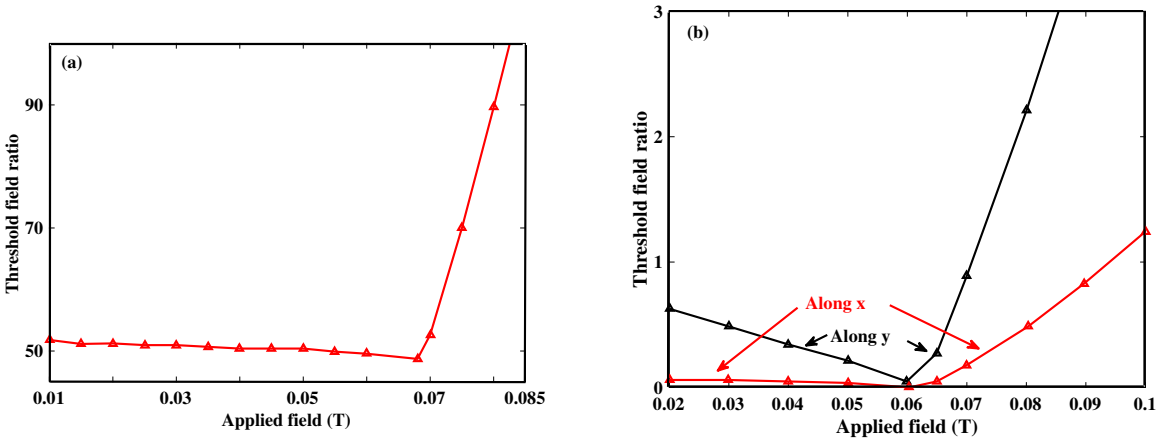

Figure 7.7: Second-order Suhl thresholds, $h^c/\Delta H$, as a function of the applied field for EuS nanostructures. (a) a $N = 1$ nanowire under perpendicular pumping at frequency $\omega_p/2\pi = 52$ GHz. (b) a $N = 1$ film under perpendicular pumping at frequency $\omega_p/2\pi = 9.0$ GHz. In the latter case the two curves refer to orientations of the pumping field along the x axis and along the y axis. The triangle symbols indicate the calculated points and the connecting lines are a guide to the eye.

similar overall form to that for Permalloy nanowire and shows one feature at 0.113 T.

Finally we present analogous calculations for one atomic layer ($N = 1$) films, taking the case of YIG. The result for the second-order Suhl threshold behavior is shown if Fig. 7.9 taking pumping at frequency $\omega_p/2\pi = 4.50$ GHz. The two curves represent the instability threshold for the film when the pumping field is along x (parallel to the film surface) and y (perpendicular to the film surface). We note that the h_x^c and h_y^c values are different, as expected, with $h_y^c > h_x^c$. Qualitatively similar results apply for Permalloy films.

7.5 Conclusions

In conclusion, we have developed a microscopic (or Hamiltonian-based) theory to study SW instability thresholds of ferromagnetic nanowires (or stripes) with rectangular cross sections as well as the wide-stripe limit of ultrathin films. The microwave pumping field is applied perpendicular to the longitudinal external magnetic field in either one of the (usually non-equivalent) transverse directions x and y. This generalizes our previous calculations for parallel (z-directed) pumping [87, 58]. It represents, however, a quite distinct case, since the two processes of first- and second-

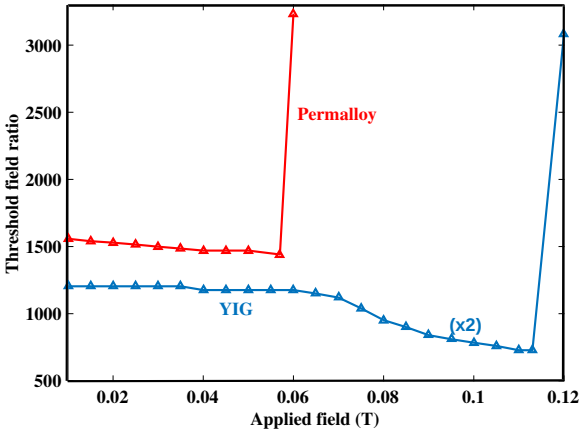

Figure 7.8: Second-order Suhl threshold $h^c/\Delta H$ as a function of the applied field H_0 for a $N = 1$ Permalloy and YIG wires under perpendicular pumping at frequency $\omega_p/2\pi = 34$ and 12 GHz respectively. The triangle symbols indicate the calculated points and the connecting lines are a guide to the eye.

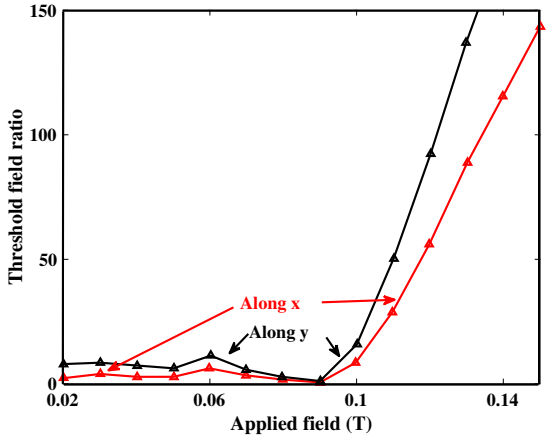

Figure 7.9: Second-order Suhl threshold $h^c/\Delta H$ as a function of the applied field for a $N = 1$ YIG film under perpendicular pumping at frequency $\omega_p/2\pi = 4.5$ GHz. The two curves refer to two different orientations of the pumping field along the x axis and the y axis. The triangle symbols indicate the calculated points and the connecting lines are a guide to the eye.

order Suhl instabilities are related to the three- and four-magnon nonlinear effects, respectively, in the stripes and ultrathin films. In most of previous work on SW instabilities a macroscopic theory has been used. However in finite samples, as in nanowires and ultrathin films with thickness or lateral dimensions less than $\sim$ 100 nm the quantization of the SW modes becomes modified. As a consequence a microscopic dipole-exchange theory is applied.

Both the first-order Suhl and the second-order Suhl configurations were considered and the results for both structures have been interpreted in terms of the SW modes. Due to the differing symmetries in these two structures, the SW modes present different quantization. The results depend sensitively on the dipolar-to-exchange ratio. This behavior was illustrated taking parameters for Permalloy and YIG (in the strong-exchange case) and EuS (in the weaker-exchange case) with different values of width and thickness in the two structures.

It would be of interest to modify the microscopic theory here to apply to SW instabilities in other related nanowire structures, such as arrays of long ferromagnetic nanocylinders or nanotubes, which are known from Brillouin light scattering experiments to have quite different linear SW spectra (see, e.g., [78, 93, 110]) from those considered here.

Chapter 8

Quantum statistics and squeezing for a microwave-driven interacting magnon system

The material in this chapter has been published as an article by me (with M. G. Cottam) listed as Ref. [111].

Since the pioneering work of Suhl and others [41, 39, 42] on the nonlinear magnetization dynamics of ferromagnetic materials, it is known that the SWs or magnons can be excited using a microwave field applied either parallel or perpendicular to the static field as discussed in earlier chapters. From the theoretical point of view, both semi-classical and quantum mechanical approaches have been utilized (for reviews, see [25, 27] and Chapter 1). The semi-classical approach is based on the magnetization torque equation of motion, whereas in the quantum-mechanical method bosonic techniques, such as those based on the Holstein-Primakoff transformation [31], are usually employed for describing the excitations of the system.

Specifically, information about the quantum-statistical properties of the SWs may be obtained by employing the representation of a coherent magnon state. Rezende and Zagury [112, 113] proposed the concept of coherent magnon states by analogy with the coherent photon state [114] in

order to obtain a correspondence between the classical and quantum-mechanical descriptions of SWs. The coherent magnon state $|\alpha_k\rangle$ can be defined as the eigenstate of the annihilation operator $c_k |\alpha_k\rangle = \alpha_k |\alpha_k\rangle$, where k is a wave-vector label and $\alpha_k = |\alpha_k| e^{i\eta}$ is a complex number which characterizes the state with η representing the phase of the coherent state. The coherent state $|\alpha_k\rangle$ can be expanded in terms of the eigenstates $|n_k\rangle$ of the unperturbed (free-magnon) Hamiltonian and has the expectation value $\langle n_k\rangle = \langle\alpha_k| n_k |\alpha_k\rangle = |\alpha_k|^2$ for the number operator $n_k = c_k^\dagger c_k$. Using the coherent magnon state representation, Rezende [102, 115, 61] studied coherent properties of the magnons in a Bose-Einstein condensation (BEC), which was observed by Demokritov *et al*. [59, 116, 117, 118, 60]. Several other works have reported on the coherence properties of parallel pumped magnons with the three-magnon [119] and four-magnon processes [120, 112] included. In quantum optics the link between coherent states and BEC (involving use of techniques such as laser cooling and laser trapping) is well established experimentally (see, e.g., [121]). Likewise Rezende's analysis of the magnon BEC experiments relies crucially on the development of quantum coherence in interacting magnon systems driven far from equilibrium by parallel pumping. This connection is emphasized in several of the references cited above and also in a recent detailed review by Rezende [122] and an article by Demokritov *et al*. [123].

Quantum squeezing [124] is a non-classical effect that refers to reducing the quantum noise of a system at certain phases to below the vacuum state value. For photons the squeezing provides a way to overcome the standard quantum limit of noise for experimental measurements. Therefore generating squeezed light has been a topic of growing interest due to the potential applications in optical interferometry and light communication networks [125]. Squeezed states were observed for the first time in 1985 for photons [126]. Soon afterwards, squeezed states in a variety of non-quantum-optics systems including molecules [127], phonons [128] , and polaritons [129], as well as in spin systems [130, 131], were realized.

The first reported experimental demonstration of magnon squeezing was in the antiferromagnetic insulators MnF_2 and FeF_2 by Zhao *et al*. [132, 133]. A theory for magnon squeezing in antiferromagnets was presented by Peng [134] on the basis of there being two sublattices of spins

on which the magnons may propagate. For ferromagnets a different process is required. In particular, Peng [135] and Wang *et al*. [136] proposed mechanisms depending on crystal-field anisotropy effects and four-magnon interactions, respectively. The generation of spin squeezed states of magnetic systems may have applications in spintronics and quantum computing.

In the present chapter, motivated by the above-mentioned studies, the non-classical properties of magnons such as the squeezing effect are studied using the coherent magnon state representation. While our emphasis is on novel effects of the parallel pumping on the ferromagnetic magnons, we also consider inclusion of the nonlinear four-magnon interactions between the magnons in our model Hamiltonian. Remarkably, we find that the nonlinearity introduced by the parallel pumping is sufficient on its own to produce squeezing effects and a super-Poissonian distribution for the magnons. It is shown that these effects can be augmented via the four-magnon interactions.

The chapter is organized as follows. In Section 8.1 we describe the theoretical model for the parallel-pumped interacting magnon system. First, for a free-magnon system, the average number $\langle n_k \rangle$ of magnons for mode k is obtained using the coherent magnon state representation. Then the possibility of controlling the collapse-and-revival phenomena for $\langle n_k \rangle$ through the pumping field is discussed in Section 8.2. The dependence of the quadrature squeezing of the magnons on the pumping field is studied in Section 8.3. Next, in Section 8.4 the possibility of generating a super-Poissonian distribution of magnons is investigated. In Section 8.5 we generalize the calculations to include the nonlinear four-magnon interactions in the model Hamiltonian. We investigate the effects of this interaction on the occupation magnon number, the squeezed magnon state and the statistical properties of the magnons. The likelihood of a super-Poissonian distribution for the magnons is discussed and we show that the four-magnon interactions enhance the super-Poissonian distributions for the pumped magnons. Finally, Section 8.6 contains the conclusions.

8.1 Theoretical formalism for parallel pumping

The SWs (or magnons) can be nonlinearly generated in a ferromagnet by means of an intense microwave pumping field. Here we consider the case of parallel pumping, where there is a direct coupling arising between magnon pairs and the pumping field. In an insulating ferromagnet a SW with wave vector k involves spins precessing with angular frequency ω_k about the equilibrium direction of magnetization. The ferromagnet is in an external magnetic field and the system is pumped by a microwave field h_p which is applied parallel to this static field. With the Holstein-Primakoff transformation [31] the interacting magnons can be treated within the second-quantization formalism using boson operators $c_k^\dagger$ and c_k that describe magnon creation and annihilation, respectively. This is analogous to what was done in an earlier chapter. The total Hamiltonian of the system, which includes exchange, dipole-dipole and Zeeman interactions, can be written as the sum of three parts as $H = H_0 + H_p + H_4$, where,

$$H_0 = \sum_k \omega_k c_k^\dagger c_k, \tag{8.1}$$

is the Hamiltonian for a system of non-interacting dipole-exchange magnons with frequencies given by ω_k. Next

$$H_p = \sum_k \frac{1}{2}\left(h_p \rho_k e^{-i\omega_p t} c_k^\dagger c_{-k}^\dagger + \text{h.c.}\right) \tag{8.2}$$

describes the interaction with the microwave field, where $\rho_k = \omega_M \sin^2\theta_k \exp(-2i\phi_k)/4\omega_k$ represents the usual coupling [22] of the pumping field amplitude h_p (at angular frequency ω_p) in a bulk material with the k and $-k$ magnons (each having $\omega_k \simeq \omega_p/2$). Also $\omega_M = 4\pi\mu_0 g\mu_B M_s$, where M_s is the saturation magnetization, θ_k is the polar angle between k and H, and ϕ_k is the azimuthal angle of k. Finally, H_4 is the four-magnon interaction term (quartic in the boson operators), which we will discuss in Section 8.5.

In order to obtain information about the statistical properties of the magnons (initially in the absence of H_4) we may work in the quantum-mechanical interaction picture [137]. The interaction Hamiltonian is given by

$$H_p^{int}(t) = e^{iH_0 t} H_p(t) e^{-iH_0 t}. \tag{8.3}$$

Here the superscript *int* is used to denote the interaction picture. The above equation can be expanded by using the Bakker-Hansdorff theorem (see, e.g., [137]):

$$e^{iH_0 t} H_p(t) e^{-iH_0 t} = H_p(t) + it\left[H_0, H_p(t)\right] + \frac{1}{2!}(it)^2\left[H_0, \left[H_0, H_p(t)\right]\right] + \cdots, \tag{8.4}$$

Using Eqs. (8.1) and (8.2) this leads explicitly to

$$H_p^{int}(t) = -e^{-i\omega_p t}\sum_k \frac{1}{2}\left(h_p \rho_k e^{2i\omega_k t} c_k(0)^\dagger c_{-k}(0)^\dagger + \text{h.c.}\right). \tag{8.5}$$

Then for calculating the state of the pumped system at any later time t (after the initial $t = 0$) the time evolution operator, which is formally defined by (see, e.g., [137]):

$$U^{int}(t) = \exp\left[-itH_p^{int}(t)\right], \tag{8.6}$$

can be used. At the usual resonance condition with $\omega_p = 2\omega_k$, as mentioned earlier for the parametric process, this leads to

$$U^{int}(t) = \exp\left[\sum_k \frac{it}{2}\left(h_p \rho_k c_k(0)^\dagger c_{-k}(0)^\dagger + \text{h.c.}\right)\right]. \tag{8.7}$$

It is now convenient to decouple the k and $-k$ modes by introducing two new operators (following [138, 120]) at time $t = 0$ by

$$a_k(0) = \frac{1}{\sqrt{2}} e^{-i\varphi_k}\left[c_k(0) + c_{-k}(0)\right], \quad b_k(0) = \frac{1}{\sqrt{2}} e^{-i\varphi_k}\left[c_k(0) - c_{-k}(0)\right], \tag{8.8}$$

where $\varphi_k = \pi/4 + \phi_k$. The inverse transformation giving $c_k(0)$ and $c_{-k}(0)$ in terms of $a_k(0)$ and $b_k(0)$ can also be straightforwardly written down. The operators $a_k(0)$ and $b_k(0)$, together with their conjugates, individually satisfy the usual boson commutation relation, whereas they also commute with one another. On substituting Eq. (8.8) into the above equation, the time evolution operator

can be obtained in a more useful form as

$$U^{int}(t) = \exp\left[\sum_k \frac{h_p t}{4} |\rho_k| \left(a_k^\dagger(0)a_k^\dagger(0) - a_k(0)a_k(0) - b_k^\dagger(0)b_k^\dagger(0) + b_k(0)b_k(0)\right)\right]. \quad (8.9)$$

The time dependence of the operators $a_k(t)$ and $b_k(t)$ are now explicitly given by

$$\begin{aligned} a_k(t) &= U^{int}(t)^{-1} a_k(0) U^{int}(t) \\ &= a_k(0)\cosh\left(|\rho_k| h_p t/2\right) + a_k^\dagger(0)\sinh\left(|\rho_k| h_p t/2\right), \end{aligned} \quad (8.10)$$

$$\begin{aligned} b_k(t) &= U^{int}(t)^{-1} b_k(0) U^{int}(t) \\ &= b_k(0)\cosh\left(|\rho_k| h_p t/2\right) - b_k^\dagger(0)\sinh\left(|\rho_k| h_p t/2\right). \end{aligned} \quad (8.11)$$

Also it follows that

$$c_k(t) = U^{int}(t)^{-1} c_k(0) U^{int}(t) = \frac{1}{\sqrt{2}} e^{i\varphi_k} \{a_k(t) + b_k(t)\}, \quad (8.12)$$

so that, with the aid of Eqs. (8.10) and (8.11) we have

$$c_k(t) = \left\{c_k(0)\cosh\left(|\rho_k| h_p t/2\right) + c_{-k}(0)^\dagger e^{2i\varphi_k}\sinh\left(|\rho_k| h_p t/2\right)\right\}, \quad (8.13)$$

It is easily verified that, in the absence of a pumping field, the time dependence of $c_k(t)$ vanishes and we get $c_k(t) = c_k(0)$.

8.2 Collapse and revival in the magnon number

In this section we explore the properties of a magnon state labeled by k. For this purpose we calculate the average of the magnon number operator $n_k(t) = c_k^\dagger(t)c_k(t)$. It is convenient to work in the coherent magnon state representation. Let us assume that the initial magnon state is a coherent state defined as $c_k|\alpha_k\rangle = \alpha_k|\alpha_k\rangle$ [113]. Using the solution obtained in Eq. (8.13) it is straightforward to calculate the time-dependent average $\langle n_k(t)\rangle$ with respect to the initial ($t = 0$)

coherent state $|\psi_k(0)\rangle = |\alpha_k\rangle$ as

$$\begin{aligned}\langle\alpha_k|\, n_k(t)\, |\alpha_k\rangle &= |\alpha_k|^2 \cosh^2\left(|\rho_k|\, h_p t/2\right) + \left(\alpha_k^2 e^{-2i\varphi_k} + \alpha_k^{*2} e^{2i\varphi_k}\right) \cosh\left(|\rho_k|\, h_p t/2\right) \sinh\left(|\rho_k|\, h_p t/2\right) \\ &+ \left(1 + |\alpha_k|^2\right) \sinh^2\left(|\rho_k|\, h_p t/2\right). \end{aligned} \tag{8.14}$$

Defining $\alpha_k = |\alpha_k|\, e^{i\eta}$, where η is a phase term, this result may be rewritten as

$$\begin{aligned}\langle n_k(t)\rangle &= |\alpha_k|^2 \cosh^2\left(|\rho_k|\, h_p t/2\right) + 2\,|\alpha_k|^2 \cos\,(2\eta - 2\varphi_k) \cosh\left(|\rho_k|\, h_p t/2\right) \sinh\left(|\rho_k|\, h_p t/2\right) \\ &+ \left(1 + |\alpha_k|^2\right) \sinh^2\left(|\rho_k|\, h_p t/2\right), \end{aligned} \tag{8.15}$$

where we have assumed $|\alpha_k|^2 = |\alpha_{-k}|^2$. From the above equation we conclude that, depending on the sign of the $\cos(2\eta)$ term, there may be an initial collapse and subsequent revival in the average number of magnons, which is a kind of non-classical effect. The oscillation of $\langle n_k(t)\rangle$ is related to the absorption and emission of magnons by the microwave pumping field. Therefore, by tuning the nonlinearity introduced by the pumping field, the sequence of collapse and revival can be manipulated.

Figure 8.1 shows the average number of magnons $\langle n_k(t)\rangle$ given by Eq. (8.15) as a function of time t for different values of the coherent state amplitude $|\alpha_k|$ and phase. In this example we have considered parameters for YIG with the saturation magnetization $4\pi\mu_0 M_s = 0.176$ T and $g\mu_B = 28$ GHz/T. In the absence of the pumping field $\langle n_k(t)\rangle = |\alpha_k|^2$ is a constant, but introducing the pumping field changes this value with time. By choosing the phase η such that $\pi/4 < (\eta - \varphi_k) < 3\pi/4$, as in Fig. 8.1(a) where $\eta = 3\pi/4$ and $\varphi_k = \pi/4$ ($\phi_k = 0$), the pumping field leads first to the collapse of the average number of magnons from the value of $|\alpha_k|^2$ and then the revival of $\langle n_k(t)\rangle$ at a later time. This effect is analogous to the collapses and revivals of the Rabi oscillations, as a non-classical effect which is well-known in quantum optics [137]. We show further results for $\langle n_k(t)\rangle$ by comparing cases where the initial state is chosen as either the vacuum state with $|\alpha_k| = 0$ or the coherent state $|\alpha_k| \neq 0$. We see that for the vacuum state the collapse-and-revival phenomena disappear. Figure 8.1(a) implies that the varying $|\alpha_k|$ provides an effective control on the time scale

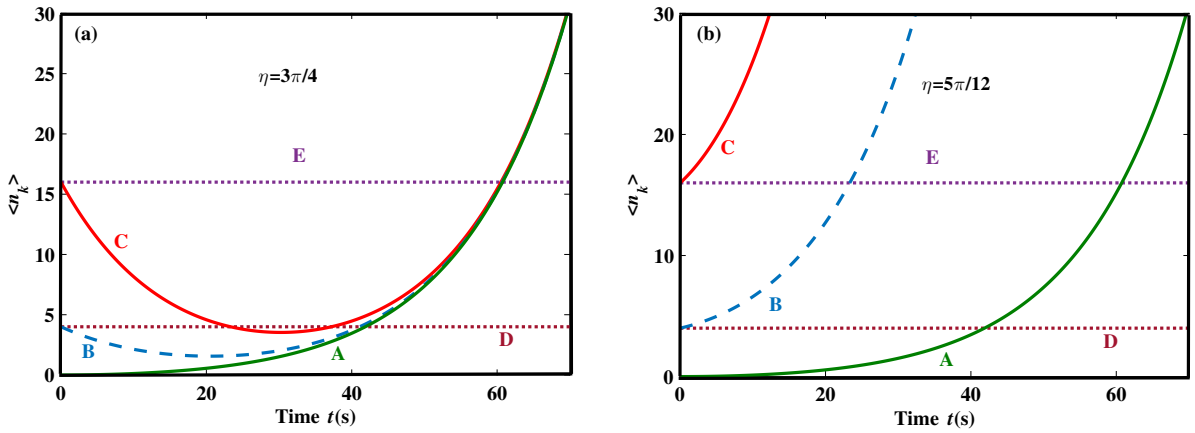

Figure 8.1: The average number of magnons as a function of time t for three different values of the coherent state amplitude with ($|\alpha_k| = 0,\ 2$ and 4) and for two pumping field amplitudes (with $\mu_0 h_p = 0$ and 0.01 T), taking other parameters as $\theta = \pi/2,\ \phi_k = 0$, and $\omega_k/2\pi = 5$ GHz: (a) $\eta = 3\pi/4$; (b) $\eta = 5\pi/12$. The lines correspond to: A, $\mu_0 h_p = 0.01$ T, $|\alpha_k| = 0$; B, $\mu_0 h_p = 0.01$ T, $|\alpha_k| = 2$; C, $\mu_0 h_p = 0.01$ T, $|\alpha_k| = 4$; D, $h_p = 0$, $|\alpha_k| = 2$; and E, $h_p = 0$, $|\alpha_k| = 4$.

of the collapses and revivals. On the other hand, if we consider a case where the coherent phase η does not correspond to $\pi/4 < \eta - \varphi_k < 3\pi/4$ the collapse-and-revival effect vanishes and the number of magnons $\langle n_k(t)\rangle$ grows monotonically with time, as can be seen in Fig. 8.1(b).

8.3 Quadrature squeezing of the magnons

In this section we study the effects of squeezing on the magnons. This is first done analytically and then illustrated through some numerical examples. The magnon quadrature components $X_{1c}(t)$ and $X_{2c}(t)$ are defined as [124, 137]

$$X_{1c}(t) = \frac{1}{2}\left(c_k(t) + c_k^\dagger(t)\right), \qquad X_{2c}(t) = \frac{1}{2i}\left(c_k(t) - c_k^\dagger(t)\right). \tag{8.16}$$

The degree of squeezing can then be measured through the squeezing parameters S_i ($i = 1, 2$) defined by

$$S_{ic}(t) = \frac{\left\langle \triangle X_{ic}(t)^2 \right\rangle - \frac{1}{2}\left|\langle [X_{1c}(t), X_{2c}(t)]\rangle\right|}{\frac{1}{2}\left|\langle [X_{1c}(t), X_{2c}(t)]\rangle\right|}, \tag{8.17}$$

where $\left\langle \triangle X_{ic}(t)^2 \right\rangle = \left\langle X_{ic}(t)^2 \right\rangle - \langle X_{ic}(t) \rangle^2$. When expressed in terms of the creation and annihilation operators of the magnons, the squeezing parameters become

$$\begin{aligned} S_{1c}(t) &= 2\left\langle c_k^\dagger(t) c_k(t) \right\rangle + 2 \text{ Re } \left\langle c_k^2(t) \right\rangle - 4 [\text{ Re } \langle c_k(t) \rangle]^2 , \\ S_{2c}(t) &= 2\left\langle c_k^\dagger(t) c_k(t) \right\rangle - 2 \text{ Re } \left\langle c_k^2(t) \right\rangle - 4 [\text{ Im } \langle c_k(t) \rangle]^2 . \end{aligned} \tag{8.18}$$

A state of the field is said to be squeezed when either one of the quadrature components X_{1c} or X_{2c} satisfies the relation $\left\langle \triangle X_{ic}(t)^2 \right\rangle < 1/4$. Then using Eq. (8.17) the condition for squeezing in the quadrature component can be written as $S_{ic} < 0$.

From Eq. (8.13) we find

$$\begin{aligned} \langle c_k(t) \rangle &= \left\langle c_k(0) \cosh\left(\rho_k h_p t/2\right) + c_{-k}^\dagger(0) e^{2i\varphi_k} \sinh\left(\rho_k h_p t/2\right) \right\rangle \\ &= \alpha_k \cosh\left(|\rho_k| h_p t/2\right) + \alpha_{-k}^* e^{2i\varphi_k} \sinh\left(|\rho_k| h_p t/2\right), \end{aligned} \tag{8.19}$$

$$\begin{aligned} \left\langle c_k^2(t) \right\rangle &= \alpha_k^2 \cosh^2\left(|\rho_k| h_p t/2\right) + \left(1 + 2|\alpha_k|^2\right) e^{2i\varphi_k} \cosh\left(|\rho_k| h_p t/2\right) \sinh\left(|\rho_k| h_p t/2\right) \\ &+ \alpha_k^{*2} e^{4i\varphi_k} \sinh^2\left(|\rho_k| h_p t/2\right). \end{aligned} \tag{8.20}$$

Therefore the squeezing parameters in Eq. (8.18) become

$$S_{1c}(t) = 2\cos(2\varphi) \cosh\left(|\rho_k| h_p t/2\right) \sinh\left(|\rho_k| h_p t/2\right) + 2\sinh^2\left(|\rho_k| h_p t/2\right) \tag{8.21}$$

$$S_{2c}(t) = -2\cos(2\varphi) \cosh\left(|\rho_k| h_p t/2\right) \sinh\left(|\rho_k| h_p t/2\right) + 2\sinh^2\left(|\rho_k| h_p t/2\right). \tag{8.22}$$

From the above equations it is clear that for the case with $\varphi_k = 0$, $S_{1c}(t) > 0$ and $S_{2c}(t) < 0$ at any time $t > 0$. More generally when $\varphi_k \neq 0$, depending on the sign of $\cos(2\varphi_k)$, the squeezing parameters can be positive or negative. The squeezing parameters are independent of $|\alpha_k|$ and η. This means that, even for the vacuum state, introducing the pumping field leads to a squeezing

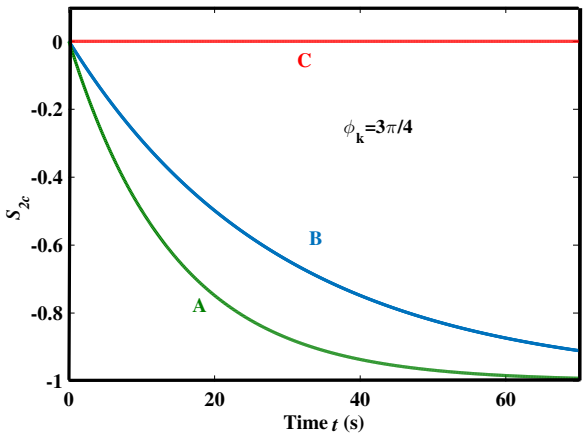

Figure 8.2: The squeezing parameter S_{2c} as a function of time t for three different values of the pumping field amplitude (with $\mu_0 h_p = 0,\ 0.008$ T and 0.01 T), taking $\theta = \pi/2$, $\omega_k/2\pi = 5$ GHz, and $\phi_k = 3\pi/4$. The lines correspond to: A, $h_p = 0.01$ T; B, $h_p = 0.008$ T; and C, $h_p = 0$.

effect. To illustrate the effects of the pumping field on the quadrature squeezing of the magnon states, the squeezing parameter $S_{2c}(t)$ is plotted as a function of time t in Fig. 8.2 for $h_p = 0$ (no pumping) and for nonzero parallel-pumping with $\mu_0 h_p = 0.008$ T and $\mu_0 h_p = 0.01$ T as examples, taking the case of $\phi_k = 3\pi/4$ (so $\varphi_k = \pi$). Also we choose the same parameters as before. In the absence of the pumping field we find $S_{2c} = 0$, as expected. Also, it is seen that with the pumping field present, we have a nonlinear model and the quadrature squeezing effect can occur. In the other words, the quadrature squeezing of the magnons is a consequence of the nonlinear interactions introduced by the pumping field in our model. We see that by introducing the pumping field the squeezing parameter S_{2c} of the magnons becomes negative as the time evolves, although the initial magnon state is an ordinary Glauber coherent state. When t is large (compared to the characteristic time $\tau = 2/|\rho_k| h_p \cong 29$ s when $\mu_0 h_p = 0.01$ T), it is found that $S_{2c}(t) \to -1$ in this example.

8.4 Statistical properties of the parallel-pumped magnons

In this section we proceed to study the magnon-counting statistics by considering the Mandel parameter $Q(t)$, which is defined as [41, 139]

$$Q(t) = \frac{\left\langle \left(c_k^\dagger(t)c_k(t)\right)^2 \right\rangle - \left\langle c_k^\dagger(t)c_k(t)\right\rangle^2}{\left\langle c_k^\dagger(t)c_k(t)\right\rangle} - 1. \tag{8.23}$$

For $Q(t) < 0$ (or $Q(t) > 0$) the statistics is sub-Poissonian (or super-Poissonian), while the state with $Q(t) = 0$ is called Poissonian.

From Eq. (8.13) we find

$$\begin{aligned}
\langle\alpha_k| \left(c_k^\dagger(t)c_k(t)\right)^2 |\alpha_k\rangle &= \left(|\alpha_k|^2 + |\alpha_k|^4\right)\cosh^4\left(|\rho_k|\, h_p t/2\right) \\
&+ \left[\left(4\,|\alpha_k|^4 + 2\,|\alpha_k|^2\right)\cos\left(2\eta - 2\varphi_k\right)\right]\cosh^3\left(|\rho_k|\, h_p t/2\right)\sinh\left(|\rho_k|\, h_p t/2\right) \\
&+ \left(4\,|\alpha_k|^2 + 4\,|\alpha_k|^4 + 2\,|\alpha_k|^4\cos\left(4\eta - 4\varphi_k\right) + 1\right) \\
&\times \cosh^2\left(|\rho_k|\, h_p t/2\right)\sinh^2\left(|\rho_k|\, h_p t/2\right) \\
&+ \left[\left(6\,|\alpha_k|^2 + 4\,|\alpha_k|^4\right)\cos\left(2\eta - 2\varphi_k\right)\right]\cosh\left(|\rho_k|\, h_p t/2\right)\sinh^3\left(|\rho_k|\, h_p t/2\right) \\
&+ \left(1 + 3\,|\alpha_k|^2 + |\alpha_k|^4\right)\sinh^4\left(|\rho_k|\, h_p t/2\right).
\end{aligned} \tag{8.24}$$

Now by substituting Eqs. (8.15) and (8.24) into (8.23) we can obtain the time evolution of the Mandel parameter $Q(t)$ for the system, initially prepared with Poissonian statistics. The analytical expressions are complicated, but in the following paragraph, we present numerical results for the dependence of $Q(t)$ on t and $|\alpha_k|$ for different h.

To illustrate the effects of the coherent state and the pumping field on the magnon statistics, some plots of $Q(t)$ as a function of t are presented in Fig. 8.3 for different coherent state amplitude $|\alpha_k|$ taking $\mu_0 h_p = 0$ and 0.01 T. In the absence of the pumping field the Mandel parameter is constant with $Q(t) = 0$, which corresponds to Poissonian statistics. When the pumping field is introduced the Mandel parameter $Q(t)$ evolves to positive values, and so the magnon-counting statistics become super-Poissonian. If t is small compared to the characteristic time $\tau = 2/|\rho_k|\, h_p$ we find to leading order that

$$Q(t) \simeq \frac{1}{2}\left(|\rho_k|\, h_p t\right)^2. \tag{8.25}$$

We see from Fig. 8.3 that even for the vacuum state the magnon-counting statistics are super-

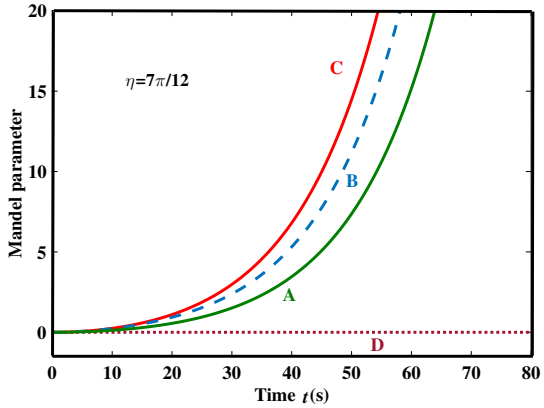

Figure 8.3: Mandel parameter $Q(t)$ as a function of time t taking $\theta = \pi/2$, $\phi_k = 0$, $\eta = 7\pi/12$ and $\omega_k/2\pi = 5$ GHz for three different values of the coherent state amplitude ($|\alpha_k| = 0,\ 1$ and 5) with pumping field amplitude ($\mu_0 h_p = 0$ and 0.01 T). The lines correspond to: A, $\mu_0 h_p = 0.01$ T, $|\alpha_k| = 0$; B, $\mu_0 h_p = 0.01$ T, $|\alpha_k| = 1$; C, $\mu_0 h_p = 0.01$ T, $|\alpha_k| = 5$; and D, $h_p = 0$, $|\alpha_k| =$ any value.

Poissonian. Taking the coherent state as the choice of initial state leads to an enhancement of the magnitude of the Mandel parameter $Q(t)$.

8.5 System with nonlinear four-magnon interactions

In this section we examine the role of the four-magnon interaction Hamiltonian term H_4, which was briefly mentioned in Section 8.1, in modifying the pumping results found in Sections 8.2 to 8.4. We will also make comparisons with the work of Wang *et al*. [136] where four-magnon effects for squeezing were considered in the absence of microwave pumping.

Although the general form of H_4 is actually more complicated, since it involves a summation over three wave-vector labels (see, e.g., [140]), a simplified form with just two wave-vector sums is often applied. This is inspired by analogies with the Bardeen-Cooper-Schrieffer (BCS) theory of superconductivity, and is especially relevant when microwave pumping is present [141, 12, 22]:

$$H_4 = \sum_{k,k'} \left(\frac{1}{2} S_{k,k'} c_k^\dagger c_{-k}^\dagger c_{k'} c_{-k'} + T_{k,k'} c_k^\dagger c_{k'}^\dagger c_k c_{k'} \right). \tag{8.26}$$

Here the four-magnon coefficients $S_{k,k'}$ and $T_{k,k'}$ for the two terms both depend on the dipole-dipole and exchange parameters of the system.

The total Hamiltonian can now be written as $H = H_0 + H'$, where $H' = H_p + H_4$. We may proceed to find the time dependence of the operators by following the same steps as in Section 8.1, but with H' replacing the role of H_p. In particular, it is found that the time evolution operator in Eq. (8.7) will be replaced by

$$\begin{aligned} U^{int}(t) &= \exp\left[\sum_k \frac{it}{2}\left(h_p \rho_k c_k^\dagger(0) c_{-k}^\dagger(0) + \text{h.c.}\right)\right. \\ &\quad \left. -it\sum_{k,k'}\left(\frac{1}{2}S_{k,k'}c_k^\dagger c_{-k}^\dagger c_{k'}c_{-k'} + T_{k,k'}c_k^\dagger c_{k'}^\dagger c_k c_{k'}\right)\right] \end{aligned} \tag{8.27}$$

in the present case. Next the above equation can be simplified by assuming a type of random-phase approximation (RPA) [140, 142, 143] to decouple the products of the four operators into products of just two operators. Specifically for the quartic terms in the above exponent, we take

$$\begin{aligned} \sum_{k,k'}\tfrac{1}{2}S_{k,k'}c_k^\dagger c_{-k}^\dagger c_{k'}c_{-k'} &\to \sum_{k,k'}\tfrac{1}{2}S_{k,k'}\left\{c_k^\dagger c_{-k}^\dagger \langle c_{k'}c_{-k'}\rangle + \left\langle c_k^\dagger c_{-k}^\dagger\right\rangle c_{k'}c_{-k'}\right\} \\ &= \sum_k c_k^\dagger c_{-k}^\dagger\left\{\sum_{k'}\tfrac{1}{2}S_{k,k'}\langle c_{k'}c_{-k'}\rangle\right\} + \text{h.c.}, \end{aligned} \tag{8.28}$$

$$\sum_{k,k'}T_{k,k'}c_k^\dagger c_{k'}^\dagger c_k c_{k'} \to \sum_{k,k'}T_{k,k'}\left\{c_k^\dagger c_k\left\langle c_{k'}^\dagger c_{k'}\right\rangle + \left\langle c_k^\dagger c_k\right\rangle c_{k'}^\dagger c_{k'}\right\} = 2\sum_k c_k^\dagger c_k \sum_{k'}T_{k,k'}\left\langle c_{k'}^\dagger c_{k'}\right\rangle, \tag{8.29}$$

assuming $T_{k,k'} = T_{k',k}$.

We see that the second of the above terms in the four-magnon Hamiltonian involves the $c_k^\dagger c_k$ operator combination, which is the same as in H_0. Hence the inclusion of the $T_{k,k'}$ term is equivalent to the replacement of ω_k by

$$\omega_k + 2\sum_{k'}T_{k,k'}\langle n_{k'}(0)\rangle\,. \tag{8.30}$$

We may therefore conclude that it corresponds to a temperature-dependent re-normalization of the SW frequency in the unperturbed Hamiltonian H_0 [140, 56]. Since it does not give us any fundamentally new information about the magnon statistics, this term in H_4 will be henceforth

disregarded.

On the other hand, the term for $S_{k,k'}$ in Eq. (8.28) involves operators $c_k^\dagger c_{-k}^\dagger$ and $c_k c_{-k}$ after these decouplings are made, as does H_p in Eq. (8.2). By substituting Eqs. (8.8) and (8.28) into (8.27), using $\langle c_{k'} c_{-k'} \rangle = \langle \alpha_{k'} | \, c_{k'} c_{-k'} \, | \alpha_{k'} \rangle = \alpha_{k'}^2$ and assuming $\eta = \phi_k$, the new time evolution operator is given by an equation having the same form as (8.9) but with the scalar factor $(h_p t/4)|\rho_k|$ replaced by $(h_p t/4)|\rho_k| + (|\alpha_{k'}|^2 t/8) S_{k,k'}$. Proceeding as in Section 8.1 it now follows that the important result for the time evolution of $c_k(t)$ can be obtained formally from Eq. (8.13) by replacing h_p with the quantity $h = h_p + h_4$, where

$$h_4 \;=\; \frac{2}{|\rho_k|} \sum_{k'} \frac{1}{4} S_{k,k'} \, |\alpha_{k'}|^2 \, . \tag{8.31}$$

This holds within the approximation corresponding to our RPA-type decoupling. The formal results in Sections 8.2 to 8.4 for the collapse-and-revival of the magnon number, the quadrature squeezing of the magnons and the statistical properties of the magnons, all still apply provided we replace h_p with h.

In principle, an estimate of the magnitude of h_4 could be made using Eq. (8.31), but this could only be achieved if the four-magnon interaction term $S_{k,k'}$ were known for a particular material at all wave vectors. Practically we know $S_{k,k'}$ only in special cases, such as when k and k' both lie within the dipole-dominated regime of very small wave vectors. Then $S_{k,k'} = 2\omega_M/4NS$ [22], which is independent of k and k' (with N denoting the number of spins). Also, for small k and k' in the exchange-dominated regime, it is known that $S_{k,k'}$ (and $T_{k,k'}$) acquire a wave-vector dependence (see, e.g., [140]).

It is interesting to note that, in the context of squeezing without pumping being applied, Wang *et al.* [136] considered only the $S_{k,k'}$ interaction and then specifically for a Heisenberg ferromagnet (i.e., in its simpler form without dipole-dipole interactions). Although their method of calculation was different from ours, it is similar in that it also involved a decoupling approximation. Also it led them to an effective Hamiltonian (their Eq. (18)) with an additional parameter denoted as Δ

which has a similar role to that of parallel pumping in our case. In the experimental context, we note that the amplitude h_p of the pumping field can be conveniently varied, wheres the effective contribution h_4 is essentially fixed (for a given material at a given temperature).

8.6 Conclusions

In conclusion, our calculations have shown that the nonlinear effects associated with parallel microwave pumping and the four-magnon interactions lead to the possibility of producing and manipulating the non-classical properties of the magnons in a ferromagnet. These include the squeezed magnon state and the collapse-and-revival effect of the average magnon number $\langle n_k(t)\rangle$. Also it was found that the time evolution of the magnon occupation number exhibits a behavior with collapse and revival, representing a kind of non-classical effect. Specifically, it was shown that applying the microwave pumping field, as well as including four-magnon interaction terms, leads to the existence of the quadrature squeezing effect in a magnon coherent state as time evolves, and its behavior can be controlled through these values of the coupling interactions. Magnon-counting statistics were demonstrated and it was found that the magnons may exhibit super-Poissonian statistics, even though the initial magnon state is a Glauber coherent state. As regards prospects for experimental studies, we emphasized in the introductory paragraphs the formation of magnon quantum coherence claimed for ferromagnets with four-magnon interactions when subjected to intense parallel pumping (as in our theoretical model).

In our simplified treatment of the four-magnon interactions, we employed a decoupling approximation of the RPA-type. For the interaction term involving $T_{k,k'}$ we found an effect that was equivalent to a temperature-dependent renormalization of the magnon frequency ω_k. More interestingly, the effect of the interaction term $S_{k,k'}$ (which was previously studied in [136] for magnon squeezing in a Heisenberg ferromagnet) could be re-interpreted in terms of an effective pumping field amplitude h_4 in addition to the actual pumping field h_p. Thus it can be considered as being like an effective renormalization of the term ρ_k in the pumping Hamiltonian H_p. We suggest that

an advantage of using parallel pumping in future experiments on magnon squeezing is that it can be effectively controlled through varying h_p to increase or decrease the effects. The technology for microwave pumping in ferromagnets is well developed (e.g., as used in experiments to detect the magnon Bose-Einstein condensation in ferromagnetic films [59]).

We remark that our calculations could usefully be modified to apply to nanostructures, such as ultrathin films, nanowires or array of nanostructures. An example for nanowires is given in the next chapter. Such calculations necessitate the inclusion of boundary conditions at surfaces and interfaces, as well as the modification of model parameters such as ρ_k and $S_{k,k'}$. Also our formalism can be extended to cases in the perpendicular pumping configuration, where the three-magnon interaction Hamiltonian would need to be added.

Chapter 9

Quantum statistics for a two-mode magnon system of nanowires with microwave pumping

The material in this chapter has been published as an article by me (with M. G. Cottam) listed as Ref. [144].

Recently, the nonlinear aspects of the SW or magnon excitations in nanostructures under microwave pumping have attracted a lot of attention (see, e.g., [62, 91, 63]). For example, intense efforts have been made to study the nonlinear behavior of magnons forming a Bose-Einstein condensation (BEC) [102, 115, 61]. The BEC of magnons has been observed at room temperature by exciting the magnons into a gas in a quasi-equilibrium state using microwave pumping [59]. More generally, magnons can be nonlinearly generated in a ferromagnet by means of an intense microwave pumping field (applied either parallel or perpendicular to the static field as considered in earlier chapters). In the parallel pumping configuration, due to the dipole-dipole interactions between the spins, SW pairs couple directly to the microwave field, while in the perpendicular pumping process, by contrast, the coupling between parametric SWs occurs through one or more uniform (i.e., zero wave-vector) SW modes, as discussed in earlier chapters. However, going

beyond pumping, additional quantum-statistical information may be obtained by employing the representation of a coherent magnon state.

As mentioned in Chapter 8, the concept of coherent magnon states was introduced by Rezende and Zagury [112, 113] in order to obtain a correspondence between the classical and quantum-mechanical descriptions of SWs. The coherent magnon states $|\alpha_k\rangle$ were defined as the eigenstates of the annihilation operator $c_k|\alpha_k\rangle = \alpha_k|\alpha_k\rangle$. Here the eigenvalue $\alpha_k = |\alpha_k|e^{i\theta}$ is a complex number which characterizes the coherent state with θ representing the phase of the state, and k is a wave-vector label. We note that the coherent states can be expanded in terms of the eigenstates $|n_k\rangle$ of the free magnon Hamiltonian $H_0 = \sum_k \omega_k c_k^\dagger c_k$ in the form [112, 137]

$$|\alpha_k\rangle = \exp\left(-|\alpha_k|^2/2\right)\sum_{n_k}(\alpha_k)^{n_k}/(n_k!)^{1/2}|n_k\rangle. \tag{9.1}$$

The eigenstates $|n_k\rangle$ are also eigenstates of the occupation number operator $n_k = c_k^\dagger c_k$. For the expectation value of the number operator, we obtain $\langle n_k\rangle = \langle\alpha_k|n_k|\alpha_k\rangle = |\alpha_k|^2$. Also the probability of finding n_k magnons in the coherent state $|\alpha_k\rangle$ is [112, 137]

$$|\langle n_k|\alpha_k\rangle|^2 = \left[|\alpha_k|^{2n_k}/(n_k)!\right]\exp(-|\alpha_k|^2), \tag{9.2}$$

which is a Poisson distribution and shows a peak at $\langle n_k\rangle = |\alpha_k|^2$.

Rezende [122] also showed that the coherent magnon states are quantum states which can be generated through microwave pumping. He studied coherent-state properties of the BEC of a magnon gas [102, 115, 61], which was observed by Demokritov *et al*. [59, 117, 118]. Special attention has been given to the coherent properties of parallel pumped magnons with the three-magnon [119] and four-magnon [112, 120] processes included.

Using the coherent magnon representation, we recently studied some non-classical properties (such as squeezing) of a microwave-driven interacting magnon system ([111] and Chapter 8). The aim now is to generalize the previous parallel pumping calculations, which were for a *bulk* ferromagnet, to apply to *two-mode* magnon systems, such as those typically realized in low-dimensional magnetic nanostructures. In quantum optics the extension from one- to two-mode processes in var-

ious atomic systems has attracted a great deal of attention because of high degree of correlation between the emitted field modes. Many aspects of two-mode boson systems in this quantum optics context have already been considered, such as temporal evolution of atomic operators [145], collapses and revivals of the Rabi oscillations [146, 147], two-mode squeezing [148, 149], non-classical statistics of the two modes [150, 151, 147], and the cross correlation between the two modes [152, 153, 147].

In this chapter, motivated by the above-mentioned work, we are interested in the two-mode boson systems of ferromagnetic nanowires formed by two lines of spins that may interact through exchange and dipole-dipole interactions. The dynamical properties of nanowires, in general, are important because of the role of the lateral edges and the surface boundary conditions in modifying the bulk magnon behavior. Our focus is a theoretical study of statistical properties for two-mode magnon systems. The emphasis is on novel effects of the parallel pumping field, in particular, with the nonlinear four-magnon interactions also being included in our model Hamiltonian. We find that the nonlinear effects associated with the parallel pumping and the four-magnon coupling lead to the occurrence of non-classical properties of the system. Assuming that initially the two modes of magnons are in coherent states, the influence of the parallel pumping and the four-magnon term on the time evolution of the occupation magnon number, magnon counting statistics, and the cross correlation between the two modes are studied.

This chapter is organized as follows. In Section 9.1 we introduce the theoretical model for the parallel-pumped two-mode magnon system and its physical realization as a ferromagnetic nanowire. Then with the help of the coherent magnon representation, we obtain the temporal evolution of the annihilation and creation magnon operators for each mode. These results are then used in Section 9.2 to investigate the influence of a parallel pumping field on the temporal evolution of various dynamical properties of the system. In Section 9.3 we generalize the formalism to include the nonlinear four-magnon interactions in the model. Next, in Section 9.4, the calculations are presented to explore the influence of the four-magnon term on the average magnon number, the magnon-counting statistics and the cross correlation between the two modes of magnons. Finally,

we summarize our results in Section 9.5.

9.1 Theory with parallel pumping

In general, a ferromagnetic nanowire (or magnetic stripe) can be modeled as having a rectangular cross section with finite dimensions in the transverse xy plane, while the system is effectively infinite in the longitudinal z direction (see, e.g., [55, 87]). Each cross section would consist of N spins (as described in Chapter 5), which are arranged for simplicity on a simple cubic lattice (with lattice constant a). In the context of metallic ferromagnetic stripes, an effective lattice constant is often used for modeling the system, with the requirement that a is chosen to be less than the so-called exchange correlation length a_{ex}. There are N modes (or branches) in the magnon spectrum.

For our study of quantum statistics due to coherent magnons in two-mode systems, we consider here the simplest case of a nanowire formed by just two interacting lines of spins ($N = 2$). The system is in an external magnetic field and is pumped by a microwave field h. These fields are both taken to be applied parallel to the longitudinal (z) axis of the nanowire, which is also the direction of static magnetization M_s.

Starting with a spin Hamiltonian that contains the usual short-range exchange interactions, the long-range dipole-dipole interactions and the Zeeman energy of the static applied field, a bosonic form of the Hamiltonian may be deduced by standard techniques (e.g., using the Holstein-Primakoff transformation [31] at low temperatures) and then "diagonalized" to obtain the dipole-exchange magnons. In the second-quantization notation the boson operators $c^{\dagger}_{k,l}$ and $c_{k,l}$ are operators for the creation and annihilation, respectively, of magnons with a 1D wave vector k (along the z axis) and mode number l ($= 1, 2$). The total Hamiltonian of the system can be written in general as the sum of three parts as $H = H_0 + H_p + H_4$, where

$$H_0 = \sum_k \left(\omega_{k,1} c^{\dagger}_{k,1} c_{k,1} + \omega_{k,2} c^{\dagger}_{k,2} c_{k,2} \right) \tag{9.3}$$

is the diagonalized Hamiltonian for the two branches of coupled dipole-exchange magnons with

frequencies given by $\omega_{k,l}$ ($l = 1, 2$) in the absence of magnon-magnon interactions. The specific expressions for the magnon frequencies are not required for most of our analysis of the quantum statistics, with the exception of the numerical applications to be considered later. They are deduced as a special case of results in [55, 87], for example, and are quoted in Appendix D.

The next Hamiltonian term is

$$H_p = h \sum_{l_1,l_2,k} \Big[\exp(-i\omega_p t) P_{l_1,l_2}(k) c^\dagger_{k,l_1} c^\dagger_{-k,l_2} + \text{h.c.} \Big], \tag{9.4}$$

which describes the interaction of the system with the parallel microwave pumping field [58] with amplitude h and angular frequency ω_p. The amplitude factor $P_{l_1,l_2}(k)$ in the rectangular nanowire geometry is given by

$$P_{l_1,l_2}(k) = g\mu_B \sum_{n=1}^{N} S^*_{n,l_1}(k) S^*_{n+N,l_2}(-k), \tag{9.5}$$

where the quantities $S_{n,l}(k)$ are matrix elements of the $2N \times 2N$ matrix $\mathbf{S}(k)$ in the generalized Bogoliubov transformation to diagonalize the H_0 Hamiltonian [70]. For the special case of a $N = 2$ nanowire, it can be shown that the $\mathbf{P}$ matrix is diagonal, since $P_{1,2} = P_{2,1} = 0$ by symmetry. Therefore we obtain

$$H_p = h \sum_{k} \sum_{l=1}^{2} \Big[\exp(-i\omega_p t) P_{l,l}(k) c^\dagger_{k,l} c^\dagger_{-k,l} + \text{h.c.} \Big]. \tag{9.6}$$

Finally, H_4 is the four-magnon interaction term, which is quartic in the boson operators. We will discuss both its form and its effect on the magnon statistics later in Section 9.3.

By analogy with our recent work on bulk magnons in a single-mode system [111], in order to study the statistical properties of the pumped magnons (initially in the absence of H_4) we work in the quantum-mechanical interaction picture, and transform the pumping Hamiltonian to $H_p^{int}(t)$ as in Eq. (8.3). An expansion is again made using Eq. (8.4), which leads to

$$
\begin{aligned}
H_p^{int}(t) &= h\sum_k \Big[\exp(-i\omega_p t)\Big\{ \exp(2i\omega_{k,1}t) P_{1,1}(k) c_{k,1}^\dagger c_{-k,1}^\dagger \\
&+ P_{2,2}(k) \exp(2i\omega_{k,2}t) c_{k,2}^\dagger c_{-k,2}^\dagger \Big\} + \text{h.c.}\Big]. \qquad (9.7)
\end{aligned}
$$

For calculating the state of the pumped system at any time t, the time evolution operator as depicted in Eq. (8.6) can be used, giving

$$
\begin{aligned}
U^{int}(t) &= \exp\Big[\sum_k (-iht)\Big\{\Big(\exp\left(it(2\omega_{k,1} - \omega_p)\right) P_{1,1}(k) c_{k,1}^\dagger c_{-k,1}^\dagger \\
&\quad + \exp\left(it(2\omega_{k,2} - \omega_p)\right) P_{2,2}(k) c_{k,2}^\dagger c_{-k,2}^\dagger \Big) + \text{h.c.}\Big\}\Big]. \qquad (9.8)
\end{aligned}
$$

It is convenient to first decouple the k and $-k$ modes by introducing two new operators [138, 120] at time $t = 0$:

$$
a_{k,l}(0) = e^{-i\varphi_{k,l}}\left[c_{k,l}(0) + c_{-k,l}(0)\right]/\sqrt{2}, \qquad b_{k,l}(0) = e^{-i\varphi_{k,l}}\left[c_{k,l}(0) - c_{-k,l}(0)\right]/\sqrt{2}, \qquad (9.9)
$$

where $l = 1, 2$ and $\varphi_{k,l}$ are arbitrary phases. The inverse transformation giving $c_{k,l}(0)$ and $c_{-k,l}(0)$ in terms of $a_{k,l}(0)$ and $b_{k,l}(0)$ can also be straightforwardly written down. The operators $a_{k,l}(0)$ and $b_{k,l}(0)$, together with their conjugates, individually satisfy the usual boson commutation relation, whereas they also commute with one another. On substituting Eq. (9.9) into Eq. (9.8), and by writing $P_{l,l}(k) = |P_{l,l}(k)|e^{i\phi_{k,l}}$, the time evolution operator can be obtained in a more useful form as

$$
U^{int}(t) = \exp\Big\{\sum_k W\Big\}, \qquad (9.10)
$$

where

$$
\begin{aligned}
W &= -i\frac{ht}{2}\Big[\Big\{|P_{1,1}(k)|e^{i\phi_{k,1}} e^{-2i\varphi_{k,1}} e^{it(2\omega_{k,1}-\omega_p)} \left(a_{k,1}^\dagger(0) a_{k,1}^\dagger(0) - b_{k,1}^\dagger(0) b_{k,1}^\dagger(0)\right) \\
&+ |P_{2,2}(k)|e^{i\phi_{k,2}} e^{-2i\varphi_{k,2}} e^{it(2\omega_{k,2}-\omega_p)} (a_{k,2}^\dagger(0) a_{k,2}^\dagger(0) - b_{k,2}^\dagger(0) b_{k,2}^\dagger(0))\Big\} + \text{h.c.}\Big]. \qquad (9.11)
\end{aligned}
$$

Suppose we now assume the usual resonance condition for pumping of each magnon branch to

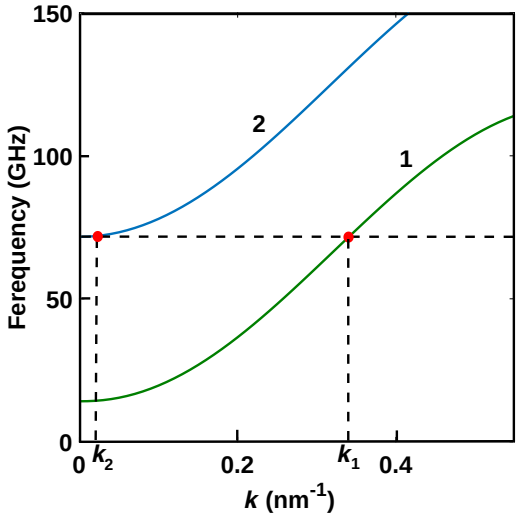

Figure 9.1: Example of SW dispersion relations ($\omega_{k,l}/2\pi$ plotted versus k) for a two-mode nanowire system, showing the resonance condition when $k_1 \cong 0.342$ nm^{-1} for mode 1 and $k_2 \cong 0.02$ nm^{-1} for mode 2. We take parameters for Permalloy with $\mu_0 H_0 = 0.005$ T. The horizontal line is drawn for $\frac{1}{2}\omega_p = \omega_{k_1,1} = \omega_{k_2,2}$, which corresponds to a frequency of 72 GHz.

be satisfied, meaning $(2\omega_{k,1} - \omega_p) = 0$ and $(2\omega_{k,2} - \omega_p) = 0$ within the exponentials of the above expression. For a fixed applied field value it then follows that these two conditions can be satisfied only at different wave vectors (denoted by k_1 and k_2) corresponding to $\omega_{k_1,1} = \omega_{k_2,2} = \frac{1}{2}\omega_p$. A necessary requirement is that $\frac{1}{2}\omega_p > \omega_{0,2}$ for the second magnon branch. A numerical example for this case is given in Fig. 9.1, where (both here and in subsequent examples) we use parameters appropriate to Permalloy ($Ni_{80}Fe_{20}$), as in Chapter 4. We also assume that $\phi_{k,l} - 2\varphi_{k,l} = \pi/2$ regarding the other phase factors in Eq. (9.11).

On the other hand, if $\frac{1}{2}\omega_p < \omega_{0,2}$ we can only satisfy the resonance condition in terms of the lower magnon branch 1. The other phase term for branch 2 will involve a time evolution like $\exp(i\Omega t)$, where $\Omega \equiv 2\omega_{k,2} - \omega_p$ is a frequency of order several GHz typically. Therefore oscillations occurs rapidly in time with this frequency, so the period of the oscillations is about 10^{-9}s, and so the effect of such terms will average out to zero over terms of (say) a few μs, effectively making $P_{2,2}(k)$ vanish. This time scale is really small compared with the typical time evolution (of order many seconds) that we will find relevant for our numerical results in Sections 9.2 and 9.4.

Returning to the case where the resonance conditions apply for both magnon branches, we find

that Eq. (9.11) simplifies to

$$\begin{aligned} W &= \frac{ht}{2}\Big[|P_{11}(k_1)|(a^{\dagger}_{k_1,1}(0)a^{\dagger}_{k_1,1}(0) - a_{k_1,1}(0)a_{k_1,1}(0) - b^{\dagger}_{k_1,1}(0)b^{\dagger}_{k_1,1}(0) + b_{k_1,1}(0)b_{k_1,1}(0)) \\ &+ |P_{22}(k_2)|(a^{\dagger}_{k_2,2}(0)a^{\dagger}_{k_2,2}(0) - a_{k_2,2}(0)a_{k_2,2}(0) - b^{\dagger}_{k_2,2}(0)b^{\dagger}_{k_2,2}(0) + b_{k_2,2}(0)b_{k_2,2}(0))\Big]. \quad (9.12) \end{aligned}$$

Using Eqs. (8.4) and (9.12) we obtain expressions for the operators $a_{k_l,l}(t)$ and $b_{k_l,l}(t)$ at time t. Then, making use of the relationships in Eq. (9.9) we can deduce the explicit time dependence of $c_{k_l,l}(t)$ for branches $l = 1, 2$ as

$$c_{k_l,l}(t) = \frac{e^{i\varphi_k}}{\sqrt{2}}\{(a_{k_l,l}(0) + b_{k_l,l}(0))X_l + (a^{\dagger}_{k_l,l}(0) - b^{\dagger}_{k_l,l}(0))Y_l\}, \quad (9.13)$$

where we define the time-dependent quantities

$$X_l = \cosh(|P_{l,l}(k_l)|ht/2), \quad Y_l = \sinh(|P_{l,l}(k_l)|ht/2). \quad (9.14)$$

It is seen that, in the absence of pumping, the time dependence of the above operator vanishes and we have $c_{k_l,l}(t) = c_{k_l,l}(0)$ as expected.

9.2 Dynamics in the absence of four-magnon terms

In this section we use the results of Section 9.1 to investigate the temporal evolution of various magnon state properties, including the collapse-and-revival phenomena for the average magnon number, the magnon counting statistics and the cross correlation between the magnon modes, and we discuss the influence of the pumping field.

9.2.1 Collapse and revival in the magnon numbers

Collapse and revival of the magnon number for either mode is related to the absorption and emission of magnons by the microwave pumping field. This phenomenon is absent if the field is considered classically. To investigate the effect of the pumping field on the magnon number, we calculate

the average of the magnon number operator $n_{k_l,l}(t) = c^{\dagger}_{k_l,l}(t)c_{k_l,l}(t)$ for each mode. For generality, it is convenient to work in the coherent magnon state representation, as in our recent studies applied to bulk magnon systems with pumping ([111] and Chapter 8). Let us assume that the initial magnon state is a coherent state defined in the two-mode case as $a_{k,l}|\alpha_{k,l}\beta_{k,l}\rangle = \alpha_{k,l}|\alpha_{k,l}\beta_{k,l}\rangle$ and $b_{k,l}|\alpha_{k,l}\beta_{k,l}\rangle = \beta_{k,l}|\alpha_{k,l}\beta_{k,l}\rangle$ by analogy with [113]. Using the solution obtained in Eq. (9.13) it is straightforward to calculate that the time-dependent average $\langle n_{k_l,l}(t)\rangle$ with respect to the initial ($t = 0$) coherent state $|\psi_{k,l}(0)\rangle = |\alpha_{k,l}\beta_{k,l}\rangle$ is

$$\langle\alpha_{k,l}\beta_{k,l}|n_{k_l,l}(t)|\alpha_{k,l}\beta_{k,l}\rangle = \frac{1}{2}\Big[(|\alpha_{k,l}|^2 + \left|\beta_{k,l}\right|^2 + \alpha^*_{k,l}\beta_{k,l} + \alpha_{k,l}\beta^*_{k,l})X_l^2$$
$$+(\alpha^2_{k,l} + \alpha^{*2}_{k,l} - \beta^2_{k,l} - \beta^{*2}_{k,l}) + X_lY_l(2 + |\alpha_{k,l}|^2 + |\beta_{k,l}|^2 - \alpha^*_{k,l}\beta_{k,l} - \alpha_{k,l}\beta^*_{k,l})Y_l^2\Big]. \tag{9.15}$$

Defining $\alpha_{k,l} = |\alpha_{k,l}|e^{i\epsilon_l}$ and $\beta_{k,l} = |\beta_{k,l}|e^{i\theta_l}$ where ϵ_l and θ_l are phase terms, we see that this result may be rewritten as

$$\langle\alpha_{k,l}\beta_{k,l}|n_{k_l,l}(t)|\alpha_{k,l}\beta_{k,l}\rangle = \frac{1}{2}\Big[\Big(|\alpha_{k,l}|^2 + |\beta_{k,l}|^2 + 2|\alpha_{k,l}\beta_{k,l}|\cos(\theta_l - \epsilon_l)\Big)X_l^2$$
$$+\Big(2|\alpha_{k,l}|^2\cos(2\epsilon_l) - 2|\beta_{k,l}|^2\cos(2\theta_l)\Big)X_lY_l$$
$$+\Big(2 + |\alpha_{k,l}|^2 + |\beta_{k,l}|^2 - 2|\alpha_{k,l}\beta_{k,l}|\cos(\theta_l - \epsilon_l)\Big)Y_l^2\Big]. \tag{9.16}$$

In the absence of a pumping field $\langle n_{k_l,l}(t)\rangle$ is just a constant (independent of t), taking the value $\frac{1}{2}[|\alpha_{k,l}|^2+|\beta_{k,l}|^2+2|\alpha_{k,l}\beta_{k,l}|\cos(\theta_l-\epsilon_l)]$, which depends on the phase terms as well as the coherent state amplitudes. Introducing the pumping field changes this value for the two branches, and gives rise to a time dependence. The appearance of the phase-related terms in the above equation, specifically those involving $\cos(2\theta_l)$, $\cos(2\epsilon_l)$, and $\cos(\theta_l - \epsilon_l)$, may lead to situations where there can be an initial *decrease* in the magnon number of either mode at small t, followed by an eventual increase at larger t. In other cases, depending on the phases, there may just be a monotonic increase with t. The phenomenon of an initial collapse and subsequent revival in the average number of magnons is a kind of non-classical effect. Our results show that it can be manipulated by tuning the nonlinearity introduced by the pumping field. This is demonstrated through examples in Figs. 9.2 and 9.3, using

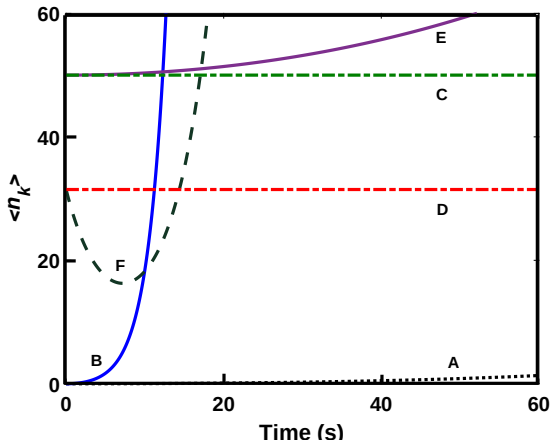

Figure 9.2: The average number of magnons as a function of time t for different choices of the coherent state amplitudes and the pumping field amplitudes, taking parameters for Permalloy with applied field 0.011 T. The pumping frequency is 144 GHz, which allows the resonance condition to be satisfied for both modes (see text). The lines correspond to: A, $l = 1$, when $\mu_0 h = 0.1$ T, $|\alpha_{k,l}| = |\beta_{k,l}| = 0$; B, $l = 2$, when $\mu_0 h = 0.1$ T, $|\alpha_{k,l}| = |\beta_{k,l}| = 0$; C, $l = 1$, when $h = 0$, $|\alpha_{k,l}| = |\beta_{k,l}| = 5$; D, $l = 2$, when $h = 0$, $|\alpha_{k,l}| = |\beta_{k,l}| = 5$; E, $l = 1$, when $\mu_0 h = 0.05$ T, $|\alpha_{k,l}| = |\beta_{k,l}| = 5$; F, $l = 2$, when $\mu_0 h = 0.05$ T, $|\alpha_{k,l}| = |\beta_{k,l}| = 5$.

parameters for Permalloy as before. In each figure the average number of magnons $\langle n_{k_l,l}(t)\rangle$ for the two branches $l = 1, 2$, given by Eq. (9.15), is plotted as a function of time t for different values of the coherent state amplitudes $|\alpha_{k,l}|$ and $|\beta_{k,l}|$ and for different phases.

In Fig. 9.2 we consider the case discussed earlier where the resonance condition applies for both magnon modes. We take $\omega_{k,1}/2\pi = \omega_{k,2}/2\pi = 72$ GHz, corresponding to wave vectors $k_1 = 0.34$ nm^{-1} and $k_2 = 0$. The phase terms in this example are $\theta_{k,1} = 0$, $\theta_{k,2} = \pi/12$, $\epsilon_{k,1} = 0$, and $\epsilon_{k,2} = \pi/2$. Lines A and B refer to pumping of the vacuum state, and it is seen that a monotonic increase of the magnon numbers $\langle n_{k_l,l}(t)\rangle$ from zero (at $t = 0$) is predicted, as expected. If there is a coherent state but no pumping, as for lines C and D, the magnon numbers remain constant. Finally, lines E and F refer to coherent states with pumping, and we see that there is collapse and revival predicted for just one of the magnon branches ($l = 2$ in this case). This effect is analogous to the collapses and revivals of the Rabi oscillations, as a non-classical effect which is well-known in quantum optics [137]. Our results imply that varying the parameters of the coherent magnon states could provide an effective control for the occurrence of the collapses and revivals (and their time scales).

Next in Fig. 9.3 we show some similar examples that correspond to a pumping field of smaller frequency, such that the resonance condition can be satisfied only for the lower ($l = 1$) magnon (i.e., when the pumping is such that $\frac{1}{2}\omega_p < \omega_{0,2}$ as discussed in the previous section). For this case we take $\omega_{k,1}/2\pi = 40$ GHz, corresponding to wave vector $k_1 = 0.214$ nm^{-1}. The phase angles are chosen as $\theta_{k,1} = \pi/8$, $\theta_{k,2} = \pi$, $\epsilon_{k,1} = \pi/2$, and $\epsilon_{k,2} = \pi$. It is again seen that a collapse-and-revival effect may occur for certain choices of coherent magnon states under pumping (see line E).

9.2.2 Magnon-counting statistics

We now proceed to study the magnon-counting statistics by considering the Mandel parameter $Q_l(t)$ for each magnon mode ($l = 1, 2$). This is defined as [137, 139]

$$Q_l(t) = \frac{\left\langle (c^\dagger_{k_l,l}(t)c_{k_l,l}(t))^2 \right\rangle - \left\langle c^\dagger_{k_l,l}(t)c_{k_l,l}(t) \right\rangle^2}{\left\langle c^\dagger_{k_l,l}(t)c_{k_l,l}(t) \right\rangle} - 1. \tag{9.17}$$

For $Q_l(t) < 0$ (or $Q_l(t) > 0$) the statistics is sub-Poissonian (or super-Poissonian), while a state with $Q_l(t) = 0$ is called Poissonian. From Eq. (9.13) and the operator time dependence discussed in Section 9.1, we obtain

$$\begin{aligned}
\langle \alpha_k\beta_k|(c^\dagger_{k_l,l}(t)c_{k_l,l}(t))^2|\alpha_k\beta_k\rangle = \frac{1}{4}\Big\{&\Big[2(\alpha_{k,l}+\beta_{k,l})(\alpha^*_{k,l}+\beta^*_{k,l}) + (\alpha_{k,l}+\beta_{k,l})^2(\alpha^*_{k,l}+\beta^*_{k,l})^2\Big]X_l^4 \\
&+\Big[(\alpha^{*2}_{k,l} - \beta^{*2}_{k,l} + \alpha^2_{k,l} - \beta^2_{k,l})^2 + 4(\alpha_{k,l}+\beta_{k,l})(\alpha^*_{k,l}+\beta^*_{k,l}) + 2(\alpha^{*2}_{k,l} - \beta^{*2}_{k,l})(\alpha^2_{k,l} - \beta^2_{k,l}) + 4 \\
&+4|\alpha_{k,l}|^2 + 4|\beta_{k,l}|^2\Big]X_l^2Y_l^2 + \Big[4 + 6|\alpha_{k,l}|^2 + 6|\beta_{k,l}|^2 - 6\beta^*_{k,l}\alpha_{k,l} - 6\alpha^*_{k,l}\beta_{k,l} \\
&+(\alpha^*_{k,l} - \beta^*_{k,l})^2(\alpha_{k,l} - \beta_{k,l})^2\Big]Y_l^4 + \Big[2(\alpha^{*3}_{k,l} - \beta^{*3}_{k,l})(\alpha_{k,l}+\beta_{k,l}) + 2(\alpha^3_{k,l} - \beta^3_{k,l})(\alpha^*_{k,l}+\beta^*_{k,l}) \\
&+2\alpha^*_{k,l}\beta^*_{k,l}(|\alpha_{k,l}|^2 - |\beta_{k,l}|^2 - \beta^*_{k,l}\alpha_{k,l} + \alpha^*_{k,l}\beta_{k,l}) + 2\alpha_{k,l}\beta_{k,l}(|\alpha_{k,l}|^2 - |\beta_{k,l}|^2 + \beta^*_{k,l}\alpha_{k,l} - \alpha^*_{k,l}\beta_{k,l}) \\
&+2(\alpha^2_{k,l} + \alpha^{*2}_{k,l} - \beta^2_{k,l} - \beta^{*2}_{k,l})\Big]X_l^3Y_l + 2(\alpha^{*3}_{k,l} + \beta^{*3}_{k,l})(\alpha_{k,l} - \beta_{k,l}) + 2(\alpha^3_{k,l} + \beta^3_{k,l})(\alpha^*_{k,l} - \beta^*_{k,l}) \\
&+2\alpha^*_{k,l}\beta^*_{k,l}(|\beta_{k,l}|^2 - |\alpha_{k,l}|^2 - \beta^*_{k,l}\alpha_{k,l} + \alpha^*_{k,l}\beta_{k,l}) + 2\alpha_{k,l}\beta_{k,l}(|\beta_{k,l}|^2 - |\alpha_{k,l}|^2 + \beta^*_{k,l}\alpha_{k,l} - \alpha^*_{k,l}\beta_{k,l}) \\
&+6(\alpha^2_{k,l} + \alpha^{*2}_{k,l} - \beta^{*2}_{k,l} - \beta^2_{k,l})\Big]X_lY_l^3\Big\}.
\end{aligned} \tag{9.18}$$

Now, by substituting Eqs. (9.15) and (9.18) into (9.17), we can obtain the time evolution of the Mandel parameter $Q_l(t)$ for each magnon mode, initially prepared with Poissonian statistics.

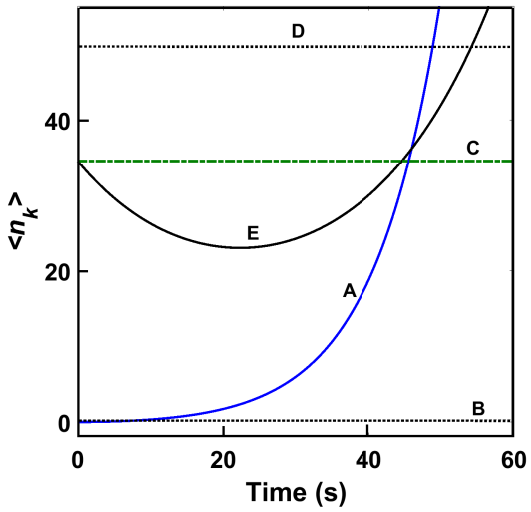

Figure 9.3: The same as in Fig. 9.2, but with a pumping frequency of 80 GHz, which allows the resonance condition to be satisfied only for the lower $l = 1$ magnon (see text). The lines correspond to: A, $l = 1$, when $\mu_0 h = 0.1$ T, $|\alpha_{k,l}| = |\beta_{k,l}| = 0$; B, $l = 2$, when $\mu_0 h = 0.1$ T, $|\alpha_{k,l}| = |\beta_{k,l}| = 0$; C, $l = 1$, when $h = 0$, $|\alpha_{k,l}| = |\beta_{k,l}| = 5$; D, $l = 2$, when $\mu_0 h = 0$ or 0.05 T, $|\alpha_{k,l}| = |\beta_{k,l}| = 5$; E, $l = 1$, when $\mu_0 h = 0.05$ T, $|\alpha_{k,l}| = |\beta_{k,l}| = 5$.

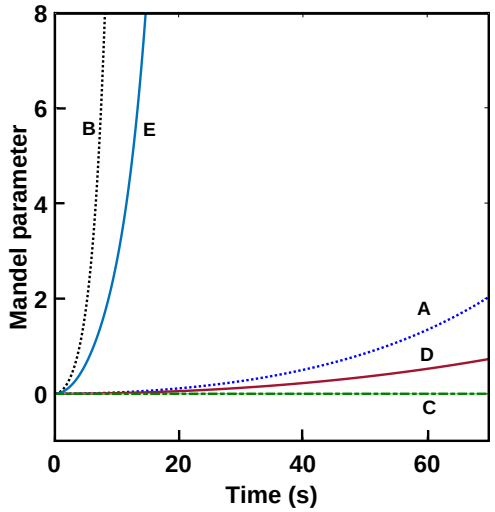

Figure 9.4: Mandel parameter $Q(t)$ as a function of time t for different values of the coherent state amplitudes and pumping field amplitudes, taking parameters for Permalloy with applied field 0.011 T and $\omega_p = 144$ GHz (see text). The lines correspond to: A, $l = 1$, when $\mu_0 h = 0.1$ T, $|\alpha_k| = 0$, $|\beta_k| = 0$; B, $l = 2$, when $\mu_0 h = 0.1$ T, $|\alpha_{k,l}| = 0$, $|\beta_{k,l}| = 0$; C, $l = 1$ or 2, when $h = 0$, $|\alpha_{k,l}| = |\beta_{k,l}| = 5$; D, $l = 1$, when $\mu_0 h = 0.05$ T, $|\alpha_{k,l}| = |\beta_{k,l}| = 2$; E, $l = 2$, when $\mu_0 h = 0.05$ T, $|\alpha_{k,l}| = |\beta_{k,l}| = 2$.

Although the general expression is complicated, we present in Fig. 9.4 numerical examples for the dependence of $Q_1(t)$ and $Q_2(t)$ on t and on coherent-state amplitudes $|\alpha_{k,l}|$ and $\beta_{k,l}|$ for different h. In the absence of a pumping field (see line C) the Mandel parameter is constant, as expected, with $Q_l(t) = 0$ corresponding to Poissonian statistics, even for coherent states. For the vacuum state with pumping included (see lines A and B) $Q_l(t)$ evolves to positive values when $t > 0$ for both magnons. Even when the pumping field is nonzero and the magnon states are coherent, as for lines D and E, we still find that the Mandel parameters evolve to positive values and increases monotonically with time, corresponding to the magnon-counting statistics being super-Poissonian when $t > 0$. A similar behavior was obtained with all other choices made for the coherent-state parameters, so we assume this is likely to be a general characteristic.

9.2.3 Two-mode quadrature squeezing

In the context of analyzing the quantum fluctuations in coupled two-mode systems (e.g., in quantum optics), the definition of squeezing is conventionally modified compared with that for the single-mode case. The appropriate definitions in the present case of two coupled magnon modes involve the quantities (e.g., see [154], page 182):

$$\sigma_I = \frac{1}{2^{3/2}}\left(c_{k_1,1} + c_{k_2,2} + c^\dagger_{k_1,1} + c^\dagger_{k_2,2}\right), \quad \sigma_{II} = \frac{1}{2^{3/2}i}\left(c_{k_1,1} + c_{k_2,2} - c^\dagger_{k_1,1} - c^\dagger_{k_2,2}\right). \tag{9.19}$$

These satisfy the commutation relation that $[\sigma_I, \sigma_{II}] \equiv \sigma_I\sigma_{II} - \sigma_{II}\sigma_I = i/2$ and their fluctuations obey the uncertainty relation

$$\Delta\sigma_I^2 \Delta\sigma_{II}^2 \geq 1/16, \tag{9.20}$$

where $\Delta\sigma_i^2 = \left\langle \sigma_i^2 \right\rangle - \langle\sigma_i\rangle^2$ $(i = I, II)$. In order to describe the compression degree of the i-th component of the magnon field, a squeezing parameter is then defined as

$$S_i = \Delta\sigma_i^2 - (1/4). \tag{9.21}$$

If $S_i < 0$ then the i-th component of the magnon field is said to be squeezed. From Eq. (9.19) we deduce that

$$\begin{aligned} S_I &= \frac{1}{4}\Big\{\langle c^\dagger_{k_1,1}c_{k_1,1}\rangle + \langle c^\dagger_{k_2,2}c_{k_2,2}\rangle + \langle c^\dagger_{k_1,1}c_{k_2,2}\rangle + \langle c_{k_1,1}c^\dagger_{k_2,2}\rangle \\ &+ \mathrm{Re}[\langle c^2_{k_1,1}\rangle + \langle c^2_{k_2,2}\rangle + 2\langle c_{k_1,1}c_{k_2,2}\rangle] - 2[\mathrm{Re}\langle c_{k_1,1}\rangle + \mathrm{Re}\langle c_{k_2,2}\rangle]^2\Big\}. \end{aligned} \tag{9.22}$$

There is a similar expression for S_{II}, but with Re replaced by Im. After substituting for the time-dependent averages in the above expression, we eventually find that the results simplify to

$$S_I = S_{II} = \frac{1}{4}[Y_1^2 + Y_2^2]. \tag{9.23}$$

Since S_I and S_{II} are both positive for $t > 0$ and increase with time, we conclude that there is no squeezing for the two modes. This contrasts with the property recently found for the individual modes in a bulk-magnon gas ([111] and Chapter 8), with the difference arising (in part) from the modified expressions for the quadrature operators in Eq. (9.19).

9.2.4 Cross correlation between the two modes

Another interesting statistical property of a two-mode field is the measure of cross correlation between the modes. As in quantum-optics applications (see, e.g., [155, 152, 153]), this can be quantified in terms of

$$\Delta_{cross}(t) = \langle c^\dagger_{k_1,1}(t)c_{k_1,1}(t)c^\dagger_{k_2,2}(t)c_{k_2,2}(t)\rangle - \langle c^\dagger_{k_1,1}(t)c_{k_1,1}(t)\rangle\langle c^\dagger_{k_2,2}(t)c_{k_2,2}(t)\rangle. \tag{9.24}$$

The four-operator average in the first term is

$$
\begin{aligned}
&\langle\psi(0)|c^{\dagger}_{k_1,1}(t)c_{k_1,1}(t)c^{\dagger}_{k_2,2}(t)c_{k_2,2}(t)|\psi(0)\rangle \\
&= \frac{1}{4}\Big\{(\alpha_1^* + \beta_1^*)(\alpha_1 + \beta_1)(\alpha_2^* + \beta_2^*)(\alpha_2 + \beta_2)X_1^2X_2^2 \\
&+[2 + (\alpha_1^* - \beta_1^*)(\alpha_1 - \beta_1)][2 + (\alpha_2^* - \beta_2^*)(\alpha_2 - \beta_2)]Y_1^2Y_2^2 \\
&+(\alpha_2^* + \beta_2^*)(\alpha_2 + \beta_2)(\alpha_1^{2*} + \alpha_1^2 - \beta_1^{2*} - \beta_1^2)X_1Y_1X_2^2 \\
&+(\alpha_1^* + \beta_1^*)(\alpha_1 + \beta_1)(\alpha_2^{2*} + \alpha_2^2 - \beta_2^{2*} - \beta_2^2)X_1^2X_2Y_2 \\
&+(\alpha_1^* + \beta_1^*)(\alpha_1 + \beta_1)[2 + (\alpha_2^* - \beta_2^*)(\alpha_2 - \beta_2)]X_1^2Y_2^2 \\
&+(\alpha_2^* + \beta_2^*)(\alpha_2 + \beta_2)[2 + (\alpha_1^* - \beta_1^*)(\alpha_1 - \beta_1)]Y_1^2X_2^2 \\
&+(\alpha_1^{2*} + \alpha_1^2 - \beta_1^{2*} - \beta_1^2)(\alpha_2^{2*} + \alpha_2^2 - \beta_2^{2*} - \beta_2^2)X_1Y_1X_2Y_2 \\
&+(\alpha_1^{2*} + \alpha_1^2 - \beta_1^{2*} - \beta_1^2)[(\alpha_2^* - \beta_2^*)(\alpha_2 - \beta_2) + 2]X_1Y_1Y_2^2 \\
&+(\alpha_2^{2*} + \alpha_2^2 - \beta_2^{2*} - \beta_2^2)[(\alpha_1^* - \beta_1^*)(\alpha_1 - \beta_1) + 2]Y_1^2X_2Y_2\Big\}, \qquad (9.25)
\end{aligned}
$$

and the components of the second term are just of the type already found in Subsection 9.2.2.

The above cross correlation is a measure of the coincidence counting of the magnons in mode 1 and mode 2 at time t and would (in principle) be measured by a Hanbury-Brown and Twiss type of experiment for interference between two different beams (one for each mode). If $\Delta_{cross}(t) = 0$ the two modes are uncorrelated. By contrast, if $\Delta_{cross}(t)$ is positive, the two modes are correlated, and if $\Delta_{cross}(t) < 0$ we say that the magnon modes 1 and 2 are anti-correlated, i.e., there would be no tendency for them to appear simultaneously.

From our analytic expressions (and confirmed by numerical calculations) we are able to conclude that the cross-correlation function vanishes identically *in the absence of* the four-magnon interactions, i.e., there is a cancellation between the two terms in Eq. (9.24) for all choices of the coherent states. Thus $\Delta_{cross}(t) = 0$ for the pumped system in the present case, but we will find later that this is modified when the four-magnon interactions are taken into account.

9.3 Inclusion of four-magnon interactions

We now examine the role of the four-magnon interaction Hamiltonian term H_4, which was briefly mentioned in Section 9.1. In particular, we are interested in how this term might modify the results for the dynamical and statistical properties found in Section 9.2. It will be shown that, when H_4 is

taken into account, certain of these properties are enhanced and some new results are obtained.

The general form of H_4 for a nanowire with $N = 2$ can be expressed (following [55, 103]) as

$$\begin{aligned} H_4 &= \sum_{l_1,l_2,l_3,l_4} \sum_{k,k',q} \Big(\Lambda_1 c^\dagger_{k,l_1} c^\dagger_{k',l_2} c_{q,l_3} c_{k+k'-q,l_4} \\ &+ \Lambda_2 c^\dagger_{k,l_1} c_{-k',l_2} c_{q,l_3} c_{k+k'-q,l_4} + \Lambda_3 c^\dagger_{k,l_1} c^\dagger_{k',l_2} c^\dagger_{-q,l_3} c_{k+k'-q,l_4} \\ &+ \Lambda_4 c^\dagger_{k,l_1} c^\dagger_{k',l_2} c^\dagger_{-q,l_3} c^\dagger_{-k-k'+q,l_4} + \Lambda_5 c_{-k,l_1} c_{-k',l_2} c_{q,l_3} c_{k+k'-q,l_4} \Big). \end{aligned} \tag{9.26}$$

Here the four-magnon coefficients $\Lambda_i \equiv \Lambda_i(k, k', q | l_1, l_2, l_3, l_4)$ (for $i = 1, 2, \cdots, 5$) are functions of the wave vectors and branch numbers and depend on the dipole-dipole and exchange parameters of the system. They will not be quoted here, but the expressions may be found in [55]. Next the above equation can be simplified by assuming a type of random-phase approximation (RPA) to decouple the products of the four operators into products of just two operators in all possible combinations [142, 143, 140]. A similar formal step was made in previous calculations for the quantum statistical properties of bulk magnons ([111, 136] and Chapter 8).

The total Hamiltonian can now be rewritten as $H = H_0 + H'$, where the perturbation term is $H' = H_p + H_{4d}$, with H_{4d} denoting the decoupled form of H_4. We then proceed formally to find the time dependence of the operators by following the same steps as in section 9.1, but with H' replacing the role of H_p. To summarize, it is found that the previous time evolution operator quoted in Section 9.1 becomes generalized such that W in Eq. (9.12) has the form

$$\begin{aligned} W &= (A + C)[a^\dagger_{k,1}(0) a^\dagger_{k,1}(0) - a_{k,1}(0) a_{k,1}(0) - b^\dagger_{k,1}(0) b^\dagger_{k,1}(0) b_{k,1}(0) b_{k,1}(0)] \\ &+ (B + C)[a^\dagger_{k,2}(0) a^\dagger_{k,2}(0) - a_{k,2}(0) a_{k,2}(0) - b^\dagger_{k,2}(0) b^\dagger_{k,2}(0) + b_{k,2}(0) b_{k,2}(0)] \\ &+ 2C(a^\dagger_{k,1}(0) a^\dagger_{k,2}(0) - b^\dagger_{k,1}(0) b^\dagger_{k,2}(0) - a_{k,1}(0) a_{k,2}(0) + b_{k,1}(0) b_{k,2}(0)). \end{aligned} \tag{9.27}$$

Here we have introduced the shorthand notations that $A = (ht/2)|P_{1,1}(k_1)|$, $B = (ht/2)|P_{2,2}(k_2)|$, and $C = \lambda(k)t/2$. We note that A and B are just the magnon pumping terms that arose previously and both are positive quantities by definition. The additional parts in Eq. (9.27) are described by the operator terms with factor C, which is also linear in t but has a proportionality factor $\lambda(k)$

that comes from the strength of the four-magnon interactions. In fact, $\lambda(k)$ can be expressed as a weighted summation (over wave vectors k' and q) of a linear combination of the Hamiltonian terms $\Lambda_i (i = 1, 2, 3, 4, 5)$. It would be impractical to evaluate such a summation here, so instead we treat $\lambda(k)$ as an effective parameter for the strength of the four-magnon interactions. Typically we expect its effect to be small compared to the pumping field coefficients, unless h is very small. In principle, depending on k, $\lambda(k)$ might be positive or negative.

It is clear that a new effect of the four-magnon interaction is to provide a coupling between the two branches 1 and 2 of the magnon spectrum, as can be seen in the last part of Eq. (9.27). Therefore we next seek a linear transformation between the various operators such that the interbranch coupling is removed in the representation with the new operators.

9.3.1 Operator transformation

We present an operator transformation to new boson operators to eliminate the coupling between the two branches, effectively to "diagonalize" W in Eq. (9.27). This can be achieved simply by defining new boson operators μ_1 and μ_2 as linear combinations of $a_{k,1}$ and $a_{k,2}$ as follows:

$$a_{k,1} = \cos(\eta)\mu_1 + \sin(\eta)\mu_2, \qquad a_{k,2} = \cos(\eta)\mu_2 + \sin(\eta)\mu_1. \tag{9.28}$$

Here η is a constant, taken to be real, and the same relations hold for the conjugates of these operators. Also we will assume analogous definitions of new boson operators ρ_1 and ρ_2 in terms of $b_{k,1}$ and $b_{k,2}$, with the same η. A solution consistent with these conditions can be found, as described below.

We proceed by transforming the operator terms in W as quoted in Eq. (9.27) above. It is straightforward to show that the interbranch part involves products of operators like $\mu^\dagger_{k,1}(0)\mu^\dagger_{k,2}(0)$ and $\mu_{k,1}(0)\mu_{k,2}(0)$. The condition for the coefficient of these interbranch terms to vanish enables us to solve for η, giving

$$\sin(2\eta) = -2C/(A + B + 2C). \tag{9.29}$$

For consistency (for η to be real), the right-hand side of the above expression must have magnitude less than unity, which will be the case provided $C > -(A+B)/4$. This is not a restrictive requirement, since we assume that the four-magnon interaction coefficient is typically small. If $C = 0$ we see that $\eta = 0$, whereas if $C < 0$ we have $0 < \eta < \pi/4$ and if $C > 0$ we have $-\pi/4 < \eta < 0$.

Next we require the transformed expression for W, which takes the form

$$\begin{aligned} W &= A'[\mu^\dagger_{k,1}(0)\mu^\dagger_{k,1}(0) - \mu_{k,1}(0)x_{k,1}(0) - \rho^\dagger_{k,1}(0)\rho^\dagger_{k,1}(0) + \rho_{k,1}(0)\rho_{k,1}(0)] \\ &+ B'[\mu^\dagger_{k,2}(0)\mu^\dagger_{k,2}(0) - \mu_{k,2}(0)x_{k,2}(0) - \rho^\dagger_{k,2}(0)\rho^\dagger_{k,2}(0) + \rho_{k,2}(0)\rho_{k,2}(0)]. \end{aligned} \tag{9.30}$$

where the modified coefficients A' and B' are given by

$$\begin{aligned} A' &= A\cos^2(\eta) + B\sin^2(\eta) + C[\cos(\eta) + \sin(\eta)]^2, \\ B' &= A\sin^2(\eta) + B\cos^2(\eta) + C[\cos(\eta) + \sin(\eta)]^2. \end{aligned} \tag{9.31}$$

When C is sufficiently small in magnitude, such that $|C| \ll (A+B)$, the approximate results are $A' \approx A + C$ and $B' \approx B + C$, with correction terms of order C^2. The general behavior is illustrated in Fig. 9.5 where we show A' and B' plotted against $C/(A+B)$. With the parameter values used in this example, we have $A = 0.0036$ and $B = 0.0476$. From the figure we see that $A' = B' = 0$ at $C = -(A+B)/4$, and there is no (real) solution when $C < -(A+B)/4$.

9.3.2 Modified time evolution

The time evolution operator can now be obtained using the expression for W quoted in Eq. (9.30) in terms of the new operators. Using $\mu_{k,l}(t) = U^{int}(t)^{-1}\mu_{k,l}(0)U^{int}(t)$ and a similar expression for $\rho_{k,l}(t)$, together with Eq. (8.4), we obtain

$$\begin{aligned} \mu_{k,1}(t) &= \mu_{k,1}(0)X' + \mu^\dagger_{k,1}(0)Y', \quad \rho_{k,1}(t) = \rho_{k,1}(0)X' - \rho^\dagger_{k,1}(0)Y', \\ \mu_{k,2}(t) &= \mu_{k,2}(0)X'' + \mu^\dagger_{k,2}(0)Y'', \quad \rho_{k,2}(t) = \rho_{k,2}(0)X'' - \rho^\dagger_{k,2}(0)Y''. \end{aligned} \tag{9.32}$$

Here we have denoted the modified time-dependent factors by

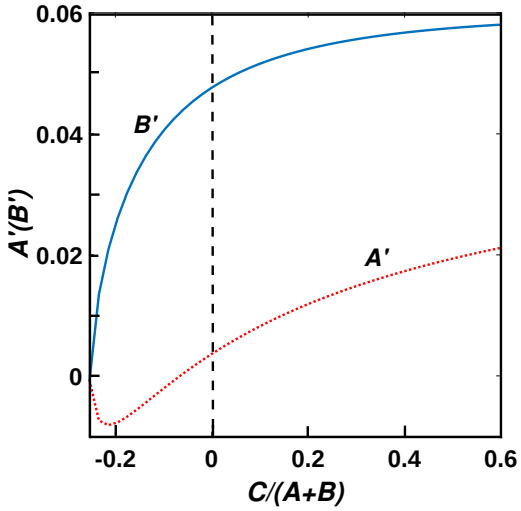

Figure 9.5: Modified coefficients A' and B' plotted versus $C/(A+B)$, taking Permalloy with the same pumping and wave-vector conditions as used in Fig. 9.2.

$$\begin{aligned} X' &= \cosh(A't), \qquad Y' = \sinh(A't), \\ X'' &= \cosh(B't), \qquad Y'' = \sinh(B't). \end{aligned} \tag{9.33}$$

We can use the above equations to deduce the time evolution of the $c_{k,l}(t)$ operators. Specifically, when $l = 1$ we eventually find from the inverse transformation to Eq. (9.28) that

$$\begin{aligned} c_{k_1,1}(t) = \; & \tfrac{1}{\sqrt{2}} e^{i\varphi_k} \Big\{ \Gamma_1 (a_{k_1,1}(0) + b_{k_1,1}(0)) + \Gamma_2 (a_{k_2,2}(0) + b_{k_2,2}(0)) \\ & + \Gamma_3 (a^\dagger_{k_1,1}(0) - b^\dagger_{k_1,1}(0)) + \Gamma_4 (a^\dagger_{k_2,2}(0) - b^\dagger_{k_2,2}(0)) \Big\}, \end{aligned} \tag{9.34}$$

where

$$\begin{aligned} \Gamma_1 &= [\cos^2(\eta) X' - \sin^2(\eta) X'']/\cos(2\eta), \quad \Gamma_2 = [X'' - X'] \tan(2\eta)/2, \\ \Gamma_3 &= [\cos^2(\eta) Y' - \sin^2(\eta) Y'']/\cos(2\eta), \quad \Gamma_4 = [Y'' - Y'] \tan(2\eta)/2. \end{aligned} \tag{9.35}$$

An analogous result is obtained for $l = 2$. It is easily verified from the above that, when $C = 0$, the expression in Eq. (9.13) for $c_{k,l}(t)$ in the absence of four-magnon interaction is recovered.

9.4 Modified dynamical properties

We may now investigate the temporal evolution of various magnon-state properties that were introduced in Section 9.2, including the influence of the four-magnon interactions on them.

9.4.1 Collapse and revival in the magnon numbers

The average number of magnons $\langle c^{\dagger}_{k_l,l}(t)c_{k_l,l}(t)\rangle$ can be recalculated using Eq. (9.34) for the modified time dependence of an operator instead of Eq. (9.13) as previously. Otherwise the theory is developed using the coherent-state representation for the magnon modes as was done in Subsection 9.2.1.

We begin by considering the statistics for the lower ($l = 1$) magnon branch, assuming an initial magnon state at $t = 0$ as a coherent state $|\alpha_{k_1,1}\beta_{k_1,1}\rangle$ as defined earlier. The result for the average number of magnons is found to be

$$\begin{aligned}\langle n_{k_1,1}(t)\rangle = (1/2)\Big\{&\Gamma_1^2(\alpha^*_{k_1,1}+\beta^*_{k_1,1})(\alpha_{k_1,1}+\beta_{k_1,1}) + \Gamma_2^2(\alpha^*_{k_2,2}+\beta^*_{k_2,2})(\alpha_{k_2,2}+\beta_{k_2,2})\\ &+\Gamma_3^2[2+(\alpha^*_{k_1,1}-\beta^*_{k_1,1})(\alpha_{k_1,1}-\beta_{k_1,1})] + \Gamma_4^2[2+(\alpha^*_{k_2,2}-\beta^*_{k_2,2})(\alpha_{k_2,2}-\beta_{k_2,2})]\\ &+\Gamma_1\Gamma_2[(\alpha^*_{k_1,1}+\beta^*_{k_1,1})(\alpha_{k_2,2}+\beta_{k_2,2})+\text{h.c.}] + \Gamma_1\Gamma_3[(\alpha^*_{k_1,1}+\beta^*_{k_1,1})(\alpha^*_{k_1,1}-\beta^*_{k_1,1})+\text{h.c.}]\\ &+\Gamma_1\Gamma_4[(\alpha^*_{k_1,1}+\beta^*_{k_1,1})(\alpha^*_{k_2,2}-\beta^*_{k_2,2})+\text{h.c.}] + \Gamma_2\Gamma_3[(\alpha^*_{k_2,2}+\beta^*_{k_2,2})(\alpha^*_{k_1,1}-\beta^*_{k_1,1})+\text{h.c.}]\\ &+\Gamma_2\Gamma_4[(\alpha^*_{k_2,2}+\beta^*_{k_2,2})(\alpha^*_{k_2,2}-\beta^*_{k_2,2})+\text{h.c.}] + \Gamma_3\Gamma_4[(\alpha^*_{k_2,2}-\beta^*_{k_2,2})(\alpha_{k_1,1}-\beta_{k_1,1})+\text{h.c.}]\Big\}. \quad (9.36)\end{aligned}$$

There is an analogous expression for the average $\langle n_{k_2,2}(t)\rangle$ of the magnon number operator for the second branch, obtained by replacing Γ_i with Γ'_i (where $i = 1, 2, 3, 4$) according to

$$\begin{aligned}\Gamma'_1 &= -\Gamma_2, \qquad \Gamma'_2 = [\cos^2(\eta)X'' - \sin^2(\eta)X']/\cos(2\eta),\\ \Gamma'_3 &= -\Gamma_4, \qquad \Gamma'_4 = [\cos^2(\eta)Y'' - \sin^2(\eta)Y']/\cos(2\eta). \quad (9.37)\end{aligned}$$

Numerical results obtained using Eq. (9.36) are presented in Fig. 9.6 where the average of the magnon number operator for the two branches ($l = 1, 2$) is plotted as a function of time t for different values of four-magnon coupling C. For the given coherent states values, the collapse-

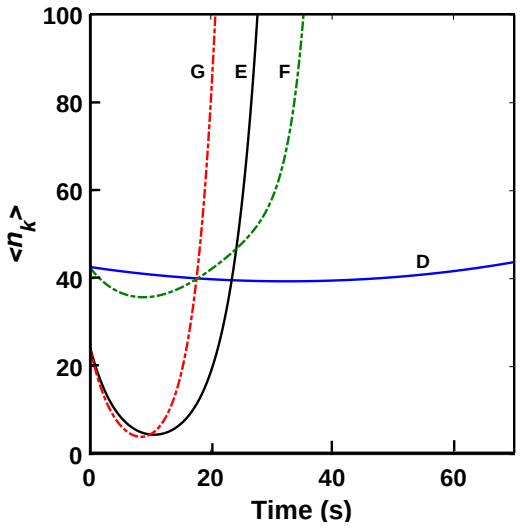

Figure 9.6: The average number of magnons as a function of time t for two different values of the four-magnon coupling C and for pumping field amplitude $\mu_0 h = 0.05$ T. Other parameters apply to Permalloy with the same values as in Fig. 9.2 The assumed coherent state is for $|\alpha_{k,l}| = |\beta_{k,2}| = 5$, $\epsilon_{k,1} = \epsilon_{k,2} = \pi/2$, and $\theta_{k,1} = \pi/4, \theta_{k,2} = 0$. The lines correspond to: D, $l = 1$, $C = 0$; E, $l = 2$, $C = 0$; F, $l = 1$, $C = (A + B)/5$; G, $l = 2$, $C = (A + B)/5$.

and-revival effect can be identified for both branches. From the figure, we can see the influence of the four-magnon interaction on the time evolution of the magnon occupation number. With the increasing value of four-magnon coupling C, the collapse-and-revival phenomenon is more pronounced. From the figure we see that, by tuning the nonlinearities introduced by the pumping field and four-magnon interaction in the system, we can manipulate the collapse and revival in the average number of magnons.

9.4.2 Magnon-counting statistics and quadrature squeezing

We now proceed to consider the influence of both the pumping field and the four-magnon term on the magnon statistics. As in Subsection 9.2.2 we employ the Mandel parameter defined in Eq. (9.17). In the absence of the parallel pumping field and the four-magnon coupling, we obtain a zero value for the Mandel parameter, $Q_l(t) = 0$, which corresponds to Poissonian statistics. With either the parallel pumping field or the four-magnon interaction being nonzero, the magnon statistics shows super-Poissonian behavior although the initial magnon state is Poissonian. Also by

varying either parallel pumping field or the four-magnon coupling coefficient, we can manipulate the magnitude of the $Q_l(t)$.

Next, we come to the quadrature squeezing of the magnons. For discussing the squeezing phenomenon for a two-mode magnon system, we use Eq. (9.22). The final result is given by

$$S_I = S_{II} = \frac{1}{4}\left[\Gamma_3^2 + \Gamma_3'^2 + \Gamma_4^2 + \Gamma_4'^2 + \Gamma_1\Gamma_1' + \Gamma_2\Gamma_2' + \Gamma_3\Gamma_3' + \Gamma_4\Gamma_4'\right]. \tag{9.38}$$

We have found, using the earlier definitions in Eqs. (9.35) and (9.37), that when $C \leq 0$ this result can be rewritten in a positive-definite form, meaning that the-two mode squeezing does not occur, even in the presence of four-magnon interactions. Through many numerical examples we find this also to be the case even when $C > 0$.

9.4.3 Cross correlation between the two modes

Here we consider the influence of the four-magnon interaction on the cross correlation between the two magnon modes. The definition of $\Delta_{cross}(t)$ as given by Eq. (9.24) is again employed, and we follow the corresponding steps to those described in Subsection 9.2.4. The outcome, however, is substantially different.

Figure 9.7 shows plots for the time evolution of the cross correlation function in the absence and presence of the four-magnon interaction. The two different cases in Fig. 9.7 (a) and (b) refer to different choices of coherent states, as examples. It is seen that in both cases $\Delta_{cross}(t)$ evolves to nonzero values for $t > 0$ whenever the four-magnon interactions are included ($C \neq 0$). By contrast, we found in Subsection 9.2.4 that in the absence of four-magnon interactions ($C = 0$) the magnon modes were uncorrelated with $\Delta_{cross}(t) = 0$ for all $t \geq 0$.

The numerical examples are with parameters applicable to Permalloy with the same conditions for the applied field and pumping field as in Fig. 9.2 (allowing the resonance conditions to be satisfied). The chosen parameters for the coherent states correspond to $|\alpha_{k,1}| = 1$, $|\alpha_{k,2}| = |\beta_{k,1}| = |\beta_{k,2}| = 0$, $\theta_{k,1} = \theta_{k,2} = 0$, and $\epsilon_{k,2} = 0$. The other phase term $\epsilon_{k,1}$ is chosen as 0 and π in Figs. 9.7(a)

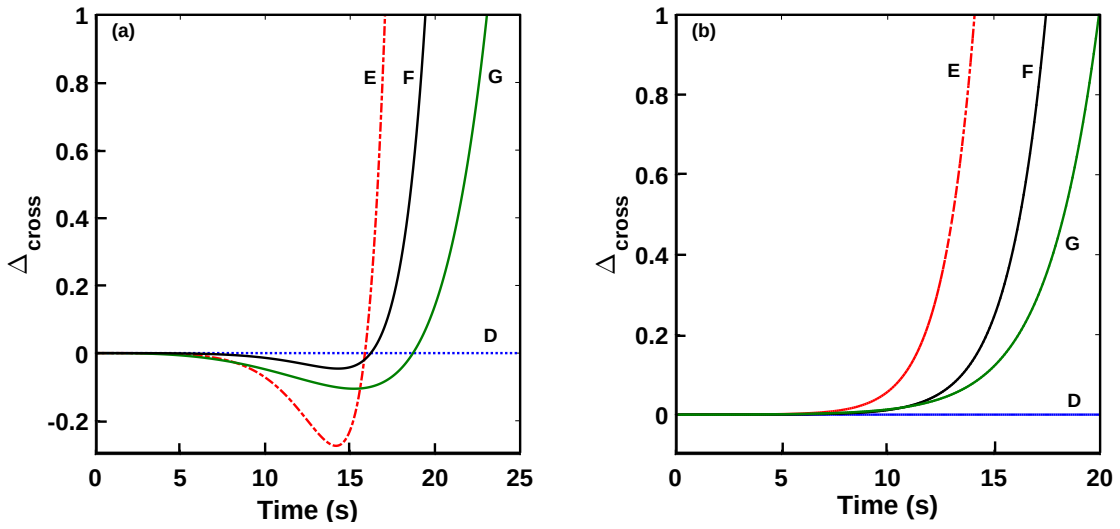

Figure 9.7: Time evolution of the cross correlation for several values of the four- magnon interaction coefficient C with $\mu_0 h = 0.05$ T and other parameters as for Permalloy (see text). The two cases correspond to different choices of phase term for the coherent states: (a) $\epsilon_{k,1} = 0$; (b) $\epsilon_{k,1} = \pi$. The lines correspond to: D, $C = 0$; E, $C = (A + B)/5$; F, $C = (A + B)/10$; G, $C = -(A + B)/10$.

and (b) respectively. We see that, with four-magnon interactions included, it is possible for $\Delta_{cross}(t)$ to take both negative and positive values, i.e., there may be anti-correlation as well as correlation generated between the two modes. This occurs with both positive and negative value of C. In other contexts, anti-correlations between pairs of modes, have been observed in light scattering by non-spherical particles [156] and also in ring lasers [157] when one mode is coherent and the other mode is chaotic above the threshold. Correlation effects between two modes are also encountered in quantum-optics systems [152]. In our present application to magnon modes, Fig. 9.7(a) shows an anti-correlation for small t (below about 15 or 20 s, depending on C); this occurs because the coefficient of the linear term proportional to t in a power series expansion has a negative coefficient when the coherent state has an appropriate phase (including the choice $\epsilon_{k,1} = 0$). The time scale for persistence of the anti-correlation can be shown to of order $(h|A'|)^{-1}$ or $(h|B'|)^{-1}$ (whichever is the larger), as can be deduced from the definitions of the time-dependent factors in Eq. (9.33). Over longer times there is a switching to correlation of the modes. It is remarkable that in comparison with the case with parallel pumping in the absence of four-magnon interaction, this system of two magnon modes shows both anti-correlation and correlation behavior.

It is interesting to note the behavior displayed by $\Delta_{cross}(t)$ in the special case of the magnons being described by the vacuum state (rather than a coherent state). The result is found from the general formalism presented here by setting $|\alpha_{k_l,l}| = |\beta_{k_l,l}| = 0$ for the mode amplitudes. With this simplification the cross correlation when four-magnon interactions are included is given by

$$\Delta_{cross}(t) \;=\; \Gamma_2\Gamma_4(\Gamma_3 - \Gamma_4')(\Gamma_1 - \Gamma_2') = \Big[\frac{\tan(2\eta)}{2\cos(2\eta)}\Big]^2 (X'' - X')^2\,(Y'' - Y')^2. \tag{9.39}$$

Here the last part of the expression was deduced by using the definitions in Eqs. (9.35) and (9.37), and the time dependence is contained in the X', X'', Y', and Y'' factors defined in Eq. (9.33). It is evident from the above expression that $\Delta_{cross}(t)$ is zero at $t = 0$ and positive (corresponding to correlation) whenever $t > 0$. The expression vanishes if $\eta = 0$, which means $C = 0$ for the coefficient of the four-magnon interactions. Also $\Delta_{cross}(t)$ increases with increasing $|\eta|$, irrespective of the sign of C. There is no anti-correlation effect found with the vacuum state, however, contrasting with the results shown in Fig. 9.7(a) for a coherent state.

9.5 Conclusions

In conclusion, we have studied the influence of both the parallel pumping and the four-magnon interactions on the quantum statistical properties of a two-mode magnon system. By applying the Holstein-Primakoff transformation, we first recast the spin Hamiltonian into an appropriate form in terms of creation and annihilation magnon operators $c_{k,l}^{\dagger}$ and $c_{k,l}$ for the two modes. The model included a general form of nonlinearity arising from both the parallel pumping field and the four-magnon terms. A general representation of the magnon modes in terms of coherent states was employed, as in our recent studies for bulk systems [111]. The specific application in the present work is to ferromagnetic nanowires, using Permalloy as an example.

We investigated various quantum statistical properties of the system. In particular, we found that both the parallel pumping field and the four-magnon interactions contribute to the phenomenon of collapse and then revival of the average magnon occupation number for the two modes ($l = 1, 2$).

We also found that parallel pumping, either with or without the four-magnon interactions, makes the magnon statistics evolve with time to be super-Poissonian. In terms of the definition of squeezing, as modified for two-mode systems, we found the effect to be absent in our model system. We also considered the cross correlation between the two magnon modes. In presence of the parallel pumping field but without the four-magnon interaction term, the modes were found to be uncorrelated with $\Delta_{cross}(t) = 0$ at all times. Remarkably, when the four-magnon interactions were included, we found that both anti-correlation and correlation effects were displayed at different times for appropriate choices of the coherent magnon states. By contrast, with the vacuum state and four-magnon interactions, only correlation effects can occur.

It would be of interest to modify the calculations here to apply to other nanostructures, such as ultrathin films, nanowires with larger size of cross section, or arrays of ferromagnetic nanostructures. Also our formalism can, in principle, be extended to systems with three- or multi-magnon modes, or to cases in the perpendicular pumping configuration (where the three-magnon interactions would need to be considered).

Chapter 10

Conclusions and future directions

In this thesis we have developed a microscopic (or Hamiltonian-based) theory to study SW properties of some low-dimensional ferromagnetic nanostructures, including their nonlinear behavior and the effects of microwave pumping. Until recently, most work in this field of magnetization dynamics had concentrated on spheres or films with dimensions of order several microns or more, and with the theoretical interpretation being made in terms of macroscopic (or continuum) methods. At smaller length scales, as in ultrathin films and nanowires with thicknesses or lateral dimensions less than about 100 nm, the discreteness of the quantized SWs and their spatial distributions near surfaces lead to important modifications, making it appropriate to employ a microscopic approach to the nonlinear dynamics of the material, described in terms of a lattice of effective spins. The microscopic method can be conveniently adapted for different sample geometries in terms of either individual magnetic elements or magnetic arrays (such as MCs). There is also the advantage that boundary conditions are incorporated naturally (in terms of either different or missing interactions near a surface), rather than being postulated phenomenologically, as is often done in macroscopic theories.

The spin Hamiltonian used for describing the systems studied here includes all the important interactions such as the exchange interaction, the magnetic dipole-dipole coupling, and the Zeeman energy of external magnetic fields applied in various directions. For the Permalloy multilayer

nanowires described in Chapter 4, the single-ion anisotropy, RKKY interaction, and the biquadratic exchange interaction are also important because of the interfaces.

The new results in this thesis fall broadly into three areas. Thus in Chapter 4 we obtained new results for linear SW properties across interfaces in composite NWs, where competing types of interface exchange were presented. Previous work on linear SWs had concentrated on trilayer films and much wider stripes. The narrower NWs considered here are of particular interest and novelty, because the shape anisotropy plays a much more important role and substantially modifies the features of the observed SWs giving additional optical SW modes. The FMR data were successfully accounted for in terms of our microscopic theory. It is also interesting that biquadratic exchange interaction became more pronounced due to the lateral edges effects.

Furthermore, in Chapters 2, 3, 5, 6 and 7 we presented a series of new results for the nonlinear instabilities (due to microwave pumping) of the SWs in NWs and ultrathin films. The previous work on the pumping of nonlinear dipole-exchange SWs had generally employed macroscopic theories. The smaller dimensions of the nanostructural NWs and films studied here are interesting because the spatial quantization of the eigenmodes become predominant and therefore our theory employs a microscopic method. Accordingly, our new results for the instability thresholds versus applied field (the butterfly curves) are significantly modified compared to those for macroscopic samples, and they show structural featured related to the discrete SW branches of the NWs. The SW properties for NWs and ultrathin films are also found to be quite different from one another, since they are characterized by 1D and 2D wave vectors, respectively. The material of Chapter 5 (which was published as a paper in Journal of Physics: Condensed Matter) was selected by the journal editors as a news highlight paper.

Finally, new results were obtained in Chapters 8 and 9 for the quantum statistical behavior of bulk and NW ferromagnets under pumping. This part of our work utilized the concept of coherent magnon states and was motivated by analogous results in quantum optics. Earlier studies on non-classical properties of magnons, such as squeezing effects, were reported for AFM materials. Mechanisms for magnon squeezing in ferromagnets were proposed by Peng (based on magnetic

anisotropy) [134, 135] and Wang (based on four-magnon interactions) [136] Our work on bulk magnons in Chapter 8 is of particular interest because we show that parallel pumping provides another mechanism to produce magnon squeezing effects. Moreover, the pumping field can be conveniently varied in an experiment, whereas the effective contribution of four-magnon interactions is fixed for a given material at a given temperature. In addition, we have shown that the pumping field can lead to the collapse in the average number of magnons and then revival at a later time. This is interesting since this phenomenon is absent if the field is considered classically. We also presented the first quantum-statistical calculations for two-mode magnon systems in Chapter 9, by analogy with two-mode bosons in quantum optics. The NW system studied here is noteworthy because four-magnon interactions were shown to lead to both anti-correlation and correlation effects between the two modes.

In terms of future research an interesting topic would be the BEC of magnons in nanostructures, typically ultrathin films, nanowires and arrays formed from these elements. The BEC experiment cited earlier were all for YIG films with thickness of several μm. Remarkably, they were all carried out at room temperature. Magnon-BEC has unique characteristics, however, making it different from the low-temperature atomic BEC, leading to potential new applications. This is because the high density of non-interacting bosons needed for creation of a magnon-BEC is achieved via external microwave pumping at high powers. The necessary theoretical framework needed to carry this out would be based on the same techniques as used in this thesis. For example, our assumed dipole-exchange Hamiltonian in Chapters 8 and 9 involved terms for both the parallel pumping and the four-magnon interactions, which are those typically employed for studying the BEC of magnons. Also our dispersion relation curves in Chapter 6 for compact NW samples (with cylindrical, tubular or square cross sections) show a more pronounced minimum of the first branch compared to those in the NW stripe or film cases. These characteristics would be important for work relating to BEC of magnons, where it is known that the minimum in the dispersion relation curves is important [122]. The role of magnon quantum coherence, as studied in our theoretical models in Chapters 8 and 9, is also believed to be essential for magnon-BEC. Hence our work pro-

vides the background steps for further investigations of BEC in various magnetic nanostructures. Currently the experiments on films are difficult, but the possibility of producing magnon-BEC states at room temperature in other nanostructures could have far-reaching impact in the new areas of quantum information, magnonics, and spintronics. BEC states are inherently coherent quantum states (motivating our studies in Chapters 8 and 9, and in [122]), which is a requirement for producing quantum bits. This, coupled with the fact that the technology of producing low-dimensional magnetic materials suitable for these applications is already well developed, makes this area of research extremely important and promising for the future of quantum technology and materials science.

Another possible extension of our work in this thesis is to explore more fully the effect of damping of the SWs, particularly in the instability process. In our calculations we introduced the role of energy dissipation into the rate equations for the operators via a phenomenological damping constant, following previous literature. In general, however, there are other ways (such as Green's function perturbation methods) available to evaluate the damping in a self-consistent formalism. For example, one approach would involve generalizing work in [55] by considering specific nonlinear mechanisms and different geometries.

Finally, another very interesting area of research is related to the frustrated spin systems. These systems typically have a highly-degenerate (but complicated) ground state. As a simple example, a system consisting of just three spin-1/2 particles on the vertices of a triangle, with a pair-wise AFM interaction between nearest neighbors, is called a frustrated system, since not all pairs can be simultaneously antiparallel, and it has a triply degenerate ground state. A general Green's function formalism could be used to study the SW excitations in more realistic frustrated systems (see, e.g., [158]), based on the microscopic dipole-exchange methodology developed here.

Appendix A

Equilibrium configuration of spins

By minimizing the energy functional E in Eq. (5.21) with respect to the canting angles $\{\alpha_n, \theta_n\}$, as explained in Subsection 5.1.2, we obtain the following two sets of equations (for $n = 1, 2, ...N$):

$$\begin{aligned}
&-S^2 \sum_m J_{n,m}(0)\,(-\sin\theta_n \sin\alpha_n \sin\theta_m \cos\alpha_m + \cos\alpha_n \sin\theta_n \sin\alpha_m \sin\theta_m) \\
&+g\mu_B H_0 S \sin\theta_n \sin\alpha_n + g^2\mu_B^2 S^2 \sum_m \Big(-D^{x,x}_{n,m}(0)\sin\theta_n \sin\alpha_n \sin\theta_m \cos\alpha_m \\
&-D^{x,y}_{n,m}(0)\sin\theta_n \sin\alpha_n \sin\alpha_m \sin\theta_m + D^{y,x}_{n,m}(0)\cos\alpha_n \sin\theta_n \sin\theta_m \cos\alpha_m \\
&+D^{y,y}_{n,m}(0)\cos\alpha_n \sin\theta_n \sin\alpha_m \sin\theta_m\Big) = 0,
\end{aligned} \tag{A.1}$$

and

$$\begin{aligned}
&-S^2 \sum_m J_{n,m}(0)\,(\cos\theta_n \cos\alpha_n \sin\theta_m \cos\alpha_m + \sin\alpha_n \cos\theta_n \sin\alpha_m \sin\theta_m - \sin\theta_n \cos\theta_m) \\
&-g\mu_B H_0 S \cos\theta_n \cos\alpha_n + g^2\mu_B^2 S^2 \sum_m \Big(D^{x,x}_{n,m}(0)\cos\theta_n \cos\alpha_n \sin\theta_m \cos\alpha_m \\
&+D^{x,y}_{n,m}(0)\cos\theta_n \cos\alpha_n \sin\alpha_m \sin\theta_m + D^{y,x}_{n,m}(0)\sin\alpha_n \cos\theta_n \sin\theta_m \cos\alpha_m \\
&+D^{y,y}_{n,m}(0)\sin\alpha_n \cos\theta_n \sin\alpha_m \sin\theta_m - D^{z,z}_{n,m}(0)\sin\theta_n \cos\theta_m\Big) = 0.
\end{aligned} \tag{A.2}$$

The canting angles $\{\alpha_n, \theta_n\}$ can be obtained by solving numerically the above coupled equations. Additionally an approximate analytic solution can be found as follows. Using the fact that the azimuthal angles $\{\alpha_n\}$ relative to the magnetic field direction are very small in most cases,

particularly if the aspect ratio $p = n_x/n_y$ is large, we can linearize Eq. (A.1) to yield

$$\begin{aligned} &-S\sum_m J_{n,m}(0)\left(\sin\theta_n\sin\theta_m\left(\alpha_m-\alpha_n\right)\right)+g\mu_B H_0\sin\theta_n\alpha_n \\ &+g^2\mu_B^2 S\sum_m\left(-D^{x,x}_{n,m}(0)\alpha_n+D^{y,x}_{n,m}(0)\sin\theta_n\sin\theta_m+D^{y,y}_{n,m}(0)\alpha_m\right)\sin\theta_n\sin\theta_m=0. \end{aligned} \tag{A.3}$$

If the polar angles $\{\theta_n\}$ are then approximated from Eq. (A.2) by assuming that $\theta_n = \theta$ for all n and small terms in α_n are neglected, we obtain

$$-g\mu_B H_0 S\cos\theta+g^2\mu_B^2 S^2\sum_m\left(D^{x,x}_{n,m}(0)\cos\theta\sin\theta-D^{z,z}_{n,m}(0)\sin\theta\cos\theta\right)=0, \tag{A.4}$$

which yields either $\cos\theta = 0$ or

$$\sin\theta=\frac{Ng\mu_B H_0}{g^2\mu_B^2 S\sum_{n,m}\left(D^{x,x}_{n,m}(0)-D^{z,z}_{n,m}(0)\right)}\,. \tag{A.5}$$

Appendix B

Hamiltonian coefficients in the transverse-field case

Here we quote the modified form of the coefficients $A^{(2)}_{n,m}(k)$ and $B^{(2)}_{n,m}(k)$ in the transverse-field case, replacing those in Eqs. (5.5) and (5.6) for a longitudinal applied field. The results are

$$\begin{aligned}
A^{(2)}_{n,m}(k) = \;& A_n\delta_{nm} - \tfrac{1}{2}S\,J_{n,m}(k)\,[\cos\theta_n\cos\theta_m\cos(\alpha_n-\alpha_m) + \sin\theta_n\sin\theta_m \\
& +\cos(\alpha_n-\alpha_m) - i\sin(\alpha_n-\alpha_m)(\cos\theta_m+\cos\theta_n)] \\
& +\tfrac{1}{2}g^2\mu_B^2 S\,[D^{x,x}_{n,m}(k)\,(\cos\theta_n\cos\alpha_n\cos\theta_m\cos\alpha_m + \sin\alpha_n\sin\alpha_m \\
& +\, i\cos\theta_n\cos\alpha_n\sin\alpha_m - i\cos\theta_m\cos\alpha_m\sin\alpha_n) \\
& +D^{x,y}_{n,m}(k)\,(\sin(\alpha_n+\alpha_m)\,(\cos\theta_n\cos\theta_m - 1) - i\cos(\alpha_n+\alpha_m)\,(\cos\theta_n-\cos\theta_m)) \\
& -D^{x,z}_{n,m}(k)\,(\cos\theta_n\cos\alpha_n\sin\theta_m + \sin\theta_n\cos\theta_m\cos\alpha_m + i\sin\theta_n\sin\alpha_m - i\sin\theta_m\sin\alpha_n) \\
& +D^{y,y}_{n,m}(k)\,(\sin\alpha_n\cos\theta_n\sin\alpha_m\cos\theta_m + \cos\alpha_n\cos\alpha_m \\
& +i\sin\alpha_m\cos\theta_m\cos\alpha_n - i\sin\alpha_n\cos\theta_n\cos\alpha_m) + D^{z,z}_{n,m}(k)\sin\theta_n\sin\theta_m \\
& -D^{y,z}_{n,m}(k)\,(\sin\alpha_n\cos\theta_n\sin\theta_m + \sin\theta_n\sin\alpha_m\cos\theta_m + i\cos\alpha_n\sin\theta_m - i\sin\theta_n\cos\alpha_m)\,],
\end{aligned} \tag{B.1}$$

with

$$
\begin{aligned}
A_n = \; & \sum_{p=1}^{N} \Big\{ S\, J_{n,p}(0) \left(\sin\theta_n \sin\theta_p \cos(\alpha_n - \alpha_p) + \cos\theta_n \cos\theta_p \right) + g\mu_B H_0 \sin\theta_n \cos\alpha_n \\
& - S\, g^2 \mu_B^2 \Big[D^{x,x}_{n,p}(0) \sin\theta_n \cos\alpha_n \sin\theta_p \cos\alpha_m + D^{x,y}_{n,m}(0) \sin(\alpha_n + \alpha_m) \sin\theta_n \sin\theta_m \\
& + D^{x,z}_{n,p}(0) \left(\sin\theta_n \cos\alpha_n \cos\theta_p + \cos\theta_n \sin\theta_p \cos\alpha_p \right) \\
& + D^{y,y}_{n,p}(0) \sin\alpha_n \sin\theta_n \sin\alpha_p \sin\theta_p + D^{y,z}_{n,p}(0) \left(\sin\alpha_n \sin\theta_n \cos\theta_p + \cos\theta_n \sin\alpha_p \sin\theta_p \right) \\
& + D^{z,z}_{n,p}(0) \cos\theta_n \cos\theta_p \Big] \Big\} \,,
\end{aligned}
\tag{B.2}
$$

and

$$
\begin{aligned}
B^{(2)}_{n,m}(k) = \; & -\tfrac{S}{4} J_{n,m}(k) \left[(\cos\theta_n \cos\theta_m - 1) \cos(\alpha_n - \alpha_m) + \sin\theta_n \sin\theta_m \right. \\
& \left. + i \left(\sin(\alpha_n - \alpha_m)(\cos\theta_n - \cos\theta_m) \right) \right] \\
& + \tfrac{S}{4} g^2 \mu_B^2 \left[(D^{x,x}_{n,m}(k) \cos\theta_n \cos\alpha_n \cos\theta_m \cos\alpha_m - \sin\alpha_n \sin\alpha_m \right. \\
& - i \cos\theta_n \cos\alpha_n \sin\alpha_m - i \sin\alpha_n \cos\theta_m \cos\alpha_m) \\
& + D^{x,y}_{n,m}(k) \left(\cos\theta_m \cos\alpha_m \sin\alpha_n \cos\theta_n + \sin\alpha_m \cos\alpha_n \right. \\
& \left. + i \cos\theta_n \cos\alpha_n \cos\alpha_m - i \sin\alpha_n \cos\theta_n \sin\alpha_m \right) \\
& + D^{y,x}_{n,m}(k) \left(\cos\theta_n \cos\alpha_n \sin\alpha_m \cos\theta_m + \sin\alpha_n \cos\alpha_m \right. \\
& \left. + i \cos\theta_m \cos\alpha_m \cos\alpha_n - i \sin\alpha_m \cos\theta_m \sin\alpha_n \right) + D^{z,z}_{n,m}(k) \sin\theta_n \sin\theta_m \\
& - D^{x,z}_{in,jm}(k) \left(\sin\theta_n \cos\theta_m \cos\alpha_m + \sin\theta_m \cos\theta_n \cos\alpha_n - i \sin\theta_n \sin\alpha_m - i \sin\theta_m \sin\alpha_n \right) \\
& - D^{y,z}_{n,m}(k) \left(\sin\alpha_n \cos\theta_n \sin\theta_m + \sin\alpha_m \cos\theta_m \sin\theta_n + i \cos\alpha_n \sin\theta_m + i \cos\alpha_m \sin\theta_n \right) \\
& + D^{y,y}_{n,m} \left(\sin\alpha_n \cos\theta_n \sin\alpha_m \cos\theta_m - \cos\alpha_n \cos\alpha_m \right. \\
& \left. \left. + i \sin\alpha_n \cos\theta_n \cos\alpha_m + i \cos\alpha_n \sin\alpha_m \cos\theta_m \right) \right] .
\end{aligned}
\tag{B.3}
$$

Appendix C

Three- and four-magnon weighting factors

The expressions for the amplitude factors $V_1(\mathbf{k},\mathbf{q}|l_1,l_2,l_3)$ and $V_2(\mathbf{k},\mathbf{q}|l_1,l_2,l_3)$ in Eq. (7.11) for the three-magnon Hamiltonian $H^{(3)}$ are

$$\begin{aligned} V_1(\mathbf{q}|l_1,l_2,l_3) &= \sum_{n,m}\Big\{-A^{(3)}_{n,m}(0)S^{\star}_{m+N,l_1}(\mathbf{q})S^{\star}_{m,l_2}(-\mathbf{q})S_{n+N,l_3}(0) + A^{(3)}_{n,m}(\mathbf{q})S^{\star}_{n,l_1}(\mathbf{q})S^{\star}_{m+N,l_2}(-\mathbf{q})S_{m+N,l_3}(0) \\ &+ A^{(3)}_{n,m}(\mathbf{q})S^{\star}_{n,l_1}(\mathbf{q})S^{\star}_{m,l_2}(-\mathbf{q})S_{m,l_3}(0) + A^{(3)\star}_{n,m}(\mathbf{q})S^{\star}_{m+N,l_1}(\mathbf{q})S^{\star}_{n+N,l_2}(-\mathbf{q})S_{n+N,l_3}(0) \\ &+ A^{(3)\star}_{n,m}(\mathbf{q})S^{\star}_{m+N,l_1}(\mathbf{q})S^{\star}_{n,l_2}(-\mathbf{q})S_{n,l_3}(0) - A^{(3)\star}_{n,m}(0)S^{\star}_{m+N,l_1}(\mathbf{q})S^{\star}_{n,l_2}(-\mathbf{q})S_{m,l_3}(0)\Big\}, \quad \text{(C.1)} \end{aligned}$$

$$\begin{aligned} V_2(\mathbf{q}|l_1,l_2,l_3) &= \sum_{n,m}\Big\{A^{(3)}_{n,m}(\mathbf{q})S^{\star}_{m+N,l_1}(\mathbf{q})S^{\star}_{n+N,l_2}(-\mathbf{q})S_{n+N,l_3}(0) + A^{(3)}_{n,m}(\mathbf{q})S^{\star}_{n,l_1}(\mathbf{q})S^{\star}_{m+N,l_2}(-\mathbf{q})S_{m,l_3}(0) \\ &+ A^{(3)}_{n,m}(\mathbf{q})S^{\star}_{n+N,l_1}(\mathbf{q})S^{\star}_{m,l_2}(-\mathbf{q})S_{m,l_3}(0) + A^{(3)\star}_{n,m}(\mathbf{q})S^{\star}_{m+N,l_1}(\mathbf{q})S^{\star}_{n+N,l_2}(-\mathbf{q})S_{n,l_3}(0) \\ &+ A^{(3)\star}_{n,m}(\mathbf{q})S^{\star}_{m,l_1}(\mathbf{q})S^{\star}_{n+N,l_2}(-\mathbf{q})S_{n+N,l_3}(0) + A^{(3)\star}_{n,m}(\mathbf{q})S^{\star}_{m,l_1}(\mathbf{q})S^{\star}_{n,l_2}(-\mathbf{q})S_{m,l_3}(0)\Big\}, \quad \text{(C.2)} \end{aligned}$$

There are analogous expressions for the terms V_3 and V_4, but we will not quote them here, since they are not required for the nonlinear instabilities.

Likewise, the only amplitude term of importance in Eq. (7.12) for the four-magnon Hamiltonian $H^{(4)}$ is found to be

$$\Lambda_1\left(\mathbf{k},\mathbf{k}^{'},\mathbf{q}|l_1,l_2,l_3,l_4\right)=\sum_{n,m}\left\{\lambda_{1A}\left(n,m\right)+\lambda_{1B}\left(n,m\right)+\lambda_{1C}\left(n,m\right)+\lambda_{1D}\left(n,m\right)\right\}, \tag{C.3}$$

where

$$\begin{aligned}
\lambda_{1A}\left(n,m\right) &= A^{(4)}_{n,m}(-\mathbf{q})S^{\star}_{m+N,l_1}(-\mathbf{k})S^{*}_{m+N,l_2}(-\mathbf{k}^{'})S_{n+N,l_3}(\mathbf{q})S_{m+N,l_4}(\mathbf{k}+\mathbf{k}^{'}-\mathbf{q})\\
&+A^{(4)}_{n,m}(-\mathbf{k}-\mathbf{k}^{'}+\mathbf{q})S^{\star}_{m+N,l_1}(-\mathbf{k})S^{\star}_{m,l_2}(-\mathbf{k}^{'})S_{m,l_3}(\mathbf{q})S_{n+N,l_4}(\mathbf{k}+\mathbf{k}^{'}-\mathbf{q})\\
&+A^{(4)}_{n,m}(-\mathbf{q})S^{\star}_{m+N,l_1}(-\mathbf{k})S^{\star}_{m,l_2}(-\mathbf{k}^{'})S_{n+N,l_3}(\mathbf{q})S_{m,l_4}(\mathbf{k}+\mathbf{k}^{'}-\mathbf{q})\\
&+A^{(4)}_{n,m}(\mathbf{k})S^{\star}_{n,l_1}(-\mathbf{k})S^{\star}_{m+N,l_2}(-\mathbf{k}^{'})S_{m,l_3}(\mathbf{q})S_{m+N,l_4}(\mathbf{k}+\mathbf{k}^{'}-\mathbf{q})\\
&+A^{(4)}_{n,m}(\mathbf{k})S^{\star}_{n,l_1}(-\mathbf{k})S^{\star}_{m+N,l_2}(-\mathbf{k}^{'})S_{m+N,l_3}(\mathbf{q})S_{m,l_4}(\mathbf{k}+\mathbf{k}^{'}-\mathbf{q})\\
&+A^{(4)}_{n,m}(\mathbf{k})S^{\star}_{n,l_1}(-\mathbf{k})S^{\star}_{m,l_2}(-\mathbf{k}^{'})S_{m,l_3}(\mathbf{q})S_{m,l_4}(\mathbf{k}+\mathbf{k}^{'}-\mathbf{q})\\
&+A^{(4)}_{n,m}(-\mathbf{k})S^{*}_{m+N,l_1}(-\mathbf{k})S^{\star}_{n+N,l_2}(-\mathbf{k}^{'})S_{n+N,l_3}(\mathbf{q})S_{n+N,l_4}(\mathbf{k}+\mathbf{k}^{'}-\mathbf{q})\\
&+A^{(4)}_{n,m}(\mathbf{k}+\mathbf{k}^{'}-\mathbf{q})S^{*}_{n+N,l_1}(-\mathbf{k})S^{*}_{n,l_2}(-\mathbf{k}^{'})S_{n+N,l_3}(\mathbf{q})S_{m,l_4}(\mathbf{k}+\mathbf{k}^{'}-\mathbf{q})\\
&+A^{(4)}_{n,m}(-\mathbf{k})S^{\star}_{m+N,l_1}(-\mathbf{k})S^{\star}_{n,l_2}(-\mathbf{k}^{'})S_{n+N,l_3}(\mathbf{q})S_{n,l_4}(\mathbf{k}+\mathbf{k}^{'}-\mathbf{q})\\
&+A^{(4)}_{n,m}(\mathbf{q})S^{\star}_{n,l_1}(-\mathbf{k})S^{\star}_{n+N,l_2}(-\mathbf{k}^{'})S_{m,l_3}(\mathbf{q})S_{n+N,l_4}(\mathbf{k}+\mathbf{k}^{'}-\mathbf{q})\\
&+A^{(4)}_{n,m}(-\mathbf{k})S^{\star}_{m+N,l_1}(-\mathbf{k})S^{\star}_{n,l_2}(-\mathbf{k}^{'})S_{n+N,l_3}(\mathbf{q})S_{n,l_4}(\mathbf{k}+\mathbf{k}^{'}-\mathbf{q})\\
&+A^{(4)}_{n,m}(\mathbf{q})S^{\star}_{n,l_1}(-\mathbf{k})S^{\star}_{n,l_2}(-\mathbf{k}^{'})S_{m,l_3}(\mathbf{q})S_{n,l_4}(\mathbf{k}+\mathbf{k}^{'}-\mathbf{q}),
\end{aligned} \tag{C.4}$$

$$\begin{aligned}
\lambda_{1B}\left(n,m\right) &= B^{(4)}_{n,m}(-\mathbf{k}-\mathbf{q})S^{\star}_{m+N,l_1}(-\mathbf{k})S^{\star}_{n+N,l_2}(-\mathbf{k}^{'})S_{m+N,l_3}(\mathbf{q})S_{n+N,l_4}(\mathbf{k}+\mathbf{k}^{'}-\mathbf{q})\\
&+B^{(4)}_{n,m}(\mathbf{k}+\mathbf{k}^{'})S^{\star}_{n+N,l_1}(-\mathbf{k})S^{\star}_{n,l_2}(-\mathbf{k}^{'})S_{m+N,l_3}(\mathbf{q})S_{m,l_4}(\mathbf{k}+\mathbf{k}^{'}-\mathbf{q})\\
&+B^{(4)}_{n,m}(-\mathbf{k}-\mathbf{q})S^{\star}_{m+N,l_1}(-\mathbf{k})S^{\star}_{n,l_2}(-\mathbf{k}^{'})S_{m+N,l_3}(\mathbf{q})S_{n,l_4}(\mathbf{k}+\mathbf{k}^{'}-\mathbf{q})\\
&+B^{(4)}_{n,m}(\mathbf{q})S^{\star}_{m,l_1}(-\mathbf{k})S^{\star}_{n+N,l_2}(-\mathbf{k}^{'})S_{n+N,l_3}(\mathbf{q})S_{m,l_4}(\mathbf{k}+\mathbf{k}^{'}-\mathbf{q})\\
&+B^{(4)}_{n,m}(\mathbf{q})S^{\star}_{m,l_1}(-\mathbf{k})S^{\star}_{m+N,l_2}(-\mathbf{k}^{'})S_{n+N,l_3}(\mathbf{q})S_{n,l_4}(\mathbf{k}+\mathbf{k}^{'}-\mathbf{q})\\
&+B^{(4)}_{n,m}(\mathbf{q})S^{\star}_{m,l_1}(-\mathbf{k})S^{\star}_{n,l_2}(-\mathbf{k}^{'})S_{m,l_3}(\mathbf{q})S_{n,l_4}(\mathbf{k}+\mathbf{k}^{'}-\mathbf{q}),
\end{aligned} \tag{C.5}$$

$$
\begin{aligned}
\lambda_{1C}(n,m) &= C^{(4)}_{n,m}(\mathbf{q})S^{\star}_{n,l_1}(-\mathbf{k})S^{\star}_{n+N,l_2}(-\mathbf{k}')S_{m,l_3}(\mathbf{q})S_{n+N,l_4}(\mathbf{k}+\mathbf{k}'-\mathbf{q}) \\
&\quad + C^{(4)}_{n,m}(\mathbf{k})S^{\star}_{n+N,l_1}(-\mathbf{k})S^{\star}_{n,l_2}(-\mathbf{k}')S_{m+N,l_3}(\mathbf{q})S_{n+N,l_4}(\mathbf{k}+\mathbf{k}'-\mathbf{q}) \\
&\quad + C^{(4)}_{n,m}(\mathbf{q})S^{\star}_{n,l_1}(-\mathbf{k})S^{\star}_{n,l_2}(-\mathbf{k}')S_{m+N,l_3}(\mathbf{q})S_{n,l_4}(\mathbf{k}+\mathbf{k}'-\mathbf{q}) \\
&\quad + C^{(4)}_{n,m}(-\mathbf{k})S^{\star}_{m,l_1}(-\mathbf{k})S^{\star}_{n+N,l_2}(-\mathbf{k}')S_{n+N,l_3}(\mathbf{q})S_{n+N,l_4}(\mathbf{k}+\mathbf{k}'-\mathbf{q}) \\
&\quad + C^{(4)}_{n,m}(-\mathbf{k}')S^{\star}_{n,l_1}(-\mathbf{k})S^{\star}_{m,l_2}(-\mathbf{k}')S_{n+N,l_3}(\mathbf{q})S_{n,l_4}(\mathbf{k}+\mathbf{k}'-\mathbf{q}) \\
&\quad + C^{(4)}_{n,m}(-\mathbf{k})S^{\star}_{m,l_1}(-\mathbf{k})S^{\star}_{n,l_2}(-\mathbf{k}')S_{n+N,l_3}(\mathbf{q})S_{n,l_4}(\mathbf{k}+\mathbf{k}'-\mathbf{q}), \qquad \text{(C.6)}
\end{aligned}
$$

$$
\begin{aligned}
\lambda_{1D}(n,m) &= D^{(4)}_{n,m}(-\mathbf{k})S^{\star}_{m+N,l_1}(-\mathbf{k})S_{n+N,l_2}(-\mathbf{k}')S^{*}_{m,l_3}(\mathbf{q})S_{n+N,l_4}(\mathbf{k}+\mathbf{k}'-\mathbf{q}) \\
&\quad + D^{(4)}_{n,m}(-\mathbf{k})S^{\star}_{m+N,l_1}(-\mathbf{k})S_{n+N,l_2}(-\mathbf{k}')S^{*}_{n+N,l_3}(\mathbf{q})S_{n,l_4}(\mathbf{k}+\mathbf{k}'-\mathbf{q}) \\
&\quad + D^{(4)}_{n,m}(\mathbf{k}+\mathbf{k}'-\mathbf{q})S^{\star}_{n+N,l_1}(-\mathbf{k})S_{n+N,l_2}(-\mathbf{k}')S^{*}_{n+N,l_3}(\mathbf{q})S_{m,l_4}(\mathbf{k}+\mathbf{k}'-\mathbf{q}) \\
&\quad + D^{(4)}_{n,m}(-\mathbf{k})S^{\star}_{m+N,l_1}(-\mathbf{k})S_{n,l_2}(-\mathbf{k}')S^{*}_{n,l_3}(\mathbf{q})S_{n,l_4}(\mathbf{k}+\mathbf{k}'-\mathbf{q}) \\
&\quad + D^{(4)}_{n,m}(\mathbf{k}+\mathbf{k}'-\mathbf{q})S^{\star}_{m+N,l_1}(-\mathbf{k})S_{n,l_2}(-\mathbf{k}')S^{*}_{m,l_3}(\mathbf{q})S_{m,l_4}(\mathbf{k}+\mathbf{k}'-\mathbf{q}) \\
&\quad + D^{(4)}_{n,m}(-\mathbf{q})S^{\star}_{n+N,l_1}(-\mathbf{k})S_{n,l_2}(-\mathbf{k}')S^{*}_{m,l_3}(\mathbf{q})S_{n,l_4}(\mathbf{k}+\mathbf{k}'-\mathbf{q})\Big\}. \qquad \text{(C.7)}
\end{aligned}
$$

Appendix D

Frequencies of the $N = 2$ magnon modes

The expressions for the linearized magnon frequencies $\omega_{k,l}$ ($l = 1, 2$), as used for a $N = 2$ nanowire in Chapter 9, are

$$\omega_{k,l} = \left[\left(A_{1,1}(k) + (-1)^l A_{1,2}(k) \right)^2 - 4 \left(B_{1,1}(k) + (-1)^l B_{1,2}(k) \right)^2 \right]^{1/2}, \tag{D.1}$$

where

$$\begin{aligned} A_{1,1}(k) &= g\mu_B H_0 + S\left[J_{1,1}(0) + J_{1,2}(0) - J_{1,1}(k) \right] \\ &- S g^2 \mu_B^2 [D^{z,z}_{1,1}(0) + D^{z,z}_{1,2}(0) + \frac{1}{2} D^{z,z}_{1,1}(k)], \end{aligned} \tag{D.2}$$

$$A_{1,2}(k) = -S J_{1,2}(k) - \frac{1}{2} S g^2 \mu_B^2 D^{z,z}_{1,2}(k), \tag{D.3}$$

$$B_{1,1}(k) = \frac{1}{4} S g^2 \mu_B^2 [D^{x,x}_{1,1}(k) - D^{y,y}_{1,1}(k)], \tag{D.4}$$

$$B_{1,2}(k) = \frac{1}{4} S g^2 \mu_B^2 [D^{x,x}_{1,2}(k) - D^{y,y}_{1,2}(k)]. \tag{D.5}$$

Here S is the spin quantum number, while $J_{1,1}(k)$ and $J_{1,2}(k)$ are wave-vector Fourier components of the intra-line and inter-line exchange, respectively. Their respective values are $2J\cos(ka)$ and

J, where J is the exchange constant coupling nearest neighbors only. Correspondingly, $D^{\nu,\nu}_{1,1}(k)$ and $D^{\nu,\nu}_{1,2}(k)$ refer to intra-line and inter-line dipole sums [87, 55], where $\nu = x, y$ or z. The lines of spins are taken to be in the xz plane with the lines parallel to the z axis. The dipole sums can be evaluated numerically.

Bibliography

[1] J. M. D Coey. *Magnetism and Magnetic Materials*. Cambridge University Press, 2010.

[2] R. C. Ohandley. *Modern Magnetic Materials: Principles and Applications*. Wiley, 1999.

[3] V. V. Kruglyak, S. O. Demokritov, and D. Grundler. *J. Phys. D: Appl. Phys.*, 43:264001, 2010.

[4] S. O. Demokritov and A. N. Slavin (Eds.). *Magnonics: From Fundamentals to Applications*. Springer, 2013.

[5] A. Thiaville B. Hillebrands (Eds.). *Spin Dynamics in Confined Magnetic Structures III*. Springer, 2006.

[6] G. Binasch, P. Grünberg, F. Saurenbach, and W. Zinn. *Phys. Rev. B*, 39:4828, 1989.

[7] M. N. Baibich, J. M. Broto, A. Fert, F. Nguyen van Dau, F. Petroff, P. Etienne, G. Creuzet, A. Friederich, and J. Chazelas. *Phys. Rev. Lett*, 61:2472, 1988.

[8] D. L. Mills and J. A. C. Bland (Eds.). *Nanomagnetism: Ultrathin Films, Multilayers and Nanostructures*. Elsevier, 2006.

[9] J. D. Jackson. *Classical Electrodynamics (3th Edition)*. Wiley, 1998.

[10] N. W. Ashcroft and N. D. Mermin. *Solid State Physics*. Saunders, 1976.

[11] D. C. Mattis. *The Theory of Magnetism I*. Springer, 1981.

[12] R. M. White. *Quantum Theory of Magnetism*. Springer, 2007.

[13] M. G. Cottam and D.R. Tilley. *Introduction to Surface and Superlattice Excitations*. IoP Publishing, 2005.

[14] K. Yosida. *Theory of Magnetism*. Springer, 1996.

[15] M. G. Cottam and D. J. Lockwood. *Light Scattering in Magnetic Solids*. Wiley, 1986.

[16] M. A. Ruderman and C. Kittel. *Phys. Rev.*, 96:99, 1954.

[17] T. Kasuya. *Progr. Theor. Exp. Phys.*, 16:45, 1956.

[18] K. Yosida. *Phys. Rev.*, 106:893, 1957.

[19] T. Kasuya. *Progr. Theor. Exp. Phys.*, 16:58, 1956.

[20] S. Neusser and D. Grundler. *Advanced Materials*, 21:2927, 2009.

[21] M. P. Kostylev, A. A. Serga, T. Schneider, B. Leven, and B. Hillebrands. *Appl. Phys. Lett*, 87:153501, 2005.

[22] S. M. Rezende, A. Azevedo, and F. M. de Aguiar. Spin-wave instabilities, auto-oscillations, chaos and control of chaos in yig spheres. In M. G. Cottam, editor, *Linear and Nonlinear Spin Waves in Magnetic Films and Superlattices*, page 335. World Scientific, 1994.

[23] I. E. Dzyaloshinskii. *Sov. Phys. JETP*, 10:628, 1960.

[24] T. Moriya. *Phys. Rev.*, 120:91, 1960.

[25] M. G. Cottam and A. N. Slavin. Fundamentals of linear and nonlinear spin-wave processes in bulk and finite magnetic samples. In M. G. Cottam, editor, *Linear and Nonlinear Spin Waves in Magnetic Films and Superlattices*. World Scientific, 1994.

[26] P. E Wigen. *Nonlinear Phenomena and Chaos in Magnetic Materials*. World scientific, 1994.

[27] D. D. Stancil and A. Prabhakar. *Spin Waves: Theory and Applications*. Springer, 2009.

[28] A. G. Gurevich and G. A. Melkov. *Magnetization Oscillations and Waves*. CRC Press, 1996.

[29] F. Bloch. *Z. Phys.*, 61:206, 1930.

[30] G. Heller and H. A. Kramers. *Proc. K. Akad. Wet.*, 37:378, 1934.

[31] T. Holstein and H. Primakoff. *Phys. Rev.*, 58:1098, 1940.

[32] C. Kittel. *Introduction to Solid State Physics (8th Edition)*. Wiley, 2005.

[33] A. S. Arrott. Magnetism in si units and gaussian units. In J. A. C. Bland and B. Heinrich, editors, *Ultrathin Magnetic Structures I: An Introduction to the Electronic, Magnetic and Structural Properties*, page 349. Springer, 1994.

[34] J. J. Sakurai and J. J. Napolitano. *Modern Quantum Mechanics*. Pearson, 2013.

[35] M. G. Cottam. *Dynamical Properties in Nanostructured and Low-Dimensional Materials*. IoP Publishing, 2015.

[36] R. W. Damon and J. R. Eshbach. *J. Phys. Chem. Solids*, 19:308, 1961.

[37] J. R. Eshbach and R. W. Damon. *Phys. Rev.*, 118:1208, 1960.

[38] P. Kabos, W. D. Wilber, C. E. Patton, and P. Grunberg. *Phys. Rev. B*, 29:6396, 1984.

[39] N. Bloembergen and R. W. Damon. *Phys. Rev.*, 85:699, 1952.

[40] N. Bloembergen and S. Wang. *Phys. Rev.*, 93:72, 1954.

[41] H. Suhl. *J. Phys. Chem. Solids*, 1:209, 1957.

[42] F. R. Morgenthaler. *J. Appl. Phys*, 31:S95, 1960.

[43] E. Schlömann, J. J. Green, and U. Milano. *J. Appl. Phys.*, 31, 1960.

[44] B. Hillebrands and K. Ounadjela. *Spin Dynamics in Confined Magnetic Structures I*. Springer, 2003.

[45] G. Gubbiotti, S. Tacchi, G. Carlotti, P. Vavassori, N. Singh, S. Goolaup, A. O. Adeyeye, A. Stashkevich, and M. Kostylev. *Phys. Rev. B*, 72:224413, 2005.

[46] G. Gubbiotti, S. Tacchi, M. Madami, G. Carlotti, A. O. Adeyeye, and M. Kostylev. *J. Phys. D: Appl. Phys.*, 43:264003, 2010.

[47] S. Tacchi, G. Gubbiotti, M. Madami, and G. Carlotti. *J. Phys. Condens. Matter*, 29:073001, 2016.

[48] R. Urban, G. Woltersdorf, and B. Heinrich. *Phys. Rev. Lett.*, 87:217204, 2001.

[49] B. Heinrich, R. Urban, and G. Woltersdorf. *J. Appl. Phys.*, 91:7523, 2002.

[50] C. Kittel. *Phys. Rev.*, 73:155, 1948.

[51] Y. Nakatani, Y. Uesaka, and N. Hayashi. *Jpn. J. Appl. Phys.*, 28:2485, 1989.

[52] M. G. Cottam and Z. Haghshenasfard. *Physics in Canada*, 72:63, 2016.

[53] H. T. Nguyen, T. M. Nguyen, and M. G. Cottam. *Phys. Rev. B*, 76:134413, 2007.

[54] C. T. Boone, J. A. Katine, J. R. Childress, V. Tiberkevich, A. Slavin, J. Zhu, X. Cheng, and I. N. Krivorotov. *Phys. Rev. Lett.*, 103:167601, 2009.

[55] H. T. Nguyen, A. Akbari-Sharbaf, and M. G. Cottam. *Phys. Rev. B*, 83:214423, 2011.

[56] V. S. L'vov. *Wave Turbulence under Parametric Excitation: Application to Magnets*. Springer, 1994.

[57] Z. Haghshenasfard, H. Nguyen, and M. G. Cottam. *Acta Physica Polonica A*, 127:192, 2015.

[58] H. T. Nguyen and M. G. Cottam. *Phys. Rev. B*, 89:144424, 2014.

[59] S. O. Demokritov, V. E. Demidov, O. Dzyapko, G. A. Melkov, A. A. Serga, B. Hillebrands, and A. N. Slavin. *Nature*, 443:430, 2006.

[60] A. V. Chumak, G. A. Melkov, V. E. Demidov, O. Dzyapko, V. L. Safonov, and S. O. Demokritov. *Phys. Rev. Lett.*, 102:187205, 2009.

[61] S. M. Rezende. *J. Phys. Condens. Matter*, 22:164211, 2010.

[62] G. A. Melkov, Yu. V. Koblyanskiy, R. A. Slipets, A. V. Talalaevskij, and A. N. Slavin. *Phys. Rev. B*, 79:134411, 2009.

[63] H. Ulrichs, V. E. Demidov, S. O. Demokritov, and S. Urazhdin. *Phys. Rev. B*, 84:094401, 2011.

[64] M. Weiler, G. Woltersdorf, M. Althammer, H. Huebl, and S. T. B. Goennenwein. In M. Wu and A. E. Hoffmann, editors, *Recent Advances in Magnetic Insulators- From Spintronics to Microwave Applications*, page 123. Elsevier, 2012.

[65] D. N. Chartoryzhskii, B. A. Kalinikos, and O. G. Vendik. *Solid State Commun.*, 20:985, 1976.

[66] G. Wiese, P. Kabos, and C. E. Patton. *J. Appl. Phys.*, 74:1218, 1993.

[67] V. B. Cherepanov and A. N. Slavin. Size effects in parametric excitation of spin waves in ferrites. In G. Srinivasan and A. N. Slavin, editors, *High Frequency Processes in Magnetic Materials*, page 250. World Scientific, 1995.

[68] R. N. Costa Filho, M. G. Cottam, and G. A. Farias. *Phys. Rev. B*, 62:6545, 2000.

[69] H. T. Nguyen and M. G. Cottam. *J. Phys. Condens. Matter*, 23:126004, 2011.

[70] T. M. Nguyen and M. G. Cottam. *Phys. Rev. B*, 71:094406, 2005.

[71] H. T. Nguyen and M. G. Cottam. *J. Phys. D: Appl. Phys.*, 44:315001, 2011.

[72] G. Wiese, P. Kabos, and C. E. Patton. *Phys. Rev. B*, 51:15085, 1995.

[73] P. Lupo, Z. Haghshenasfard, M. G. Cottam, and A. O. Adeyeye. *Phys. Rev. B*, 94:214431, 2016.

[74] K. Wagner, A. Kakay, K. Schultheiss, A. Henschke, T. Sebastian, and H. Schultheiss. *Nature Nanotech.*, 11:432, 2016.

[75] D. Kumar A. Haldar and A. O. Adeyeye. *Nature Nanotech.*, 11:437, 2016.

[76] D. Kumar, O. Dmytriiev, S. Ponraj, and A. Barman. *J. Phys. D: Appl. Phys.*, 45:015001, 2012.

[77] G. Gubbiotti, P. Malago, S. Fin, S. Tacchi, L. Giovannini, D. Bisero, M. Madami, G. Carlotti, J. Ding, A. O. Adeyeye, and R. Zivieri. *Phys. Rev. B*, 90:024419, 2014.

[78] G. Gubbiotti, S. Tacchi, H. T. Nguyen, M. Madami, G. Carlotti, K. Nakano, T. Ono, and M. G. Cottam. *Phys. Rev. B*, 87:094406, 2013.

[79] Q. Wang, H. Zhang, G. Ma, Y. Liao, X. Tang, and Z. Zhong. *Scientific Reports*, 4:5917, 2014.

[80] S. A. Bunyaev, V. O. Golub, O. Yu. Salyuk, E. V. Tartakovskaya, N. M. Santos, A. A. Timopheev, N. A. Sobolev, A. A. Serga, A. V. Chumak, B. Hillebrands, and G. N. Kakazei. *Scientific Reports*, 5:18480, 2015.

[81] G. Gubbiotti, M. Kostylev, N. Sergeeva, M. Conti, G. Carlotti, T. Ono, A. N. Slavin, and A. Stashkevich. *Phys. Rev. B*, 70:224422, 2004.

[82] X. M. Liu, P. Lupo, M. G. Cottam, and A. O. Adeyeye. *J. Phys. D: Appl. Phys.*, 118, 2015.

[83] S. Goolaup, A. O. Adeyeye, N. Singh, and G. Gubbiotti. *Phys. Rev. B*, 75:144430, 2007.

[84] I. S. Maksymov and M. Kostylev. *Physica E: Low. Dimens. Syst. Nanostruct.*, 69:253, 2015.

[85] S. Tacchi, M. Madami, G. Gubbiotti, G. Carlotti, S. Goolaup, A. O. Adeyeye, N. Singh, and M. P. Kostylev. *Phys. Rev. B*, 82:184408, 2010.

[86] X. M. Liu, H. T. Nguyen, J. Ding, M. G. Cottam, and A. O. Adeyeye. *Phys. Rev. B*, 90:064428, 2014.

[87] Z. Haghshenasfard and M. G. Cottam. *J. Phys. Condens. Matter*, 28:186001, 2016.

[88] M. R. Scheinfein and E. A. Price. LLG micromagnetics simulator, software for micromagnetic simulations, http//llgmicro.hom.mindspring.com (last access: 24/09/2016).

[89] M. Kostylev, Z. Yang, I. S. Maksymov, J. Ding, S. Samarin, and A. O. Adeyeye. *J. Phys. D: Appl. Phys*, 119:103903, 2016.

[90] P. A. Grünberg. *Prog. Surf. Sci.*, 18:1, 1985.

[91] C. W. Sandweg, Y. Kajiwara, A. V. Chumak, A. A. Serga, V. I. Vasyuchka, M. B. Jungfleisch, E. Saitoh, and B. Hillebrands. *Phys. Rev. Lett.*, 106:216601, 2011.

[92] A. A. Serga, C. W. Sandweg, V. I. Vasyuchka, M. B. Jungfleisch, B. Hillebrands, A. Kreisel, P. Kopietz, and M. P. Kostylev. *Phys. Rev. B*, 86:134403, 2012.

[93] H. T. Nguyen, G. Gubbiotti, M. Madami, S. Tacchi, and M. G. Cottam. *Microelectr J*, 40:598, 2009.

[94] G. Gubbiotti, M. Madami, S. Tacchi, G. Carlotti, H. Tanigawa, and T. Ono. *J. Phys D: Appl. Phys*, 41:134023, 2008.

[95] Z. Duan, I. N. Krivorotov, R. E. Arias, N. Reckers, S. Stienen, and J. Lindner. *Phys. Rev. B*, 92:104424, 2015.

[96] J. Ding, M. Kostylev, and A. O. Adeyeye. *Phys. Rev. Lett.*, 107:047205, 2011.

[97] S. S. Kalarickal, P. Krivosik, M. Wu, C. E. Patton, M. L. Schneider, P. Kabos, T. J. Silva, and J. P. Nibarger. *J. Appl. Phys*, 99:093909, 2006.

[98] A. Aharoni. *J. Appl. Phys*, 83:13432, 1998.

[99] W. F. Brown. *Magnetostatic Principles in Ferromagnetism*. North-Holland, 1962.

[100] Z. K. Wang, M. H. Kuok, S. C. Ng, D. J. Lockwood, M. G. Cottam, K. Nielsch, R. B. Wehrspohn, and U. Gösele. *Phys. Rev. Lett.*, 89:027201, 2002.

[101] Z. Haghshenasfard and M. G. Cottam. *IEEE Magnetics Letters*, 7:1, 2016.

[102] S. M. Rezende. *Phys. Rev. B*, 79:174411, 2009.

[103] Z. Haghshenasfard, H. T. Nguyen, and M. G. Cottam. *J. Magn. Magn. Mat.*, 426:380, 2017.

[104] M. Bauer, J. Fassbender, B. Hillebrands, and R. L. Stamps. *Phys. Rev. B*, 61:3410, 2000.

[105] W. Wernsdorfer, C. Thirion, and D. Mailly. *Nature Mater.*, 2:524, 2003.

[106] A. Yu. Dobin and R. H. Victora. *J. Appl. Phys.*, 95:7139, 2004.

[107] C. Stamm, I. Tudosa, H. C. Siegmann, J. Stöhr, A. Yu. Dobin, G. Woltersdorf, B. Heinrich, and A. Vaterlaus. *Phys. Rev. Lett.*, 94:197603, 2005.

[108] M. dAquino, W. Scholz, T. Schrefl, C. Serpico, and J. Fidler. *J. Appl. Phys.*, 95:7055, 2004.

[109] P. H. Bryant, C. D. Jeffries, and K. Nakamura. *Phys. Rev. A*, 38:4223, 1988.

[110] G. Gubbiotti, H. T. Nguyen, R. Hiramatsu, S. Tacchi, M. Madami, M. G. Cottam, and T. Ono. *J. Phys. D, Appl. Phys*, 47, 2014.

[111] Z. Haghshenasfard and M. G. Cottam. *J. Phys. Condens. Matter*, 29:045803, 2017.

[112] N. Zagury and S. M. Rezende. *Phys. Rev. B*, 4:201, 1971.

[113] S. M. Rezende and N. Zagury. *Physics Letters A*, 29:47, 1969.

[114] R. J. Glauber. *Phys. Rev.*, 131:2766, 1963.

[115] S. M. Rezende. *Phys. Rev. B*, 81:020414, 2010.

[116] V. E. Demidov, O. Dzyapko, M. Buchmeier, T. Stockhoff, G. Schmitz, G. A. Melkov, and S. O. Demokritov. *Phys. Rev. Lett.*, 101:257201, 2008.

[117] V. E. Demidov, O. Dzyapko, S. O. Demokritov, G. A. Melkov, and A. N. Slavin. *Phys. Rev. Lett.*, 100:047205, 2008.

[118] O. Dzyapko, V. E. Demidov, G. A. Melkov, and S. O. Demokritov. *Phil. Trans. R. Soc. A*, 369:3575, 2011.

[119] C. B. de Araujo and S. M. Rezende. *Phys. Rev. B*, 9:3074, 1974.

[120] C. B. de Araujo. *Phys. Rev. B*, 10:3961, 1974.

[121] D. F. Walls and G. J. Milburn. *Quantum Optics*. Springer, 2008.

[122] S. M. Rezende. Magnon coherent states and condensates. In S. O. Demokritov and A. N. Slavin, editors, *Magnonics From Fundamentals to Applications*. Springer, 2013.

[123] S. O. Demokritov, V. E. Demidov, O. Dzyapko, G. A. Melkov, and A. N. Slavin. *New J. Phys.*, 10:045029, 2008.

[124] Z. Ficek and P. D. Drummond. *Quantum Squeezing*. Springer, 2013.

[125] H. Yuen and J. Shapiro. *IEEE Trans. Inf. Theory*, 24:657, 1978.

[126] R. E. Slusher, L. W. Hollberg, B. Yurke, J. C. Mertz, and J. F. Valley. *Phys. Rev. Lett.*, 55:2409, 1985.

[127] I. Averbukh and M. Shapiro. *Phys. Rev. A*, 47:5086, 1993.

[128] S. L. Johnson, P. Beaud, E. Vorobeva, C. J. Milne, E. D. Murray, S. Fahy, and G. Ingold. *Phys. Rev. Lett.*, 102:175503, 2009.

[129] M. Artoni and J. L. Birman. *Phys. Rev. B*, 44:3736, 1991.

[130] R. Auccaise, A. G. Araujo-Ferreira, R. S. Sarthour, I. S. Oliveira, T. J. Bonagamba, and I. Roditi. *Phys. Rev. Lett.*, 114:043604, 2015.

[131] M. Kitagawa and M. Ueda. *Phys. Rev. A*, 47:5138, 1993.

[132] J. Zhao, A. V. Bragas, D. J. Lockwood, and R. Merlin. *Phys. Rev. Lett.*, 93:107203, 2004.

[133] J. Zhao, A. V. Bragas, R. Merlin, and D. J. Lockwood. *Phys. Rev. B*, 73:184434, 2006.

[134] F. Peng. *Europhys. Lett.*, 54:688, 2001.

[135] F. Peng. *Physica B*, 334:183, 2003.

[136] J. Wang, Z. Cheng, Y. Ping, J. Wan, A. A. Serga, and Y. Zhang. *Phys. Lett. A*, 353:427, 2006.

[137] M. O. Scully and M. S. Zubairy. *Quantum Optics*. Cambridge University Press, 1997.

[138] R. I. Joseph and E. Schlömann. *J. Appl. Phys*, 38, 1967.

[139] R. Loudon. *The Quantum Theory of Light*. Oxford Science Publications, 2000.

[140] F. Keffer. *Ferromagnetism / Ferromagnetismus*. Springer, Heidelberg, 1966.

[141] V. E. Zakharov, V. S. L'vov, and S. S. Starobinets. *Phys. Usp.*, 17:896, 1975.

[142] J. W. Negele and H. Orland. *Quantum Many-particle Systems*. Addison-Wesley Publishing Company, 1998.

[143] G. Rickayzen. *Green's Functions and Condensed Matter*. Dover Publications, 2003.

[144] Z. Haghshenasfard and M. G. Cottam. *J. Phys. Condens. Matter*, 29:195801, 2017.

[145] C. C. Gerry and J. H. Eberly. *Phys. Rev. A*, 42:6805, 1990.

[146] A. Joshi and R. R. Puri. *Phys. Rev. A*, 42:4336, 1990.

[147] F. DellAnno, S. De Siena, and F. Illuminati. *Phys. Rep.*, 428:53, 2006.

[148] C. Eichler, D. Bozyigit, C. Lang, M. Baur, L. Steffen, J. M. Fink, S. Filipp, and A. Wallraff. *Phys. Rev. Lett.*, 107:113601, 2011.

[149] M. M. Ashraf and M. S. K Razmi. *Phys. Rev. A*, 45:8121, 1992.

[150] C. T. Lee. *Phys. Rev. A*, 42:1608, 1990.

[151] B. Arvind and N. Mukunda. *J. Phys. A*, 29:5855, 1996.

[152] M. H. Nader. *Canad. J. Phys.*, 85:1071, 2007.

[153] M. Mohammadi. *Europ. Phys. J. D*, 62:255, 2011.

[154] C. Gerry and P. Knight. *Introductory Quantum Optics*. Cambridge, 2005.

[155] H. Paul. *Rev. Mod. Phys.*, 54:1061, 1982.

[156] W. G. Griffin and P. N. Pusey. *Phys. Rev. Lett.*, 43:1100, 1979.

[157] M. M. Tehrani and L. Mandel. *Phys. Rev. A*, 17:677, 1978.

[158] K. A. Ross, L. Savary, B. D. Gaulin, and L. Balents. *Phys. Rev. X*, 1:021002, 2011.

Curriculum Vitae

Name:	Zahra Haghshenasfard
Post-Secondary Education and Degrees:	University of Western Ontario London, ON, Canada 2013 - 2017 Ph.D. in Physics
Honors and Awards:	Robert and Ruth Lumsden Fellowship in Science University of Western Ontario 2016 Teaching Assistant Award of Excellence University of Western Ontario 2014 - 2015
Publications:	Z. Haghshenasfard, M. H. Naderi, and M. Soltanolkotabi, "*Subluminal to superluminal propagation of an optical pulse in an f-deformed Bose–Einstein condensate*", J. Phys. B: At. Mol. Opt. Phys. 41 165501 (2008). Z. Haghshenasfard, M. H. Naderi, and M. Soltanolkotabi, "*The influence of atomic collision on collective spontaneous emission from an f-deformed Bose–Einstein condensate*", J. Phys. B: At. Mol. Opt. Phys. 42 065505 (2009). Z. Haghshenasfard, M. H. Naderi, and M. Soltanolkotabi, "*Controlling subluminal to superluminal behavior of group velocity in an f-deformed Bose–Einstein condensate beyond the rotating wave approximation*", Optics Communications 282 3530 (2009). Z. Haghshenasfard, M. H. Naderi, and M. Soltanolkotabi, "*The influence of atomic collisions on spectrum of light scattered from an f-deformed Bose–Einstein condensate*", J. Phys. B: At. Mol. Opt. Phys. 42 195501 (2009).

Z. Haghshenasfard and M. G. Cottam,
"*Controlling the repetition rate of a mode-locked laser using an f-deformed Bose-Einstein condensate*", J. Phys. B: At. Mol. Opt. Phys. 45 025501 (2012).

Z. Haghshenasfard and M. G. Cottam,
"*Collective spontaneous emission from a Bose-Einstein condensate in the framework of a multiphoton q-deformed Dicke model*",
Eur. Phys. J. D. 66 30059 (2012).

Z. Haghshenasfard and M. G. Cottam,
"*q-deformed model of nonclassical quantum-statistical behavior for an atom laser*",
Eur. Phys. J. D. 67 195 (2013).

Z. Haghshenasfard, H. T. Nguyen, and M. G. Cottam,
"*Spin-wave instability theory for ferromagnetic nanostructures*",
Acta Phys Pol A 127 192 (2015).

M. G. Cottam and Z. Haghshenasfard,
"*Progresses for magnons in ferromagnetic nanostructures*",
Physics in Canada 72, 63 (2016).

Z. Haghshenasfard and M. G. Cottam,
"*Spin-wave instabilities of ferromagnetic nanowire stripes under parallel pumping*",
J. Phys. Condens. Matter 28, 18 (2016).

P. Lupo, Z. Haghshenasfard, M. G. Cottam, and A. O. Adeyeye,
"*Ferromagnetic resonance study of interface coupling for spin waves in narrow NiFe/Ru/NiFe multilayer nanowires*", Phys. Rev. B 94, 214431 (2016).

Z. Haghshenasfard and M. G. Cottam,
"*Parallel Pumping of Spin Waves for Ferromagnetic Nanowires and Nanotubes With Circular Cross Sections*", IEEE Magnetics Letters 1, 7 (2016).

Z. Haghshenasfard, H. T. Nguyen, and M. G. Cottam,
"*Suhl instabilities for spin waves in ferromagnetic nanostripes and ultrathin films*",
J. Magn. Magn. Mat. 426, 380 (2017).

Z. Haghshenasfard and M. G. Cottam,
"*Quantum statistics and squeezing for a microwave-driven interacting magnon system*", J. Phys. Condens. Matter 29, 045803 (2017).

Z. Haghshenasfard and M. G. Cottam, "*Quantum statistics for a two-mode magnon system with microwave pumping: Application to coupled ferromagnetic nanowires*",
J. Phys. Condens. Matter 29, 195801 (2017).